

University of Windsor

## Scholarship at UWindor

---

Electronic Theses and Dissertations

Theses, Dissertations, and Major Papers

---

2016

### Wake characteristics of single and tandem emergent cylinders in shallow open channel flow

Mehdi Heidari  
*University of Windsor*

Follow this and additional works at: <https://scholar.uwindsor.ca/etd>

---

#### Recommended Citation

Heidari, Mehdi, "Wake characteristics of single and tandem emergent cylinders in shallow open channel flow" (2016). *Electronic Theses and Dissertations*. 5733.

<https://scholar.uwindsor.ca/etd/5733>

This online database contains the full-text of PhD dissertations and Masters' theses of University of Windsor students from 1954 forward. These documents are made available for personal study and research purposes only, in accordance with the Canadian Copyright Act and the Creative Commons license—CC BY-NC-ND (Attribution, Non-Commercial, No Derivative Works). Under this license, works must always be attributed to the copyright holder (original author), cannot be used for any commercial purposes, and may not be altered. Any other use would require the permission of the copyright holder. Students may inquire about withdrawing their dissertation and/or thesis from this database. For additional inquiries, please contact the repository administrator via email ([scholarship@uwindsor.ca](mailto:scholarship@uwindsor.ca)) or by telephone at 519-253-3000ext. 3208.

# Wake characteristics of single and tandem emergent cylinders in shallow open channel flow

By

Mehdi Heidari

A Dissertation

Submitted to the Faculty of Graduate Studies  
through Civil and Environmental Engineering  
in Partial Fulfillment of the Requirements for  
the Degree of Doctor of Philosophy at the  
University of Windsor

Windsor, Ontario, Canada

2016

© 2016 Mehdi Heidari

# Wake Characteristics of Single and Tandem Emergent Cylinders in Shallow Open Channel Flow

by

Mehdi Heidari

APPROVED BY:

---

A.S. Ramamurthy, External Examiner  
Concordia University

---

R. Barron  
Department of Mechanical, Automotive & Materials Engineering

---

S. Cheng  
Department of Civil & Environmental Engineering

---

N. Biswas  
Department of Civil & Environmental Engineering

---

R. Balachandar, Co-advisor  
Department of Civil & Environmental Engineering

---

V. Roussinova, Co-advisor  
Department of Civil & Environmental Engineering

20 May 2016

## DECLARATION OF CO-AUTHORSHIP / PREVIOUS PUBLICATION

### I. Co-Authorship Declaration

I hereby declare that this thesis incorporates material that is result of joint research, as follows:

*This thesis incorporates the outcome of a research undertaken under the supervision of Dr. Vesselina Roussinova and Professor Ram Balachandar. The collaboration is covered in chapters 4, 5, 6 and 7 of the thesis. In all cases, the key ideas, primary contributions, experimental designs, data analysis and interpretation, were performed by the author, and the contribution of co-authors was primarily through the provision of supervision.*

I am aware of the University of Windsor Senate Policy on Authorship and I certify that I have properly acknowledged the contribution of other researchers to my thesis, and have obtained written permission from each of the co-author(s) to include the above material(s) in my thesis.

I certify that, with the above qualification, this thesis, and the research to which it refers, is the product of my own work.

### II. Declaration of Previous Publication

This thesis includes 3 original papers that have been previously published/submitted for publication in peer reviewed journals, as follows:

Thesis Chapter	Publication title/full citation	Publication status
<i>Chapter 5</i>	Characteristics of flow past a slender, emergent cylinder under shallow open channel condition	<i>To be submitted</i>
<i>Chapter 5</i>	Experimental study of wake characteristics of shallow flow past a single cylinder, <i>River flow 2016</i>	<i>Accepted</i>
<i>Chapter 6</i>	POD analysis on the wake of an emergent single cylinder in a shallow open channel flow	<i>To be submitted</i>



I certify that I have obtained a written permission from the copyright owner(s) to include the above published material(s) in my thesis. I certify that the above material describes work completed during my registration as graduate student at the University of Windsor.

I declare that, to the best of my knowledge, my thesis does not infringe upon anyone's copyright nor violate any proprietary rights and that any ideas, techniques, quotations, or any other material from the work of other people included in my thesis, published or otherwise, are fully acknowledged in accordance with the standard referencing practices. Furthermore, to the extent that I have included copyrighted material that surpasses the bounds of fair dealing within the meaning of the Canada Copyright Act, I certify that I have obtained a written permission from the copyright owner(s) to include such material(s) in my thesis.

I declare that this is a true copy of my thesis, including any final revisions, as approved by my thesis committee and the Graduate Studies office, and that this thesis has not been submitted for a higher degree to any other University or Institution.

## ABSTRACT

The present thesis deals with the vertical variability of the wake characteristics behind emergent single and tandem circular cylinders in shallow open channel flow at two Reynolds numbers ( $Re_D = 925, 3000$ ) in order to conceptually investigate the flow past vegetation. The tandem configuration includes two and three slender cylinders arranged in-line with different gap lengths ( $G$ ) while the cylinders are rigid with a small diameter ( $D = 6.4$  mm). The experiments were conducted in a wide water flume, where a small blockage ratio ( $\sim 0.5\%$ ) was achievable. Velocity measurement was performed using particle image velocimetry (PIV) in vertical and horizontal planes in the wake region. The focus of the study is to explore the wake flow characteristics in terms of mean velocity profiles, turbulent parameters and coherent structures along the water depth for all test cases. Proper orthogonal decomposition (POD) was applied to educe information about the coherent structures in the flow in the different horizontal planes.

The results show that the bed and the free surface influence the wake development at both Reynolds numbers for all test cases. The bed suppression effect was found stronger at the lower Reynolds number, as the transverse growth of the wake was more restricted compared to the high Reynolds number flow. The free surface shows more deformation in the wake region at high Reynolds number and results in lower turbulence compared to the low Reynolds number flow. The size, shape and development of the re-circulation region behind the single cylinder also indicate vertical variability at both Reynolds numbers.

The POD results indicate that in the mid-depth and near-free surface planes, the von Kármán vortex street and the separated shear layer (SSL) instability are the dominant mechanisms at both Reynolds numbers. In the near-bed plane, the most energetic coherent structures are determined to be the base vortex, horseshoe vortex structures and SSL instability at low Reynolds number, while at high Reynolds number the dominant structures are von Kármán vortex structures and the SSL instability.

In the case of tandem cylinders, the gap length ( $G$ ) between the cylinders has a key role in the wake flow characteristics. At  $G = 1.9D$ , the downstream cylinder is sheltered by the lead cylinder for both Reynolds numbers, particularly in the mid-depth region. While at  $G = 3.9D$  the second cylinder has local effect on the wake flow for both

Reynolds numbers, particularly in the mid-depth. A higher turbulence is noticed in the wake region for the larger gap. The bed suppression effect is noticed for all tandem cases with the stronger effect at lower Reynolds number. Wider turbulence profiles are noticed for the larger gap near the free surface at low Reynolds number, while such expansion is not observed at the high Reynolds number flow.

## DEDICATION

To  
My parents  
and  
My wife, *Mozhgan*

## ACKNOWLEDGEMENTS

I should acknowledge many people who contributed to this work and made this dissertation possible. First, my sincere thanks and gratitude go to my advisors, Prof. Balachandar and Dr. Roussinova for their guidance, ideas, patience and support during my PhD study at the University of Windsor.

I would like to express special appreciations to Dr. Barron for his valuable time and suggestions for the study, particularly during the group meetings. Special gratitude should go to Dr. Shinneeb, who has been kind enough to teach me the fundamentals of PIV and share his ideas for this study. Special thanks to Matt St. Louis, for helping me and preparing the water flume for conducting the experiments and letting me borrow everything from the workshop in support of my study.

I would also like to thank all of my friends in our group; Vimal, Kohei, Gus, Mohammadali, Sudharsan, Vinod, with whom we shared ideas and group discussions for the last 4 years.

Last but not the least, appreciations go to my wife and our parents for their sacrifices, patience, supports and our loss of precious time together.

**TABLE OF CONTENTS**

DECLARATION OF CO-AUTHORSHIP / PREVIOUS PUBLICATIONS..... iii  
ABSTRACT.....v  
DEDICATION..... vii  
ACKNOWLEDGEMENTS..... viii  
LIST OF TABLES..... xiii  
LIST OF FIGURES ..... xv  
LIST OF SYMBOLS ..... xxii

**Chapter 1: INTRODUCTION**

1.1 General view..... 1  
1.2 Shallow flow ..... 3  
1.3 Modeling the vegetation flow ..... 4  
1.4 Objectives..... 6  
1.5 Thesis scope..... 7

**Chapter 2: LITERATURE REVIEW**

2.1 General comments..... 8  
2.2 Wake flow..... 8  
2.3 Bed-mounted finite cylinders..... 10  
    2.3.1 Near-bed effect..... 11  
        2.3.1.1 Horseshoe vortex structures..... 12  
        2.3.1.2 Base vortex..... 16  
    2.3.2 Tip vortex structures..... 18  
    2.3.3 Free surface effect..... 21  
2.4 Tandem cylinders..... 24

### **Chapter 3: EXPERIMENTAL DETAILS**

3.1 General comments.....	36
3.2 Experimental setup.....	36
3.2.1 Open channel re-circulating flume.....	36
3.2.2 Cylinders in flow.....	37
3.2.3 Approaching flow.....	38
3.2.4 Measurement locations and details.....	39
3.3 Particle image velocimetry.....	40
3.3.1 General remarks.....	40
3.3.2 Seeding particles.....	41
3.3.3 Laser and optical setup.....	43
3.3.4 Camera set.....	44
3.3.5 Image analysis.....	44
3.3.6 Removal and replacement of spurious vectors.....	46
3.4 Uncertainty analysis.....	48

### **Chapter 4: APPROACHING OPEN CHANNEL FLOW**

4.1 General comments.....	68
4.2 Introduction .....	68
4.3 A brief review of near-wall turbulent flow.....	71
4.4 Estimation of friction velocity from velocity measurements.....	72
4.4.1 Power law.....	73
4.4.2 Total shear stress method.....	75
4.5 Results.....	76
4.5.1 Friction velocity.....	76
4.5.2 Evaluation of von Kármán coefficient.....	77
4.5.2.1 Derivative method.....	77
4.5.2.2 Scatter method.....	77
4.5.2.3 Fitting method (least-squares method).....	78

4.5.3 Velocity profile and log-law.....	79
4.5.4 Eddy viscosity.....	80
4.5.5 Mixing length.....	81
4.5.6 von Kármán coefficient.....	82
4.6 Conclusions.....	83

## **Chapter 5: SHALLOW FLOW PASSING A SINGLE CYLINDER**

5.1 General remarks.....	97
5.2 Instantaneous velocity pattern.....	98
5.2.1 Instantaneous velocity vectors in horizontal ( $x, z$ ) planes.....	98
5.2.2 Instantaneous velocity vectors in vertical ( $x, y$ ) plane.....	100
5.3 Mean velocity fields of the wake flow.....	102
5.4 Validation of the far-wake region.....	106
5.5 Near-wake flow development.....	108
5.6 Time-averaged results.....	111
5.6.1 Horizontal plane profiles.....	111
5.6.2 Vertical plane profiles .....	118
5.7 Conclusion .....	123

## **Chapter 6: COHERENT STRUCTURES**

6.1 General description.....	142
6.1.1 Coherent structures.....	142
6.1.2 Proper orthogonal decomposition (POD) method.....	144
6.1.2.1 POD analysis.....	144
6.2 Energy of the POD modes.....	148
6.3 POD modal shapes.....	150
6.4 Effect of the bed on the structures of the near-wake region .....	155
6.5 Eduction of large-scale structures by POD reconstructed velocity field.....	157



6.6 Conclusion .....	160
----------------------	-----

### **Chapter 7: SHALLOW FLOW PASSING TANDEM CYLINDERS**

7.1 General remarks.....	175
7.2 Proper length scale.....	175
7.3 Time-averaged results in horizontal plane profiles.....	177
7.4 Conclusion .....	184

### **Chapter 8: CONCLUSIONS AND FUTURE RECOMMENDATIONS**

8.1 Main conclusions .....	199
8.2 Recommendations for future work .....	201

REFERENCES.....	202
VITA AUCTORIS.....	220

## LIST OF TABLES

Table 3.1: The flow properties of two Reynolds numbers .....	62
Table 3.2: The position, size and resolution of the fields-of-view (FOV) in different cylinder configurations at low Reynolds number flow .....	63
Table 3.3: The position, size and resolution of the fields-of-view (FOV) in different cylinder configurations at high Reynolds number flow .....	64
Table 3.4: Instrumentation used for the particle image velocimetry measurement ...	65
Table 3.5: Summary of uncertainty estimation of mean velocity using Student's t-distribution, Prasad and Westerweel methods for different horizontal and vertical FOVs at low Reynolds number flow .....	66
Table 3.6: Summary of uncertainty estimation of mean velocity using Student's t-distribution, Prasad and Westerweel methods for different horizontal and vertical FOVs at high Reynolds number flow .....	67
Table 4.1: Reported values of $\kappa$ from different sources .....	92
Table 4.2: Experimental details.....	93
Table 4.3: Bed shear velocity, $u_* \times 10^{-2}$ ( $\text{ms}^{-1}$ ) calculated using different power law methods .....	94
Table 4.4: Estimates for $u_* \times 10^{-2}$ ( $\text{ms}^{-1}$ ) for the present experiments using different power law methods .....	95
Table 4.5: Summary of the friction velocity calculated using total stress and power law methods. For power law methods, an average value is reported .....	95
Table 4.6: Comparison between different methods for $\kappa$ and B .....	96

Table 5.1: Selected experimental studies of flow passing a single circular cylinder	140
Table 5.2: Summary of different length scale values along the wake centreline.....	141

## LIST OF FIGURES

Figure 2.1: The wake flow formation behind an infinite circular cylinder in a steady uniform cross-flow (Sumner, 1999) .....	30
Figure 2.2: The wake flow classification behind a circular cylinder object positioned in a steady uniform cross-flow for different Reynolds numbers (Coutanceau and Defay, 1991).....	31
Figure 2.3: Flow structures around a finite length wall-mounted cylinder (Wang et al. 2006) .....	32
Figure 2.4: Connection of the tip vortex and the von Kármán tubes with the strands behind a wall-mounted square cylinder (Hosseini et al., 1997).....	32
Figure 2.5: Arch type vortex structures around a short length wall-mounted cylinder (Lee, 1997) .....	33
Figure 2.6: The mean vortex structures at free-end ( <i>a</i> ) and base ( <i>b</i> ) of the cylinder consequence of the tip and near-bed structures, respectively for different cylinder aspect ratios (Rostamy et al., 2012) .....	33
Figure 2.7: Mean separation pattern with the vortex core lines of different structures near the free surface in the near-wake region (Suh et al., 2011) .....	34
Figure 2.8: The flow classification for the circular cylinders in tandem at different gap lengths (Zhou and Yiu, 2006) .....	34
Figure 2.9: The flow classification for the square cylinders in tandem (Yen et al., 2008).....	35
Figure 3.1: The experimental flume setup .....	53

Figure 3.2: The cylinders configuration .....	54
Figure 3.3: A sample picture of cylinders in the flow (C2L) .....	55
Figure 3.4: The normalized streamwise velocity (a) and turbulence intensity (b) profiles for high and low Reynolds numbers on smooth bed .....	56
Figure 3.5: Schematic of the three horizontal planes of measurement as near-bed, mid-depth and near-free surface FOV and a vertical plane of measurement as the mid-plane FOV .....	57
Figure 3.6: Schematic diagram of PIV setup and the instruments .....	58
Figure 3.7: Schematic diagram of laser and camera setup arrangement for vertical plane (left) and horizontal plane (right) measurements .....	59
Figure 3.8: A sample field-of-view with spurious vectors shown in boxes .....	60
Figure 3.9: The U-uncertainty contours (%) for the single cylinder case at mid-depth in LR (a) and HR (b) flow based on Student t-distribution method .....	61
Figure 4.1: Typical turbulent flow regions in OCF .....	85
Figure 4.2: Variation of $\frac{dU^+}{dy^+}$ vs. $\frac{1}{y^+}$ using the derivative method .....	86
Figure 4.3: Determining $\kappa_s$ and $B_s$ for different experiments using scatter method .	87
Figure 4.4: Variation of $\frac{dU^+}{dy^+}$ vs. $\frac{1}{y^+}$ using the derivative method .....	88
Figure 4.5: Dimensionless eddy viscosity distribution based on Coles' wake function (a) and Krogstad's wake function (b) .....	89
Figure 4.6: Dimensionless mixing length distributions (outer scaling) .....	90
Figure 4.7: Dimensionless mixing length distributions (inner scaling) .....	90

Figure 4.8: Variation of $\kappa_1$ with $Re_\theta$ .....	91
Figure 5.1: Examples of instantaneous velocity fields measured in the low Reynolds number flow on the horizontal planes; mid-depth (a, b, c), near-bed (d, e, f) and near-free surface (g, h, i) .....	125
Figure 5.2: Examples of instantaneous velocity fields measured in the high Reynolds number flow on the horizontal planes; mid-depth (a, b, c), near-bed (d, e, f) and near-free surface (g, h, i) .....	126
Figure 5.3: Examples of instantaneous velocity fields measured in the vertical mid-plane; at low Reynolds number flow .....	127
Figure 5.4: Examples of instantaneous velocity fields measured in the vertical mid-plane; at high Reynolds number flow .....	128
Figure 5.5: Mean velocity vector fields measured on the horizontal planes at mid-depth (a, d), near-bed (b, e), and near-free surface (c, f) for low (LR) and high (HR) Reynolds numbers, respectively .....	129
Figure 5.6: Mean velocity vector fields measured on the vertical mid-plane ( $z/D = 0$ ) for low Reynolds number (a) and high Reynolds number (b) .....	130
Figure 5.7: Schematic of deficit scales in wake flow .....	131
Figure 5.8: The spanwise profiles at mid-depth located at $x = 10D$ : normalized mean streamwise velocity (a), deficit scale (b), dimensionless streamwise turbulence intensity (c), dimensionless spanwise turbulence intensity (d) and dimensionless shear stress (e) .....	132
Figure 5.9: The streamwise profiles at mid-depth located at central wake plane: normalized mean streamwise velocity (a), dimensionless streamwise turbulence intensity (b) and dimensionless spanwise turbulence intensity (c) .....	133

Figure 5.10: The normalized mean streamwise velocity profiles at different $x/D$ locations at mid-depth (a, b, c, d, e), near-bed (f, g, h, i, j) and near-free surface (k, l, m, n, o) planes. Open circle represents the LR case and solid circle represents the HR case .....	134
Figure 5.11: The streamwise turbulence intensity profiles at different $x/D$ locations at mid-depth (a, b, c, d, e), near-bed (f, g, h, i, j) and near-free surface (k, l, m, n, o) planes. Open circle represents the LR case and solid circle represents the HR case. The dotted lines show the location of the edges of the cylinder .....	135
Figure 5.12: The spanwise turbulence intensity profiles at different $x/D$ locations at mid-depth (a, b, c, d, e), near-bed (f, g, h, i, j) and near-free surface (k, l, m, n, o) planes. Open circle represents the LR case and solid circle represents the HR case .	136
Figure 5.13: The dimensionless shear stress profiles at different $x/D$ locations at mid-depth (a, b, c, d, e), near-bed (f, g, h, i, j) and near-free surface (k, l, m, n, o) planes. Open circle represents the LR case and solid circle represents the HR case .	137
Figure 5.14: Normalized mean streamwise velocity (a, b, c, d, e) and normalized mean vertical velocity profiles (f, g, h, i, j) at central wake plane at different $x/D$ locations. Open circle represents the LR case and solid circle represents the HR case .....	138
Figure 5.15: streamwise turbulence intensity (a, b, c, d, e), transversal turbulence intensity (f, g, h, i, j) and dimensionless shear stress (k, l, m, n, o) profiles at central wake plane at different $x/D$ locations. Open circle represents the LR case and solid circle represents the HR case .....	139
Figure 6.1: The number of snapshots effect on the contribution of TKE (%) of the first six modes .....	162

Figure 6.2: Turbulent kinetic energy (TKE) and their cumulative profiles for different POD modes at different horizontal planes at mid-depth (a), near-bed (b) and near-free surface (c) .....	163
Figure 6.3: Spatial POD modes in the mid-depth plane for LR in the form of normalized contours .....	164
Figure 6.4: Spatial POD modes in the mid-depth plane for HR in the form of normalized contours .....	165
Figure 6.5: Spatial POD modes in the near-free surface plane for LR in the form of normalized contours .....	166
Figure 6.6: Spatial POD modes in the near-free surface plane for HR in the form of normalized contours .....	167
Figure 6.7: Spatial POD modes in the near-bed plane for LR in the form of normalized contours .....	168
Figure 6.8: Spatial POD modes in the near-bed plane for HR in the form of normalized contours .....	169
Figure 6.9: Turbulent kinetic energy (TKE) and their cumulative profiles for different POD modes at near-bed surface for the reduced ( $6D \times 5D$ ) FOV .....	170
Figure 6.10: Spatial POD modes in the near-bed plane for LR in the form of normalized contours for the reduced ( $6D \times 5D$ ) FOV .....	171
Figure 6.11: Spatial POD modes in the near-bed plane for HR in the form of normalized contours for the reduced ( $6D \times 5D$ ) FOV .....	172



Figure 6.12: The instantaneous velocity vectors for original velocity vectors (I) Galilean decomposition of the reconstructed velocity vectors based on POD Modes 1 and 2 (II) Galilean decomposition of the reconstructed velocity vectors based on POD Modes 3 (III) in the mid-depth plane for LR .....	173
Figure 6.13: The instantaneous velocity vectors for original velocity vectors(I) Galilean decomposition of the reconstructed velocity vectors based on POD Modes 1 and 2 (II) Galilean decomposition of the reconstructed velocity vectors based on POD Modes 3(III) in the near-bed plane for LR .....	174
Figure 7.1: The normalized mean streamwise velocity profiles at different $x/D$ locations in mid-depth for LR (a, b, c, d) and HR (e, f, g, h).....	185
Figure 7.2: The normalized mean streamwise velocity profiles at different $(G+x)/D$ locations in mid-depth for LR (a, b, c, d) and HR (e, f, g, h) .....	186
Figure 7.3: The normalized mean streamwise velocity profiles at different $(G+x)/D$ locations in near-bed plane for LR (a, b, c, d) and HR (e, f, g, h) ...	187
Figure 7.4: The normalized mean streamwise velocity profiles at different $(G+x)/D$ locations in near-free surface plane for LR (a, b, c, d) and HR (e, f, g, h)	188
Figure 7.5: The streamwise turbulence intensity profiles at different $(G+x)/D$ locations in mid-depth plane for LR (a, b, c, d) and HR (e, f, g, h) .....	189
Figure 7.6: The streamwise turbulence intensity profiles at different $(G+x)/D$ locations in near-bed plane for LR (a, b, c, d) and HR (e, f, g, h) .....	190
Figure 7.7: The streamwise turbulence intensity profiles at different $(G+x)/D$ locations in near-free surface plane for LR (a, b, c, d) and HR (e, f, g, h) .....	191
Figure 7.8: The spanwise turbulence intensity profiles at different $(G+x)/D$ locations in mid-depth plane for LR (a, b, c, d) and HR (e, f, g, h) .....	192

Figure 7.9: The spanwise turbulence intensity profiles at different $(G+x)/D$ locations in near-bed plane for LR (a, b, c, d) and HR (e, f, g, h) .....	193
Figure 7.10: The spanwise turbulence intensity profiles at different $(G+x)/D$ locations in near-free surface plane for LR (a, b, c, d) and HR (e, f, g, h) .....	194
Figure 7.11: The Reynolds shear stress profiles at different $(G+x)/D$ locations in mid-depth plane for LR (a, b, c, d) and HR (e, f, g, h) .....	195
Figure 7.12: The Reynolds shear stress profiles at different $(G+x)/D$ locations in near-bed plane for LR (a, b, c, d) and HR (e, f, g, h) .....	196
Figure 7.13: The Reynolds shear stress profiles at different $(G+x)/D$ locations in near-free surface plane for LR (a, b, c, d) and HR (e, f, g, h) .....	197

## LIST OF SYMBOLS

$A$	the number of bits of the camera (-)
$a_n(t)$	temporal coefficient (-)
$AR$	cylinder aspect ratio (-)
$B$	log-law of the wall constant (-)
$B_f$	width of the flume (m)
$B_l$	law of the wall constant using fitting method (-)
$B_{bias}$	bias uncertainty
$B_s$	log-law of the wall constant using scatter method (-)
$C$	coefficient (-)
$C_f$	bed friction coefficient ( $C_f = 2 \left(\frac{u_*}{U_{mean}}\right)^2$ ) (-)
$C_l$	coefficient (-)
$D$	cylinder's diameter (m)
$d_p$	particles diameter (m)
$d_{ratio}$	particle image diameter to the pixel size ratio
$Fr$	Froude number ( $Fr = U_{mean} / \sqrt{gH}$ ) (-)
$f_s$	vortex shedding frequency ( $s^{-1}$ )
$f_d$	particle drag coefficient (-)
$G$	gap length (m)
$H$	water depth (m)
$k$	conversion factor in Manning Eq. ( $m^{1/3} s^{-1}$ )
$L$	submerged length of the cylinder (m)
$l_c$	length of the re-circulation region (m)
$L_e$	eddy length (m)
$lu_{rms}$	length scale (m)
$lw_{rms}$	length scale (m)
$n$	the Manning-Strickler's coefficient (-)
$R^2$	regression correlation coefficient (-)
$R_h$	hydraulic radius of the cross-section (m)

$Re_D$	wake / stem Reynolds number $Re_D = \frac{U_e D}{\nu}$ (-)
$Re_H$	Reynolds numbers based on H and $U_e$ (-)
$Re_R$	Reynolds number based on $R_h$ and $U_{mean}$ (-)
$Re_p$	particle Reynolds number ( $Re_p = \frac{d_p u_T}{\nu}$ ) (-)
$Re_\delta$	Reynolds number based on $\delta$ and $U_{mean}$ (-)
$Re_\theta$	Reynolds number based on $\theta$ and $U_e$ (-)
$S$	stability parameter ( $S = C_f D/H$ ) (-)
$S(x, y)$	displacement vector (m)
$S_0$	channel bed slope (-)
$S_t$	Strouhal number ( $S_t = f_s \frac{D}{U_e}$ ) (-)
$St$	Stokes number ( $St = \frac{\tau_p}{\tau_F}$ ) (-)
$TKE$	turbulent kinetic energy ( $m^2 s^{-2}$ )
$t_{95}$	value of the $t$ distribution at the 95% confidence level
$U$	mean streamwise velocity ( $ms^{-1}$ )
$U_\phi$	streamwise velocity for the POD modes
$U^+$	dimensionless mean streamwise velocity by the shear velocity (-)
$U^*$	normalized streamwise velocity (-)
$u_*$	shear velocity ( $ms^{-1}$ )
$U_{ave}$	cross-sectional average velocity ( $ms^{-1}$ )
$U_{Def}$	streamwise mean velocity deficit ( $ms^{-1}$ )
$U_{Def(Max)}$	maximum streamwise mean velocity deficit ( $ms^{-1}$ )
$U_e$	free stream velocity ( $ms^{-1}$ )
$U_{mean}$	depth-averaged velocity ( $ms^{-1}$ )
$U$	mean streamwise velocity ( $ms^{-1}$ )
$U_S$	mean streamwise approaching velocity at the specific depth ( $ms^{-1}$ )
$u_T$	particle settling velocity ( $ms^{-1}$ )
$u_{rms}$	streamwise root mean velocity ( $ms^{-1}$ )
$UN$	uncertainty value
$-\overline{u'v'}$	Reynolds shear stress ( $m^2 s^{-2}$ )

$-\overline{u'w'}$	Reynolds shear stress ( $\text{m}^2\text{s}^{-2}$ )
$V$	mean vertical velocity ( $\text{ms}^{-1}$ )
$V(IA, t)$	velocity vector in the IA ( $V(IA, t) = \frac{S}{\Delta t}$ ) ( $\text{ms}^{-1}$ )
$v_{rms}$	vertical root mean velocity ( $\text{ms}^{-1}$ )
$W_\phi$	spanwise velocity for the POD modes
$W^*$	normalized spanwise velocity (-)
$w_{rms}$	spanwise root mean velocity ( $\text{ms}^{-1}$ )
$w(\eta)$	wake function (-)
$x$	distance along the streamwise direction (m)
$y$	normal distance from the wall (m)
$y^+$	normalized distance from the wall by the viscous length (-)
$z$	distance along the spanwise direction (m)

### Greek letters

$\alpha$	Barenblatt parameters (-)
$\alpha_l$	coefficient (-)
$\beta_l$	coefficient (-)
$\Delta t$	time interval between two laser pulses (s)
$\delta$	boundary layer thickness (m)
$\delta^+$	Reynolds number based on $\delta$ and $u_*$ (-)
$\delta^*$	displacement thickness (m)
$\eta$	normalized distance from the wall ( $\eta = y/\delta$ ) (-)
$\theta$	momentum thickness (m)
$\phi_n(x)$	spatial POD modes (-)
$\ell_m$	mixing length (m)
$\kappa$	von Kármán coefficient (-)
$\kappa_l$	coefficient (-)
$\kappa_{der}$	von Kármán coefficient by derivative method (-)
$\kappa_l$	von Kármán coefficient by fitting method (-)

$\kappa_S$	von Kármán coefficient by scatter method (-)
$\rho$	fluid density ( $\text{kg m}^{-3}$ )
$\rho_P$	particles density ( $\text{kg m}^{-3}$ )
$\mu$	fluid dynamic viscosity (Pa s)
$\sigma$	standard deviation
$\tau_F$	fluid timescale (s)
$\tau_P$	particle response time (s)
$\nu$	fluid kinematic viscosity ( $\text{m}^2\text{s}^{-1}$ )
$\nu_t$	eddy viscosity ( $\text{m}^2\text{s}^{-1}$ )
$\Pi$	wake strength (-)
$\tau_w$	wall shear stress (Pa)
$\omega$	vorticity ( $\text{s}^{-1}$ )
$\omega^*$	normalized vorticity (-)

## **Chapter 1: INTRODUCTION**

### **1.1 General view**

Vegetation patches in rivers and streams can be modeled as bluff bodies that interact with flow. These fluid-vegetation interactions create complex flow patterns, promote turbulence and can influence river ecosystems. Therefore, it is important to understand the effect that vegetation in aquatic environment has on the flow characteristics of the surrounding environment, in an effort to provide information that can be applied to the river restoration projects. It is now well recognized that aquatic vegetation creates spatial heterogeneity in the stream velocity which promotes biodiversity (Luhar et al., 2008). In addition, aquatic plants and flow together can provide diverse habitat for numerous micro and macro organisms, different species of fish and animals. Turbulent mass exchange across the aquatic canopy–water interface can regulate the supply of nutrients needed for growth of these organisms which will sustain the life in the aquatic system (Ghisalberti and Nepf, 2009). Vegetation plays an effective role in improving the ecology of the aquatic systems by uptaking nutrients, producing oxygen, purifying water and by filtering heavy metals such as lead, mercury and arsenic. In each of these important functions the flow structure and turbulence that is created downstream from the vegetation in a river influence the ability of the river system to carry out these essential tasks. Thus, preservation efforts of natural or artificial river systems require better management of the aquatic vegetation, understanding of the restored hydrology and typical flow characteristics.

In river engineering, studies of flow through vegetation require information for the bed shear stress which will allow for improved prediction of the erosion, sediment transport and dispersion of the contaminants and nutrients in rivers. The ability to quantify the influence of vegetation and its roughness in particular, on river flow and floodplain hydraulics will also help engineers to control and manage the river watershed during floods. However, diversity of vegetation in terms of type, length, stem dimension, mechanical properties and its seasonal behavior makes accurate quantification of these flow parameters a very challenging task (Mckay and Fischenich, 2011). Studying

different aspects of vegetation and their effect on the flow will help to better understand the vegetation flow.

Earlier studies considered vegetation as a source of flow resistance, and in order to improve water conveyance in rivers, especially to reduce flooding during extreme flow conditions, plants have been removed from bed and banks (Kouwen and Unny, 1973). Hydraulic resistance of vegetation in rivers depends on different biomechanical properties of the vegetation such as flexural rigidity, degree of foliation, vegetation density, length of vegetation patch, height of the plants compared to the water depth (submerged or emergent plants), stem diameter and vegetation type. There are two basic methods for evaluation of the vegetation resistance. The first method is based on the bottom roughness coefficient arising from bed shear stress, which can be related to the size of bed roughness elements using proper roughness coefficient (e.g., Manning-Strickler's coefficient) in estimating the velocity. In the Manning equation, the cross-sectional average velocity ( $U_{ave}$ ) is estimated by

$$U_{ave} = \frac{k}{n} R_h^{2/3} S_0^{1/2} \quad (1.1)$$

Here,  $n$  is the Manning-Strickler's coefficient,  $R_h$  is the hydraulic radius of the channel cross-section,  $S_0$  is the channel bed slope and  $k$  is units' conversion factor. Although, the use of the conventional Manning equation for vegetated channels has provided favorable results on design models simulating floodplain flow, translating all vegetation characteristics into simple resistance parameters, such as Manning's friction factors, is complex and challenging (Luhar et al., 2008). For Manning's and other one dimensional models, the roughness for the channel reach is not explicitly stated but is represented by a single parameter whose value is taken as a measure for the overall resistance. Hydraulic researchers have criticized using this simple model to account for local turbulence throughout the flow depth, particularly in the case of emergent vegetation where resistance is exerted primarily from the stem drag rather than by the bed shear stress (Kadlec, 1990 and James et al., 2004). The second method includes vegetation resistance locally by accounting for the plants' drag (including the leaves and stems) through the flow depth which is added to the momentum equation as additional component of the total drag.



To quantify the vegetation resistance, flow through long submerged canopy has been conducted in laboratory flumes with rods or live vegetation. Fundamental laboratory studies of Wu (2008) and Nezu and Onitsuka (2001) have reported considerable effect of the vegetation canopy on flow and turbulence characteristics, secondary currents and coherent structures. Most studies on long and uniform patches of vegetation discuss enhanced deposition within vegetated regions due to the reduction of the velocity. On the other hand, vegetation promotes localized erosion near the boundaries of finite or short vegetated patches due to the increase of the shear stress along the vegetation edge (Fonseca et al., 1983; Bouma et al., 2007; Bennett et al., 2008; Rominger et al., 2010). Such localized effect is more apparent in the near-wake region behind the vegetation patch where the erosion process is severe. And yet, little has been discovered about the wake flow characteristics created by vegetation and the influence of the vegetation on the sediment transport and the erosion process in rivers. This requires a good evaluation of the wake formation due to the aquatic vegetation in natural streams. Since most of the streams and rivers are considered shallow, the wake evaluation in a shallow condition is an important subject which is considered in this study. Before discussing the objectives of this study, a brief review about the characteristics of the shallow flow and modeling the vegetation flow are discussed in the following sections.

## **1.2 Shallow flow**

Following Jirka and Uijttewaai (2004), open channel flows can be classified as shallow flow when the horizontal/transverse length scale of a typical eddy ( $L_e$ ) are significantly larger than the flow depth ( $H$ ) as the vertical length scale,

$$L_e/H \gg 1.0 \quad (1.2)$$

In addition, in open channel flows, the shear force on the channel boundaries (bed and sides) is the main resisting force opposed the driving component of the weight of the liquid along the slope of the channel. This shear-supporting force is another dynamic requirement for the shallow flow, which influences on the velocity profile. In the uniform flow condition the resisting force and the driving weight component are equal and cancel

each other out in the momentum equation which will result to stop accelerating/decelerating condition in the flow.

In shallow open channel flow, strong turbulence anisotropy in the largest scales is observed where the vertical scale of the largest structures is limited by the flow depth. At smaller scales, the turbulence properties are not so much linked to the flow geometry resulting in increasing isotropy towards the smallest dissipative scales. The sizes of the largest flow structures are governed by geometrical length scales of the boundaries and the dynamic response of the flow to channel geometry. The turbulence generated at the bed can reach the free surface where the vertical turbulence intensity is distributed into streamwise and spanwise (horizontal) components (Maheo, 1999). In shallow flow, due to the strength of the boundaries and the relatively small depth, the anisotropy effect may persist to the mid-depth of the flow. Furthermore, the confinement of the bed and free surface boundaries is responsible for filtering the large scale turbulent motions corresponding to large vertical coherent structures (larger than flow depth), meanwhile the vortical structures may grow into the two-dimensional large-scales in the spanwise direction. Thus, the length scales in turbulent motion can vary between small sizes of three-dimensional motion to large scales of two-dimensional turbulent motions in the spanwise direction, while some interactions between these small scale structures and the large ones may occur (Jirka and Uijttewaal, 2004).

Nezu and Nakagawa (1993) believe that the secondary currents are generated near the side walls of open channel flows and their influence on the flow in the central section of the channel is dependent on the width to depth ratio of the channel. They suggest that the side wall effects can be negligible on the flow in the central section for large width to depth ratio (larger than 5) in shallow open channel flows. This ratio can be a proper length scale for determining the shallowness in open channel flows.

### **1.3 Modeling the vegetation flow**

In examining the flow through vegetation it is important to determine the downstream flow characteristics. Systematic fundamental investigations on vegetation flow require careful understanding of the flow passing a vegetation patch which consists

of group of plants. Since plants can vary in size, shape, rigidity, vegetation density, etc., in the water current, a single laboratory flow study cannot address all types of plants in the rivers. In the present study, the plants in the flow are modeled as rigid, emergent cylinders. Although vegetation stems of various diameters have been reported in literature of flow passing rigid, emergent vegetation, the most cited diameter was found to vary between 6 to 12 mm while the stem Reynolds number ( $Re_D$ ) varies between 1,000 and 4,000 (Leonard and Luther, 1995; Lightbody and Nepf, 2006a). Here, the stem Reynolds number is based on the cylinder diameter ( $D$ ) and the free stream velocity ( $U_e$ ). Jarvela (2002) studied the flow resistance of natural plants in a laboratory flume. The plants were studied in various combinations under different flow conditions as submerged and emerged conditions in a total of 350 test runs. The willows (*Salix* sp.) with a diameter of 8.6 mm were used as emergent, leafless, rigid plants in the experiments, while  $620 \leq Re_D \leq 4,025$ . Nepf (1999) studied the drag, turbulence, and diffusion of nutrients in flow passing a canopy of *Spartina alterniflora* (smooth cord grass). The vegetation was modeled using wooden dowels with 6.4 mm diameter for various  $Re_D$  ranging between 200 and 600. Chen et al. (2012) studied the wake structure behind a finite circular patch of emergent vegetation of different patch diameters and densities. In their studies vegetation was modelled using wooden cylinders with the diameter of 6.4 mm. The stem Reynolds number in their experiment was kept constant at 630.

A common example of a type of aquatic vegetation that resembles smooth cylinder is soft-stem bulrush. Soft-stem bulrush is most commonly found in water depths of 0.15 to 0.3 m., but can grow in water up to depths of 1.5 m (Crites et al., 2006). These plants are found on the shorelines of the water bodies they inhabit, where the soil moisture is high. They grow tall, without any branch, with round stems that are around 6.4 mm in diameter. In this study the acrylic cylinder with a diameter of 6.4 mm is used to model this wetland plant as an obstruction in the shallow flow.

## 1.4 Objectives

Although, the characteristics of wake flow have been addressed in literature for a single bluff body, such studies are rarely focused on the wake flow behind a group of bluff bodies in a patch not just in the shallow flow but even in the deep case. Since the bluff bodies in a patch are sitting in the wake of the other bodies, the wake region behind the whole patch will be influenced not just because of the shape of any individual bluff body but also the arrangement of the bodies in the patch (Meftah et al., 2014). The plants in nature grow in a way that they can reach to the richest environment for growth. Diversity in the configuration of modeled plant such as tandem, side by side and staggered arrangement in the patches with sparse, dense or mixed densities will make the flow past vegetation study more difficult. Since considering the entire configurations in a study is not feasible, in the present study the focus is on the tandem configuration as the fundamental arrangement and a single bluff body (cylinder) for comparison with tandem cases.

The purpose of this work is to improve the understanding of the mean flow characteristics and turbulent structure of the wake flow behind the single and tandem configurations in the shallow depth. The objectives may be achieved by:

- Investigating the velocity, turbulence intensity, and Reynolds shear stress fields in the near-wake region
- Exploring the effects of bed and free surface on the near-wake region
- Examining the gap effect on the mean flow characteristics in tandem cases
- Studying the influence of Reynolds number on the mean flow characteristics in the single cylinder and tandem cases
- Investigating the dynamics of coherent structures which can be performed by exposing large coherent structures using the proper orthogonal decomposition (POD) technique

## 1.5 Thesis scope

A typical shallow wake is generated behind the rigid, emergent, cylindrical bluff bodies in a shallow open channel flow at two flow conditions with different Reynolds numbers. The depth of flow is maintained constant at 70 mm at all the experiments and the channel aspect ratio is 17.3. In all tests, the flow is in turbulent state and subcritical condition ( $Fr = 0.17$  and  $0.55$ ). The bed shear velocity and bed friction coefficient of the approaching shallow flow is estimated using velocity distribution. Particle image velocimetry (PIV) measurements are carried out at three horizontal planes near-bed, mid-depth and near-free surface along with a vertical plane at the wake centreline. The PIV technique can provide instantaneous two-dimensional velocity fields with acceptable spatial resolution to expose the large scale structures. 2000 image pairs are acquired in each plane in order to extract statistical information for the behaviour of mean flow, turbulence and coherent structures. The proper orthogonal decomposition (POD) technique is used for analysis of the energetic coherent structures.

A review of the available literature on the wake flow is presented in Chapter 2. Chapter 3 contains the description of the particle image velocimetry (PIV) system used in the present measurements, the flume setup, the cylinder's configurations and the estimates of the uncertainty in the velocity measurement. Chapter 4 investigates the approaching flow and appropriate estimation of the bed shear velocity. This chapter examines the validity of log-law of the wall in shallow open channel flow. Chapter 5 includes analysis of the single cylinder case in shallow flow. The discussion examines the effect of Reynolds number on the near-wake region in terms of the mean velocity and turbulence parameters at different planes. The coherent structures at the near-bed, mid - depth and near-free surface region has been educted using proper orthogonal decomposition (POD) technique and the results are discussed in Chapter 6. Chapter 7 covers the influence of gap distance between the cylinders on the wake flow behind the multiple cylinders in tandem configuration for two Reynolds numbers in shallow condition in terms of the mean velocity and turbulence parameter profiles. Lastly, the thesis ends by summarizing the conclusions and recommending a possible path for future study.

## **Chapter 2: LITERATURE REVIEW**

### **2.1 General comments**

This chapter provides a review of existing studies on wake flow generated behind a single cylinder and that produced by cylinders in a tandem configuration. First, the classical wake flow behind an infinite cylinder is presented. Next, the wake of a bed-mounted cylinder in an approaching boundary layer type flow is reviewed. Emphasis is given to wake studies in shallow open channels where the flow is influenced by the combined effect of the bed and the free surface. Review of the large scale coherent structures formed in the wake and in the junction region of the cylinder and the bed, along with their role in influencing the flow characteristics is highlighted. The case of the emergent rigid cylinder that pierces the free surface is also reviewed in the context of the interaction of the free surface and the wake perturbation. Finally, the flow passing tandem cylinders and its wake flow classification is discussed.

### **2.2 Wake flow**

Wake generated by a bluff body is one of the classical flow fields often discussed in fluid mechanics textbooks. Flows past cylinders (including circular and rectangular cross-sectional shapes) are often used as simple models for the applications involving flow past buildings, chimney stacks, bridges, cables, and for the flow through plants and trees. The wake flows have been extensively addressed in literature by Dennis and Chang (1970), Gerrard (1978), Schlichting (1979), Williamson (1996), Zdravkovich (1997), among others. Most of the early wake studies deal with the cylinder in cross flow where the cylinder is infinite and the wake flow is essentially two-dimensional.

For the classical case of uniform flow passing a cylinder, the flow field is characterized by the formation of the separated shear layers (SSL) along the sides of the body as shown in Figure 2.1. These shear layers roll up at downstream locations and generate the vortices with a periodic, alternate formation. This regular pattern of vortices observed in the wake is known as the von Kármán vortex street. Following Zdravkovich (1997), the separation of the laminar boundary layers occurs near  $\pm 82^\circ$  from the

upstream stagnation point on the surface of the cylinder and the von Kármán vortex shedding occurs in the turbulent wake flow at almost a constant Strouhal number (non-dimensional shedding frequency) of 0.2 ( $S_t = f_s \frac{D}{U_e}$ ). Here,  $f_s$  is the vortex shedding frequency from the cylinder. It is worth mentioning that as the SSL from either sides of the cylinder are stretched in the streamwise direction, they become thinner. This thin layer is unstable and will be influenced by the von Kármán shedding, particularly at high Reynolds number (Thompson and Hourigan, 2005).

Norberg (1998) and Sumner et al. (2004) have shown that the wake flow characteristics behind a circular cylinder are mainly dependent on the Reynolds number. The Reynolds number effect on the wake flow is schematically shown in Figure 2.2. Following the studies by Coutanceau and Defay (1991) and Zdravkovich (1997) on the flow past a circular cylinder the flow regime is classified into seven different regimes: *creeping* flow, *bubble* flow, *low transitional* flow, *subcritical* flow, *critical* flow, *supercritical* flow and *post-critical* flow. Apart from the classical alternate vortex shedding (von Kármán vortex street) in the wake region, signatures of other type of vortices have been also identified by Wu et al. (1996), Norberg (1998) and Parnaudeau et al. (2008). These vortex motions are known as the longitudinal vortices which form along the length of the cylinder and are inclined in the streamwise direction.

In the near-wake region, in addition to the Reynolds number effect, the shape and geometry of the bluff body also become important (Singha et al., 2009). Although the far-wake region has been well addressed in literature, the near-wake region is relatively less investigated. Norberg (1998) studied the Reynolds number effect on the near-wake region using laser Doppler velocimetry (LDV) in the *sub-critical* regime. He reported two local maxima in the streamwise turbulence intensity profile along the wake centreline for relatively low Reynolds numbers ( $Re_D < 8,000$ ). Here,  $Re_D = \frac{U_e D}{\nu}$  is the wake Reynolds number, where  $U_e$  is the free stream velocity;  $D$  is the cylinder diameter (or the width of the bluff body) and  $\nu$  is the fluid kinematic viscosity. As the Reynolds number increased only one maximum was observed. Also, he noticed that with increasing Reynolds number the length of the re-circulation region becomes smaller. Perrin et al. (2006, 2007) studied the near-wake of a circular cylinder experimentally and numerically using the PIV

technique and DES. Their studies have documented turbulence properties around a cylinder at Reynolds number flow of 140,000. Information about the coherent structures in the near-wake region was also provided from proper orthogonal decomposition (POD) and phase averaging techniques. The main structure was found to be the von Kármán alternating vortices.

Rodriguez et al. (2015) applied large eddy simulation (LES) on the flow past a circular cylinder to investigate the wake characteristics and vortex shedding for *supercritical* and *critical* regimes. Their simulation shows a symmetrical flow pattern including the streamtraces and vorticity contours in the near-wake region for the supercritical regime ( $Re_D > 3.8 \times 10^5$ ) which has a stable flow. They observed that, the shear layer separation occurs at  $\pm 128^\circ$  from the upstream stagnation point in this regime, which forms a small re-circulation region behind the cylinder. In the *critical* regime ( $Re_D = 2.5 - 3.8 \times 10^5$ ), the asymmetries in the flow around the cylinder and near-wake region are noticed. In this region, they observed the flow separation delay on one side of the cylinder ( $\sim 128^\circ$ ) due to the formation of a small laminar separation bubble while the other side remains in the same flow separation point as is common for sub-critical regime ( $\sim 90^\circ$ ). Their streamtrace plots indicated two re-circulation regions behind the cylinder with different sizes, but larger than its corresponding in the *supercritical* regime.

The wake flow classification provided above signifies the importance of Reynolds number effect on the wake characteristics, the development of the SSL and the formation of von Kármán alternating vortices in the wake region. It has to be noted that although this classification is for the infinite cylinder where the boundaries are far from the wake region, it can help one to better understand the main features of the wake flow even for a shallow flow condition or a bed-mounted cylinder.

### **2.3 Bed-mounted finite cylinder**

The wake flow of a wall-mounted finite bluff body becomes more complex particularly due to the influence of the bed and the finite size of the bluff body. Sumner et al. (2004), Parnaudeau et al. (2008) and Rostamy et al. (2012) have observed distinct



flow pattern changes along the height of the cylinder from the base to the tip that differs from the “infinite” case. These changes not only affect the mean flow parameters but also influence the coherent structures present in the near-wake region. As observed in Figure 2.3, apart from the von Kármán vortices other types of coherent structures are formed near the bed and at the free-end of the cylinder, which makes the wake flow strongly three-dimensional along the cylinder’s height. While the bed friction has a suppression effect on the wake flow, *horseshoe vortex* and *base vortex* are identified as the coherent structures in the bed region (Sumner et al., 2004; Wang and Zhou, 2009). In a fully submerged body in the flow, *tip vortex* structures are generated near the free-end of the cylinder. These structures may interact with each other in the near-wake or far-wake regions and increase the complexity of the flow. These near-bed and near-free-end structures are discussed in the next sections to better understand their influence on the flow.

### **2.3.1 Near-bed effect**

Complex eddy motions in the wake region of islands can trap sediments and pollutants and create poor water quality on the sheltered side of islands. Understanding of this kind of flow may lead one to investigate the wake flow in the shallow condition which is different from the deep cases. Studies of Ingram and Chu (1987) and Chen and Jirka (1995) showed that the flow characteristics behind the bluff bodies in shallow water are different from the ones in deep conditions, particularly at low aspect ratios ( $AR = L/D < 0.6$ ). Here,  $L$  is the submerged length of the cylinder in the flow. They concluded that limited water depth prevents the development of three-dimensional instabilities. They noticed that the bed friction suppresses the wake region and attenuates the transverse growth of disturbances. They believed that bed suppression is strong enough to influence the characteristics in the whole flow depth in the shallow wake region. Ingram and Chu (1987) and Balachandar et al. (1999) defined a dimensionless wake stability parameter ( $S$ ) to account for the stabilizing effect of the transverse shear. The stability parameter is based on the ratio of the loss of small scale kinetic energy to the production of large-scale turbulent kinetic energy. It is defined as  $S = C_f D/H$  for the bluff body. Here,  $C_f$  is the bed friction coefficient and  $H$  is the water depth. Following Chen and Jirka (1995), critical

values of  $S$  were defined in order to classify the different instability mechanisms. The von Kármán vortex street forms when  $S < 0.2$ . The steady-bubble wake occurs as a result of the suppression of large-scale instabilities by the bed friction at  $S > 0.5$ . For  $0.2 < S < 0.5$ , an unsteady-bubble wake occurs. Besides the suppression effect of the bed friction on the wake flow, other large scale instabilities that exist above the bed in the junction flow will influence the dynamics of the wake flow.

### 2.3.1.1 Horseshoe vortex structures

Following Figure 2.3, the flow past a vertically wall-mounted bluff body is characterized by horseshoe vortex structures (HVS) formed upstream of the bluff body in the junction region near the bed. As the boundary layer approaches the bluff body, there will be an adverse pressure gradient in front of the body which is the source of generation of the HVS. The horseshoe vortex system forms behind the flow separation line upstream of the body (known as the horseshoe core region) and extends around the cylinder in the form of vortex tubes, known as the horseshoe necklace. These vortex tubes are stretched farther downstream of the bluff body in the wake region and their direction is altered from the spanwise to the streamwise direction (known as the horseshoe legs). These vortices are responsible for high turbulence intensities in the wake region above the bed.

The HVS is classified into different regimes which are dependent on the Reynolds number and the characteristics of the approaching boundary layer (Visball, 1991; Wei et al., 2001; Lin et al., 2003). Following the classification by Greco (1990) and Seal et al. (1997), the laminar HVS can be categorized into five regimes: *steady vortex system*, *small displacement sub-regime system*, *amalgamating sub-regime*, *breakaway sub-regime* and *transitional sub-regime*.

In the *steady vortex system* regime, the position of the horseshoe core region and necklace vortices are almost fixed in their location over time and behave like laminar structures. Also, in the HVS not just one but several necklace vortices are observed and the number of necklace vortices increases with the increase in Reynolds number (Visbal, 1991; Williamson, 1996). By increasing the Reynolds number, the HVS becomes unsteady. The critical value for the Reynolds number depends strongly on the approaching boundary layer thickness ratio, (e.g.,  $\delta/D$ ). Following Kirkil and

Constantinescu (2012), the critical Reynolds number value ranges between 1,000 and 2,000. In the unsteady HVS, the oscillatory *small displacement sub-regime* vortex system is observed when the necklace vortices start oscillating back and forth over a small distance, but do not interact with each other. Greco (1990) has observed this regime in his experiments for  $1,700 < Re_D < 1,900$ .

By increasing the Reynolds number, the oscillatory *amalgamating sub-regime* is observed. In this regime, while more of the HVS sets are stagnant one set which is denoted as the primary vortex system is moved towards the bluff body (cylinder). At a certain point close to the body, the primary vortex is returned back to the formation region to start another cycle. In the new cycle, the primary vortex set merges with a newly generated vortex set that was shed from the formation region and eventually form a new primary vortex set (Kirkil and Constantinescu, 2012). Although, this sub-regime is rarely observed in the experimental studies, Greco (1990) was successful to observe this sub-regime in his experiments at  $Re_D = 2,500$ .

A further increase of the Reynolds number ( $Re_D > 4,700$ ) induces transition to the *breakaway sub-regime*. Following Lin et al. (2003), in this sub-regime three main co-rotating vortices are observed. The first co-rotating vortices are known as the developing vortex set which is broken away from the formation region. The other vortex set is situated close to the upstream face of the bluff body (cylinder) and is called as the corner vortex. The final vortex set is called as the primary vortex which transfers the developing vortex sets to the relatively stable corner vortex. The transfer process is not cyclic as discussed in the *amalgamating sub-regime* but more like a continuous pattern in which the primary vortex moves towards the body, merges with the original corner vortex, and eventually form a new corner vortex set. Greco (1990) has observed this sub-regime in his experiments for  $Re_D = 4,750$  while Lin et al. (2003) have notice this sub-regime for  $4,700 < Re_D < 6,000$  depending on the approaching boundary layer thickness ratio. Wei et al. (2001) have shown a single peak in the velocity spectral for this region. In this region, the necklace vortices start to break down as the primary vortex set behaves like a transferring coherent structure in the HVS. In the *transitional sub-regime*, the primary vortex set of HVS alters from the organized oscillatory pattern to more or less chaotic pattern. Wei et al. (2001) have shown multiple peaks in the velocity spectral analysis for

relatively high Reynolds number ( $5,000 < Re_D < 10,000$ ). Following the HVS classification, if  $Re_D$  becomes larger than 14,000, the HVS will be categorized as the *turbulent vortex system*. Similarly, Lin et al. (2003) have classified the HVS into three main type regimes: *steady vortex system*, *periodical oscillatory vortex system* and *turbulent vortex system* based on the Reynolds number ( $Re_D$ ) and the boundary layer displacement thickness ratio ( $\delta^*/D$ ).

Previous investigations studied the HVS and the wake region separately. The relation between the HVS and the Kármán vortex shedding was rarely discussed in literature, particularly for turbulent flows. This might be attributed to the very few quantitative experimental studies that concern the whole flow field around the bluff bodies, in the near-wall region. In this regard, Kirkil et al. (2008) investigated the interactions between the HVS and Kármán vortices. They studied the coherent structures in the shallow flow past a vertical circular cylinder on a mobile bed with the equilibrium scour hole condition by applying large eddy simulations (LES) and laboratory flume flow visualizations. Their study showed the interaction of the HVS with the detached shear layers formed along the sides of the cylinder and the near bed turbulence within the scour hole at  $Re_D = 16,000$ . Their simulation captured the considerable motion of the HVS in time and space resembling chaotic oscillations of the primary necklace vortex observed inside the scour hole region almost all the time. Analysis of the mean bed shear stress shows high values beneath the primary necklace vortex set in the scour hole region and a *junction vortex* set at the base of the cylinder. The large instantaneous bed shear stress values are observed beneath the vorticity patches detached from the legs of the necklace vortices in the near-wake region. These vorticity patches are found to be the main structures responsible for the formation of the scour hole. Similarly, Roulund et al. (2005) believed that the HVS is the major structure responsible for high local bed shear stress and pressure fluctuations that results in local scour in movable beds. The *junction vortex* (Kirkil et al., 2008) was identified as a very coherent vortex structure at the base of the cylinder which persists in time. Following their study, this vortex structure was formed on the front surface of the cylinder, while its rotation is in opposite sign of other horseshoe vortices. It should be mentioned that the *junction vortex* seems to be the *base*

*vortex structure* since it has all the features explained for a *base vortex* (see Section 2.3.1.2).

Simpson (2001) believed as flow passes a circular cylinder, the location, size and turbulence intensity of HVS vary in time while the legs of horseshoe vortex sets are stretched downstream and become almost parallel to the direction of incoming flow for a flat smooth bed. The turbulent kinetic energy content of the legs of horseshoe vortex is smaller compared to the core and the necklace vortex even at *steady vortex system*. Kirkil and Constantinescu (2012) investigated the dynamics of the vortical structures of HVS in the *breakaway sub-regime*. They conducted LES of flow past a circular cylinder mounted on the flat bed with an aspect ratio of 1.12 in an open channel flow at  $Re_D = 4460$ . As they studied a full cycle of development of the HVS, they found that as some parts of the corner horseshoe (i.e. the nearest HVS to the cylinder among the other sets) legs is oriented towards the axis of symmetry at about  $1.7D$  downstream of the cylinder near the bed, the other parts of the legs of the corner vortex set merge with the legs of other HVS and lose their coherence and breakdown into irregular vorticity patches. During this cycle, there is a strong interaction between these detached horseshoe legs with eddies of separated shear layers shed from the sides of the cylinder in the near-wake region. Similar, phenomenon has been experimentally observed by Greco (1990), as the legs of a necklace vortex interacted with the channel bed and lost their coherence in the near-wake region. Kirkil and Constantinescu (2012) believed that such interactions between the legs of the necklace vortices and the separated shear layers will influence the shear layers to roll up with an angle with axis of the cylinder. These inclined vortex tubes indicate the *oblique shedding* phenomena compared to *parallel shedding* phenomena for relatively large aspect ratio cases. They concluded that the vortex tubes associated with *oblique shedding* phenomena induce higher bed shear stress values as they are convected downstream in the wake region and the vortex tubes do not lose their coherence.

Nasif et al. (2015) studied the characteristics of the large coherent structures in the wake region of open channel shallow flow passed a sharp edge bluff body using detached eddy simulation (DES). The aspect ratio of the bluff body was 3.3 and the flow Reynolds number was  $Re_D = 13,500$ . Their findings show the stable HVS and a corner HVS (they denoted it as a *collar vortex tube*) which is attached to the upstream surface of the bluff

body above the bed. The legs of the HVS are found to become parallel to the inflow direction at about  $2.2D$  distance from the central wake plane, while the legs of the collar vortex structure lose their coherence at far downstream locations ( $x > 2D$ ).

Kirkil and Constantinescu (2015) studied the subcritical and turbulent HVS and the near-wake flow past a circular cylinder with aspect ratio of 1.12 at two Reynolds numbers ( $Re_D = 16,000$  and  $500,000$ , respectively). Their LES and DES study indicate changes in mean flow and turbulence statistics within the horseshoe vortex region, where the necklace vortices wrap around the base of the cylinder due to difference in  $Re_D$ . They also observed a variation of mean flow parameters and turbulence statistics between the bed and free surface region in the near-wake flow. They discussed the effect of Reynolds number on the coherent structures and the dynamics of the HVS generated upstream of the cylinder. Their main findings, regardless of Reynolds number value, show a primary vortex system with a large oscillatory motion of the core. They also observed that the higher bed shear stress values occur in the region of strong flow acceleration near the front surface of the cylinder ( $\sim 50^\circ$  from the front stagnant point) for both Reynolds numbers, while the bed shear stress beneath the primary vortex core is found to be more than 50% smaller. The bed shear stress was found to be larger for lower Reynolds number case.

It can be summarized that there are multiple horseshoe vortex structures formed in front of a finite mounted cylinder near the bed. Each set of these structures consists of a core, a necklace and legs. Different names have been adopted for the same structures in literature. The dynamics of these structures seem to be dependent on the Reynolds number, inflow conditions as well as geometry of the bluff body. The above review confirms the limited information about the mutual interaction of these structures with each other or with the other structures in the incident flow. It is possible that these interactions might lead one or more of the coherent structures to become dominant in the flow.

### **2.3.1.2 Base vortex**

Following the studies of Etzold and Fiedler (1976), Sumner et al. (2004) and Wang and Zhou (2009), in the wake of bed mounted cylinders another vortex structure,

apart from the horseshoe vortex set, is formed on the base of the cylinder known as base vortex structures as shown in Figure 2.3. These base vortex structures are associated with the upwash flow behind the cylinder. As a result, the spanwise vortices near the bed are suppressed and loose strength, which reduces the Reynolds shear stress (Wang et al., 2006; Adaramola et al., 2012). These structures are observed, immediately behind the body in the flow near the bed for relatively large aspect ratio cylinders ( $AR \geq 6$ ). The effect of the approach flow is not well understood on the base vortex structure. Mason and Morton (1987), Sumner et al. (2004), Wang and Zhou (2009) believed that the base vortex structure would be present in the junction flow in relatively thick boundary layer ( $\delta/D > 1.0$ ). However, Krajnovic (2011) has reported similar base vortex structures in his LES study in relatively thin boundary layer approaching flow ( $\delta/D = 0.07$ ) very close to the bed behind a tall finite cylinder ( $AR = 6$ ). It should be mentioned that the base vortex set is not as robust as the tip and horseshoe structures and the conditions of its formation are not well-understood.

The most frequent explanation cited in literature (e.g., Etzold and Fiedler, 1976; Wang and Zhou, 2009) for the source of generation of the base structures is the oblique spanwise shear layers on the sides of the body near the bed, which initially move downwards, interact with the bed and form the streamwise vortices behind the body. Sumner et al. (2004) hypothesize that the base vortices are the projection of von Kármán vortices with an inclined axis for large aspect ratio cylinders.

Mason and Morton (1987) performed qualitative flow visualizations to observe the flow structures around the low aspect ratio obstacles submerged in a steady flow at low Reynolds number ( $Re_D < 120$ ). They noticed the existence of upwash flow behind the obstacle with other vortex motion which was generated upstream of the obstacle in the region of adverse pressure gradient similar to the horseshoe vortex, but of opposite sign. They suggested that a dominant vortex pair with a central upwash flow (i.e. a base vortex) will appear for wide bluff bodies with small aspect ratio ( $AR \leq 1$ ).

Sumner et al. (2004) confirmed that the criteria offered by Mason and Morton (1987) for observing the base vortex structures is not valid for the flow passing a finite circular cylinder of large aspect ratio ( $AR = 9, 7, 5, 3$ ) at high Reynolds number ( $Re_D = 6 \times 10^4$ ) in relatively thick boundary layer approaching flow ( $\delta/D = 2.6$ ). They observed

the presence of base vortex structures within the boundary layer thickness behind the cylinder in all the cases except the smallest aspect ratio cylinder. Similarly, Tanaka and Murata (1999) noticed the absence of the base vortex structures for cylinders of small aspect ratio cylinder. Sumner et al. (2004) reported that the strength of the base vortex will reduce as one moves far from the cylinder in streamwise direction in the wake region. They found a monotonic decrease in base vortex strength as the cylinder's aspect ratio reduced from 9 to 5. Similar observation is reported by Wang and Zhou (2009) for a wall mounted square prism with the aspect ratio varying from 7 to 3 at  $Re_D = 9300$ . In addition, their study shows that in the case of small aspect ratio cylinder ( $AR = 3$ ), the base vortex will decay faster in the streamwise direction than for the bluff bodies with larger aspect ratios.

### 2.3.2 Tip vortex structures

As shown in Figure 2.3, the free-end of the cylinder is the source of generation of counter-rotating streamwise vortex tubes which are known as the *tip* or *trailing vortices* (Tanaka and Murata, 1999; Sumner et al., 2004). The *tip vortices* are formed very close to the free-end of the cylinder and are responsible for the downward velocity at the wake central plane known as the downwash flow. In the near-wake region, Sumner et al. (2004) showed that the von Kármán vortex street shed from the cylinder is strongly influenced by these tip vortices along the cylinder height.

Although various flow visualization studies have been reported in literature, the origin of these tip vortex structures is still a subject of discussion. Gould et al. (1968), Okamoto and Yagita (1973), Kawamura et al. (1984) believed that the *tip* vortex structures are originated a short distance below the free-end of the cylinder from the separation point of the boundary layer on the sides of the cylinder. Etzold and Fiedler (1976), Park and Lee (2000) believed that this origin is located on the leading (front) edge of the free-end. From both hypothesis it can be concluded that number of *tip* vortex structures is more than a pair, that is why in some observations the origin of the dominant pair is on the sides and for some it is located on the front edge (Roh and Park, 2003).

The interaction of the tip vortex structures with other coherent structures in the wake region is also important, since it will influence on the wake flow characteristics.



The *tip* vortices interfere with the separated shear layers along the sides of the cylinder. This interaction influences and somehow prevents rolling-up of the shear layers and will suppress the von Kármán vortex formation. As a result the von Kármán vortex shedding frequency will decrease and a lower Strouhal number is observed near the free-end of the cylinder (Farivar, 1981; Luo, 1993; Hoang et al., 1999 among others). Following Okamoto and Yagita (1973) and Kitagawa et al. (1997, 1999, 2002), the Strouhal number has a broad-banded profile with a weak strength in the velocity spectrum near the free-end of the cylinder. As a result, the peak is not well-determined in the velocity spectrum profile to indicate the dominant von Kármán vortex shedding frequency up to  $2D$  from the tip. In range between  $2D$  and  $4D$  from the free-end, although a peak in the velocity spectrum profile indicate the Strouhal number of the von Kármán vortex shedding, its value is lower than the common Strouhal number for the “infinite” case. The latter confirms the suppression effect of the tip even at  $4D$  below the free-end in the near-wake region. Moving further from the free-end, the Strouhal number increases and if the cylinder’s aspect ratio is sufficiently tall (cylinder length  $(L) > 30D$ ), the Strouhal number will eventually attain the value for the “infinite” cylinder (Farivar, 1981; Lee and Wang, 1987). Comparing the variation of such vortex shedding behavior with the constant Strouhal number value for the “infinite” cylinder, better confirms the importance of wake flow studies of finite length objects, particularly in fluid-structure interactions.

Wang et al. (2006) and Adaramola et al. (2006, 2012) studied the influence of the boundary layer thickness ( $\delta$ ) of the approaching flow and the cylinder’s aspect ratio on the tip vortex structures and their interaction with the von Kármán vortex. However, the physical explanation of the influence of the boundary layer thickness on the wake structures is still lacking, its effect is very important, particularly for small aspect ratio roof top-mounted stacks that are fully or partially immersed in the boundary layer, since pollutants can be brought towards the ground (Johnston and Wilson, 1997). Similar studies apply to the submerged vegetation stems in shallow rivers. Bourgeois et al. (2011) investigated the turbulent wake of the rectangular cylinder in a thick boundary layer. Their streamtrace analysis showed the deformation of von Kármán vortices near the tip of the cylinder due to the effect of the free-end vortices. Their study showed that the vertical coherent structures at mid-height of the cylinder will be oriented in the streamwise

direction in the upper-height of the cylinder, near the free-end. Since the rotation of the vortices generated from the free-end is opposite to the Kármán vortices on the same side, this structure is connected to the Kármán structure tube on the opposite side of the cylinder via streamwise connector strand as observed in Figure 2.4. After this connection, two principal cores are generated on each side of the cylinder in the farther downstream streamwise locations.

Various studies (e.g., Lee, 1997; Sumner et al., 2004; Adaramola et al., 2006) have discussed the existence of a critical aspect ratio, below which the tip vortex will highly suppress the other structures and wake flow structures behave like *arch vortex shedding* as shown in Figure 2.5. The vortex shedding in such a flow is more or less in a symmetric pattern which distinctly differs from the antisymmetric von Kármán vortex shedding (Okamoto and Sunabashiri, 1992; Lee, 1997). The critical aspect ratio value appears to be sensitive to the experimental conditions particularly, the boundary layer thickness ratios (i.e.,  $\delta/D$  or  $\delta/L$ ) of the approaching flow (Luo, 1993). Kawamura et al. (1984) showed that the critical aspect ratio increases with increase in  $\delta/D$  while the cylinder is mounted normal to the ground plane and the boundary layer thickness is relatively large. Fox and West (1993) observed that the critical aspect ratio is less influenced by the boundary layer thickness for the cylinders ending with a small plate (i.e., small boundary layer thickness). In this case the end plate disturbance does not extend more than  $3.5D$  along the height of the cylinder. Sumner et al. (2004) denoted a wide range of critical aspect ratio varying between 1 and 7 for different experiments.

While there is less systematic studies on the critical value of AR using a small incremental change in AR, Adaramola et al. (2006) and Rostamy et al. (2012) studied the turbulent mean quantity (mean velocity, turbulence intensity and Reynolds shear stress) distribution in the wake region of the bed mounted cylinder of small aspect ratios (AR = 9, 7, 5 and 3) with a constant boundary layer thickness ratio ( $\delta/D = 3.0$ ) in a more systematic fashion. Their results denote similar turbulent mean profiles in the wake region of the cylinders of AR = 5, 7 and 9 while a distinctly different distribution of turbulent mean quantities is observed in the cylinder of AR = 3 case. Their findings confirm the results reported by Sumner et al. (2004) that the flow, turbulence quantities are similar for cylinders greater than the critical aspect ratio but have unique properties

for cylinders smaller than the critical aspect ratio. Also, following Park and Lee (2002), if the finite cylinder is immersed in an atmospheric boundary layer, there will be a reduction in the vortex formation length, the width of the near-wake and the value of Strouhal number at mid-height, compared to the cases which the boundary layer thickness ratio is small.

Following Adaramola et al. (2006), more studies have presented whole-field measurements of the mean velocity field and turbulence fields (Hain et al., 2008; Mahjoub Said et al., 2008; Palau-Salvador et al., 2010). These studies have presented the variation of the time-averaged attached re-circulation zone behind the cylinder along the cylinder height.

In the open channel flows, the free surface restricts the vertical development of the flow beneath it. If the cylinder intrudes the free surface, while no effect of *tip* vortices is observed, other coherent structures appear around the cylinder and beneath the free surface. So, understanding of such coherent structures becomes more important in the shallow flow as the increased turbulence from the bed can influence their characteristics.

In addition to the discussed vortical structures, Krajnović (2011) and Rostamy et al. (2012) noticed two other stationary cross-stream vortex structures in the near-wake region, just behind the cylinder. As observed in Figure 2.6 one of them is located immediately downstream and below the free-end of the cylinder and the second one is near the bed plane behind the cylinder-wall junction. These structures are the consequence of the tip and base vortex structures in the cross-stream direction, which are clearly observed in the central wake plane behind the cylinder. Similar near-bed vortex structures are reported by Akilli and Rockwell (2002), Kirkil and Constantinescu (2015) and Nasif et al. (2015) in the shallow wake flow behind the bodies.

### **2.3.3 Free surface effect**

In shallow open channel flow, the free surface effect on the flow is not well established in literature. In the case of surface piercing bluff bodies in shallow open channel flow, the perturbation of the free surface is expected to play an important role in the vertical variability of the wake. Only a few studies have reported detailed investigations of the hydrodynamics of such complex interactions

Inoue et al. (1993) conducted experiments on the flow past a free surface piercing circular cylinder using a servo type wave height meter and a hot-film anemometer for measuring the wave height and flow velocity, respectively. The study was conducted in the deep open channel flow at Reynolds numbers  $Re_D = 27,000$  and  $29,000$  with their corresponding Froude numbers of  $Fr = 0.8$  and  $Fr = 1.0$ . While, the periodic vortex shedding and von Kármán street vortex was apparent in the near mid-depth region, in the near-free-surface region, the velocity spectra contained broad band higher frequencies. The higher frequencies are related to the random velocity fluctuations while the periodic frequency of the velocity fluctuations is smaller. The free surface showed intense oscillations in the near-wake region. It was reported that the free surface oscillations start to appear at the locations where the wave height gradient vanishes. Inoue et al. (1993) suggested that the free surface attenuates the periodic von Kármán vortex shedding mechanism. Other instability mechanisms (different from the Kármán mode) plays an important role in that region.

Maheo (1999) investigated experimentally the structure and dynamics of turbulent wake and shear layers in the presence of free surface using particle image velocimetry (PIV) technique. The shear flows were generated by a sharp, smooth, two-dimensional splitter plate, which extended through the free surface of the water. The purpose of Maheo's study was to determine the extent and characteristics of the free surface on the underlying fluid structures. He found that the free surface only affects the velocity components in a thin layer beneath the surface. Inside this layer, the vertical velocity fluctuations were retarded and the turbulent kinetic energy in the vertical direction gets redistributed to the horizontal velocity components in the streamwise and transverse directions. A signature of surface current was observed in the far-wake region. The surface current is attributed to the streamwise vorticity tubes which are buried inside the surface layer.

Akilli and Rockwell (2002) investigated the near-wake of a surface piercing cylinder in shallow open channel flow at  $Re_D = 10,052$  using a combination of flow visualization marker and PIV method. Their observations indicate a strong upward velocity conjugated with a swirling vortical motion behind the cylinder that results a significant distortion on the free surface. In addition, it was noted that the vorticity and

Reynolds stress distributions were concentrated in a narrow region and directed to the symmetric plane near the bed while they were broadly distributed in the transverse direction and deviated from the symmetric plane as approaching the free surface. Similar transversal expansion of the shear stress and turbulence intensity distribution along the flow depth have been observed in the flow passing a sharp edge bluff body in a shallow open channel water by Singha et al. (2009) and Nasif et al. (2015).

Vlachos and Tellionis (2008) studied the free surface effect on the vortex shedding generated from the inclined circular cylinder at  $Re_D = 1,700$  and  $6,000$ , and  $Fr = 0.3, 0.65$  and  $1.06$  using hydrogen-bubbles and particle flow visualizations. It was noted that when the upper part of the cylinder was inclined in the streamwise direction (positive inclination angle), the vortex shedding appeared near the free surface. In the negative inclination angle a less-organized wake vortex pattern was observed near the free surface. In the vertical cylinder case (zero inclination angle) the vortex shedding beneath the free surface was suppressed by the free surface at a high Froude number value ( $Fr = 1.06$ ). Their results suggest that the positive inclination angle counteracts the free surface effect on the vortex shedding, in contrast in the negative inclination angle case, supports the attenuation of the vortex shedding by the free surface.

Kawamura et al. (2002) used LES to investigate the influence of surface waves on the wake region behind a circular cylinder at a constant Reynolds number ( $Re_D = 27,000$ ) and different Froude numbers ( $Fr = 0.2, 0.5$  and  $0.8$ ). It was found that at a small Froude number ( $Fr = 0.2$ ), the surface wave amplitude was small and its influence on the wake flow was negligible. On the other hand, surface waves became steeper and wave–wake interaction was also stronger at a large Froude number ( $Fr = 0.8$ ). Numerical simulation predicted significant surface fluctuations inside the re-circulation zone immediately after the surface wave crest. In addition, they were able to visualize the attenuation of vortex shedding near the free surface. Similarly, Yu et al. (2008) studied flows past a free surface piercing cylinder at Froude numbers up to  $Fr = 3.0$  and Reynolds numbers up to  $Re_D = 1 \times 10^5$ . They also observed the attenuation of organized vortex shedding at the free surface. This effect was stronger at a larger Froude number, but it was reduced as the Reynolds number increased. In addition, Suh et al. (2011) investigated the effect of air–water interface on the vortex shedding from a vertical surface piercing circular cylinder

using LES and level set method. Their simulation was conducted at two Froude numbers ( $Fr = 0.2$  and  $0.8$ ) while the Reynolds number was fixed at  $Re_D = 27,000$ . They found that the vortex shedding is well organized and periodic in the deep flow while it is attenuated by the interface and replaced by small-scale vortices beneath the free surface. As observed in Figure 2.7, their simulation showed the von Kármán vortex core, formed longitudinally and parallel to the cylinder (V1). Also, their results show that the von Kármán vortices are inclined and attached on the cylinder wall at the interface, while two types of vortex core lines are observed inside the separated shear layer region near the interface (See Figure 2.7). One is like a streamwise vortex tube near the edge of separation region beneath the free surface (V2) and the other is the inclined V shape vortex tube inside the separation region which approaches the first vortex core at downstream (V3). They believe that the separated shear layers from the sides of the cylinder are influenced by the streamwise vorticity and the spanwise velocity generated near the interface region. They suggest that such effects on the shear layer cause the deviation on the shear layers that eventually avoids forming the periodic vortex shedding at the interface. In general, following Suh et al. (2011) the free surface adds great complexities to the flow due to the generation of waves in various forms and their interaction with the body and shed vortices.

Following the literature review, the influence of free surface on the wake flow, it can be suggested that the free surface behaves like an attenuation layer which dampens the vortex shedding in the wake region beneath the free surface. The vertical (normal to the free surface) turbulence intensity beneath the free surface gets retarded and redistributed to the horizontal (streamwise and spanwise) turbulence intensity components.

## **2.4 Tandem cylinders**

Flow passing tandem cylinders with different cross-sections has been studied by Lin et al. (2002), Zhou and Yiu (2006) and Tsutsui (2012). While the literature is mostly focused on the tandem cylinders with circular or rectangular cross-section in uniform flow, the shallow flow passing tandem cylinders is rarely addressed, particularly for the case of a cylinder with relatively large aspect ratio.

Lin et al. (2002) studied the instantaneous and mean flow parameters of flow generated from two identical circular cylinders in tandem using PIV. Their focus was on the flow characteristics in the gap region between the cylinders and the near-wake region behind the downstream cylinder. The gap length ( $G$ ) between the cylinders ranged from  $1.15D$  to  $5.1D$  and the Reynolds number was  $Re_D = 1 \times 10^4$ . Here,  $G$  is the center-to-center distance between two cylinders. They observed both symmetrical and asymmetrical patterns within the gap. The near-wake flow behind the downstream cylinder was substantially altered by the upstream cylinder in terms of vortex shedding and mean flow pattern, compared to the single cylinder case. In the case of large gap ( $G = 5.1D$ ), the von Kármán vortices formed in the gap between the cylinders. This increased the wake width and the Reynolds shear stress magnitudes in the near-wake of the downstream cylinder, compared to that of the smaller gap ( $G < 2D$ ).

Tsutsui (2012) examined the flow behaviour around two tandem circular cylinders by using the smoke-wire and surface oil-film methods. While the gap between the cylinders was almost constant ( $1.2D - 1.3D$ ), the Reynolds number ( $Re_D$ ) ranged from  $3.8 \times 10^4$  to  $1.3 \times 10^5$ . He found that the separated shear layers from the sides of the upstream cylinder alternately reattach to the surface of the downstream cylinder at all ranges of Reynolds number. After the reattachment, some portion of the shear layer flows into the gap and the gap flow is pushed back to interact with the rear surface of the upstream cylinder.

Singha and Sinhamahapatra (2010) performed 2-D simulation of laminar flow passing two circular cylinders in tandem. They investigated the effects of the gap as well as Reynolds number on the vortex structure in the gap and the wake region behind the downstream cylinder. The gap ratio ( $G/D$ ) varied between 0.2 and 4.0. At the lowest Reynolds number ( $Re_D = 40$ ), the flow remains laminar and steady with a closed re-circulation in the gap region regardless of the gap length. At  $Re_D = 70$ , the gap flow remains steady with a closed re-circulation for  $G/D < 2.0$  and it becomes unsteady for  $G/D > 3.0$ . For higher Reynolds number ( $Re_D \geq 100$ ), the gap flow was found to be unsteady for all  $G/D$ . While at small gap ratios ( $G/D < 2.0$ ), the unsteady gap flow was found to be characterized by the separated shear layers from the upstream cylinder, the downstream cylinder elongates the formation of vortices in the near-wake of the

downstream cylinder. At larger gap ratios ( $G/D \geq 3.0$ ), the shed vortices from the upstream cylinder impinge on the surface of the downstream cylinder and vortex streets similar to the Kármán vortex street develop behind the downstream cylinder. They believed that flow field in tandem cylinders is significantly influenced by Reynolds number and the gap ratio. The latter conclusion has been reported by other researchers (such as Xu and Zhou, 2004; Zdravkovich, 1987; Igarashi, 1981, 1984).

Different approaches have been applied to classify the flow behavior when a steady flow passes tandem cylinders. Zdravkovich (1987) is one of the pioneers in multiple cylinder studies, and he classified the flow behaviour into two basic types: *wake interference* and *proximity interference*. In the case of *wake interference*, the cylinders are partially or entirely positioned in the wake of the other cylinder. In the case of *proximity interference*, the cylinders are located close to each other and neither of them is immersed in the wake of the other one. In tandem configuration, since two and three cylinders are located in-line in the streamwise direction, the downstream cylinder is positioned in the wake of the upstream cylinder. According to Zdravkovich's classification, tandem cylinders belong to the *wake interference* group.

Following Zdravkovich's approach for multiple cylinders, Xu and Zhou (2004) and Zhou and Yiu (2006) classified the flow pattern of tandem circular cylinders into three subdivisions based on the wake interference behavior for  $Re_D = 800 - 42,000$ . At a small gap ratio ( $G/D < 2$ ), where the two cylinders are sufficiently close to act as a single bluff body, the flow regime is defined as *extended-body regime*. In this regime which is also known as single bluff-body behavior by Igarashi (1981, 1984) the separated free shear layers from the upstream cylinder overshoot the downstream cylinder and form a vortex street far behind the downstream cylinder. Also, the flow in the gap region was found stagnant. For intermediate  $G/D$ , where the separated free shear layers from the upstream cylinder touch the surface of the downstream cylinder, the flow is classified as *reattachment regime*. In this regime, as shown in Figure 2.8, the shed vortices from the upstream cylinder are formed just behind the downstream cylinder, while flow in the gap is still insignificant. This region is also known as shear layer reattachment behavior by Igarashi (1981, 1984). Zhou and Yiu (2006) found that in the *reattachment regime*, two different flow structures and vortex movement can be observed. This subdivision of flow



depends on whether the detached free shear layers from the upstream cylinder reattach on the rear or front surface of the downstream cylinder. Their studies show that, shear layer reattachment occurs more often on the rear surface of the downstream cylinder when  $G/D = 2-3$ , while when  $G/D = 3-5$  the shear layers often reattach on the front side (see Figure 2.9). At larger gap ratios ( $G/D > 5$ ), each cylinder sheds its own von Kármán vortices individually and the flow regime is defined as *co-shedding regime*. In this region, the downstream cylinder is completely submerged in the wake flow of the upstream cylinder. The shear layers roll up alternately in the gap region between the cylinders and no more stagnant flow is observed, thus the gap flow significantly influences the wake region behind the downstream cylinder. Igarashi (1981, 1984) has classified this region as *Kármán vortex shedding behavior*.

In the case of tandem square cylinders, Yen et al. (2008) classified the flow into three main characteristic modes. They studied the flow interactions of two tandem square cylinders at relatively low Reynolds number ( $250 < Re_D < 1,100$ ) in a vertical water tank using PIV. They examined the effect of the Reynolds number, gap ratio and rotation angle of the downstream square cylinder on flow characteristics including the velocity vector field, streamtraces and vortex shedding properties. As shown in Figure 2.9, their flow field classification is more or less similar to the tandem circular cylinder classification while the Reynolds number influence is more pronounced on the classification. The three characteristic modes are: *vortex sheet of the single mode*, *reattached mode* and *binary mode*. In *single mode* the vortex shedding resembles the vortex sheet of the single cylinder model. In *reattached mode* the separated flow from the upstream square reattaches the side surfaces of the downstream square cylinder. In the binary mode each cylinder experience its wake flow as the gap ratio is large enough.

Following Yen et al. (2008), the effect of flow shallowness on the square tandem cylinders were examined by Pinarbasi et al. (2015). They investigated the wake flow of the shallow flow passing the two identical square cylinders with small aspect ratio ( $H/D = 0.5$ ) in tandem using PIV. Their study was focused on the effect of gap ratio ( $1.5 < G/D < 6$ ) in a relatively medium Reynolds number ( $Re_D = 4,470$ ) on the gap region and near-wake region behind the downstream cylinder. The streamtrace patterns in the vertical mid-plane in the gap region show the existence of two counter-rotating vortices on top of

each other above the bed for small gap ratio ( $G/D = 1.5$ ). Also, they reported that, as the gap ratio increases, the bottom vortex moves towards the bottom corner of the downstream cylinder, meanwhile the top vortex is attached to the rear side of the upstream cylinder above the bed. For large gap ratios ( $G/D \geq 4$ ), another set of vortex was observed in the gap region located near the free surface attached to the front side of the downstream cylinder. Furthermore, their measurement in the horizontal plane, showed that in small gap ratio ( $G/D \leq 2$ ), the separated flow from the side edge of upstream cylinder overshoot the downstream cylinder similar to the study by Yen et al. (2008). By increasing the gap ratio, while the separated flow from the upstream cylinder impinges and reattaches on the lateral surface of the downstream square cylinder, both positive and negative vortices get closer to the upstream cylinder. This is different from the results of Yen et al. (2008) whose experiments were performed for lower Reynolds number under deep flow condition. The detailed physics of vortex development in the shallow near-wake is expected to be complex, due to the effects of bottom and free surfaces and the relatively small distance between them. For medium range of gap ratios ( $G/D = 1.5-3.0$ ), while Pinarbasi et al. (2015) reported two large-scale vortices in the gap region, Yen et al. (2008) observed two small-scale vortices between the cylinders more attached to the lateral surfaces of the downstream cylinder rather than in the gap region. For large gap ratio ( $G/D = 5.0$ ), the existence of two vortices in the gap region is reported by both researcher groups. Also, Pinarbasi et al. (2015) concluded that as the gap ratio increases the Reynolds shear stress magnitudes in the gap region will increase accordingly. In addition, they believed that the peak in the Reynolds shear stress distribution in the wake region of downstream cylinder will shift towards upstream and the Reynolds shear stress contours elongate in spanwise direction with the increase in the gap ratio.

Ataie-Ashtiani and Aslani-Kordkandi (2013) investigated the near-wake and gap region of the flow passing two tandem circular cylinders mounted on the rough bed using the acoustic Doppler velocimeter (ADV) and compared the results with the single bed mounted case. The Reynolds number ( $Re_D$ ) was considered to be  $3.1 \times 10^4$  and  $3.2 \times 10^4$  for tandem cylinders and single case, respectively at the gap ratio of 3 and the cylinder aspect ratio of 2.8. Their results indicate that the downstream cylinder greatly modifies

the flow structure, particularly in the near-wake region in comparison with the wake flow behind the single cylinder. Also by comparing the wake flow of both cases, they concluded the presence of weaker vortical structures in the wake of tandem cylinders. Furthermore, they found that in the gap region between the two cylinders, a stronger upwash flow is shaped particularly at the central wake plane, while weaker spanwise velocity is observed compared to the wake of single cylinder case. They also, reported of presence of two re-circulation zones just upstream of the sheltered cylinder, one close to the bed and another near the free surface similar to the observation by Pinarbasi et al. (2015) for large gap ratios.

Following the literature review, one can conclude that the wake flow generated by two identical tandem circular cylinders in the uniform approaching flow is classified into different regimes which is dependent on the gap ratio and the Reynolds number. Although this classification is for the infinite cylinders, it can help to understand the main features for a shallow flow condition. On the other hand, though the gap ratio and Reynolds number are important to classify the wake flow regime, the wake flow generated by the leading cylinder has a key role on the wake behind the tandem configuration. Due to this fact, understanding the wake flow features behind the tandem cylinder set requires a good understanding of the wake flow characteristics behind the single cylinder. In the forthcoming sections of the study, an attempt has been made to characterize the wake flow of a single cylinder in the shallow condition before discussing about the wake feature of the tandem cases.

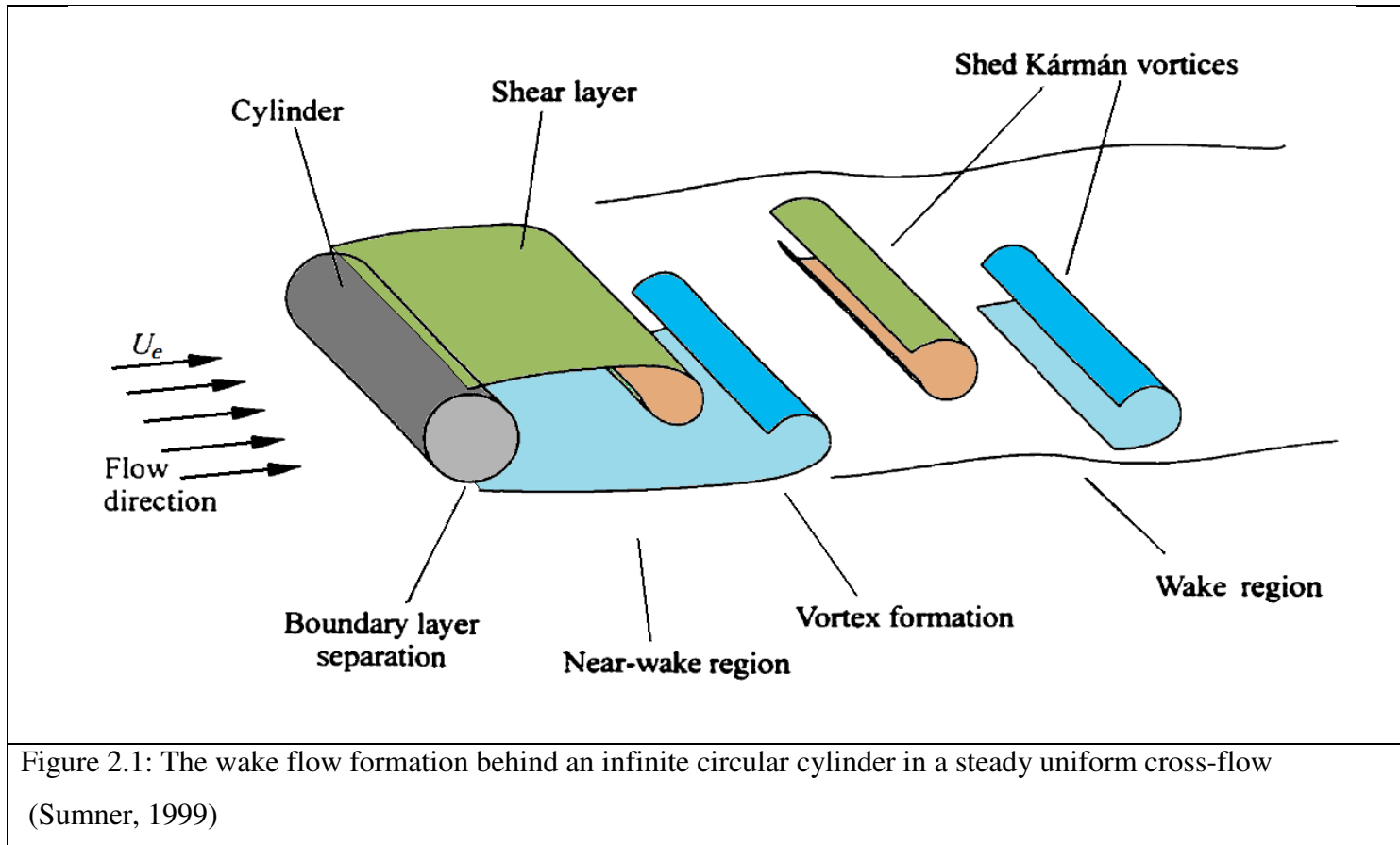


Figure 2.1: The wake flow formation behind an infinite circular cylinder in a steady uniform cross-flow (Sumner, 1999)

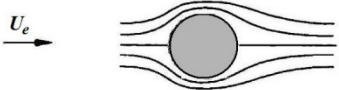
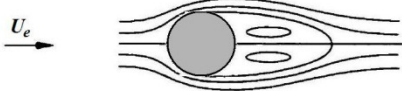





(a)		creep flow ( $Re_D < 5$ )
(b)		bubble flow ( $5 < Re_D < 40$ )
(c)		low transitional flow ( $40 < Re_D < 350$ )
(d)		subcritical flow ( $350 < Re_D < 2 \times 10^5$ )
(e)		critical flow ( $Re_D \sim 3 \times 10^5$ )
(f)		supercritical flow ( $Re_D \sim 7 \times 10^5$ )
(g)		post-critical flow ( $Re_D > 3.5 \times 10^6$ )

Figure 2.2: The wake flow classification behind a circular cylinder object positioned in a steady uniform cross-flow for different Reynolds numbers (Coutanceau and Defay, 1991)

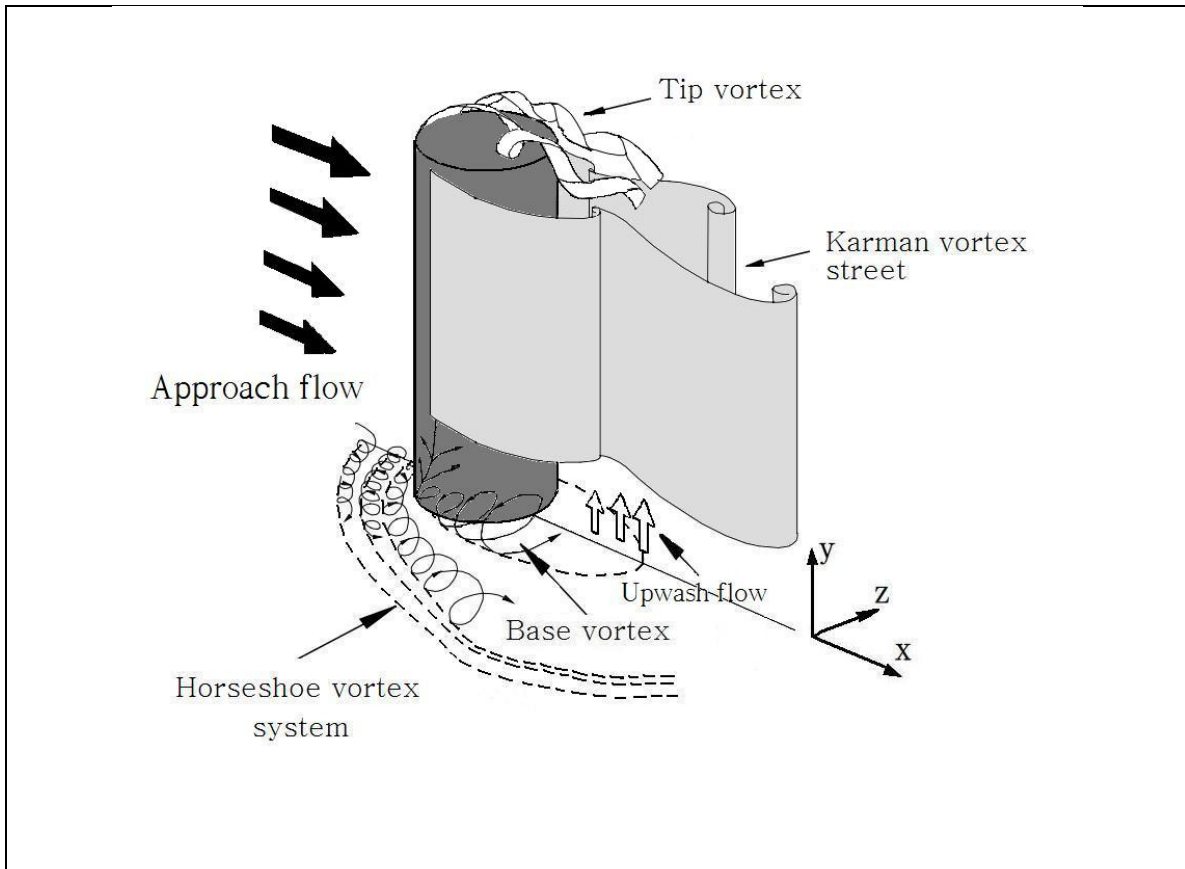


Figure 2.3: Flow structures around a finite length wall-mounted cylinder (Wang et al., 2006)

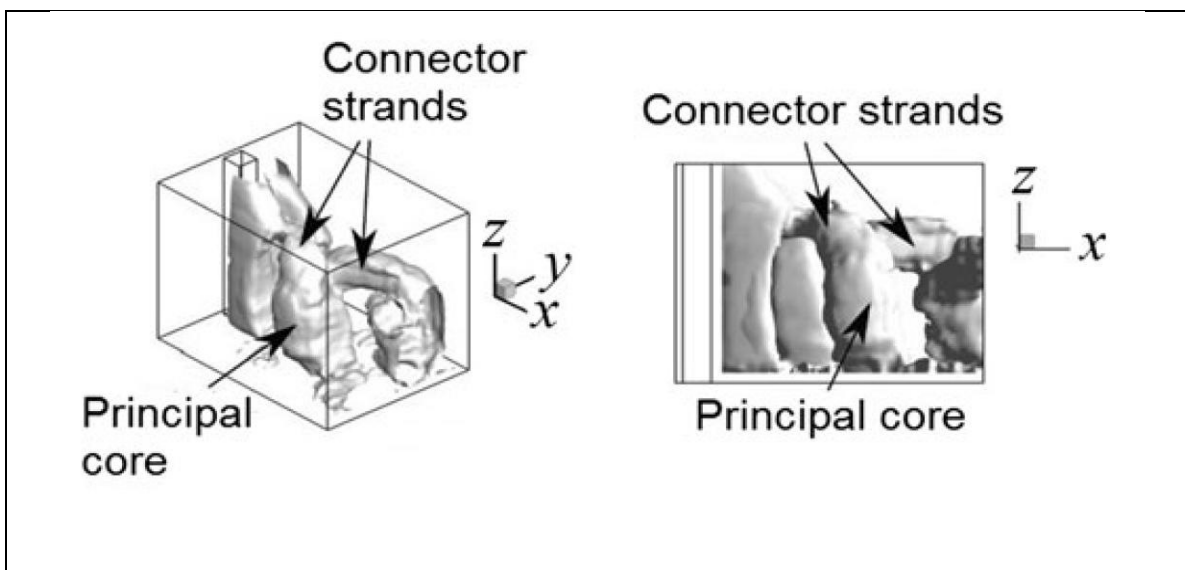


Figure 2.4: Connection of the tip vortex and the von Kármán tubes with the strands behind a wall-mounted square cylinder (Hosseini et al., 1997)

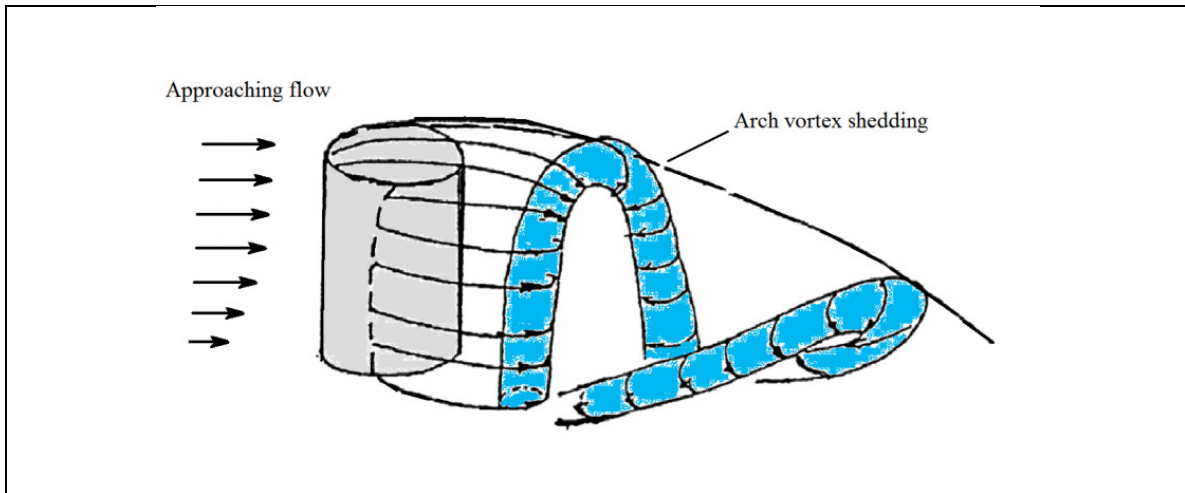


Figure 2.5: Arch type vortex structures around a short length wall-mounted cylinder (Lee, 1997)

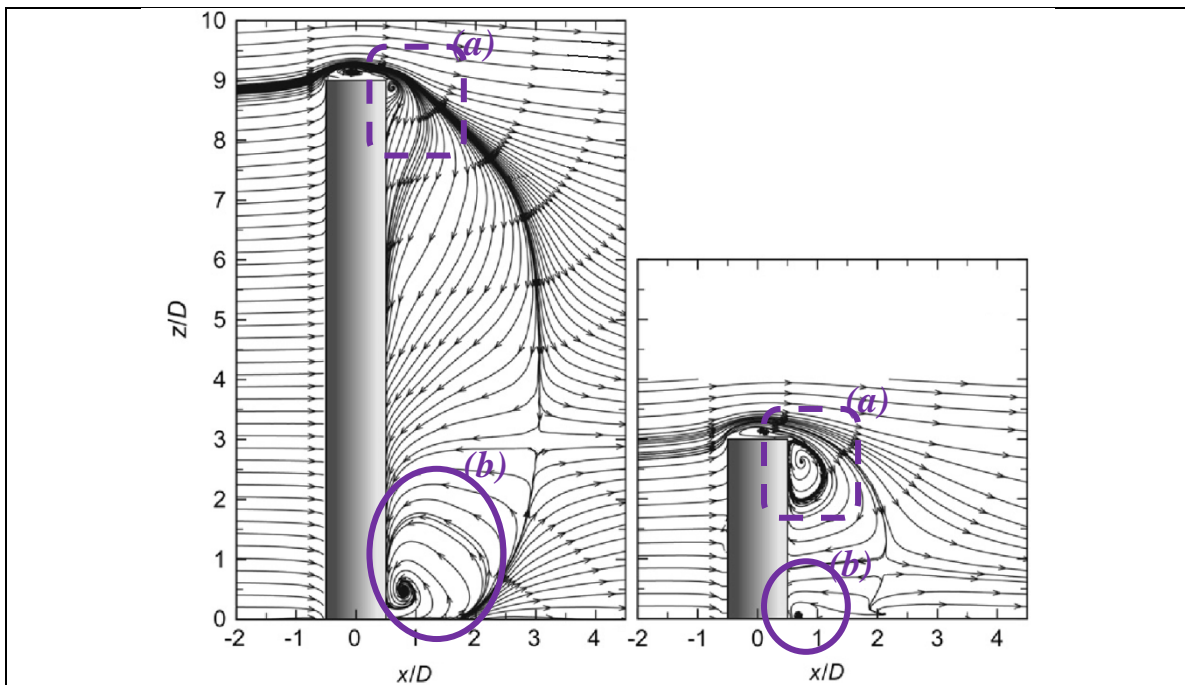


Figure 2.6: The mean vortex structures at free-end (a) and base (b) of the cylinder consequence of the tip and near-bed structures, respectively for different cylinder aspect ratios (Rostamy et al., 2012)

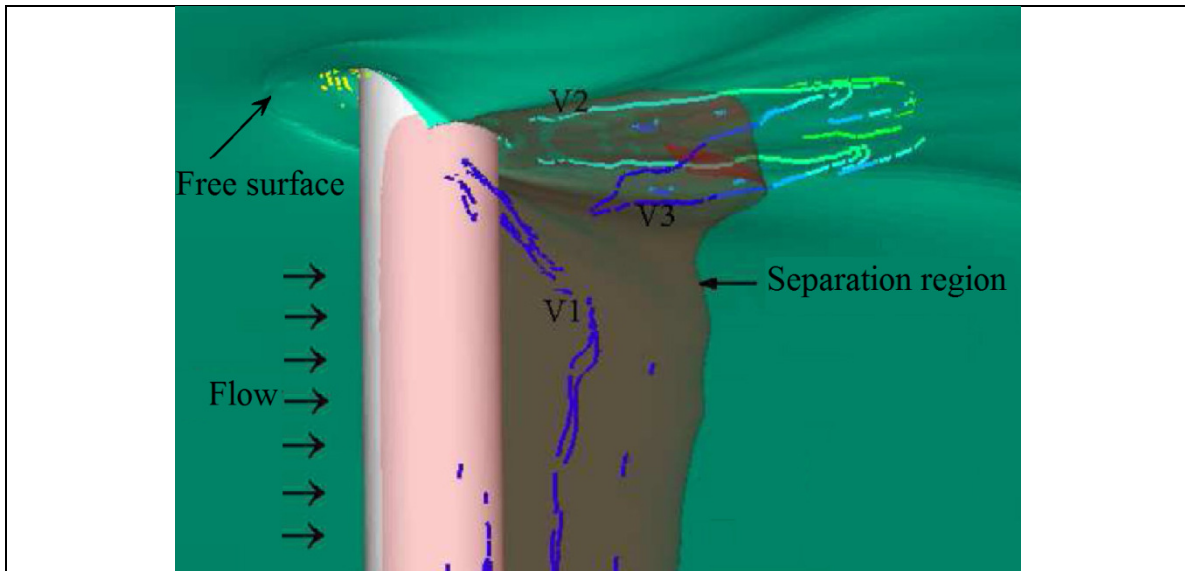


Figure 2.7: Mean separation pattern with the vortex core lines of different structures near the free surface in the near-wake region (Suh et al., 2011)

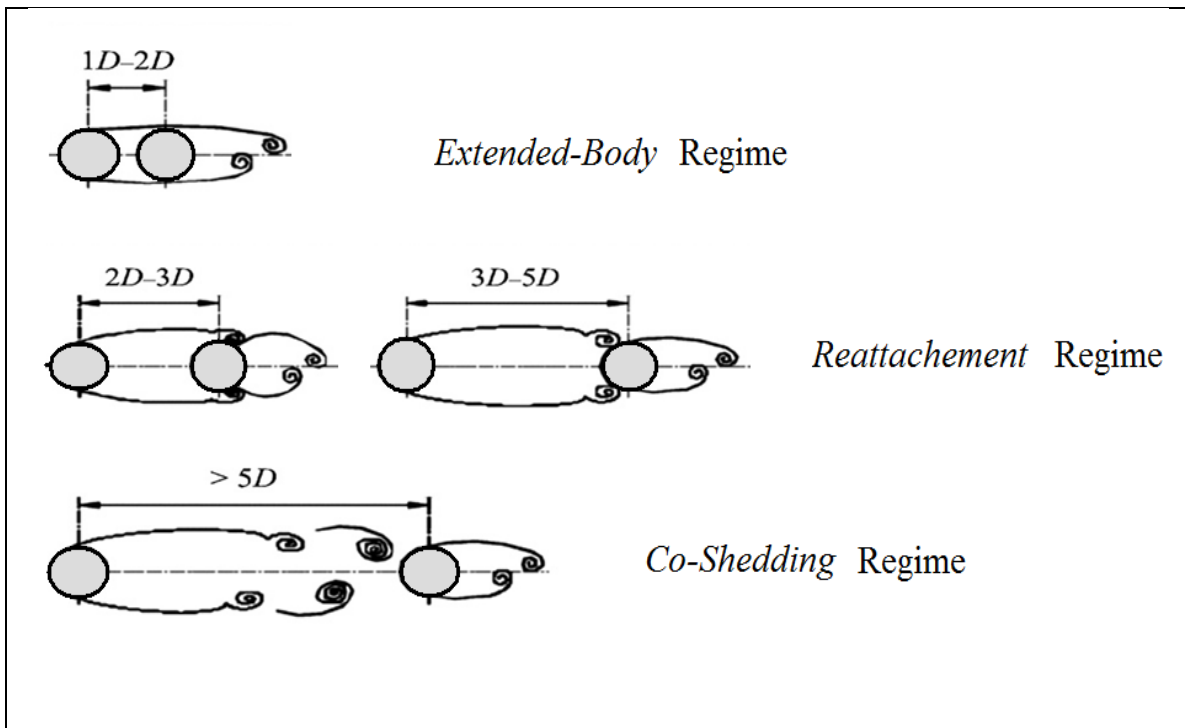


Figure 2.8: The flow classification for the circular cylinders in tandem at different gap lengths (Zhou and Yiu, 2006)



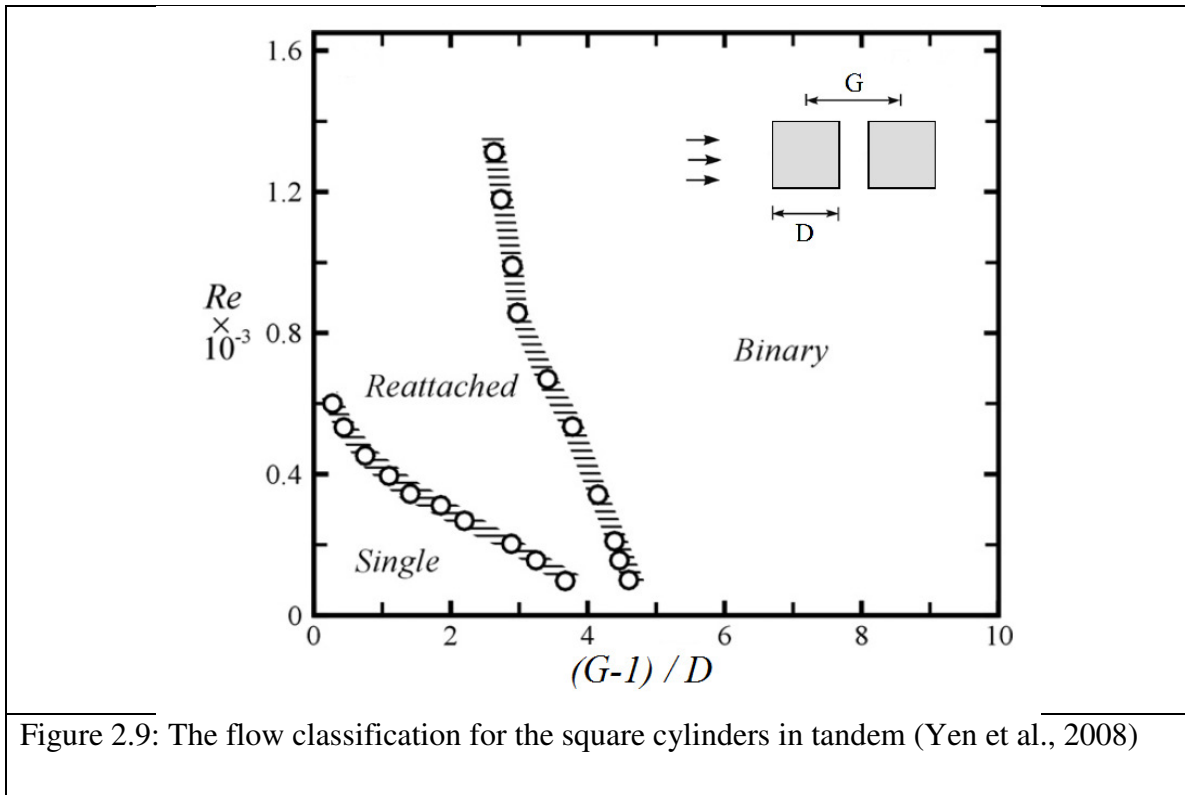


Figure 2.9: The flow classification for the square cylinders in tandem (Yen et al., 2008)

## **Chapter 3: EXPERIMENTAL DETAILS**

### **3.1 General comments**

This chapter describes the experimental setup and measuring procedures used in this study. A detailed description of the Particle Image Velocimetry (PIV) including image analysis; and data analysis algorithms (variable threshold outlier rejection technique (Shinneeb et al., 2004)) and uncertainty analysis are discussed.

### **3.2 Experimental setup**

#### **3.2.1 Open channel re-circulating flume**

The present experiments are conducted in a rectangular cross-section open channel flume at the Hydraulic Engineering Laboratory in the Center of Engineering Innovation (CEI), University of Windsor. A schematic of the experimental flume is shown in Figure 3.1. The re-circulating flume is 0.80 m deep, 1.22 m wide ( $B_f$ ) and 16 m long. The purpose of the loop in the re-circulating flume is to provide a steady flow during the experimental runs. A centrifugal pump is used to facilitate the re-circulating water flow in the flume from the downstream reservoir to an upstream settling tank. In the upstream section of the flume a flow straightener and turbulence stilling arrangements are used to minimize the entrance effects and lower the inlet turbulence levels. The measurement section is located at 4.5 m downstream of the flow straightener. A false bottom is designed and installed inside of the flume which allows slope to be adjustable for the bed. The water depth in the flume is controlled by the downstream weir. The false bottom and the downstream weir allow for the necessary control of the flow to reach a uniform condition. In the present study, the uniform flow condition with the water depth ( $H$ ) of 70 mm along the flume length is used in all the experiments.

The sidewalls in the mid-portion of the flume are made of transparent acrylic plates to facilitate optical access. The flow is tripped by a wire located 2.5 m upstream of the measuring section which spans the width of the flume to ensure formation of fully developed turbulent flow at the measurement location on the smooth bed. Tap water was

initially filtered through a 5  $\mu\text{m}$  filter and is used as the working fluid in all the experiments. The flow was seeded with spherical hollow glass particles (mean diameter of 10  $\mu\text{m}$ ) to facilitate the velocity measurements using the PIV system. All velocity measurements are made in the center of the channel, where it is generally accepted that the effect of the secondary flow is negligible. It should be noted that secondary flows are not expected to play any major role since the channel aspect ratio defined as  $B_f/H$  is greater than five (Nezu and Nakagawa, 1993).

### 3.2.2 Cylinders in flow

Following the discussion in Chapter 1, in vegetated flows, the effect of the emergent plant stems their foliage and arrangements in regular or random patterns affect the flow resistance. To model the emergent plant stems, following the studies of Jarvela (2002), Zong and Nepf (2010) and Chen et al. (2012), rigid circular cylinders of diameter  $D = 6.4$  mm were chosen for this study. In addition, the diameter of the cylinders was chosen to be small enough to reduce the flow blockage and minimize the effect of the side walls. The blockage ratio defined as  $D/B_f$  is 0.5% which is less than 10% as suggested by Lasher (2001).

The cylinders are made of acrylic with high rigidity to ensure that they do not bend in the flow particularly at high Reynolds number. The acrylic material is transparent and it can reduce the laser light reflections during the PIV experiments. The optical mismatch between the refraction index of the acrylic and water results in a shadow region formed on the opposite side of the illumination and thus no velocity vectors are reported in this region. The cylinders are placed in the central plane of the flume. As the flow depth is kept constant at  $H = 70$  mm, the cylinder's aspect ratio ( $H/D$ ) is about 11 which is unique since most of the shallow flow studies were conducted in smaller  $H/D$  (e.g.,  $H/D = 0.5, 1.0, 2.0$  by Akilli and Rockwell, 2002;  $H/D = 1.9$  by Sadeque et al., 2009 and  $H/D = 1.12$  by Kirkil and Constantinescu, 2012, 2015). To investigate the effect of the plant configurations, Figure 3.2 displays different test cases in the present study: a single cylinder, two-cylinder and three-cylinder tandem configurations. The gap between the two cylinders (C2) in the two-cylinder tandem configuration with short gap (C2S) and large gap (C2L) are  $G = 1.95D$  and  $G = 3.9D$ , respectively. In three-cylinder case denoted

as C3, the distance between cylinders is kept constant as  $1.95D$ . The cylinders are oriented to be vertical and affixed to the bed for all test cases. The origin of the coordinate system is located at rear side of the most downstream cylinder as shown in Figure 3.2. The vertical location  $y = 0$  is located on the bed and it is directed upwards towards the free surface. A sample picture of the cylinders in the flume is shown in Figure 3.3.

### 3.2.3 Approaching flow

In the present study, flow is investigated at two flow conditions with different Reynolds numbers denoted as LR and HR for low and high Reynolds numbers, respectively. The LR flow condition corresponds to  $Re_H = 10,340$  based on a free stream velocity ( $U_\infty$ ) of 0.16 m/s and the depth of flow. The local shear velocity ( $u_*$ ) for the approach flow in the central plane was estimated to be 7.6 mm/s based on the power law method. The free stream velocity at the high Reynolds number flow is 0.51 m/s, with the corresponding depth based Reynolds number,  $Re_H = 33,000$ . The shear velocity is higher and estimated to be 21.8 mm/s. Following Section 1.2 as the horizontal length scale is significantly larger than the flow depth ( $B/H \gg 1$ ) and the flow is resisted by the shear force particularly from the bed that will influence the velocity profile, it can be concluded that the flow is shallow. Since the present study is focused on shallow flow, the bed shear stress is an important quantity. Chen and Jirka (1995) estimated the bed friction coefficient in a smooth shallow flow as the ratio of shear velocity and depth-averaged velocity ( $U_{mean}$ ) given as  $C_f = 2 \left( \frac{u_*}{U_{mean}} \right)^2$ . The bed friction coefficients for low and high flow Reynolds number are found to be  $6.1 \times 10^{-3}$  and  $4.6 \times 10^{-3}$ , respectively. Figure 3.4 illustrates the streamwise velocity and turbulence intensity profiles for both Reynolds number flows. As observed in Figure 3.4.b, the lower Reynolds number flow exhibits higher turbulence intensity values compare to the HR flow at locations far from the bed, although both profiles resemble a typical turbulent intensity profile in open channel flow. Also, at both Reynolds numbers, the velocity profiles obey the log-law equation very well, which shows the occurrence of overlap region in the velocity profile of the shallow flow (see Figure 3.4-a). These features also indicate the existence of turbulent boundary

layer flow over the bed. Successful production of the developed velocity profiles in this open channel flume is discussed in detail in Chapter 4.

The typical methods used to estimate the bed shear stress or bed friction velocity on a smooth channel are not appropriate for vegetated channels, in part because the shear stress acting on the bed is only a fraction of the total flow resistance (Luhar et al., 2008). The presence of the bluff body alters the flow field by creating wakes which induces additional flow resistance. To compare the effect of the approaching flow on the wake region it is a common practice to define the stem/wake Reynolds number ( $Re_D$ ) based on the cylinder diameter ( $D$ ) and the free stream velocity ( $U_e$ ) apart from the depth based Reynolds number ( $Re_H$ ). In this study, the wake Reynolds number is found to be 925 and 3000 for LR and HR, respectively. Table 3.1 describes the flow parameters at these two Reynolds numbers.

### **3.2.4 Measurement locations and details**

For the present study, different velocity measurements are performed at horizontal and vertical planes behind the cylinder(s). Three horizontal planes at near-bed ( $y/H = 0.07$ ), mid-depth ( $y/H = 0.50$ ) and near-free surface ( $y/H = 0.92$ ) are chosen for this study to observe the development of the wake in each plane and compare this development with each other to better evaluate the flow characteristics. The vertical plane is positioned at the center plane behind the cylinder(s) at  $z/D = 0$ . All the horizontal and vertical planes are schematically demonstrated in Figure 3.5. The size of the field-of-views (FOV) of the horizontal planes cover the axial locations between  $0 \leq x/D \leq 6$ , while the vertical planes cover axial locations between  $0 \leq x/D \leq 9$ . Velocity fields in the vertical planes enable us to evaluate the effect of the bed and free surface on the shallow wake. Tables 3.2 and 3.3 summarized information for the experiments providing details for the location and resolution of the field-of-view (FOV) for each case.

The bed in the measurement section was covered with non-reflective, black paint, in order to reduce the excessive light reflections when illuminated. This allows velocity measurements in the vertical plane for the whole water depth including the near bed region. Although light reflection from the bed was substantially reduced, still some reflection is observed on the images originating from the painted bed. This light

reflection increases the noise level in the horizontal plane measurements by the evidence of increase in the number of the spurious vectors in the FOV, particularly at  $y/H < 0.07$ . The criterion for fixing the near-bed plane at  $y/H = 0.07$  is chosen as the ratio of spurious and total vectors less than 10 % in the FOV. Similarly, the deformation of the free surface along with the occasional movement of small bubbles, restrict the near-free surface measurements to a vertical location of  $y/H = 0.92$ . To mitigate the effect of the free surface and avoid the image distortion, a small floating piece of thin Plexiglas (200 mm  $\times$  200 mm) is used on the top of the free surface over the length of the field of view.

### **3.3 Particle image velocimetry**

#### **3.3.1 General remarks**

Particle image velocimetry (PIV) is a non-intrusive multiple point measurement system technique which can be used to evaluate the velocity field in an Eulerian description. The basic principle of a planar PIV is to measure the displacements of markers (seed particles) in the flow within a plane. The velocity vector is obtained by calculating correlations for a small interrogation area (IA). Figure 3.6 displays the standard components of the PIV system. A typical PIV system consists of four subsystems: laser and optics for generation of light sheet, CCD camera for recording images, synchronizer for managing time events needed to make PIV measurements and computer for data acquisition and data analysis. Table 3.4 presents detailed specifications of each subsystem used in the present study.

The PIV measurements rely on the light reflecting particles (tracers) suspended in the flow to provide velocity information for the continuous liquid medium. Once the seeding particles are added to the flow, they are illuminated by the laser sheet at the measurement plane. The laser illumination occurs twice within a known short time interval ( $\mu\text{s}$ ). The reflected light by each of the tracers is recorded with the CCD camera either in a single frame, or in multiple frames depending on the type of application. The frames are split into a large number of interrogation areas (IA), or windows. By using a statistical cross-correlation technique for each IA, the displacement vector of tracer particles can be calculated. It should be noted that there are different statistical techniques

(such as auto-correlation method) applied to find the particle displacements. With the evolution of the PIV system got developed, the cross-correlation method has been recognized to be the most accurate method particularly for the flows with low density particles while the velocity gradients are not strong (Brevis et al., 2011). After determining the displacement vectors, velocity vectors are found by dividing the displacement vectors by the known time interval.

As discussed above, PIV requires high-tech instrumentation and accurate statistical methodologies in order to produce accurate velocity fields. The next subsections discuss the steps involved in a successful PIV experiment.

### **3.3.2 Seeding particles**

The tracer particles are critical component of the PIV system since their displacements determine velocity of the fluid. Hence, particle characteristics become very important in matching the fluid properties so that they represent the fluid motion in an acceptable way. The seed particles must be small enough so that it can follow the flow faithfully at every instant of time. The large difference between the fluid density and particle density may influence the particle's ability to track the flow fluctuations and turbulence. On the other hand, the seeding tracers should be large enough and with refraction index different from the refraction index of the fluid so that they reflect a sufficient amount of light that can be recorded by the camera (Raffel et al., 2007). Also, large seeding particles may cause attenuation of the turbulence in critical flow areas where large gradients of velocity are expected, such as vortex cores and shear layers. It has been established (Prasad et al., 1992) that to minimize bias error due to the sub-pixel interpolation the diameter of the particle image should not be less than two pixels. This also ensures that each particle's position can be accurately determined. The latter criterion depends on many parameters such as particle's material properties, refraction index, laser light intensity and resolution of the CCD camera (Raffel et al., 2007).

In the present experiments, hollow glass-beads of mean diameter ( $d_p$ ) 10  $\mu\text{m}$  and specific gravity of 1.1 manufactured by Potters Industries are used as the tracer particles. Clift et al. (1978) has used the Stokes settling velocity law in stagnant fluid to confirm

that seeding particles can follow the fluid motion satisfactorily. The particle settling velocity is given by

$$u_T = \frac{gd_p^2(\rho_p - \rho)}{18\mu} \quad (3.1)$$

Here  $\rho_p$  and  $d_p$  are particle's density and diameter,  $u_T$  is the particle settling velocity and  $\mu$  and  $\rho$  are the dynamic viscosity and density of the fluid. By using Eq. (3.1), the settling velocity for the present particles is found to be 0.0055 mm/s, which corresponds to a particle Reynolds number  $Re_p = \frac{d_p u_T}{\nu} = 5.4 \times 10^{-5}$ . Following the study of Milojevic (1990) the particle response time  $\tau_p$  can be calculated by

$$\tau_p = \frac{d_p^2 \rho_p}{18 \mu f_d} \quad (3.2)$$

Here  $f_d = 1.0 + 0.15 Re_p^{0.687}$  is the particle drag coefficient. By determining the fluid's timescale ( $\tau_F$ ), the Stokes number which is defined as the ratio of the particle response time to the fluid timescale ( $St = \frac{\tau_p}{\tau_F}$ ) can be compared with the criterion proposed by Clift et al. (1978) to confirm if the seed particles can follow the turbulent fluctuations of the flow

$$St \ll \frac{2 \frac{\rho_p}{\rho} + 1}{9} \quad (3.3)$$

In a conservative estimate for all the FOVs, the fluid's timescale is determined from the single cylinder case where larger turbulence intensities are observed in the near-wake region compared to the other test cases. The smallest  $\tau_F$  value is determined ( $\tau_F = 2.00 \mu s$ ) on the axis of symmetry at  $x/D \sim 2.0$  where the highest turbulent kinetic energy is observed. The Stokes number is found to be 0.0028 which is much smaller than the criterion (0.36) to require that the particles are following the flow faithfully.

Adrian (1991) suggested that image interrogation area should cover at least 15-20 seeding particles to reduce the noise level in PIV measurement. In order to satisfy this criterion, the approximate amount of seeding particles is estimated based on the dimensions of the field-of-view (FOV). The seeding particles were mixed with a small volume of water to prepare a high density stock solution. The stock solution was added to the filtered water in the flume to better control the particle concentration of water in the flume and to ensure that no lump-deposition of the particles occur in the flow.



### 3.3.3 Laser and optical setup

The light source and optical setup are required to generate a thin laser sheet to illuminate the particles in the flow. In the present PIV system, the light source is a double-pulsed Nd-YAG laser (New Wave Research Solo PIV) that produces an energy of 50 mJ/pulse at 532 nm wavelength. The duration between the laser pulses is 6 - 10 ns which yields a very short exposure time for each frame. This avoids image blurring and excessive reflection in the image. The latter issue can be caused by motion of the seeding particles during the camera's exposure time. The illumination intensity must be high enough to allow for detection of the individual particles in the flow. Furthermore, the separation time between the two laser pulses must be long enough to allow particles to move almost 1/4 to 1/3 length of the interrogation area (Adrian, 1991). In the present study, the maximum repetition rate of the laser was 15 Hz, so two identical lasers are operated in straddle mode controlled by a synchronizer (TSI 610035) to emit two laser pulses in a short time interval. The total number of 2000 image pairs was recorded at each field-of-view (FOV), with a frequency of 0.73Hz which is smaller than the laser repetition rate.

The optical setup consists of spherical and cylindrical lenses. The generated laser beam passes through a combination of spherical and cylindrical lenses and to generate a thin light sheet. While the spherical lens controls the thickness of the light sheet the cylindrical lens controls its height. The light sheet needs to be two dimensional or thin enough to avoid the out of plane motion of the seeding particles; also thinner light sheet provides higher light intensity in the flow.

In the present study, a spherical lens with 500 mm focal length and a cylindrical lens with -15 mm focal length are used to generate a laser sheet of high light intensity with about 1 mm thickness. The laser sheet was illuminated from the side of the flume for horizontal plane measurements while for the vertical plane measurements; the laser sheet was emitted from the top of the flume. Figure 3.7 illustrates the laser and camera arrangements for horizontal and vertical planes measurements.

### **3.3.4 Camera set**

In this study, a charged-coupled device (CCD) camera is utilized to record images in a double-exposure double-frame mode. The reflected light from the seed particles is recorded on CCD array. The CCD camera sensor consists of a large number of light sensitive cells or pixels, which are capable of producing an electric charge proportional to the amount of incident light. This electrical charge is transferred to the computer during data acquisition and saved as grey-scale intensity image files with the resolution of the sensors in either direction. The TSI Powerview plus 4MP camera is used in this study which has the resolution of  $2048 \times 2048$  pixels. The number of discretized intensity levels at each pixel is  $2^A$ , where A is the number of bits of the camera. As the grey-scale images are recorded by 12-bit camera, so the entire intensity range of the images is discretized into 4096 levels where zero represents black and 4096 represents white in the images.

The camera is fitted with a 70 – 300 mm Nikkor lens to obtain the best view in the field of interest. It has to be motioned that before each run, image calibration is required to determine the pixel size of the images. Image calibration is achieved by taking a picture of two perpendicular tempered steel rulers with 1 mm divisions to confirm that there is no distortion over the FOV by the optics of the camera.

Furthermore, by knowing the pixel size of the image, the size of interrogation area can be determined. The time interval ( $\Delta t$ ) between two laser pulses is estimated so that the seeding particles would travel approximately 8 to 10 pixels in the interrogation area at the maximum expected velocity in the FOV.

### **3.3.5 Image analysis**

The main purpose of the PIV technique is to determine the displacement of the seeding particles between two recorded images. The images are processed with INSIGHT 4G (by TSI) which implements advanced correlation and deformation processors used to determine the shift in particle's position between two nearly identical particle images. There are two correlation methods available in use; the auto-correlation and cross-correlation methods. The first method is commonly used for multiple-exposure images on

a single frame while the cross-correlation technique is used for multiple-exposure images on two separate frames.

Before applying the cross-correlation technique, each image was subdivided into several small areas called interrogation areas (IA). The interrogation areas are considered sufficiently small so that second order effects, such as displacement gradient would not affect it. In many PIV systems, typical interrogation area size are chosen to be  $16 \times 16$ ,  $32 \times 32$  or  $64 \times 64$  pixels. It is important to note that each IA should contain enough particles (at least 15) to reduce the measurement noise (Adrian, 1991). In each image pair, the first image shows the information about the particles' location. The second image that is recorded at the time delay  $\Delta t$ , is supposed to contain the same particles' information which have moved a short distance due to flow. The discretized cross-correlation function  $CC(x,y)$  is given by

$$CC(x, y) = \sum_{i=-m}^m \sum_{j=-n}^n I_1(i, j) I_2(i + x, j + y) \quad (3.4)$$

Here  $I_1$  and  $I_2$  are the pixel intensity of the interrogation area extracted from two separate frames images.  $CC(x,y)$  is calculated for each IA in its size range of  $(-m \leq i \leq m, -n \leq j \leq n)$  and the maximum value is used to find the displacement vector  $S(x, y)$ . Statistically, the cross-correlation technique represents the degree of matching (correlation) between the two IAs for the given displacement. The highest value of the cross-correlation indicates the correct displacement vector for that particular IA. Once the displacement and the time interval ( $\Delta t$ ) between the image pairs are known, the velocity vector at time  $t$  for the particular IA can be determined as

$$V(IA, t) = \frac{S}{\Delta t} \quad (3.5)$$

The INSIGHT 4G correlation engines implement direct correlation and FFT correlation techniques. Since the whole image is discretized into IAs, the FFT can be applied on the pixel intensity of each IA pair to speed up the cross-correlation process faster than the direct cross-correlation method (Raffel et al., 2007).

In the present image analysis, the correlation process is performed in two passes. A coarse size (e.g.,  $64 \times 64$  pixels) of the IA is chosen to determine the initial displacements using FFT based cross-correlation method. This estimate is further reanalyzed on the finer grid with 50 % overlapping to produce the final displacement of the IA (e.g.,  $16 \times 16$  pixels). Since the size of FOV in all the test cases is not constant,

different sizes of IA are chosen to keep the spatial resolution constant at about 0.5 mm. This resolution is sufficient to capture the large scale vortical structures. The actual spatial resolution of the processed velocity field in different FOVs is presented in Tables 3.2 and 3.3.

### **3.3.6 Removal and replacement of spurious vectors**

PIV measurements are prone to errors in determining the displacement vectors. These errors appear as spurious vectors in the calculated velocity field. Many sources of noise such as insufficient number of tracer particles in the IA, poor image quality, poor image resolution, excessive out of plane particles' displacement or large velocity gradients can influence calculation of the cross-correlation function in the image processing. As a result of the wrong detection, spurious vectors are calculated in the velocity field. Figure 3.8 shows a vector field with spurious vectors obtained from the PIV measurement after image analysis. Regardless of how carefully the measurements are conducted, these spurious vectors occur in the velocity field and should be carefully validated and even removed before further processing. Raffel et al. (2007) defined some indicators to identify the spurious vectors. They believed that typical spurious vectors deviate considerably from the surrounding neighbor vectors in their magnitude and direction. They have also noticed that more spurious vectors are observed at the edges of the FOV's. Manual checking and replacement of spurious vector with a correct one is not feasible for a large number of recorded images. Suitable automated algorithm satisfying some criteria should be applied. According to Raffel et al. (2007), the ideal algorithms should identify all suspicious vectors and reject them from the PIV dataset. In each algorithm, choosing a proper parameter as the threshold is the key to making the algorithm universal. Amongst different spurious vector detection methods, a cellular neural network (CNN) based algorithm was found to be superior compared to other methods (Liang et al., 2003). In this algorithm, increasing the threshold level makes the detection method less aggressive; and it tends to tag some spurious vectors as valid ones. Shinnee et al. (2004) overcome this draw back by proposing variable threshold outlier technique (VCNN). In this method the initial threshold value is calculated based on the vector field itself and a constant value defined by the user. In the next step, a new

variable threshold field is estimated based on the initial neighbour threshold values and then it is applied to the original vector field to detect the spurious vectors. The superior benefit of this method compared with the CNN algorithm is the self-adjustment of the threshold value at different regions of the flow-field depending on the velocity gradient. In contrast, the CNN algorithm implements constant threshold value for the whole flow-field. A brief description of the VCNN method is presented below.

The velocity vectors  $u$  and  $v$  in  $x$  and  $y$  directions are defined at each grid point  $i$ . If the absolute difference in  $u$ -velocity component from the neighbor point  $j$  is  $R_{ij}^u = |u_i - u_j|$  and  $\tilde{T}_i^u$  represents the threshold for spurious vector detection for  $u$  at  $i^{th}$  grid point given by

$$\tilde{T}_i^u = \frac{1}{n} \sum_{j=1}^n R_{ij}^u + K \quad (3.6)$$

Here  $K$  is a constant and  $n$  is the total number of neighboring points to  $i^{th}$  grid point.  $\tilde{T}_i^u$  is dependent on the value of constant  $K$  as well. Eq. (3.6) confirms that the threshold  $\tilde{T}_i^u$  is not constant for the whole flow field and varies from point to point. It represents a mean deviation in the  $u$ -velocity component for each grid point  $i$  from its neighboring points.

In order to make the threshold less dependent on  $K$ , which is selected by the user, the threshold is filtered by a Gaussian kernel to highlight the effect of the neighboring threshold. In the Gaussian method the distance of  $i^{th}$  grid point to each neighbor point  $j$  is defined as  $L_{ij}$ . In order to normalize the distances between two grid points a length  $\sigma = 3 \times \text{grid size}$  is used to determine the Gaussian kernel coefficient  $\alpha_{ij}$ .

$$L_{ij} = \sqrt{(x_i - x_j)^2 + (y_i - y_j)^2} \quad (3.7)$$

$$\alpha_{ij} = \exp\left(-\frac{1}{2} \left(\frac{L_{ij}}{\sigma}\right)^2\right) \quad (3.8)$$

By applying the Gaussian kernel for all the neighboring points, the final threshold ( $T_i^u$ ) value for point  $i$  in the grid is defined as

$$T_i^u = \frac{\sum \alpha_{ij} \tilde{T}_j^u}{\sum \alpha_{ij}} \quad (3.9)$$

After determining the threshold value the CNN method (Liang et al., 2003) is used for further process in the algorithm for detecting the spurious vectors. In  $u$ -velocity domain, the weight between neighbor points  $i$  and  $j$  is defined as

$$W_{ij}^u = \text{MAX}(-T_i^u, T_i^u - R_{ij}^u) \quad \text{and} \quad W_{ii}^u = 0 \quad (3.10)$$

In this weight scheme, there is no self feedback to the weight that is why  $W_{ii}$  is set to zero. The cumulative weighted function ( $S_i^u$ ) at  $i^{th}$  grid point is calculated by

$$S_i^u = \sum_{j=1}^n W_{ij}^u \gamma_j^{k-1} \quad (3.11)$$

Here  $\gamma_j$  is the validity state (0 or 1) of the neighbor point  $j$  at the previous iteration. Initially all the vectors in the flow-field are considered to be valid so,  $\gamma$  at all grid points is set to one. Following the calculation of the sum, in the  $k^{th}$  iteration, the validity state of point  $i$  changes to zero if  $S_i^u < 0$ . It should be mentioned, this iterative algorithm converges very fast. Usually if the algorithm convergence does not occur in less than 10 iterations, it denotes that the state of some vectors oscillate between 0 and 1. These latter vectors are detected as spurious vectors in the algorithm.

Eventually after detecting each  $i^{th}$  spurious vector in the velocity field, it is replaced with a new vector with the Gaussian-weighted average method as:

$$u_i = \frac{\sum \alpha_{ij} u_j}{\sum \alpha_{ij}} \quad (3.12)$$

The neighbor zone surrounding grid point  $i$  is considered to be a  $5 \times 5$  square region, while near the edges of FOV it changes to  $3 \times 3$ . The same procedure is applied for the  $v$ -velocity component.

In the present study, the percentage of rejected vectors varied from 2% to 8%. Most of the rejected vectors were at the edges of the velocity fields and near the cylinder in the areas where the accuracy of the displacement was affected by the cylinder shadow.

### 3.4 Uncertainty analysis

Successful velocity measurement with PIV requires operation of different complex subsystems. The uncertainty generated from each of these subsystems should be considered not only individually but also as a coupled system in evaluating the absolute measurement uncertainty. The approach to the uncertainty analysis of a PIV measurement is a combination of a variety of aspects ranging from the imaging process to the method of image analysis. While PIV is an established experimental technique for determining a velocity field, quantifying the uncertainty related with this method remains a challenging task and it is a subject of ongoing research.

As a general definition, the uncertainty in any physical measurement can be divided into systematic (bias) and random errors (Coleman and Steele, 2009). The bias errors in PIV measurement are caused by timing error of the laser pulse, calibration errors, error due to the large image particle diameter, inadequate interrogation size for finding the displacement vectors and improper algorithm to calculate the maximum displacement. In the present study, the most dominant contributing term can be discussed as the inappropriate sub-pixel peak-estimation in the evaluation the displacement of seed particles in the IA, while other terms may have less contribution in the total bias error. The latter can be addressed as the appropriate calibration method used for each FOV, using a proper synchronizer subsystem to control the laser pulse duration time and using suitable seeding particles to make sure the particles track the fluid motion faithfully. Eventually, the bias error is determined just due to error in displacement estimation. Willert and Gharib (1991) showed that the displacement error can vary from 1 % to 10 % for different seeding particle densities. Also, Forliti et al. (2000) discussed that the error in the mean particle displacement is almost in the range 0.05 – 0.1 pixel in the Gaussian-fitting algorithm. In a conservative error estimate (0.1 pixel displacement), the estimated mean displacement error in cross-correlation function is found to be almost 1.2 %. Prasad et al. (1992) believed that the bias error increases as the seeding particle image diameter is much less than the image pixel resolution. Huang et al. (1997) believed that while change in particle size will influence the sub-pixel accuracy in the particle displacement estimation, it may not result a significant difference in random error. In contrast, Adrian (1991), Prasad et al. (1992) and Westerweel (2000) concluded that increase in particle diameter will raise the random error in the uncertainty.

Multiple factors such as electronic noise in the pixel readout, pairing loss in the second image, irregular seed particle images and strong velocity gradient can raise the random error as pointed out by Sciacchitano et al. (2015). One of the major issues that increases the random error in PIV measurement is the loss of some information in the second image of a pair due to change in the laser light intensity and out-plane motion of seed particles in particular. Also, non-spherical particles may show distortion of seed particles from one exposure to another one, which implies the two images in a pair lose some of their correlation with each other that can increase the random error in

measurements (Prasad et al., 1992). In addition, strong in-plane velocity gradients in both directions such as shear layers and near-bed flows can raise random errors in these regions. Therefore, before starting any further analysis it is wise to reduce the random errors by conducting accurate experiments and altering the spurious vectors with proper ones.

In this study three methods have been applied to determine the uncertainty in each FOV. The first method for estimating the uncertainty is based on the Student's  $t$ -distribution method for 95% of confidence level. The second method is based on the work of Prasad et al. (1992) study of the effect of interrogation area resolution and particle image diameter on the total uncertainty. The third method that is known as Westerweel method, discusses the influence of particle image diameter and the particle density on uncertainty estimation (Westerweel, 2000).

One of the regular methods to estimate the uncertainty is using the Student's  $t$ -distribution method. In this method the uncertainty is calculated at the confidence level of 95% that can be assessed a representative of the true uncertainty value as

$$UN = \sqrt{B_{bias}^2 + (t_{95}\sigma)^2} \quad (3.13)$$

Here,  $B_{bias}$  is the bias uncertainty and the product,  $t_{95}\sigma$  is known as the random error.  $t_{95}$  is the value of the  $t$  distribution at the 95% confidence level which for 2000 samples it becomes 1.96, and  $\sigma$  is the standard deviation of the measured velocity. By substituting the bias error magnitude and the standard deviation of the velocity field ( $u_{rms}/U$ ) for each FOV in Eq. (3.13), the relative uncertainty in the velocity field is given by

$$UN (\%)|_U = \sqrt{1.2^2 + (1.96 u_{rms}/U)^2} \quad (3.14)$$

The contour distribution of calculated total U-uncertainty value using the Student's  $t$ -distribution method for the single cylinder at mid-depth for LR and HR cases are displayed in Figure 3.9. As shown in the plots of Figure 3.9, the maximum uncertainty value for C1-LR and C1-HR cases at mid-depth plane is 1.4% and 1.3%, respectively. The Student's  $t$ -distribution method uncertainty value for each FOV is

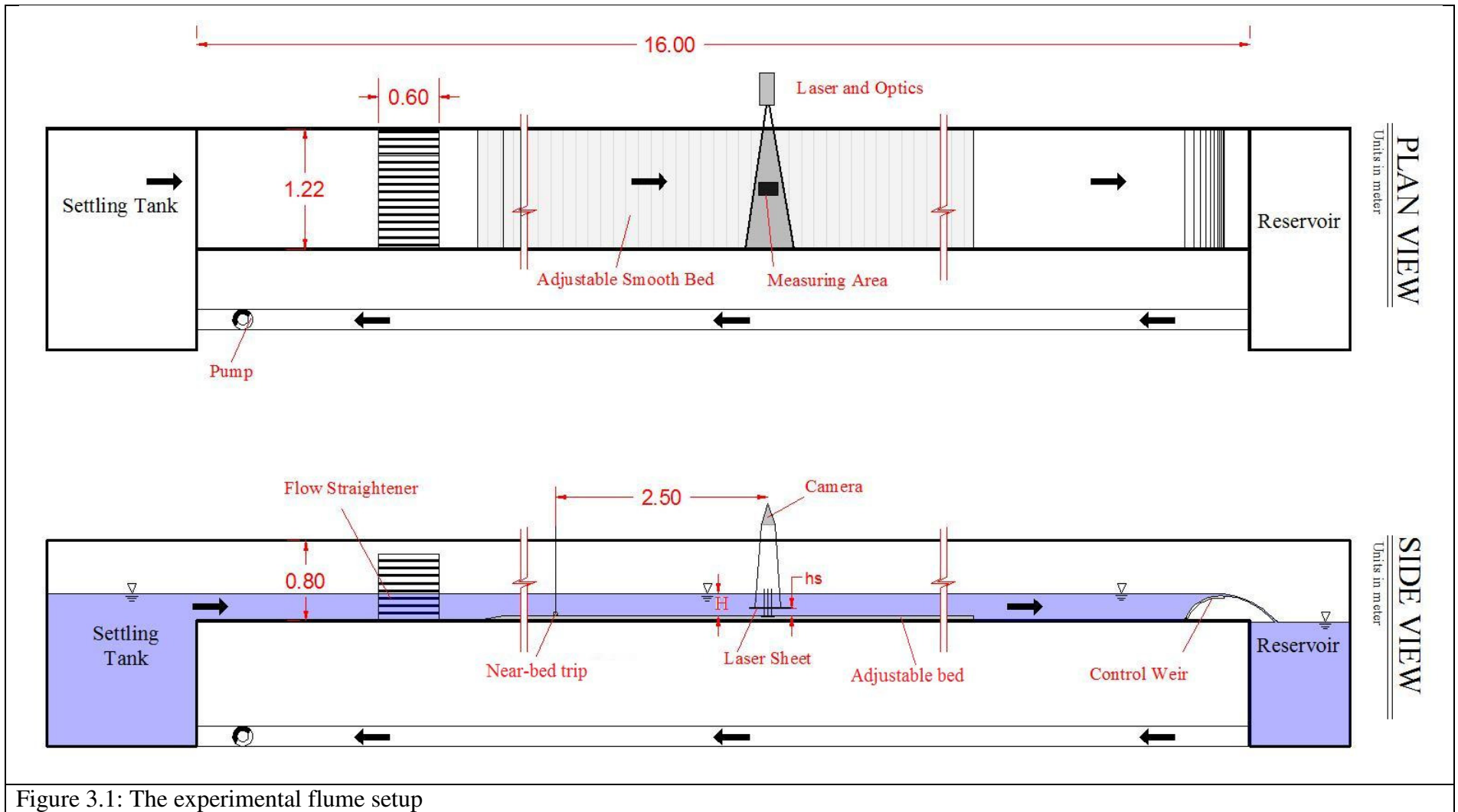


calculated and its maximum value is listed in Tables 3.5 and 3.6 for low and high Reynolds number cases, respectively.

Prasad et al. (1992) used the translation and rotation of photograph technique to determine the uncertainty error for each effect. They also studied the effect of interrogation area resolution on the bias error. Following Prasad et al. (1992) if the ratio of particle image diameter to the pixel size ( $d_{ratio}$ ) is larger than 3 the random error in PIV uncertainty becomes more dominant than the bias error. In the present study, the mean particle image size in different FOVs is found to be between 3 and 6 pixels, as shown in Tables 3.5 and 3.6. Also, Adrian (1991) believed that the random error for relatively large and irregular particles is proportional to the particle diameter (random error =  $C_1 \times d_{ratio}$ ). Prasad et al. (1992) discussed that this coefficient for the translation photographs will be 0.05 and 0.07 for the mean diameter of the seed particles of 40  $\mu\text{m}$  and 60  $\mu\text{m}$ , respectively while in a turbulent flow the total uncertainty (including bias and random error) estimation can be approximated by 0.10 of  $d_{ratio}$  if the mean diameter of the seed particles is 35  $\mu\text{m}$ . In this study the coefficient may reduce to 0.024 since the mean seed particle size is 10  $\mu\text{m}$ . As observed in Tables 3.5 and 3.6 the estimated total uncertainty values of mean velocity using the Prasad method ranges from 0.9% to 1.7% for all the measurements.

Following Prasad's method, Westerweel (2000) explored the sub-pixel displacement error by deriving analytical expression in terms of the particle density and particle image diameter on the synthetic PIV images. Westerweel (2000) believed that the linear relation proposed by Adrian (1991) underestimates the error if the particle image diameter ratio is larger than 2.0. He showed in his study that the total error (including bias and random) increases proportional to  $d_{ratio}^2$ . The total uncertainty value based on Westerweel method for each FOV is calculated and listed in Tables 3.5 and 3.6 for both Reynolds numbers. In general, the uncertainty calculated based on Westerweel method shows higher values than the two other methods. In a conservative estimation, the total uncertainty of mean velocity can be considered as 2.2% for all FOVs and for both Reynolds numbers.

By applying the Student's t-distribution method, the uncertainty values for root mean square velocity in streamwise and spanwise directions ( $u_{\text{rms}}$  and  $w_{\text{rms}}$ , respectively) are calculated for each FOV as well. By considering the maximum of the total uncertainty values of root mean square velocity in all FOVs for both Reynolds numbers, the total uncertainty values for  $u_{\text{rms}}$  and  $w_{\text{rms}}$  are reported as 2.0%, 3.5%, respectively.



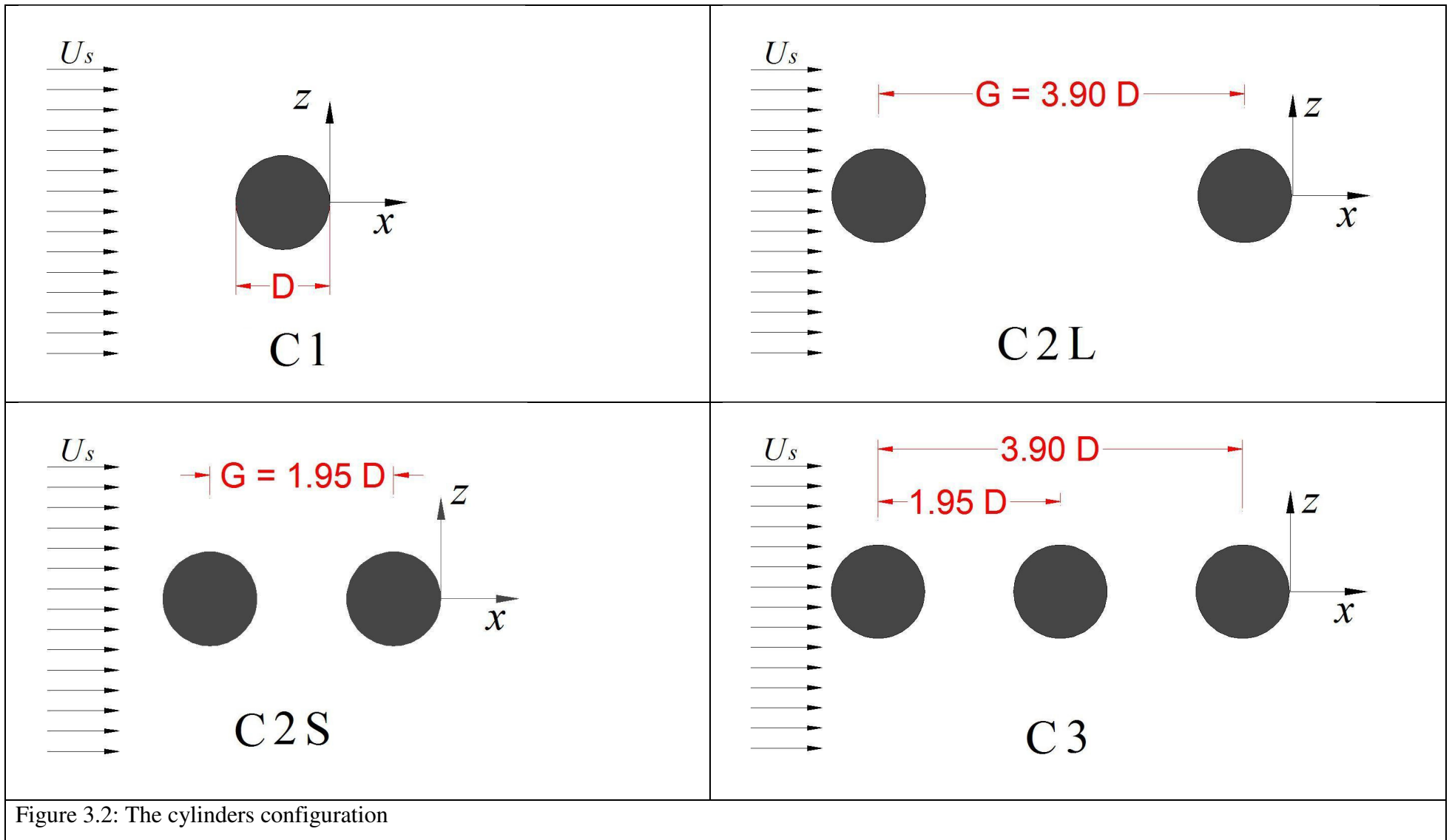




Figure 3.3: A sample picture of cylinders in the flow (C2L)

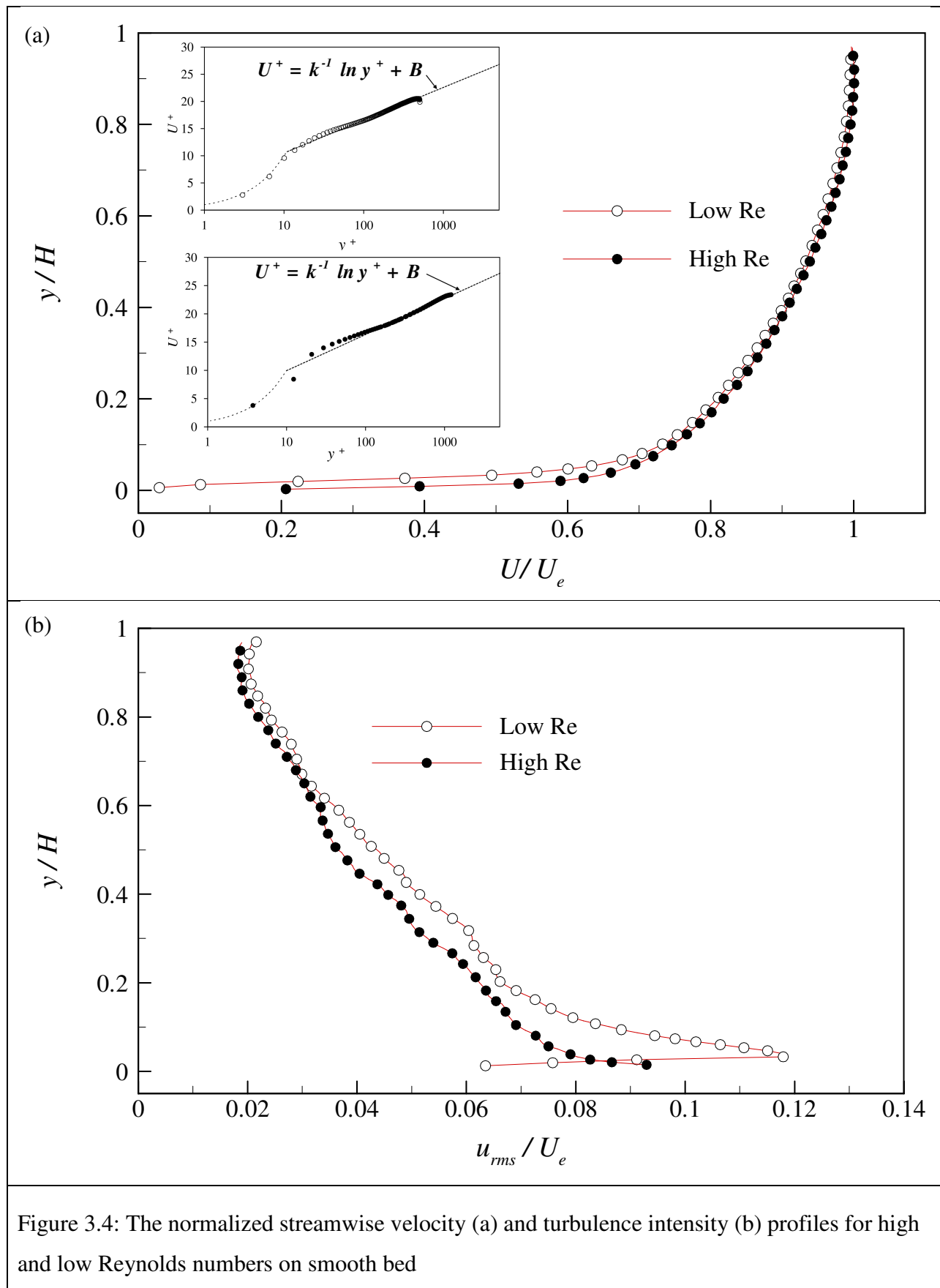


Figure 3.4: The normalized streamwise velocity (a) and turbulence intensity (b) profiles for high and low Reynolds numbers on smooth bed

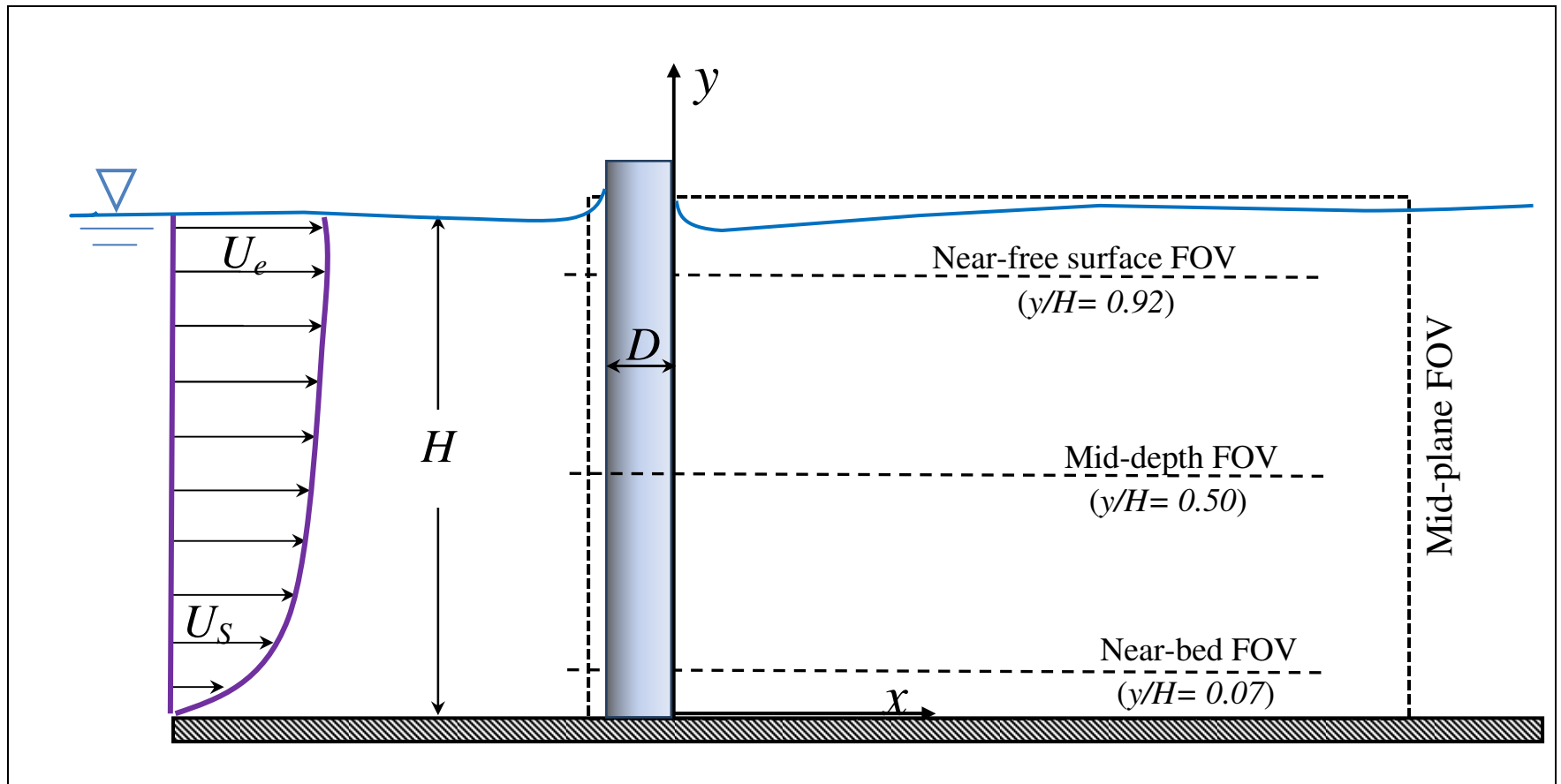
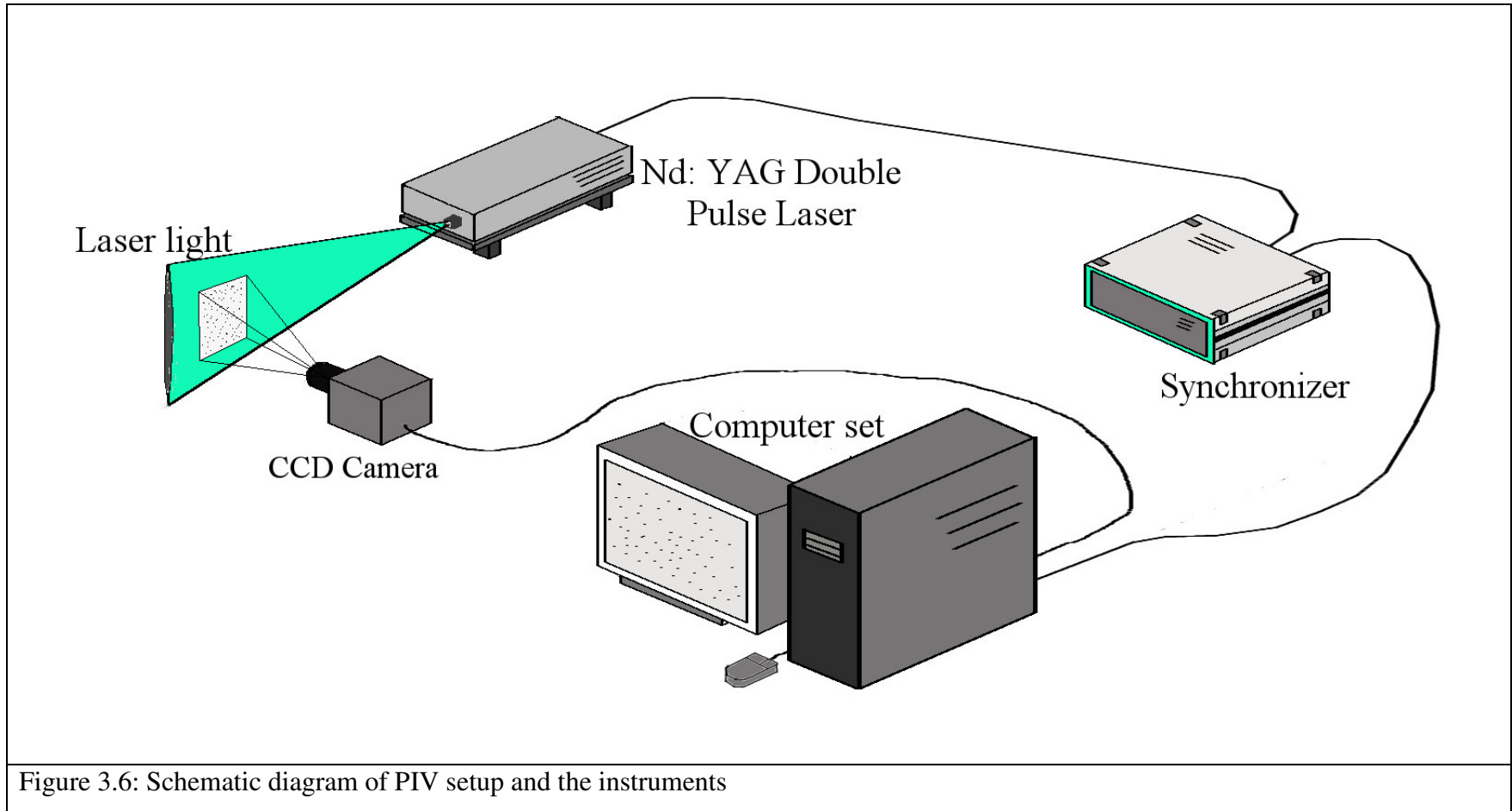
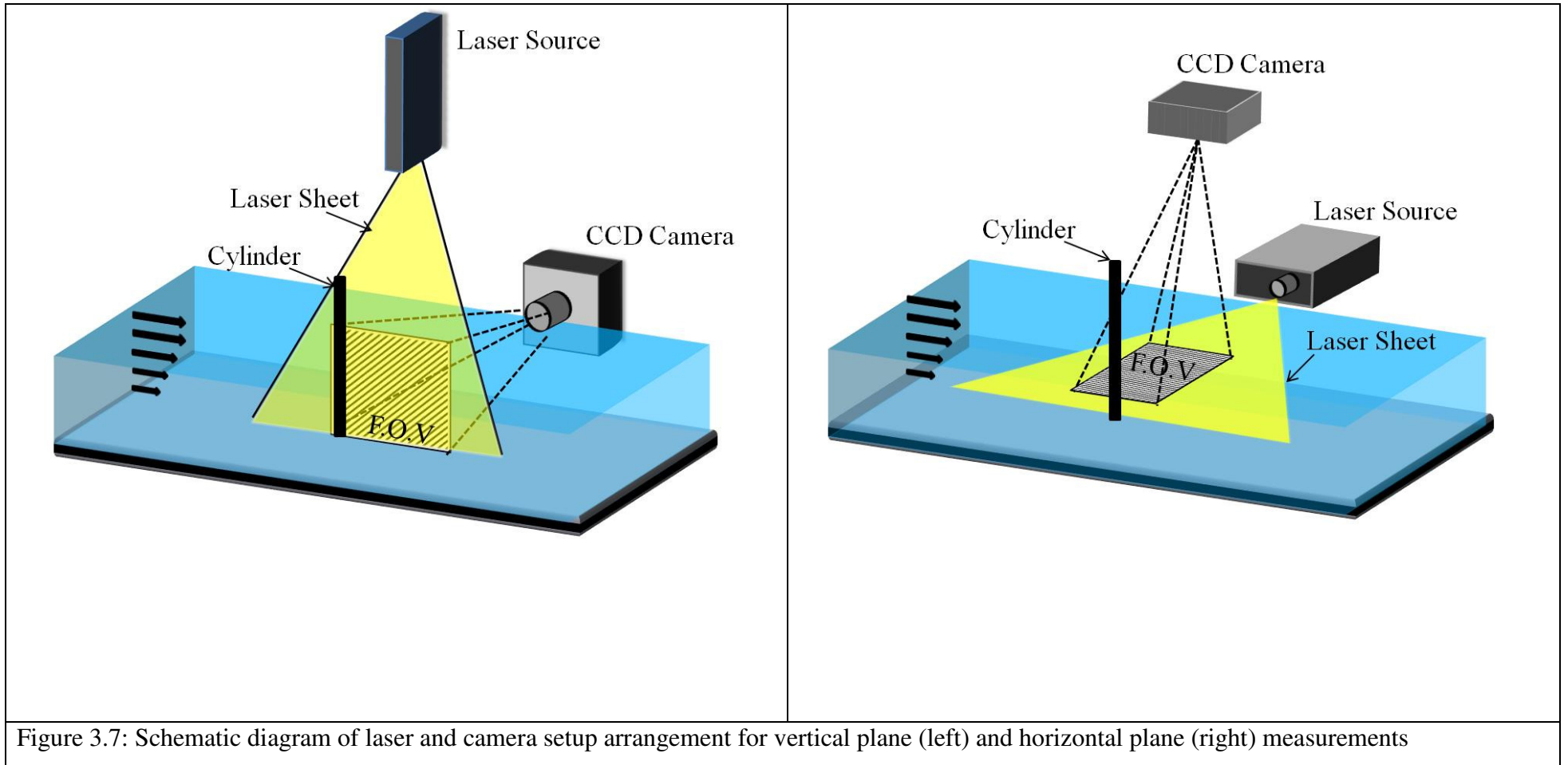


Figure 3.5: Schematic of the three horizontal planes of measurement as near-bed, mid-depth and near-free surface FOV and a vertical plane of measurement as the mid-plane FOV









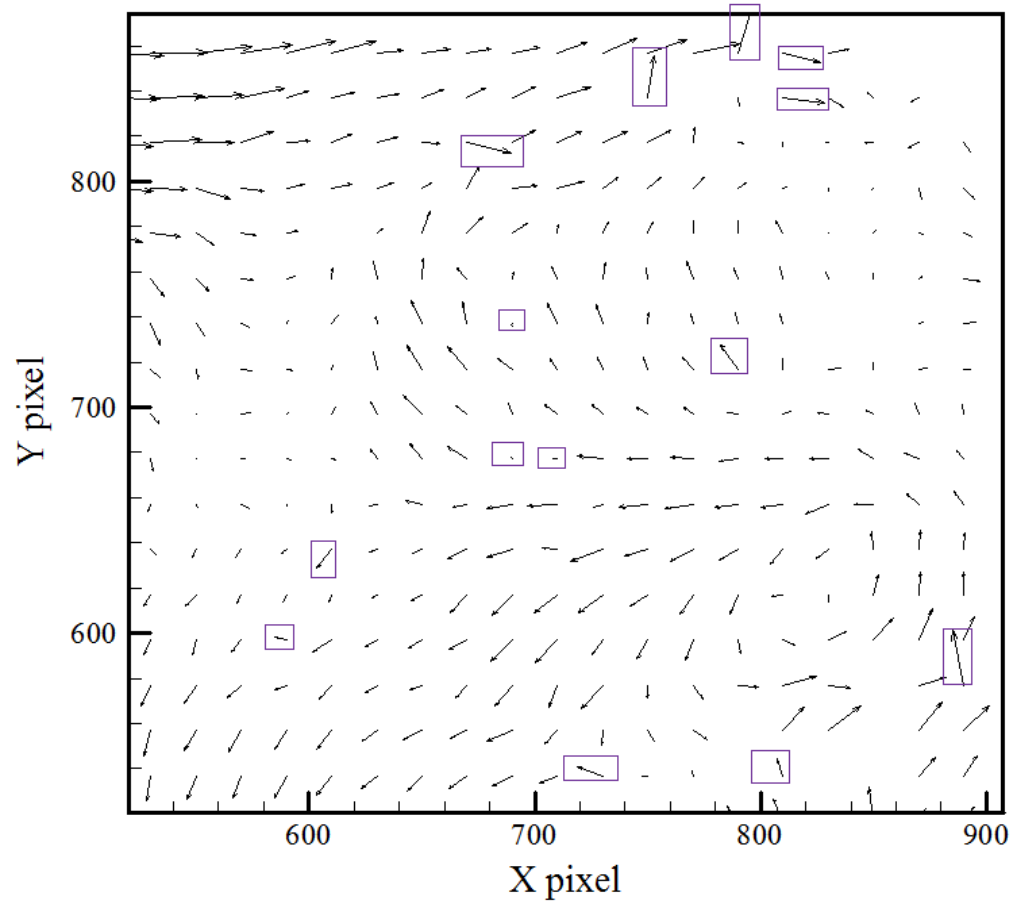


Figure 3.8: A sample field-of-view with spurious vectors shown in boxes

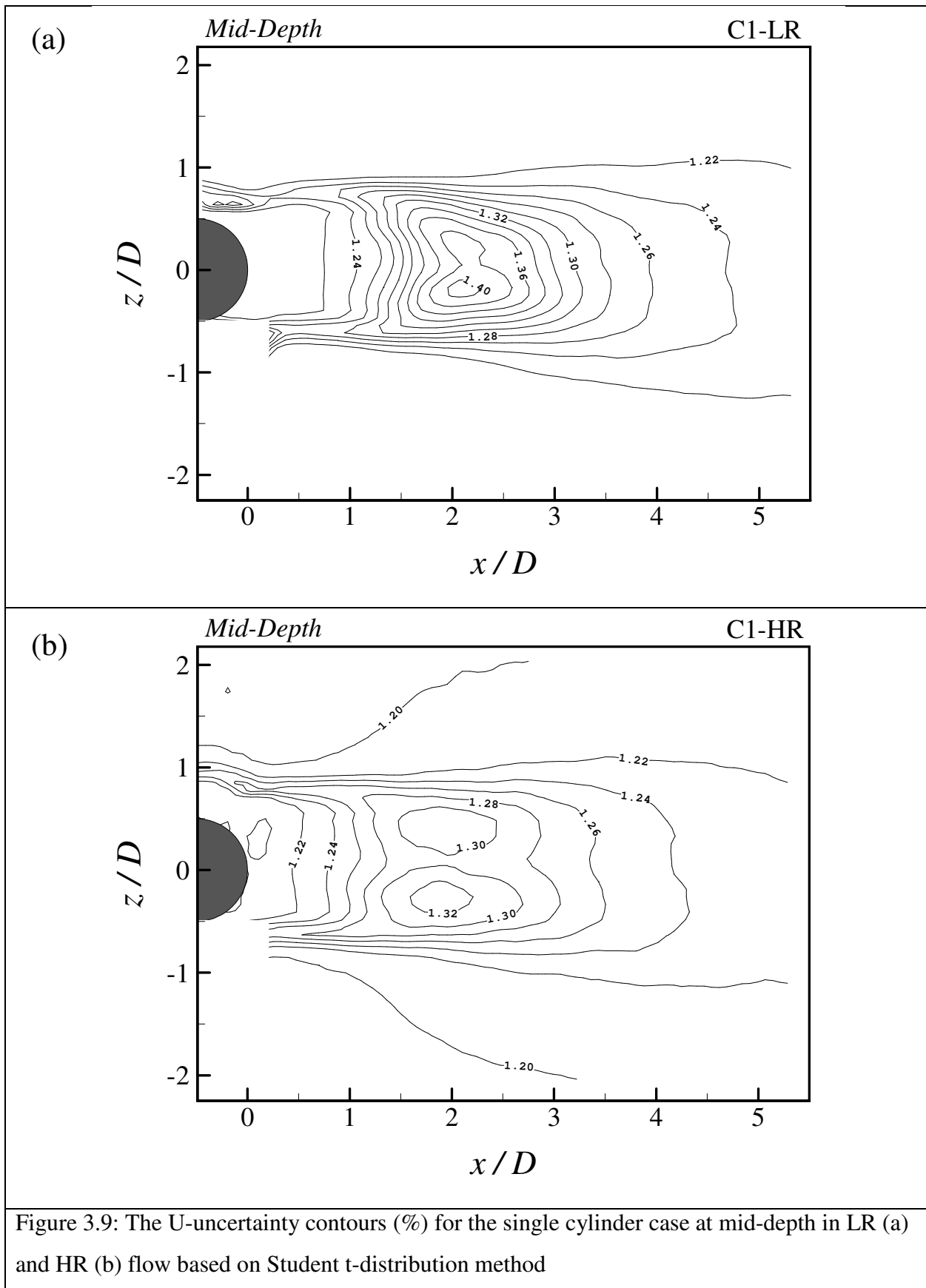


Figure 3.9: The U-uncertainty contours (%) for the single cylinder case at mid-depth in LR (a) and HR (b) flow based on Student t-distribution method

Table 3.1: The flow properties of two Reynolds numbers											
Flow conditions	H (m) $\times 10^{-2}$	$U_e$ (m/s) $\times 10^{-2}$	$u_*$ (m/s) $\times 10^{-3}$	$C_f$ $\times 10^{-3}$	$Re_H$	<sup>1</sup> Fr	<sup>2</sup> $\theta$ (m) $\times 10^{-3}$	<sup>3</sup> $Re_\theta$	<sup>4</sup> $\delta/H$	<sup>5</sup> h	$B_f/H$
Low Re	7.0	15.6	7.6	6.1	10,340	0.17	5.7	839	0.77	1.44	17.3
High Re	7.0	51.1	21.8	4.6	33,047	0.55	5.3	2,516	0.73	1.47	17.3

<sup>1</sup> Froude number based on mean velocity ( $U_{\text{mean}}$ ),  $Fr = U_{\text{mean}} / \sqrt{gH}$

<sup>2</sup> momentum thickness

<sup>3</sup> Reynolds number based on momentum thickness ( $\theta$ ) and free stream velocity  $Re_\theta = U_e \theta / \nu$

<sup>4</sup> Boundary layer thickness defined based on  $0.99 U_e$

<sup>5</sup> Shape factor,  $h = \text{displacement thickness} / \text{momentum thickness}$

Table 3.2: The position, size and resolution of the fields-of-view (FOV) in different cylinder configurations at low Reynolds number flow						
	Cylinder Configuration	Horizontal / Vertical FOV	$y/H$	Size of FOV (mm)	$z/D$	Spatial Resolution (mm)
Low Reynolds number flow	C1	Near-bed (H)	0.07	64.0	-2.80 to 7.20	0.51
		Mid-depth (H)	0.50	59.1	-5.24 to 4.00	0.47
		Near-free surface (H)	0.92	59.2	-3.65 to 5.59	0.47
		Vertical plane (V)	all	90.0	0.00	0.49
	C2S	Near-bed (H)	0.07	64.0	-2.93 to 7.07	0.51
		Mid-depth (H)	0.50	62.7	-2.87 to 6.93	0.50
		Near-free surface (H)	0.92	61.5	-2.87 to 6.74	0.49
	C2L	Near-bed (H)	0.07	63.8	-2.88 to 7.09	0.51
		Mid-depth (H)	0.50	63.0	-2.96 to 6.88	0.50
		Near-free surface (H)	0.92	61.6	-2.90 to 6.73	0.49
	C3	Near-bed (H)	0.07	64.0	-2.94 to 7.05	0.51
		Mid-depth (H)	0.50	63.0	-2.93 to 6.92	0.50
Near-free surface (H)		0.92	61.9	-2.75 to 6.92	0.49	

Table 3.3: The position, size and resolution of the fields-of-view (FOV) in different cylinder configurations at high Reynolds number flow						
	Cylinder Configuration	Horizontal / Vertical FOV	$y/H$	Size of FOV (mm)	$z/D$	Spatial Resolution (mm)
High Reynolds number flow	C1	Near-bed (H)	0.07	95.0	-4.01 to 10.85	0.47
		Mid-depth (H)	0.50	95.5	-4.39 to 10.54	0.47
		Near-free surface (H)	0.92	95.2	-4.85 to 10.03	0.47
		Vertical plane (V)	all	87.3	0.00	0.48
	C2S	Near-bed (H)	0.07	95.1	-3.93 to 10.93	0.47
		Mid-depth (H)	0.50	95.6	-4.40 to 10.54	0.47
		Near-free surface (H)	0.92	95.4	-4.79 to 10.12	0.47
	C2L	Near-bed (H)	0.07	95.0	-4.00 to 10.85	0.47
		Mid-depth (H)	0.50	95.7	-4.87 to 10.08	0.47
		Near-free surface (H)	0.92	95.4	-4.84 to 10.06	0.47
	C3	Near-bed (H)	0.07	95.2	-3.95 to 10.92	0.47
		Mid-depth (H)	0.50	95.6	-4.48 to 10.46	0.47
Near-free surface (H)		0.92	95.4	-4.87 to 10.04	0.47	

Table 3.4: Instrumentation used for the particle image velocimetry measurement		
Data acquisition computer		
	Processor	<i>Intel P4 processor</i>
	RAM size	<i>1 GB</i>
	Camera connection	<i>frame-grabber card</i>
	Operating system	<i>Windows XP Professional</i>
	Software	<i>INSIGHT ®3G</i>
Synchronizer		
	Laser pulse synchronizer	<i>TSI 610035</i>
Illumination system		
	Laser	<i>New Wave Research SOLO PIV (Nd-YAG)</i>
	Wavelength	<i>532 nm</i>
	Power	<i>50 mJ/pulse</i>
	Spherical lens focal length (f)	<i>500 mm</i>
	Cylindrical lens focal length	<i>-15 mm</i>
Camera set		
	PIV camera	<i>TSI Powerview Plus 4MP</i>
	Type	<i>Cross-correlation</i>
	CCD chip	<i>12 bit resolution, greyscale</i>
	Image size	<i>2048×2048 pixels</i>
	Mode	<i>Double-frame double exposure mode</i>
	Lens	<i>AF 70-300mm Nikkor (Nikon ED)</i>
	Focal length	<i>70 - 300mm</i>
	Maximum aperture	<i>f 4.0</i>

Table 3.5: Summary of uncertainty estimation of mean velocity using Student's t-distribution, Prasad and Westerweel methods for different horizontal and vertical FOVs at low Reynolds number flow

					Mean velocity uncertainty (%)		
	Cylinder Configuration	Horizontal / Vertical FOV	$d_{ratio}$	Max random error (%)	Student t-distribution method	Prasad method	Westerweel method
Low Reynolds number flow	C1	Near-bed (H)	4.8	0.7	1.4	1.4	1.6
		Mid-depth (H)	4.3	0.7	1.4	1.3	1.3
		Near-free surface (H)	5.6	0.6	1.3	1.7	2.2
		Vertical plane (V)	3.5	0.4	1.3	1.1	0.9
	C2S	Near-bed (H)	3.0	0.6	1.3	0.9	0.6
		Mid-depth (H)	4.0	0.6	1.3	1.2	1.1
		Near-free surface (H)	3.1	0.6	1.3	0.9	0.7
	C2L	Near-bed (H)	5.2	0.6	1.3	1.6	1.9
		Mid-depth (H)	5.1	0.5	1.3	1.5	1.8
		Near-free surface (H)	3.4	0.5	1.3	1.0	0.8
	C3	Near-bed (H)	5.4	0.7	1.4	1.6	2.0
		Mid-depth (H)	3.9	0.6	1.3	1.2	1.1
Near-free surface (H)		5.3	0.5	1.3	1.6	2.0	



Table 3.6: Summary of uncertainty estimation of mean velocity using Student's t-distribution, Prasad and Westerweel methods for different horizontal and vertical FOVs at high Reynolds number flow

					Mean velocity uncertainty (%)		
	Cylinder Configuration	Horizontal / Vertical FOV	$d_{ratio}$	Max random error (%)	Student t-distribution method	Prasad method	Westerweel method
High Reynolds number flow	C1	Near-bed (H)	4.5	0.7	1.4	1.4	1.4
		Mid-depth (H)	4.0	0.6	1.3	1.2	1.1
		Near-free surface (H)	5.3	0.6	1.3	1.6	2.0
		Vertical plane (V)	5.3	0.4	1.3	1.6	2.0
	C2S	Near-bed (H)	3.2	0.5	1.3	1.0	0.7
		Mid-depth (H)	4.9	0.5	1.3	1.5	1.7
		Near-free surface (H)	4.9	0.6	1.3	1.5	1.7
	C2L	Near-bed (H)	3.2	0.5	1.3	1.0	0.7
		Mid-depth (H)	3.9	0.7	1.4	1.2	1.1
		Near-free surface (H)	5.1	0.5	1.3	1.5	1.8
	C3	Near-bed (H)	3.5	0.5	1.3	1.1	0.9
		Mid-depth (H)	4.5	0.6	1.3	1.4	1.4
Near-free surface (H)		5.4	0.5	1.3	1.6	2.0	

## Chapter 4: APPROACHING OPEN CHANNEL FLOW

### 4.1 General comments

This chapter is devoted to address the approaching flow characteristics in a shallow condition on a smooth bed. The most important aspects include the determination of the bed friction velocity and validity of logarithmic law in the velocity profile. Since the von Kármán coefficient for the classical log-law is considered to be constant with a universal value of 0.41, a detailed introduction about different values reported for von Kármán coefficient in the turbulent boundary layer type flow in the literature is presented. A brief review of turbulent flow near the wall is discussed. In addition, various methods of estimation of bed friction velocity are presented and the results are validated with the ones available in literature. Also, different methods to determine the von Kármán coefficient of the logarithmic law of the wall are discussed. This chapter concludes with specific conclusions relevant to this section and identifies the flow conditions that were used to evaluate the characteristics of flow past circular cylinders.

### 4.2 Introduction

Near-wall flows have been extensively investigated because of their importance in many engineering applications, particularly for quantifying the drag, wall shear stress or bed friction. In 1930, von Kármán (Pope, 2000) described the mean velocity distribution of a pipe flow in a logarithmic form, given by the expression

$$U^+ = \frac{1}{\kappa} \ln y^+ + B \quad (4.1)$$

Here  $U^+ = \frac{U}{u_*}$  and  $y^+ = \frac{y u_*}{\nu}$ , where  $U$  is the mean streamwise velocity,  $y$  is the normal distance from the wall,  $u_*$  is the friction velocity and  $\nu$  is the fluid kinematic viscosity. In the classical law of the wall, Eq. (4.1), the coefficient  $\kappa$  is referred to as the von Kármán constant, and is considered to have a universal value of 0.41. The value of the constant  $B$  depends on flow type, geometry and wall conditions. Most turbulence models used in commercial software depend on the assumption that the near-wall flow can be described by Eq. (4.1). However, Spalart (2006) suggested that a 2% decrease in  $\kappa$  makes a 1% decrease in the

overall drag estimate. For example, aircraft manufacturers would prefer to perform simulations using a smaller value of  $\kappa$ , since the fuel consumption would appear to be more economical than a competitor's estimate with higher value of  $\kappa$  which determine the actual drag (George, 2007). In river engineering, the uncertainty in determining the value of  $\kappa$  can lead to substantial over- or under-prediction of the value of the shear stress in flows where sediment transport and erosion occur. Though a significant body of literature has been developed using direct numerical simulation (DNS) to solve the Navier–Stokes equations, its use is still restricted to flows at low Reynolds numbers that are not readily applicable to complex engineering flows. To develop predictive methods for calculating near-wall turbulence, one must therefore continue to rely on appropriate turbulence models. Model developers must carefully formulate and validate the new models using experimental databases. The limited availability of large-scale experimental facilities and the exorbitant costs involved in operating such facilities coupled with the experimental difficulties have resulted in the vast majority of laboratory data being acquired at relatively lower Reynolds numbers. It is therefore critical to understand the dependence of  $\kappa$  on Reynolds number. Using a correct value of  $\kappa$  in the wall functions, particularly for near-wall treatment, is a matter of importance in numerical analysis of turbulent flows.

Since the original development of Eq. (4.1) for pipe flows, its use to describe the mean velocity distribution in different wall-bounded flows such as the atmospheric boundary layer (ABL), turbulent boundary layers (TBL) and open channel flow (OCF) have been successfully used by many researchers. The development of laser based measurement techniques in the 1980s has provided access to accurate velocity measurements near the wall. It has now become a standard procedure for any near-wall measurements to confirm the validity of the logarithmic law of the wall. Many open channel flow studies (e.g., Sarma et al., 1983; Steffler et al., 1985; Nezu and Rodi, 1986) have studied the logarithmic overlap layer of the velocity distribution including evaluating the values of  $u_*$  and  $B$ . While many of the above-mentioned studies had the objective of obtaining a reliable value of  $u_*$  by assuming a constant value of the von Kármán coefficient, recently there has been evidence that  $\kappa$  may not be a constant and that it can depend on Reynolds number (Segalini et al., 2013; Nagib and Chauhan, 2008).

For many years, turbulence researchers simply used  $\kappa = 0.41$ , and thereby implicitly accepted that  $\kappa$  was a universal constant. However, different approaches to determine the von Kármán constant from the velocity measurements have been proposed. In the earliest field experiments by Sheppard (1947) and Pasquill (1950),  $\kappa$  was found to be 0.46 and 0.37, respectively. Later, in the well-known Kansas experiments, a smaller value of  $\kappa = 0.35$  was obtained by Businger et al. (1971) for atmospheric boundary layers.

There have also been attempts to compute  $\kappa$  for flow over a smooth wall with homogeneous turbulence. For instance, Long et al. (1993) analyzed the turbulent flow in smooth pipes and obtained  $\kappa = 0.408$ . Lo et al. (2005) estimated  $\kappa$  for wall-bounded turbulence based on the similarity with homogeneous constant shear turbulence, and obtained  $\kappa = 0.42$ . Gaudio and Dey (2013) reported that  $\kappa$  is not universal in flows with bed and suspended load transport. To date, the research community has not been able to reach a consensus on a single value of  $\kappa$ , with the values ranging between 0.36 and 0.44 for different canonical flow cases. Table 4.1 shows values of  $\kappa$  from several sources. It has only very recently become more common to refer to  $\kappa$  as the von Kármán coefficient (rather than a constant), thereby allowing for a pressure gradient dependence (Nickels, 2004; Nagib and Chauhan, 2008).

There is even less consensus in literature about the value of coefficient  $B$  in Eq. (4.1). In zero pressure gradient turbulent boundary layer, traditional estimates of  $B$  range between 4.9 and 5.1. Recent estimates cover a much wider range of  $B$  from 4 to 10. Surprisingly, the lack of apparent universality of  $B$  seems to be of far less concern than the precise value of  $\kappa$  (George, 2007).

This chapter is concerned with evaluating the von Kármán coefficient ( $\kappa$ ) and log-law constant ( $B$ ) in uniform open channel flow. For this purpose, a new set of experiments are conducted in a smooth open channel flow using a laser Doppler velocimetry (LDV) and particle image velocimetry (PIV), covering a depth Reynolds number ( $20,000 < Re_H < 60,000$ ) normally encountered in laboratory flumes. Mean streamwise velocity profiles were used to estimate friction velocity by applying various power law methods. The validity of the power law was established not only with open channel flow data available in the literature (Nezu and Rodi, 1986; Kirkgöz, 1989) but also with  $u_*$  obtained from

Reynolds shear stress distributions method extracted available from the two component velocity measurements. Different procedures for calculating  $\kappa$  are explored using the velocity distributions from the new experiments. Finally, by evaluating the eddy viscosity and implementing the Prandtl's mixing length theory, the variation of the von Kármán coefficient with Reynolds number is presented.

### 4.3 A brief review of near-wall turbulent flow

Fully developed turbulent boundary layer flow has been traditionally divided into two regions; inner and outer. The inner region represents 10–20% of the entire boundary layer thickness. In the near-wall region, the flow strongly depends on the wall shear stress ( $\tau_w$ ), density ( $\rho$ ), kinematic viscosity ( $\nu$ ) and vertical distance from the wall ( $y$ ). As such, friction velocity,  $u_* (= \sqrt{\tau_w/\rho})$  becomes the appropriate velocity scale, and the length scale is viscosity dependent and defined as  $\nu/u_*$ . For flow over a smooth bed, the inner region where the generation of turbulent kinetic energy is higher than the rate of dissipation (Nezu and Nakagawa, 1993), is further divided into the viscous sublayer, the buffer zone and the overlap region as shown in Figure 4.1. In the viscous sublayer, the viscosity is dominant and the velocity distribution is described by  $U^+ = y^+$ . The shear stress in this region is calculated based on the velocity gradient, i.e.,  $\tau_w = \mu \frac{\partial U}{\partial y}$ .

In the outer region, the effect of viscosity is inconsequential. Outer scales depend on a global length scale such as boundary layer thickness ( $\delta$ ) and on the free stream velocity ( $U_e$ ). In the outer region, the velocity profile can be described with the following equation:

$$U^+ = \frac{1}{\kappa} \ln y^+ + B + \frac{2\Pi}{\kappa} w(\eta) \quad (4.2)$$

where,  $w(\eta)$  is the wake function and  $\eta = y/\delta$  where  $\delta$  is the boundary layer thickness, defined as the distance from the wall where the velocity is equal to 99% of the free stream velocity. The parameter  $\Pi$  in Eq. (4.2) determines the strength of the wake. For the zero pressure gradient turbulent boundary layer, the value of  $\Pi$  was considered to be a constant. However,  $\Pi$  is dependent on the nature of the near-wall perturbations imposed on the boundary layer (Afzal et al., 2009). In the

case of open channel flow, the value of  $\Pi$  and the wake function can be influenced by the presence of the free surface, especially at shallow flow (Balachandar et al., 2002). Different functional forms have been proposed for the wake function in the case of turbulent boundary layer over a smooth wall, the most commonly used being those proposed by Coles (1956):

$$w(\eta) = \sin^2\left(\frac{\pi}{2}\eta\right) \quad (4.3)$$

and by Krogstad et al. (1992):

$$w(\eta) = \frac{1}{2\Pi} [(1 + 6\Pi) - (1 + 4\Pi)\eta]^2 \quad (4.4)$$

Nezu and Rodi (1986) and Kirkgöz (1989) have checked the validity of the Coles' wake function as applied to open channel flow and obtained values of  $\Pi = 0.2$  and  $0.1$ , respectively. By applying Coles' equation, Cardoso et al. (1991) noted that  $\Pi$  varies between  $-0.02$  and  $0.27$  in smooth uniform OCF. The wake function proposed by Krogstad et al. (1992) has been validated for flow in open channels by Tachie et al. (2000) and Afzal et al. (2009). The value of  $\Pi$  for smooth OCF has been reported to be between  $0.10$  and  $0.16$  based on different channel aspect ratios (Roussinova et al., 2008). Further, bed roughness has also been shown to modify the value of the wake parameter  $\Pi$  (Krogstad et al., 1992).

#### **4.4 Estimation of friction velocity from velocity measurements**

For evaluating the friction velocity and better comparing the friction velocity estimation methods, different velocity profiles were measured along the water depth of open channel flow in various Reynolds numbers. Velocity measurements were carried out along the centreline of the flume (Figure 3.1) using the particle image velocimetry (PIV) techniques as discussed in Chapter 3 and a two-dimensional laser Doppler velocimetry (LDV). The LDV system uses a 300mW, Ar laser (Ion Laser Technology). The transmitting probe was fitted with a 800-mm focal length lens and mounted on an adjustable tilting table. The measuring volume, based on the Gaussian intensity distribution cut off point, was  $0.39 \times 0.39 \times 16.4 \text{ mm}^3$ . This facilitated measurements to be made fairly close to the bed. The LDV probe was mounted on a two-dimensional computer controlled traverse system driven by stepper motors with a position accuracy of  $\pm 0.01 \text{ mm}$  for each direction. The LDV system was operated in the backward scatter mode. A summary of important test parameters is given in Table 4.2. Experiments T1-T5

were conducted with the LDV, while T6 and T7 were conducted using PIV. Here, Froude number ( $Fr$ ) is defined based on the average velocity.

#### **4.4.1 Power law**

The friction velocity ( $u_*$ ) can be easily determined if sufficient velocity measurements are available in the viscous sublayer. In open channel flow, this layer is thin and the commonly used velocity measuring instruments are not capable of acquiring accurate velocity information. The theoretical description of the turbulent boundary layer provides for the existence of an overlap region, where the inner and outer regions meet. This overlap region can be described by a proper mathematical functional form (logarithmic or power) from which the friction velocity can be estimated. The specific form of the scaling law in the overlap region depends on the assumptions made in the course of the matching process. Barenblatt (1993) discussed the logarithmic law and the power law derivations using similarity and asymptotic considerations of the kinematic quantities. In fact, the two laws differ in their assumptions. One of the controversial questions is whether the Reynolds number independent logarithmic law or the Reynolds number dependent power law is the more appropriate velocity scaling law in this region. Experimental and numerical studies are available to support both descriptions. The log-law assumes that the velocity gradient is independent of fluid viscosity at arbitrarily large Reynolds number. In contrast, the power law assumes that the velocity gradient remains dependent on dynamic viscosity, in other words, at arbitrary large Reynolds number the effect of the viscosity remains not only in the viscous sublayer, but also in the entire boundary layer (Barenblatt and Prostokishin, 1993). In general, it has been emphasized that neither the logarithmic law nor the power law should be considered as convenient representations of experimental data. The power law will be useful in the determination of the friction velocity since the number of unknown parameters is less than that in the log-law. In addition, by adding the number of measuring points with lesser uncertainty (in the case of LDV/PIV measurements) in the outer region to the measuring points in the overlap region, the power law method tends to become more accurate.

Different forms of power law have been used to describe the velocity distribution and determine the bed shear stress. By considering viscous effects, the power law scaling for the mean velocity distribution has been proposed in papers by Barenblatt (1993) and Barenblatt et al. (1997). They proposed the power law equation for a smooth surface in the form

$$U^+ = C (y^+)^{\alpha} \quad (4.5)$$

The parameters  $C$  and  $\alpha$  in Eq. (4.5), known as the Barenblatt parameters, are Reynolds number dependent and defined by

$$C = \frac{1}{\sqrt{3}} \ln Re_{\delta} + 2.5 \quad \text{and} \quad \alpha = \frac{3}{2 \ln Re_{\delta}} \quad (4.6)$$

Here,  $Re_{\delta} = \frac{2\delta U_m}{\nu}$  is the Reynolds number based on the mean velocity ( $U_m$ ) of the boundary layer. Kailasnath (1993) proposed a similar equation with the  $C$  and  $\alpha$  defined as:

$$C = 2.8 Re_{\delta}^{-0.077} + 2.277 \quad \text{and} \quad \alpha = 0.314 Re_{\delta}^{-0.077} \quad (4.7)$$

Zagarola and Smits (1997, 1998) re-examined the power law equation and defined their own parameters:

$$C = 0.7053 \ln Re_{\delta} + 0.3055 \quad \text{and} \quad \alpha = \frac{1.085}{\ln Re_{\delta}} + \frac{6.535}{(\ln Re_{\delta})^2} \quad (4.8)$$

Balachandar et al. (2002) conducted a series of experiments in shallow open channel flow for a range of Reynolds numbers ( $10,000 < Re_H < 90,000$ ), where  $Re_H = \frac{HU_e}{\nu}$  is based on the water depth,  $H$ . They found that the power law coefficients were not dependent on Reynolds number, and proposed values of  $C = 7.957$  and  $\alpha = 0.1551$  to provide an accurate distribution of velocity in the range  $50 < y^+ < 500$  at different Froude numbers.

Another method, similar to the Clauser chart method, was proposed by Buschmann and Meinert (1999). This method determines the friction velocity using the data in the overlap region ( $25 < y^+ < 1000$ ) and a form of the power law given by Eq. (4.5). Since only data in the overlap region are used, velocity measurements in the viscous sublayer are not required. To estimate the friction velocity, they proposed to curve fit the linearized Eq. (4.5) and calculate the slope of the line ( $\alpha_1$ ) and intercept value ( $\beta_1$ ) in the equation

$$\ln U = \alpha_1 \ln y + \beta_1 \quad (4.9.1)$$

Using these values for  $\alpha_1$  and  $\beta_1$ ,  $u_*$  is calculated as



$$u_* = \exp\left(\frac{\beta_1 + \alpha_1 \ln v - \ln C_1}{\alpha_1 + 1}\right) \quad (4.9.2)$$

where,  $C_1 = \frac{5\alpha_1 + \sqrt{3}}{2\alpha_1}$ .

The above discussion indicates that many power law functions are presently in use with different coefficients. These coefficients are Reynolds number dependent and vary for different velocity profiles, while the log-law coefficients (Eq. 4.1) are considered to be independent of Reynolds number but according to Nagib and Chauhan (2008), they vary with the flow geometry. Reynolds number dependency of the coefficients is a major argument between power law and log-law theories (Buschmann and Meinert, 1999; Vinuesa et al., 2014). Here, in this study the focus is not on this argument, but to evaluate the friction velocity based on the available velocity measurements in the outer layer. Our assumption is that both log-law and power-law formulations are equivalent at a particular Reynolds number producing single value of friction velocity for identical values of  $\delta$  and  $U_e$ . This approach is further validated by applying a power law to velocity measurements in open channel flow available in the literature. This procedure is used to obtain an estimate for the friction velocity that is independent on the value of  $\kappa$ .

#### 4.4.2 Total shear stress method

The total stress method is based on the assumption that a region of constant shear stress exists in the inner part of the boundary layer equal to the wall shear stress. The total stress is calculated at the plateau of the Reynolds shear stress profile in the overlap region of the boundary layer by summing the viscous and turbulent stress contributions and it has been successfully used for both smooth and rough walls boundary layers.

In open channel flow, experiments by Nezu and Nakagawa (1993) have shown that in fully developed turbulent open channel flow the total shear stress decreases linearly from the maximum value at the wall to near zero at the free surface. Since the viscous shear stress is negligible in the outer region above the wall, the Reynolds shear stress is the only dominant component for the total shear stress. The linear variation of Reynolds stress is described with the following equation:

$$-\overline{u'v'} = u_*^2(1 - y/H) \quad (4.10)$$

Here  $-\overline{u'v'}$  is the Reynolds shear stress. Equation (4.10) indicates that by measuring the Reynolds shear stress profile along the water depth, the friction velocity can be evaluated from the slope of the profile.

## 4.5 Results

### 4.5.1 Friction velocity

For flow over smooth surfaces, the availability of accurate near-wall velocity measurements is limited, which precludes the estimation of the velocity gradient needed for evaluating the friction velocity. In this study, different power law methods (Barenblatt, 1993; Zagarola and Smits, 1998; Kailasnath, 1993 and Balachandar et al., 2002) have been adopted to determine  $u_*$ . To validate the procedure, these methods were first used to estimate the friction velocity for the open channel flow experiments of Nezu and Rodi (1986), Kirkgoz (1989) and Steffler et al. (1983, 1985). The calculated values for friction velocity obtained from different power laws are reported in Table 4.3. All power laws used in Table 4.3 produced estimates of the friction velocity with less than 5% difference from the reported value for the case of smooth uniform open channel flows at different Froude and Reynolds numbers. The power law methods are easy to implement numerically, since just one unknown parameter ( $u_*$ ) has to be determined. Conversely, the composite log-law based on either Coles' or Krogstad's wake function requires three parameters to be determined.

Different power law methods were also applied to the present measurements. Table 4.4 presents the estimates for the friction velocities for each experimental set. It can be observed that  $u_*$  determined by applying the different power law methods to the measured data are in good agreement with each other.

In addition, the Reynolds stress distributions for some of the data sets for which two dimensional measurements were available, are plotted to validate the friction velocity with Reynolds stress distribution method. The bed shear stress has been evaluated from the slope of the best fit line of the Reynolds stress profile above the bed. Table 4.5 shows that the friction velocity results are in good agreement with the values resulted from the power law methods.

## 4.5.2 Evaluation of von Kármán coefficient

### 4.5.2.1 Derivative method

At relatively high  $Re_\theta$ , the value of  $\kappa$  can be found by using the logarithmic law of the wall. Differentiating Eq. (4.1) gives

$$\frac{dU^+}{dy^+} = \frac{1}{\kappa} \frac{1}{y^+} \quad (4.11)$$

As a result,  $\frac{dU^+}{dy^+}$  is a linear function of  $\frac{1}{y^+}$ , with slope  $\frac{1}{\kappa}$ . The variation of  $\frac{dU^+}{dy^+}$  versus  $\frac{1}{y^+}$  is demonstrated in Figure 4.2 for each of the experiments in this study.

The slope of the best-fit line passing through the origin represents the inverse of the von Kármán coefficient. This procedure is sensitive to noise and data scatter due to the inherent uncertainty associated with experimental data. The experimental uncertainties are further amplified when  $\frac{dU^+}{dy^+}$  is calculated directly by using finite differencing on the experimental data. To overcome this difficulty, a common remedy is to average multiple profiles in the log-law region. Since this remedy is not applied here, small fluctuations in  $\frac{dU^+}{dy^+}$  profiles are observed in Figure 4.2. Throughout this paper,  $\frac{dU^+}{dy^+}$  is determined numerically using a second-order central-difference scheme. In the derivative method, the log-law region is considered to occur between  $70 < y^+ < 700$ , where  $y^+ \left( \frac{dU^+}{dy^+} \right)$  should reach a constant value (Österlund et al., 2000).

The analytical expression for calculating the von Kármán coefficient ( $\kappa_{\text{der}}$ ) can be written as

$$\frac{1}{\kappa_{\text{der}}} = \frac{1}{N} \sum_{i=1}^N \left[ y_i^+ \left( \frac{dU^+}{dy^+} \right)_i \right] \quad (4.12)$$

Here,  $N$  is the number of data points located in the logarithmic region. For all experimental runs (T1-T7), the correlation coefficient of the expected line and the experimental data was above 95 %, and the values of  $\kappa_{\text{der}}$  are shown in Figure 4.2.

### 4.5.2.2 Scatter method

The scatter method, which has recently been discussed by Segalini et al. (2013), is based on the re-arrangement of Eq. (4.1) in the following form

$$\kappa B = \kappa U^+ - \ln y^+ \quad (4.13)$$

Here, each pair of  $y_i^+$ ,  $U_i^+$  values that belong to the overlap region should follow Eq. (4.13), with corresponding coefficients denoted as  $\kappa_s$  and  $B_s$ . In other words, for all pairs of  $(y_i^+, U_i^+)$  in the overlap region, B can be calculated from Eq. (4.13) for a specific  $\kappa$  value. As  $\kappa$  varies then the calculated B will change respectively for all pairs of  $(y_i^+, U_i^+)$  in the overlap region. Figure 4.3 shows that while  $\kappa \neq \kappa_s$  different values of B are obtained in the overlap region. For this method the overlap region is supposed to be between  $30 < y_i^+ < 0.2\delta^+$ . As discussed in Segalini et al. (2013), having a large number of velocity measurements in this region increases the accuracy of prediction. In this method, attaining  $\kappa_s$  and  $B_s$  as the locus where all pairs of  $(y_i^+, U_i^+)$  in the overlap region lie, is feasible. Theoretically, this locus should be a point, but in a practical solution the locus will be similar to a short line with the length of  $\Delta B$  (*i.e.*  $\kappa_s$  and  $B_s \pm \frac{\Delta B}{2}$ ). Figure 4.3 shows the evaluated values for  $\kappa_s$  and  $B_s$  for the present experiments.

#### 4.5.2.3 Fitting method (least-squares method)

This method is equivalent to the classical approach for the von Kármán coefficient estimation and it is mostly used to determine the shear velocity under the assumption that  $\kappa$  and B take the universal values. According to Eq. (4.1), the velocity profile in the logarithmic region should obey the linear relationship and the values of  $\kappa$  and B can be determined through a least-squares linear fit. By minimizing the error from the least-squares, the values of  $\kappa_f$  and  $B_f$  can be obtained:

$$\kappa_1 = \frac{N \sum_{i=1}^N \ln^2 y_i^+ - (\sum_{i=1}^N \ln y_i^+)^2}{N \sum_{i=1}^N U_i^+ \ln y_i^+ - \sum_{i=1}^N U_i^+ \sum_{i=1}^N \ln y_i^+} \quad (4.14.1)$$

$$B_1 = \frac{\sum_{i=1}^N \ln^2 y_i^+ \sum_{i=1}^N U_i^+ - (\sum_{i=1}^N \ln y_i^+) (\sum_{i=1}^N \ln y_i^+ U_i^+)}{N \sum_{i=1}^N \ln^2 y_i^+ - (\sum_{i=1}^N \ln y_i^+)^2} \quad (4.14.2)$$

The accuracy obtained from the least-squares fit is sensitive to the number of velocity measurements in the overlap region and the lower and upper bounds of the logarithmic region. In this study,  $70 < y_i^+ < 700$  is chosen for the bound of the logarithmic region. The values of  $\kappa_1$  and  $B_1$  obtained from the least-squares method are summarized in Table 4.6. Here, the regression correlation coefficient

is above 99 % for all tests. Table 4.6 also includes the estimates for  $\kappa$  and B obtained from the derivative and scatter methods.

The above methods lead to different values of  $\kappa$  and B for the same flow condition (e.g., test condition T2). The difference is primarily because of the uncertainty in each method and the number of points that correspond to the log-law region. Additional details for uncertainty evaluation can be found in the study by Segalini et al. (2013). In the current study, the results show that the least-squares method predicts the values for  $\kappa$  and B with higher regression correlation coefficient value compared to the derivative method. Also it should be mentioned that one of the advantages of the least-squares method lies in the simultaneous evaluation of  $\kappa$  and B, unlike the derivative method. In addition, in the scatter method, B is assumed to be dependent on the value of  $\kappa$  but not vice versa, whereas these parameters are dependent on each other. Different  $\kappa$  values provide different slopes for the streamwise mean velocity profiles in the overlap region compared to the universal value. Applying the least-squares method on other smooth open channel flow experimental data by Nezu and Rodi (1986), Kirkgoz (1989) and Steffler et al. (1983, 1985) shows that the von Kármán coefficient varies between 0.35 and 0.51 and the variation of B is from 3.0 to 7.6. The least-squares method is used in the remainder of this paper and the proposed values for the log-law coefficients are based on this method.

### 4.5.3 Velocity profile and log-law

The streamwise mean velocity profile in inner scaling for the present tests is shown in Figure 4.4. As stated above, the friction velocity is evaluated from the power law equations and the values for  $\kappa$  and B are obtained from the least-squares method. Moreover, for tests T1, T4 and T7, only one point was in the viscous sublayer that shows agreement with the viscous sublayer law ( $U^+ = y^+$ ). In other words, it provides an endorsement of the method used for evaluating the shear velocity. On the other hand, for large  $y^+$  values ( $y^+ > 700$ ) the experimental data does not obey the trend of the overlap region. This is due to the wake feature which is more obvious in tests T2, T5, T6 and T7.

In this study the variation of von Kármán coefficient is in agreement with the findings of other studies by Coleman (1981, 1986) and Gaudio and Dey.

(2013). Different relations have been proposed to define the dependency of  $\kappa$  on Reynolds number. The most well known equations are Simpson's (1970) interpretation and Wosnik et al. (2000) estimation. In the current work, the classical Prandtl's mixing-length theory is applied to find the von Kármán coefficient. Determination of mixing length for different velocity profiles requires the eddy viscosity evaluation and its variation along the depth of flow.

#### 4.5.4 Eddy viscosity

As discussed earlier, the most common wake functions used for the outer region are Krogstad's and Coles' equations. By applying these wake functions and finding the wake parameter for each velocity profile, the eddy viscosity can be obtained. Based on Reynolds number, the eddy viscosity and mixing length can change and as a result the von Kármán coefficient can be affected.

In fully developed two-dimensional open channel flow, the total shear stress can be evaluated as (Cebeci and Smith, 1974):

$$-\overline{u'v'} + \nu \frac{dU}{dy} = u_*^2(1 - \eta) \quad (4.15)$$

Here  $-\overline{u'v'}$  is the Reynolds shear stress and  $\eta = y/\delta$ . One of the simplest models to eliminate the Reynolds shear stress in Eq. (4.15) is to use the concept of eddy viscosity, defined by  $-\overline{u'v'} = \nu_t \frac{dU}{dy}$ . Combining this with Eq. (4.15) yields the following expression for the eddy viscosity:

$$\nu_t = u_*^2(1 - \eta) \left(\frac{dU}{dy}\right)^{-1} \quad (4.16)$$

Equation (4.16) can be used to evaluate eddy viscosity if explicit information for the velocity distribution is available. Using Coles' wake function for high Reynolds numbers, the eddy viscosity is given by

$$\frac{\nu_t}{u_*\delta} = \kappa(1 - \eta) \left(\frac{1}{\eta} + \pi\Pi \sin \eta\pi\right)^{-1} \quad (4.17)$$

Although the effect of the wake parameter  $\Pi$  on eddy viscosity is often neglected, Nezu and Rodi (1986) were among the first to show a significant effect of  $\Pi$  on eddy viscosity, especially in the overlap and outer regions.

Another expression for the eddy viscosity can be obtained by applying the wake function proposed by Krogstad et al. (1992), yielding

$$\frac{v_t}{u_*\delta} = \kappa(1 - \eta) \left[ \frac{1}{\eta} + 2(1 + 6\Pi)\eta - 3(1 + 4\Pi)\eta^2 \right]^{-1} \quad (4.18)$$

Figures 4.5.a and 4.5.b show profiles of eddy viscosity for all experimental cases (T1-T7, Nezu and Rodi 1986; Kirkgoz, 1989; Roussinova et al., 2008 and Afzal et al., 2009) together with the theoretical curves according to Eqs. (4.17) and (4.18). As observed in Figure 4.5.a, the eddy viscosity based on Coles' wake function (Eq. 4.17) starts from zero near the bed, attains a maximum at  $y/\delta \approx 0.5$  and terminates at zero for  $y = \delta$ . Krogstad's wake function shown in Figure 4.5.b predicts better the eddy viscosity since its value does not approach zero near the free surface ( $y > \delta$ ) similar to the DNS results of Spalart (1988). Also, the maximum dimensionless eddy viscosity value evaluated by Eq. (4.18) occurs at 0.091 which is near the maximum dimensionless eddy viscosity value of 0.097 reported by Spalart (1988). As previously shown we have established the existence of sizable logarithmic region in all experimental data and the eddy viscosity distribution was evaluated, using composite velocity profile incorporating the wake function proposed by Krogstad et al. (1992). Given the availability of the OCF velocity profiles, the mixing length was further examined.

#### 4.5.5 Mixing length

The mixing length  $\ell_m$  is defined as a turbulent length scale that the fluid parcel will travel, conserving its properties, before completely mixing with the surrounding fluid. Based on Prandtl's mixing-length theory, the eddy viscosity is evaluated from the velocity gradient  $dU/dy$  and the mixing length as

$$v_t = \ell_m^2 \frac{dU}{dy}. \quad (4.19)$$

In Eq. (4.19), the mixing length depends on the nature of the flow and in general, is space dependent (Nezu and Nakagawa, 1993). The distribution of  $\ell_m$  in boundary layer flows has been conventionally described by two separate regions. The first region is the outer region where  $\delta$  is assumed as the length scale and the outer mixing length  $(\ell_m)_o$  is assumed to be proportional to  $\delta$  ( $\ell_m \sim \delta$ )<sub>o</sub>. In the inner layer, the variation of the mixing length is assumed to be proportional to the distance from the wall ( $\ell_m \sim y$ )<sub>i</sub>. Based on von Kármán's postulation the proportionality coefficient is  $\kappa$  and the mixing length in the inner region can be determined from the location to the wall ( $\ell_m = \kappa y$ )<sub>i</sub>. From the latter assumption,

the log-law of the wall was proposed (Cebeci and Smith, 1974). Figure 4.6 shows the variation of normalized mixing length with increase of  $y/\delta$ , where the mixing length is calculated based on the eddy viscosity obtained from Eq. (4.18).

As expected, the mixing length changes for different locations, confirming its space dependency. Figure 4.6 shows that the mixing lengths approach similar values near the wall for all experiments, when the wall distance is normalized in outer scaling. Near the bed at  $y/\delta < 0.2$ , all mixing length profiles collapse on each other, since the effect of the wake parameter in this region is insignificant. Far from the bed, at  $y/\delta > 0.2$ , the mixing length profiles vary at different wall distances because of changes in flow properties such as Reynolds number and wake parameter effects. Also, the effect of the von Kármán coefficient on the mixing length cannot be distinguished well in Figure 4.6 since the mixing length distribution is plotted in the outer scaling ( $\delta$ ).

Figure 4.7 shows the near-wall variation of normalized mixing length with  $y^+$  for the range of data near the wall. The linear relation between  $\ell_m/\delta$  and  $y^+$  confirms the first assumption for the log-law boundary layer equation. Here, the linear relation between  $\ell_m/\delta$  and  $y^+$ , specifies a slope  $\kappa_1$  (i.e.  $\ell_m/\delta = \kappa_1 y^+$ ) that is not constant and varies according to  $Re_\theta$ . Figure 4.7 shows that as  $Re_\theta$  increases the coefficient  $\kappa_1$  decreases which will definitely change the von Kármán coefficient. In other words, it shows that the von Kármán coefficient is Reynolds number dependent and that the classical idea for log-law which assumes that all the constants in log-law equation (Eq. 4.1) are independent of Reynolds number can be challenged.

#### 4.5.6 von Kármán coefficient

Based on the present LDV measurements and the results discussed above, the classical claim that the von Kármán coefficient has a universal constant value can be refuted, at least in open channel flows. Although many studies show that  $\kappa$  vary with Reynolds number (e.g., Zanoun et al., 2003; Segalini et al., 2013), there is still considerable discussion about the relationship between the von Kármán coefficient and the Reynolds number.

As discussed earlier, Figure 4.7 shows the variation of dimensionless mixing length with  $Re_\theta$ . Basically, it shows the hidden contribution of von



Kármán coefficient in the mixing length variation. This contribution is known as parameter  $\kappa_1$ , and its variation with  $Re_\theta$  is presented in Figure 4.8. The Reynolds number ( $Re_\theta$ ) range in this study is between 330 and 6200. Figure 4.8 shows that  $\kappa_1$  decreases sharply as  $Re_\theta$  increases. For high  $Re_\theta$ ,  $\kappa_1$  reaches an asymptotic value which is approximately  $1.6 \times 10^{-4}$ . It should be mentioned that based on the definition for mixing length in the inner region, the von Kármán coefficient is related to  $\kappa_1$  by

$$\kappa = \kappa_1 \delta^+ \quad (4.20)$$

In Eq. (4.20),  $\delta^+$  is known as the Kármán number, which explicitly reveals that there is a scale separation between the largest and smallest lengths in the flow. The Kármán number is directly proportional to  $Re_\theta$  and its variation is shown in the inset of Figure 4.8. By considering Eq. (4.20) and Figure 4.8, the variation of von Kármán coefficient with  $Re_\theta$  can be simplified and expressed as

$$\kappa \approx 0.2725 Re_\theta^{0.038} \quad (4.21)$$

It should be mentioned that Eq. (4.21), which is derived for near uniform smooth OCF in a specific range of Reynolds number ( $Re_\theta = 2,500$  to  $6,200$ ), is another way to predict the Kármán coefficient for the log-law equation rather than using the constant assumption.

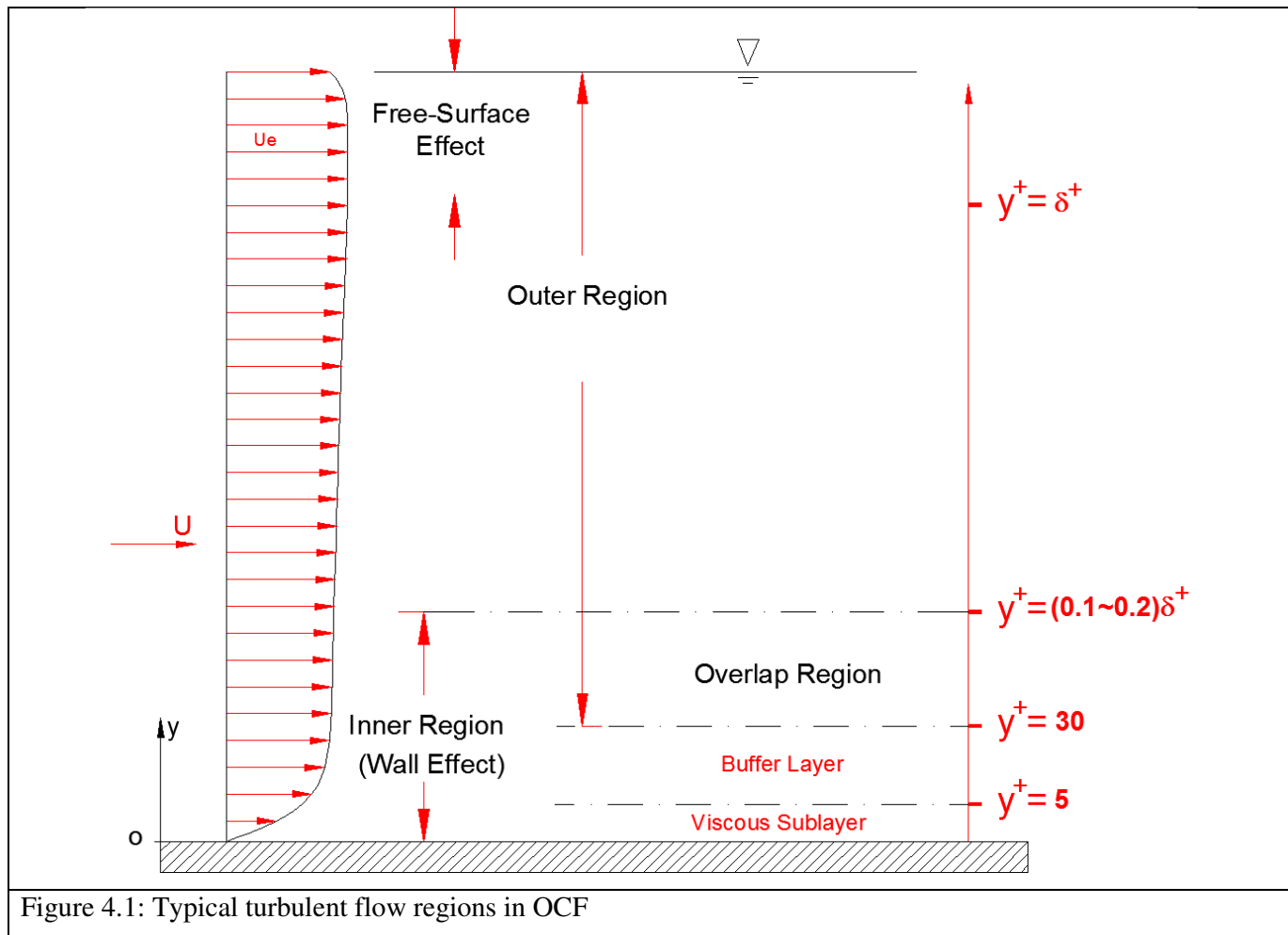
## 4.6 Conclusions

In order to determine the log-law equation in the smooth open channel flow for the mean streamwise velocity profile, three basic parameters ( $u_*$ ,  $\kappa$ , B) must be evaluated. Bed shear velocity can be estimated from other techniques or methods independent of the log-law. Although,  $\kappa$  and B are conventionally assumed to be constant ( $\kappa = 0.41$ , B varies from 5 to 8.5 depending on the flow type and wall condition), the value of the von Kármán coefficient and log-law constant have been challenged in different turbulent boundary layer flows. The evaluation of the bed shear velocity and log-law coefficients in smooth open channel flow are re-examined in this study for  $Re_\theta < 6,200$ . The main findings of the present study can be summarized as follows:

- The friction velocity is evaluated accurately from the streamwise velocity profile at different Froude and Reynolds numbers by applying different forms

of power law in open channel flow. The power law methods are straightforward to implement numerically based on appropriate Reynolds number, as only friction velocity has to be determined.

- The present study discusses various methods used to determine the von Kármán coefficient. Analytical expressions have been developed by different methods for fitting the streamwise velocity profiles. Values of  $\kappa$  and  $B$  were estimated based on the least squares method, since this method has a higher regression correlation and also is more accurate compared to the derivative and scatter methods.
- The mixing length in open channel flow is evaluated based on the eddy viscosity distribution assuming a composite velocity profile incorporating the wake function proposed by Krogstad et al. (1992). The mixing length is found to vary with the wall distance, as reported earlier by Nezu and Rodi (1986). This also confirms that the size of eddies is proportional to their distance from the wall. In the outer region far from the bed ( $y/\delta > 0.2$ ), the flow properties such as Reynolds number and wake strength influence the mixing length. In contrast, in the inner region where  $y/\delta < 0.2$ , the mixing length is only a function of the location from the wall and  $Re_\theta$ . The Reynolds number effect on the inner mixing length is presented as the coefficient  $\kappa_1$  and the Kármán number  $\delta^+$  which, when multiplied together gives the von Kármán coefficient  $\kappa$ . In other words, the von Kármán coefficient is not constant and it is dependent on Reynolds number. The universal constant assumption for  $\kappa$  will lead to under or over prediction of other important parameters such as friction velocity and wall shear stress.
- The flow conditions denoted by tests T6 and T7 are used as the characteristics of approaching condition in evaluating the flow past circular cylinders in various arrangements.



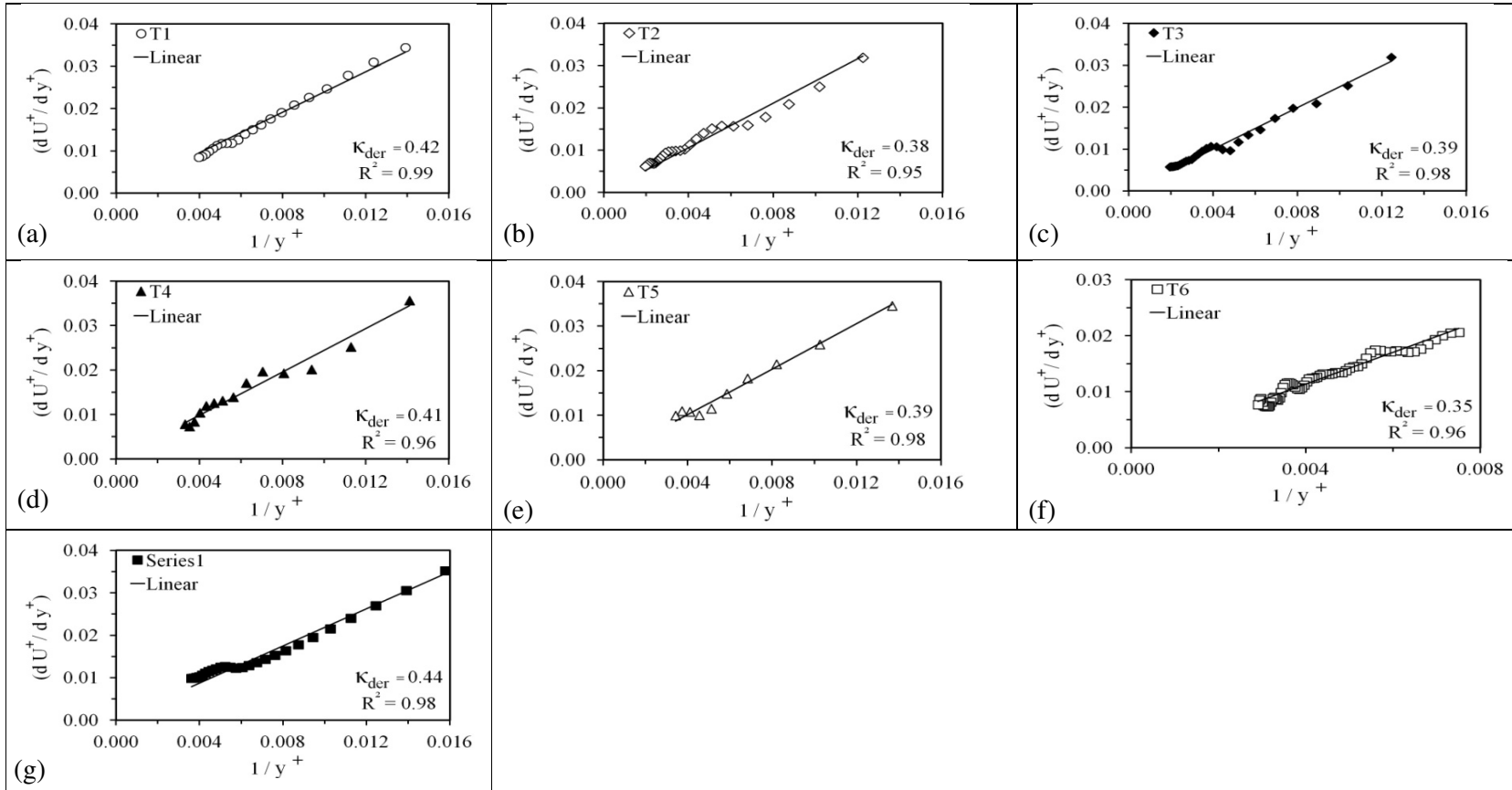
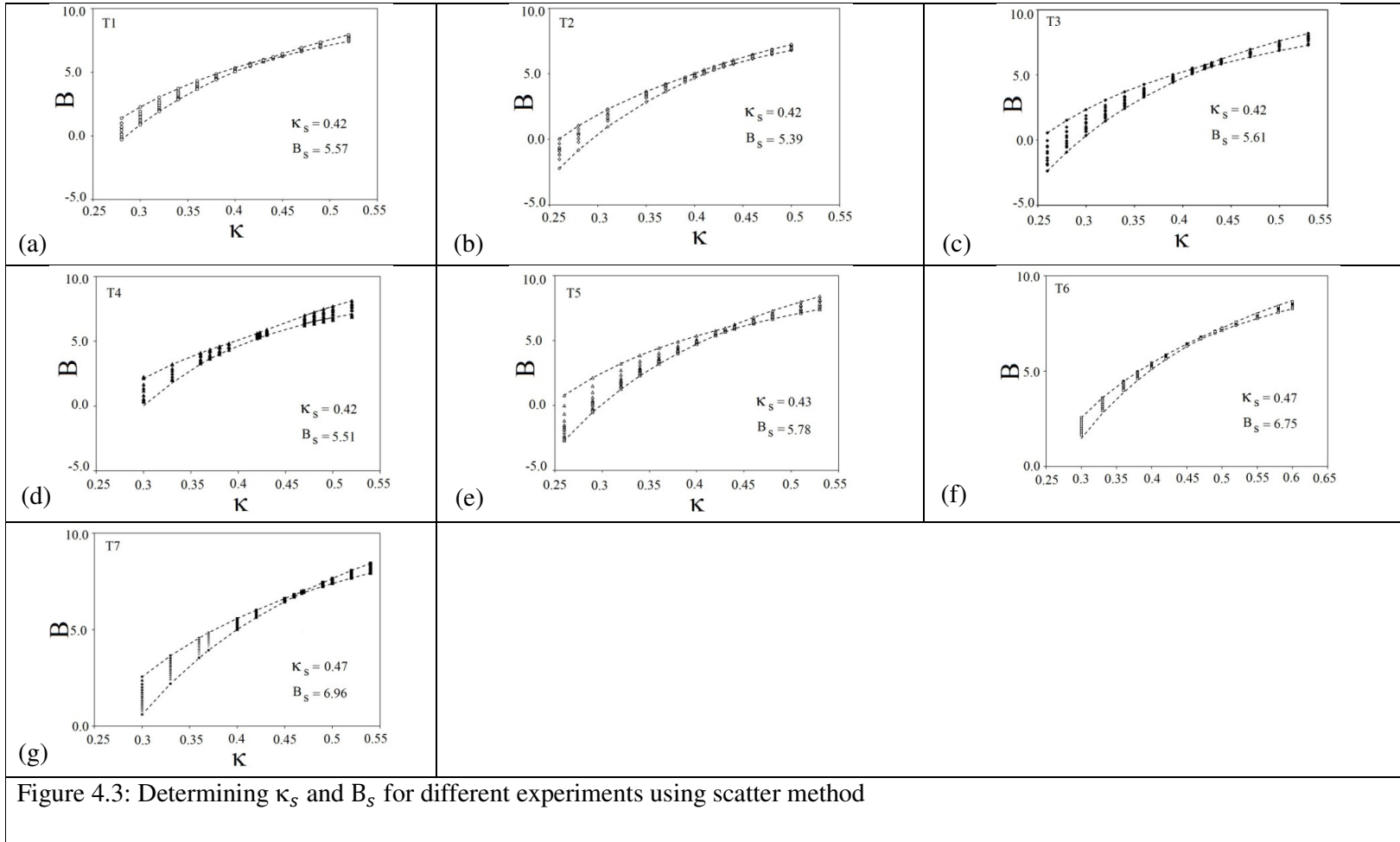


Figure 4.2: Variation of  $\frac{dU^+}{dy^+}$  vs.  $\frac{1}{y^+}$  using the derivative method



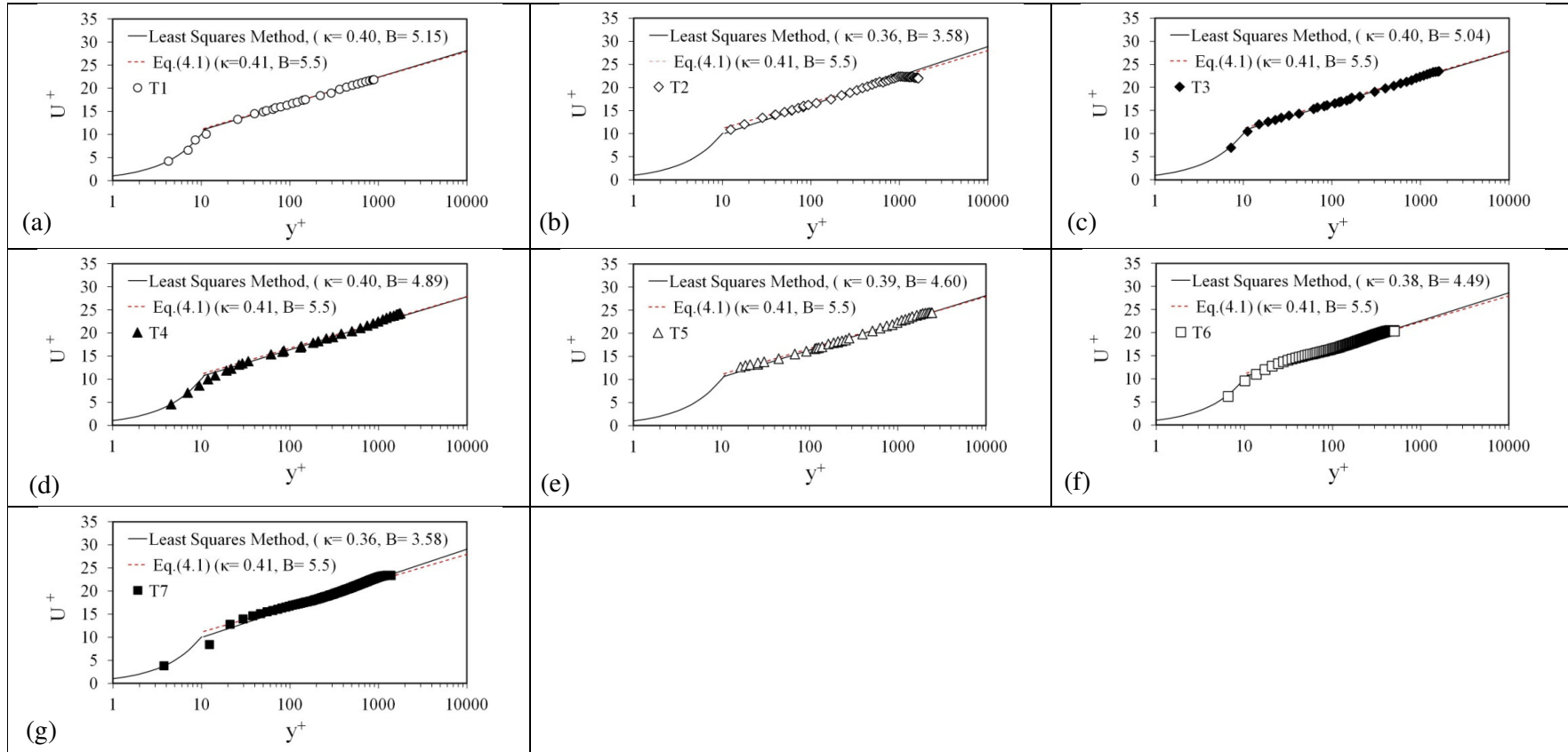


Figure 4.4: Variation of  $\frac{dU^+}{dy^+}$  vs.  $\frac{1}{y^+}$  using the derivative method

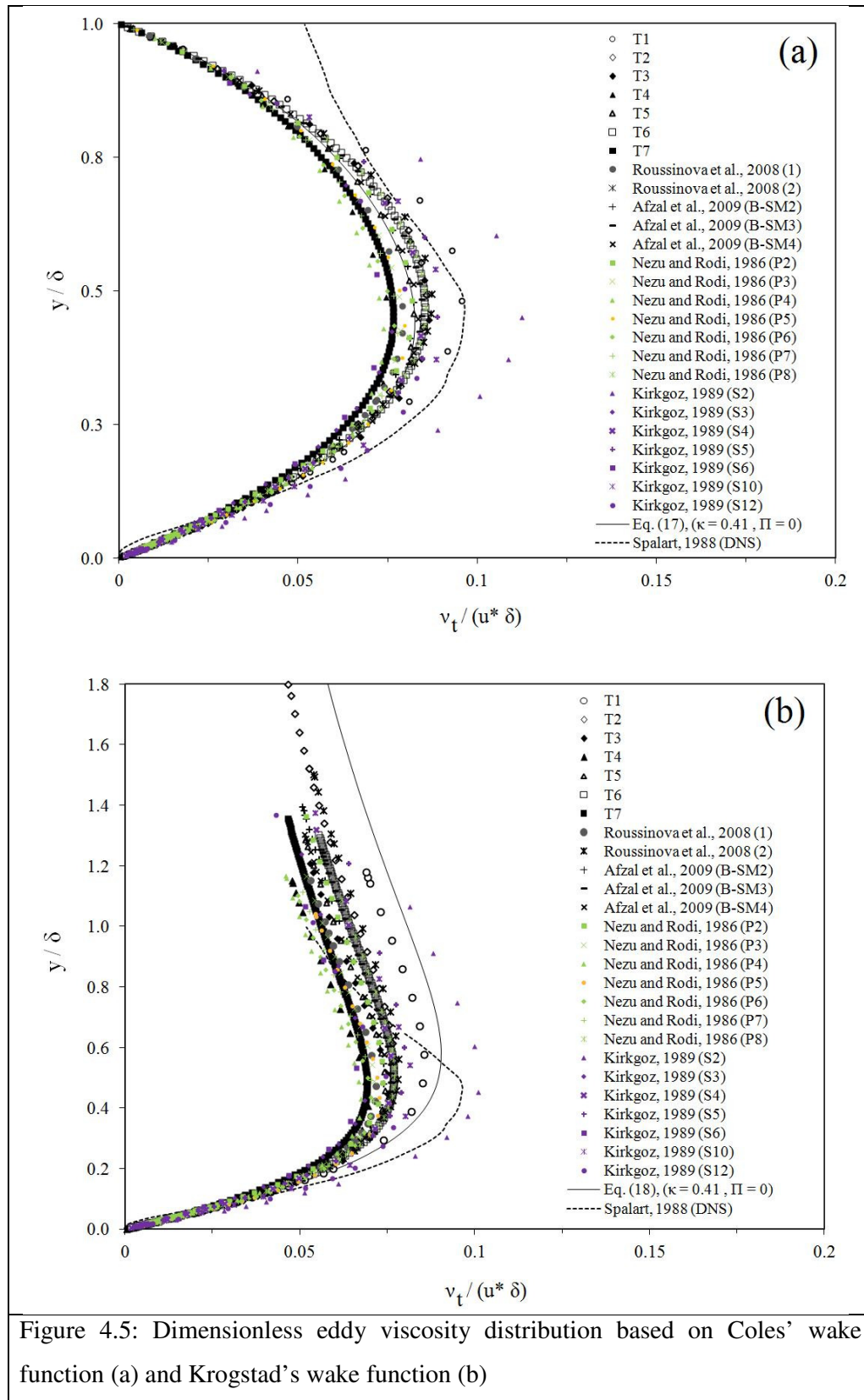
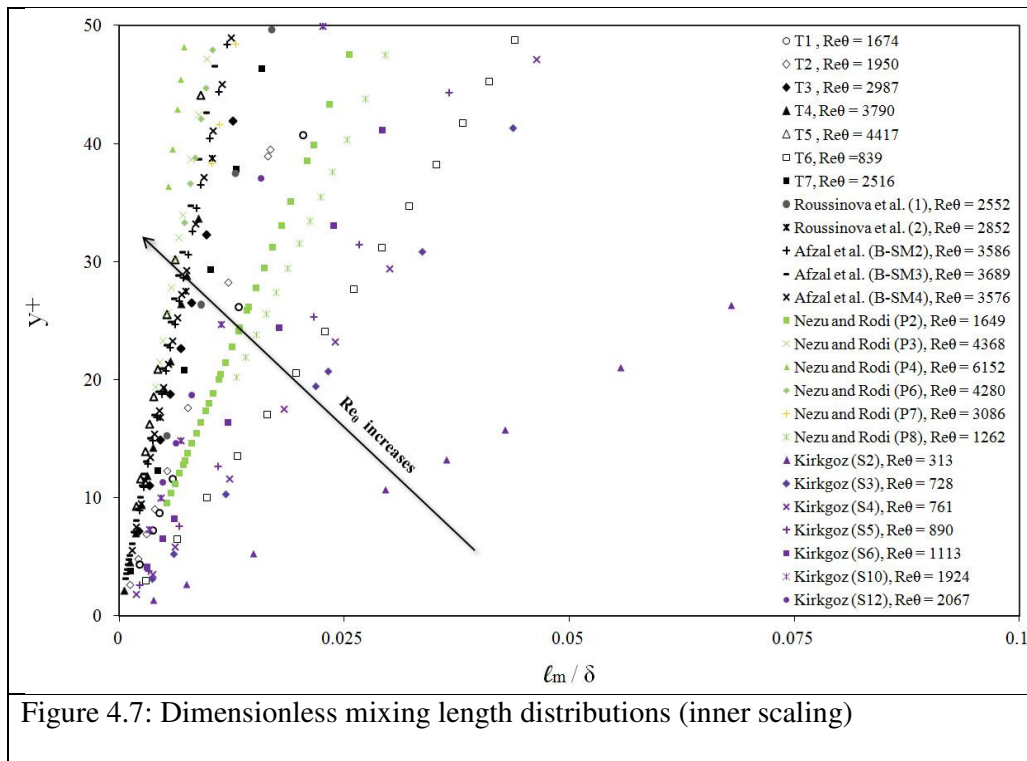
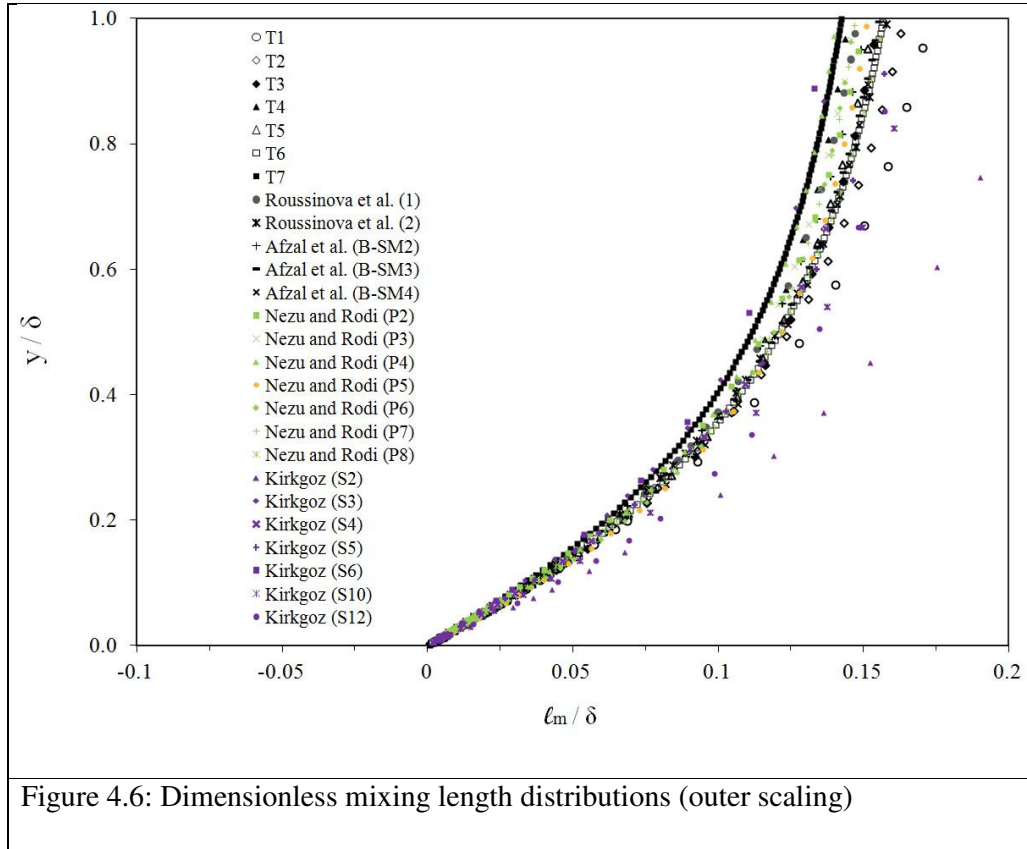


Figure 4.5: Dimensionless eddy viscosity distribution based on Coles' wake function (a) and Krogstad's wake function (b)





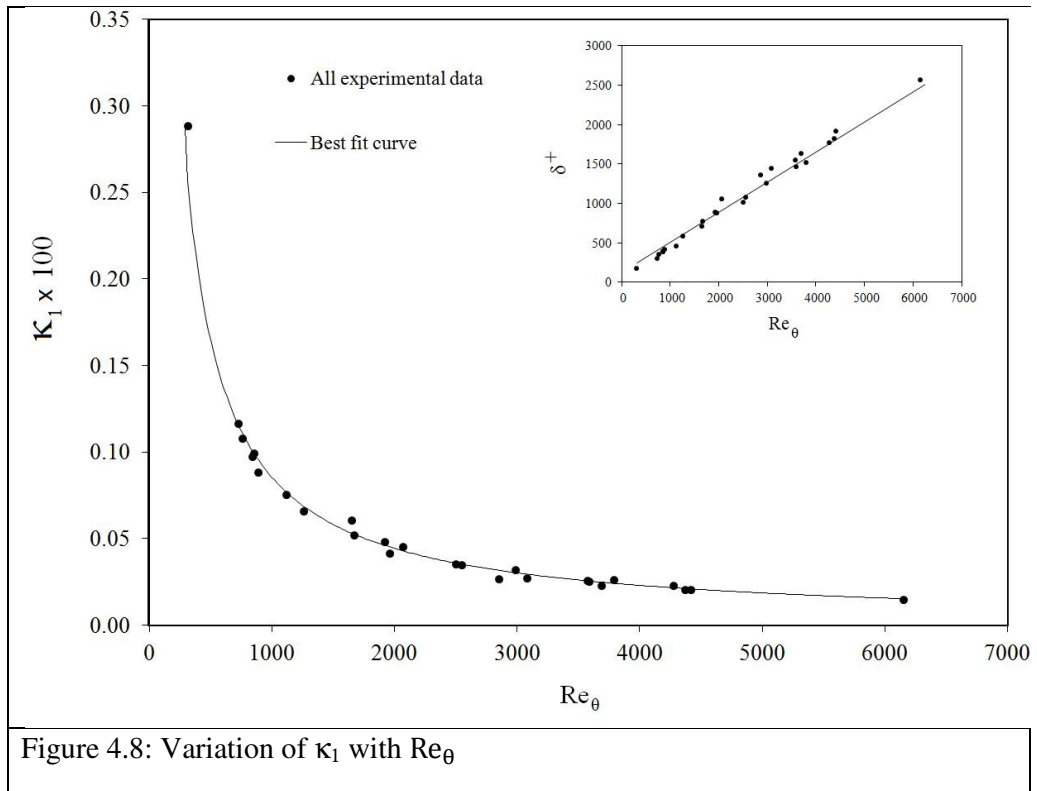


Table 4.1: Reported values of $\kappa$ from different sources			
Reference	Experimental / Numerical	Reported value for $\kappa$	Details
von Kármán (1930)	Smooth pipe	0.41	Laboratory measurement
Sheppard (1947)	ABL	0.46	Field measurement
Pasquill (1950)	ABL	0.37	Field measurement
Businger et al. (1971)	ABL	0.35	Field measurement
Tennekes (1973)	TBL	0.35	Wind tunnel
Francey and Garratt (1981)	ABL	0.38	Field measurement
Coleman (1981, 1986)	OCF	0.26-0.60	Suspended sediment flow
Nezu and Rodi (1986)	OCF	0.41	<sup>1</sup> $Re_R = 23,000 - 440,000$
Kim et al. (1987)	DNS	0.40	<sup>2</sup> $\delta^+ = 180$
Oncley et al. (1990)	ABL	0.364	Re-analysis of field measurements
Long et al. (1993)	Smooth pipe	0.408	<sup>3</sup> $Re_d = 1,000 - 100,000$
Moser et al. (1999)	DNS	0.45-0.33	<sup>2</sup> $\delta^+ = 590$
Österlund et al. (2000)	TBL	0.38	<sup>4</sup> $Re_\theta = 2,500 - 27,000$ , Wind tunnel
Zanoun et al. (2003)	Channel flow	0.37	<sup>2</sup> $\delta^+ = 4,800$
Monty (2005)	Duct flow	0.389	<sup>2</sup> $\delta^+ = 4,000$ , Smooth wall
Hoyas and Jimenez (2006)	DNS	0.41	<sup>2</sup> $\delta^+ = 2,000$
Gaudio and Dey (2013)	OCF	0.35-0.42	Sediment transport
Segalini et al. (2013)	TBL	0.36-0.44	<sup>4</sup> $Re_\theta = 2500 - 27000$

<sup>1</sup> Reynolds number based on hydraulic radius ( $R_h$ ) and mean velocity ( $Re_R = 4R_h U_m/\nu$ )

<sup>2</sup> Reynolds number based on boundary layer thickness ( $\delta$ ) and friction velocity ( $\delta^+ = \delta u_*/\nu$ )

<sup>3</sup> Reynolds number based on pipe diameter ( $d$ ) and friction velocity ( $Re_d = 0.5d u_*/\nu$ )

<sup>4</sup> Reynolds number based on momentum thickness ( $\theta$ ) and free stream velocity  $Re_\theta = U_e \theta/\nu$

Table 4.2: Experimental details							
Test	$U_e \times 10^{-2}$ ( $\text{ms}^{-1}$ )	$H \times 10^{-2}$ (m)	$B_f/H$	$\delta \times 10^{-2}$ (m)	$Re_\theta$	Fr	$Re_H$
T1	32.0	6.3	19.4	5.3	1,674	0.35	20,466
T2	24.0	15.4	7.9	8.2	1,962	0.18	36,849
T3	44.8	8.4	14.5	6.8	2,987	0.44	36,418
T4	57.9	7.2	16.9	6.3	3,790	0.61	37,306
T5	57.1	10.4	11.7	8.1	4,417	0.51	60,370
T6	15.6	7.0	17.3	5.4	839	0.17	10,340
T7	51.1	7.0	17.3	5.1	2516	0.55	33,047

Experiments	Power law methods				Average value	Reported value	Difference (%)
	Barenblatt (1993)	Kailasnath (1993)	Zagarola et al. (1997)	Balachandar et al. (2002)			
Nezu and Rodi (P1)*	0.42	0.43	0.41	0.43	0.42	0.43	2.3
Nezu and Rodi (P2)*	0.95	0.97	0.95	0.96	0.96	0.95	1.1
Nezu and Rodi (P3)*	2.18	2.20	2.21	2.22	2.20	2.20	0.0
Nezu and Rodi (P4)*	2.98	3.01	3.03	3.04	3.02	3.04	0.7
Nezu and Rodi (P5)*	4.75	4.80	4.85	4.89	4.80	4.66	3.0
Nezu and Rodi (P6)*	2.67	2.73	2.70	2.74	2.71	2.71	0.0
Nezu and Rodi (P7)*	4.05	4.09	4.11	4.12	4.09	3.99	2.5
Nezu and Rodi (P8)*	2.20	2.23	2.23	2.23	2.22	2.22	0.0
Steffler et al. (SRP1)*	3.34	3.38	3.38	3.36	3.37	3.35	0.6
Steffler et al. (SRP2)*	1.66	1.69	1.66	1.68	1.67	1.64	1.8
Kirkgoz (S2)*	0.27	0.28	0.26	0.28	0.27	0.28	3.6
Kirkgoz (S3)*	1.07	1.09	1.05	1.07	1.07	1.04	2.9
Kirkgoz (S4)*	0.60	0.61	0.59	0.61	0.60	0.59	1.7
Kirkgoz (S5)*	6.50	6.60	6.40	6.59	6.52	6.58	0.9
Kirkgoz (S6)*	0.84	0.85	0.83	0.85	0.84	0.85	1.2
Kirkgoz (S10)*	2.53	2.56	2.53	2.54	2.54	2.47	2.8
Kirkgoz (S12)*	3.82	3.87	3.82	3.83	3.84	3.82	0.5

\*The number in the brackets corresponds to different flow conditions with respect to Reynolds number and Froude number as reported.

Table 4.4: Estimates for  $u_* \times 10^{-2}$  ( $\text{ms}^{-1}$ ) for the present experiments using different power law methods

Test	Power law methods					Average value
	Barenblatt (1993)	Kailasnath (1993)	Zagarola et al. (1997)	Balachandar et al. (2002)	Buschmann and Meinert (1999)	
T1	1.43	1.45	1.43	1.44	1.42	1.43
T2	1.06	1.07	1.07	1.07	1.06	1.07
T3	1.89	1.91	1.91	1.91	1.88	1.90
T4	2.37	2.40	2.39	2.39	2.36	2.38
T5	2.31	2.34	2.33	2.33	2.31	2.33
T6	0.75	0.77	0.74	0.77	0.76	0.76
T7	2.18	2.20	2.17	2.18	2.16	2.18

Table 4.5: Summary of the friction velocity calculated using total shear stress and power law methods. For power law methods, an average value is reported.

Test	$u_* \times 10^{-2}$ ( $\text{ms}^{-1}$ )	
	Total shear stress	Power law (average value)
T4	2.33	2.38
T6	0.77	0.76
T7	2.23	2.18
Roussinova et al. (2008) (1)	2.17	2.19
Roussinova et al. (2008) (2)	2.14	2.11
Afzal et al. (2009) (B-SM2)	1.57	1.58

Table 4.6: Comparison between different methods for $\kappa$ and B								
Test	Derivative method		Scatter method			Least-squares method		
	$\kappa_{\text{der}}$	$R^2$ (%)	$\kappa_s$	$B_s$	$\Delta B/2$	$\kappa_l$	$B_l$	$R^2$ (%)
T1	0.42	98.7	0.42	5.57	0.11	0.40	5.15	99.9
T2	0.38	95.4	0.42	5.39	0.14	0.36	3.58	99.4
T3	0.39	98.6	0.42	5.61	0.15	0.40	5.04	99.8
T4	0.41	96.0	0.42	5.51	0.19	0.40	4.89	99.4
T5	0.39	98.3	0.43	5.78	0.15	0.39	4.60	99.7
T6	0.35	96.1	0.47	6.75	0.04	0.38	4.49	99.0
T7	0.44	98.2	0.47	7.00	0.03	0.36	3.58	99.4

## Chapter 5: SHALLOW FLOW PASSING A SINGLE CYLINDER

### 5.1 General remarks

As mentioned in Chapter 3, the first set of experiments denoted as C1 is carried out to study a shallow flow passing a single emergent cylinder. Two flow conditions at low Reynolds number (LR) and high Reynolds number (HR) are investigated using PIV. The wake Reynolds numbers ( $Re_D$ ) based on the cylinder diameter ( $D$ ) and the free stream velocity ( $U_e$ ) are evaluated to be 925 and 3000 for LR and HR flows, respectively. The corresponding bed friction coefficients ( $C_f$ ) in the approaching turbulent boundary layer flow are evaluated to be  $6.1 \times 10^{-3}$  and  $4.6 \times 10^{-3}$  while their corresponding stability parameter ( $S = C_f D/H$ ) are determined to be  $5.5 \times 10^{-4}$  and  $4.2 \times 10^{-4}$ . Here,  $H$  is the flow depth that is constant at 70 mm for both flow conditions. Table 3.1 summarizes the flow parameters at these two Reynolds numbers.

In the present study, the cylinder aspect ratio ( $H/D$ ) is near 11 but this parameter cannot be a proper representative for flow classification as shallow or deep (in contrast with the flow shallowness definition by Chen and Jirka, 1995). As discussed in Section 3.2.3, the maximum horizontal eddy length scale in the approaching flow is significantly larger than the flow depth ( $B_t/H = 17.3 \gg 1$ ) and the bed shear stress is strong enough to influence the flow and mean velocity profile. Following the definition by Jirka and Uijttewaai (2004) discussed in Section 1.2, these conditions are the basic requirements for classifying the flow as shallow.

Chapter 5 is devoted to address the horizontal and vertical variation of the instantaneous, mean and turbulence parameters of the shallow wake for both Reynolds numbers. The uniqueness of the flow field chosen herein is that it is shallow, the cylinder aspect ratio is very large and the blockage ratio is very small. The mean velocity, the turbulence intensities and Reynolds shear stresses at different stations are compared and validated with similar experimental studies available in literature. In spite of the extensive results available in literature in flow past a cylinder, the results presented herein can offer a new perspective.

## 5.2 Instantaneous velocity pattern

Samples of the instantaneous velocity fields are first presented. To have a better visualization of the wake behind a single cylinder and to examine the effect of the Reynolds number, velocity fields in three horizontal ( $x, z$ ) planes and one vertical ( $x, y$ ) plane are analyzed. Since the spatial resolution in all planes is kept  $\sim 0.5$  mm as shown in Table 3.2, displaying all measured vectors can clutter the figures. In the forthcoming figures, for clarity in the vector field different vector resolutions are adapted.

### 5.2.1 Instantaneous velocity vectors in horizontal ( $x, z$ ) planes

Selected examples of instantaneous velocity vectors in different horizontal planes behind the cylinder are displayed in Figures 5.1 and 5.2 for low and high Reynolds number flows, respectively. Each row consists of three plots displaying velocity fields at mid-depth, near-bed and near-free surface planes. These plots are not correlated in time and they are selected in away to highlight the most frequently occurring flow patterns observed. Only the very near-wake region is shown in the figures. The instantaneous flow fields in the mid-depth plane are presented in the first row of Figures 5.1 and 5.2 to enable a direct comparison with the traditional two-dimensional flow results available in literature. Note that  $x$  and  $z$  locations are normalized by the cylinder diameter,  $D$ . In the figures, for clarity every second and fourth vector is displayed in  $x, z$  directions for fine and coarse vector resolution regions, respectively. Fine vector resolution region is in the wake region and determined where the normalized vector size is less than 0.8 and elsewhere is considered to be coarse.

A preliminary review of the velocity fields in the mid-depth plane shows that the general characteristics of the wake resemble that observed by several researchers who studied the two-dimensional flow past an infinite circular cylinder. As one would expect, the velocity vectors in the wake region near the central wake axis ( $z/D = 0$ ) show smaller magnitude compared to the outer region. Also, the flow is represented by instantaneous clockwise (CW) and counter-clockwise (CCW) swirling regions in the mid-depth, which correspond to the von Kármán vortex street observed in the wake. These swirling motions strongly influence on entrainment of high velocity flow of the outer region into the wake region, as observed in the dash rectangles in the first row of Figures 5.1 and 5.2. This



feature generates the zig-zag pattern of velocity vector patches as the von Kármán vortex street develops in downstream. In this zig-zag pattern, large cross-stream velocity vectors are observed that generate flow instability in the near-wake region. Also, this zig-zag pattern provides strong cross-stream flow, whose influence is later shown to affect the flow field over the entire depth. Also, Due to the entrainment of the outer region flow into the wake region, the magnitude of velocity vectors and the wake width in this region increase in downstream locations at  $x/D > 3.5$  compared to the locations at  $x/D < 2.0$  for both cases.

By comparing the plots at three vertical locations, the zig-zag pattern and the size of the wake behind the cylinder varies as shown in Figures 5.1 and 5.2. In the near-free surface plane, the zig-zag pattern is clearly formed at LR but this formation is weakly distinguished at HR. Also, the outer flow entrainment into the wake region with the raise in the velocity vector size in the wake region is more pronounced at LR flow compared to HR at this plane. In addition, the width of the wake behind the cylinder at near-free surface plane is relatively larger for the HR case compared to LR. These differences can be due to the free surface effects, which are more prevalent in the high Reynolds number flow and will be discussed in forthcoming sections. As observed in the middle row of plots in Figures 5.1 and 5.2, the zig-zag pattern is not noticed at near-bed plane, which suggests that the wake flow at near-bed region is devoid of von Kármán vortex street for both Reynolds numbers. The wake size in the near bed-plane is the smallest compared with the other planes, which one can suggest the stabilization influence of bed on the wake flow (Balachandar et al., 1999). The presence of strong bed shear stress suppresses the development of the swirling motions and stabilizes the wake flow. It is noticed that at this plane the wake size depends on the Reynolds number, as the narrow wake is observed at lower Reynolds number where the bed friction coefficient is high and the bed suppression is stronger.

While the swirling motions at both Reynolds numbers in the mid-depth and near-free surface planes are detached from the cylinder, in the near-bed plane they are attached to the rear surface of the cylinder. While the asymmetric swirling patterns appear to drive the flow in the wake region by showing multiple vortices at mid-depth and near-free surface planes (Figures 5.1 and 5.2), at the near-bed plane, usually two re-circulating

patterns are observed (Figures 5.1.e and 5.2.f). These patterns also show the role of the bed in suppressing the formation of the wake vortices. The insets in the middle row of the figures provide an enhanced view of the vector field. In addition, at the near-bed plane, the velocity vectors show frequent sweeping flow pattern just behind the cylinder at low Reynolds number case (Figure 5.1.f), while such pattern is not observed at high Reynolds number. This sweeping flow pattern, which moves the fluid away behind the cylinder with relatively large spanwise velocity vectors, could be signature of the presence of a vortical structure different from the von Kármán vortex street.

### **5.2.2 Instantaneous velocity vectors in vertical ( $x, y$ ) plane**

Figures 5.3 and 5.4 illustrate two samples of instantaneous velocity fields in the vertical mid-plane behind the cylinder for low and high Reynolds numbers, respectively. In these figures, every second and all vectors are displayed in  $x$  and  $y$  directions for coarse and fine vector resolution regions, respectively. The dash line separates the coarse and fine vector resolution regions from each other.

At first glance, two different flow patterns are noticeable in Figures 5.3 and 5.4. The first flow pattern occurs near the cylinder (fine vector resolution region). An interesting observation in this region is the presence of predominantly upward vertical flow just behind the cylinder especially above the bed for LR and HR flows. Such strong upward flow is also observed even at mid-depth ( $y/D = 5.5$ ) (indicated by upward arrow A in Figures 5.3 and 5.4), particularly in LR case. Although the upward vertical velocity pattern reaches near the free surface at LR, it decays beyond  $y/D > 6$  at the HR case. Similar upwash flow in the near-wake region was observed in the experiments of Akilli and Rockwell (2002), Singha and Balachandar (2011) and in the numerical simulations of Kirkil and Constantinescu (2015) and Nasif et al. (2015). As one can notice, there is a downward velocity patch beneath the free surface behind the cylinder for HR flow, which is denoted as downwash arrow B. This downwash flow seems to be the source of generation of strong swirling motion behind the cylinder below the free surface. Such velocity pattern is not observed at LR. Another observation in this region indicates the presence of some swirling (represented by ellipse with arrows) and quasi-rotational

motions (represented by curve-lines with arrows). Most of these swirling and quasi-rotational motions are observed in the upper half-portion of the flow depth.

The second pattern (coarse vector resolution) illustrates recovery of the flow in the streamwise direction as shown on the right side of the dashed line. The dashed line for each plot is determined at the location where the value of  $u$  equals to  $\sim 0.1u_{max}$  which indicates the start of the flow recovery. Here  $u_{max}$  is the maximum  $u$  velocity in the field-of-view. Although, the location of the flow division into two regions varies with time even for the same Reynolds number, its variation along the depth is more noticeable. For example, at high Reynolds number, the location of the flow division near the bed is observed between  $x/D = 0.8$  and  $1.2$ , while at mid-depth ( $y/D = 5.5$ ) the division line is varying between  $x/D = 2.0$  to  $3.0$ . This also confirms the unsteady, three-dimensionality of the velocity field behind an emergent cylinder in the shallow flow. The swirling and quasi-rotational motions are more or less hindered by the strong streamwise velocity in the recovery region (second flow pattern). This suggests that vortices in the recovery region possess larger convection velocity compared to the ones observed in the first zone.

In addition, there is a small downward velocity vector trend near the bed as observed in the dashed rectangle in the figures. This downward flow is observed in the second zone in both cases. Also, there are large-magnitude velocity vectors just above the bed where the second zone starts denoted with arrow C in Figures 5.3 and 5.4. These vectors are oriented on the angle of  $\sim 15^\circ$  with respect to the streamwise direction, which show the contribution of significant upward flow into the developing region. At HR the free surface fluctuations are stronger compared to the LR case. In LR flow, the free surface is not deformed and it appears as a straight horizontal line at the near-wake region. For the case of HR, there is a dip by about  $0.2D$  at  $x/D = 2.4$  and  $0.3D$  at  $x/D = 1.9$  in the free surface as illustrated in Figures 5.4.a and 5.4.b, respectively. While no significant change is observed in the velocity vectors beneath the free surface at LR, velocity vectors beneath the dip at the HR case are larger and oriented downwards into the developing region flow as indicated by the arrow D in Figure 5.4. The overall size of these velocity vectors is in the same order of magnitude of velocity vectors near the bed indicated by arrow C. One may suggest that the free surface effect is more pronounced on the wake region for the HR case compared to LR.

### 5.3 Mean velocity fields of the wake flow

This section presents analysis of the mean velocity fields of the shallow wake behind the cylinder in the vertical and horizontal planes for the two Reynolds numbers. Figure 5.5 illustrates the velocity fields in different horizontal planes at mid-depth ( $y/D = 5.5$ ), near-bed ( $y/D = 0.8$ ) and near-free surface ( $y/D = 10$ ) as a combination of velocity vector field and streamtraces in the re-circulation wake region. The interesting feature that is observed in all horizontal FOVs is the presence of almost stagnant with very small negative streamwise velocities in the region behind the cylinder showing re-circulating flow. In Figure 5.6, the mean velocity fields in the vertical mid-plane are shown for both Reynolds numbers. Strong upward velocity vectors are present in the region close to the cylinder. This region is coincident with the stagnant region observed in the horizontal planes. The strong positive vertical velocity ( $V$ ) contributes into the horizontal stagnant region as shown in Figure 5.5 in accordance with the conservation of mass and compensation for the momentum deficit. The length of the re-circulation region ( $l_C$ ) along the central wake plane ( $z/D = 0$ ) shown in Figure 5.5 is changing not only in the three horizontal planes but also at different Reynolds numbers. As shown in Figure 5.5, for each horizontal plane,  $l_C$  is determined as the length on the wake on the centreline where only negative streamwise velocity is observed. For the LR case, the length of the re-circulation region is found to be equal to  $0.6D$ ,  $2.3D$  and  $2.4D$ , at near-bed, mid-depth and near-free surface planes, respectively; while for the HR case, the re-circulation length is observed to be  $0.7D$ ,  $2.2D$  and  $2.7D$ , correspondingly. As one would expect, due to the bed suppression effect the size of the re-circulation zone at near bed plane is smaller compared to the other horizontal planes. Away from the bed, the re-circulation length increases and the bed suppression effect decays. A similar pattern has also been reported by Akilli and Rockwell (2002). In addition, the length of the re-circulation zone in the near-bed plane is smaller for LR compared to the HR case, due to higher bed friction coefficient in low Reynolds number flow. Kirkil and Constantinescu (2015) studied the shallow flow behind a single cylinder with much smaller cylinder aspect ratio of  $H/D = 1.12$ . Their large scale PIV measurements, indicate that the length of the re-circulation

near the free surface is  $1.6D$  and  $0.7D$  for low and high Reynolds number flows ( $Re_D = 1.6 \times 10^4$  and  $5 \times 10^5$ ), respectively. These values are much smaller than the values obtained in the present study. Kirkil and Constantinescu (2015) also reported the re-circulation length as  $1.2D$  for the near-bed region for both Reynolds numbers which is almost double the value observed in the present study. One should note that these differences could be due to the differences in the cylinder aspect ratio and Reynolds number ( $Re_D$ ). By comparing the length of the re-circulation zone at mid-depth plane for both cases, one can suggest that the re-circulation length is dependent on the flow Reynolds number and it tends to decrease with increasing Reynolds number. Comparison of the re-circulation length at mid-depth with other studies is discussed further in Section 5.5.

The patterns of streamtraces in the wake region in the different horizontal planes are noticeably different as observed in Figure 5.5. At mid-depth, the streamtraces are observed to be more-or-less symmetrical with two unstable foci (following the classification of Perry and Steiner's, 1987 classification) located at  $z/D \approx \pm 0.2$  and  $x/D \approx 1.9$  and  $1.6$  for low and high Reynolds number flows, respectively. The term unstable focus refers to the process where the in-plane streamtraces are generated from the node and if they are degenerated to the node the focus is defined as stable. Similarly, two unstable foci are observed near the free surface (third column in Figure 5.5) at almost the same streamwise positions while their spanwise positions are noticed to be at  $z/D \approx \pm 0.2$  and  $\pm 0.4$  for LR and HR, respectively. It is clear that the presence of the free surface influences the re-circulation region for HR.

At near-bed plane (middle column of plots in Figure 5.5), the streamtraces are asymmetrical along the  $x/D$  axis for both Reynolds numbers. In this plane, for LR, two stable foci (at  $x/D \approx 0.35$ ) are observed near the cylinder while in HR, one stable focal node is determined at  $x/D \approx 0.26$  and one center focal node at  $x/D \approx 0.38$ . Akilli and Rockwell (2002) have shown the owl face shape in the near-bed streamtraces study behind a circular cylinder with two stable foci. Perry and Chong (1986) had shown similar owl face pattern in the laminar flow passing an inclined missile-shaped object. El Hassan et al. (2015) have reported the observation of two foci in their near bed flow visualization of flow passing a bed mounted square cylinder. Nasif et al. (2015) have

observed similar owl face spiral structure close to the bed in their DES model of shallow wake flow behind the sharp edge bluff body. They believed that these stable foci are associated with the existence of a coherent three-dimensional structure attached to the bed, which is called turbulent bulge structure. Nasif et al. (2015) noticed that as one moves a bit far from bed ( $y/H > 0.08$ ), the bulge structure diminishes and the stable foci change to unstable ones. Based on the reported bed shear velocity of the approaching flow, the near-bed planes discussed by Nasif et al. (2015) are located in the buffer layer at  $y/H < 0.08$  or  $y^+ < 80$ . It is plausible that appearance of stable/unstable foci depend on the proximity of the bed expressed in wall units ( $y^+$ ). In the present study, the near-bed plane is located at  $y^+ = 35$  for LR, where the viscous contribution to the shear stress is significant (Pope, 2000). In contrast in the HR case, the near-bed plane is located at  $y^+ = 110$  ( $y/\delta \sim 0.1$ ) in the outer layer, where the direct effect of the viscosity on the mean velocity is considered to be negligible. It should be noted that the  $y^+$  values are determined based on the bed shear velocity of the approaching flow evaluated in Chapter 3.

It is noticeable that while the velocity vectors on the side of the cylinder (as shown by the dashed rectangle in Figure 5.5) at mid-depth and near-free surface planes are oriented outwards, they are almost parallel to the streamwise direction at near-bed plane in both Reynolds numbers. It shows that the shear layer separation at mid-depth and near-free surface occur sooner on the side of the cylinder than at the near-bed plane. Kirkil and Constantinescu (2015) have reported similar variation of the shear layer separation at different planes, as  $88^\circ$ ,  $85^\circ$  and  $84^\circ$  for near-bed, mid-depth and near-free surface planes, respectively at their low Reynolds number flow ( $Re_D = 1.6 \times 10^4$ ). Following the stagnant wake region, the flow gradually transitions into a developing flow in all three planes.

Once again referring to Figure 5.6, it can be seen that flow is divided into two zones (shown by a “dividing streamtrace” in Figure 5.6), similar to the flow division in the instantaneous velocity fields shown in Figures 5.3 and 5.4. The first zone of the mean velocity field starts just behind the cylinder with a noticeable upward flow. In this zone, small negative  $U$  velocity is observed and the upward flow originates from the bed and extends along the whole water depth behind the cylinder. The effect of the Reynolds

number is observed near the free surface where strong downward velocity vectors, denoted by arrow A, are observed for HR. This downwash flow is not observed in the near free surface region for the LR case. A small re-circulation region denoted by a dashed circle in Figure 5.6.b appeared in the first zone just beneath the free surface. No such re-circulation is visible at LR case. A saddle point can also be located in the vertical plane. The location of the saddle point is also dependent on the Reynolds number. While the saddle point is located beneath the free surface at  $x/D = 3.2$  and  $y/D = 10.5$  for LR, it moves further downwards and closer to the cylinder to a position of  $x/D = 2.5$  and  $y/D = 8.5$  for the HR case.

In Figure 5.6, in the second zone, the mean flow is predominantly in the streamwise direction and it seems the velocity slightly increases as one moves downstream behind the dividing streamtrace. The location of the flow division into two zones along the  $x/D$  direction varies with  $y/D$  and Reynolds number. The location of flow division streamtrace just above the bed is almost  $x/D = 0.6$  and  $0.8$  for LR and HR, respectively. At mid-depth ( $y/D = 5.5$ ) the position of the flow division point is at  $x/D = 2.0$  and  $2.3$ , while this occurs at  $x/D = 3.0$  and  $2.4$  for near the free surface region ( $y/D = 10$ ) for low and high Reynolds number flows, respectively. As observed in Figure 5.6, the velocity vectors beneath the free surface show downwash flow for HR case (denoted by arrow B), which confirms the free surface effect of on the flow. It can be conjectured that the free surface behaves like a flexible membrane which deforms in the interaction with the turbulent motions beneath it. As in HR, these turbulent motions contain higher turbulent kinetic energy than LR case, the deformation in the free surface is more pronounced. Therefore, local changes in the free surface influence the flow motion beneath it.

Following the literature, Rostamy et al. (2012) have reported the flow division into two zones in the near-wake region behind a bed-mounted finite length cylinder. In their study, the flow behind a cylinder with different aspect ratios are compared while the boundary layer thickness ( $\delta$ ) of the approaching flow is fixed at  $\delta/D = 1.6$  and  $Re_D$  remains constant at  $4.2 \times 10^4$ . It is interesting to mention that although their study is not conducted in a shallow flow and the free end of the cylinder had a major role in generating the division streamtrace in the near-wake flow, the presence of the upwash

flow above the bed and a small re-circulation region near the tip of the cylinder is noticed.

Two-zone flow division, with predominantly upward velocity in the first zone, has been reported by Akilli and Rockwell (2002) in their study on vortex formation behind the single cylinder in shallow water. They have reported that the division line is almost vertical along the water depth far from the bed. Sadeque et al. (2009a) presented similar vertical division streamline at  $1.25D$  behind the bed-mounted circular cylinder in their ADV measurement in shallow open channel flow. Kirkil and Constantinescu (2015) indicated similar division line in their LES study on flow passing a single bed mounted cylinder. In contrast to the above-mentioned bed-mounted studies, the division line in the center wake plane of the present study is found to be inclined along the water depth for both Reynolds numbers. A slight bending backward of the division line is observed near the free surface for HR flow. This difference in the trend of the division line can be due to the dissimilar aspect ratio of the present study compared with previous ones.

It is worth mentioning that the free surface for the HR case does not appear as straight horizontal line for the whole FOV as in the LR case shown in Figure 5.6. For the HR flow, although the free surface is almost horizontal behind the cylinder up to about  $x/D = 2$ , it gradually starts to dip by about  $0.25D$  at  $x/D = 3.0$  and it remains at the same level until the end of FOV. The dip in free surface creates local changes in flow beneath the free surface, which are discussed in Section 5.6.2.

#### **5.4 Validation of the far-wake region**

In order to validate the results of the present study, the far-wake region is chosen for comparison with other studies due to its exclusive flow features. In this region, the wake flow is sufficiently far from the bluff body and the effect of shear layers emanating from the sides of the cylinder have almost disappeared (Shamloo et al., 2001 and Sadeque et al., 2009). The wake width and velocity defect scales are more appropriate scales in the shallow far-wake region, as suggested by Balachandar et al. (2000). The wake width ( $b$ ) is defined as the distance between the transverse locations ( $z$ ) where the velocity defect  $U_{Def} (= U - U_S)$  equals one-half of the maximum velocity defect ( $U_{Def(Max)}$ ) as shown in Figure 5.7. Here,  $U_S$  refers to the mean streamwise approaching velocity at the



corresponding depth of water.  $U_{Def(Max)}$  is expected to occur in the central wake plane ( $z/D = 0$ ) where the minimum streamwise velocity is observed. Following Pope (2000), the far-wake flow is found to be two-dimensional and self-similar in the wake plane, when  $U_{Def}/U_s < 1/10$ . Also, Pope (2000) suggested that in the far-wake plane, the normalized defect velocity is a function of the spanwise direction scaled to the wake width as

$$U_{Def} / U_{Def(Max)} = f(z/b) \quad (5.1)$$

Eq. 5.1 is considered as the flow characteristic in the far-wake plane. Here, the streamwise location  $x = 10D$  is chosen to enable comparison in the far-wake with other studies, which satisfies the latter criterion as well. In the present study, the wake flow is influenced by the effect of the bed and free surface and it is clearly three-dimensional. In order to lessen the bed and free surface effects, profiles in the mid-depth horizontal planes are chosen for better comparison with other studies. Validation has been performed in the horizontal mid-depth plane assessing spanwise and streamwise scaling of the velocity profiles in the far-wake.

Figure 5.8 presents the distribution of time averaged dimensionless streamwise velocity ( $U/U_s$ ), deficit velocity, turbulence intensity and Reynolds shear stress at  $x/D = 10$ . The streamwise velocity profiles are generally symmetrical about the wake central plane ( $z/D = 0$ ) where a minimum velocity occurs in the inner region ( $|z/D| < 0.5$ ). The  $U/U_s$  profiles of both Reynolds numbers agree well with other experimental results that are reported in Table 5.1. The spanwise width of the velocity profiles where  $U/U_s$  asymptotes to 1.0, is larger for the present study compared to Zhou and Antonia (1993), Ong and Wallace (1996) and Noseir et al. (2012), but is almost similar to that shown by Veale (2005). One set of results of Adaramola et al. (2006) matches the present trend in the profile, while that of Adaramola et al. (2012) is quite removed from all other data sets. This can perhaps be due to the effect of the bed and free surface, which makes the wake behind the cylinder three-dimensional even at mid-depth. The results of Adaramola et al. (2006) and Adaramola et al. (2012) are also influenced by the flow separating from the top of the cylinder.

Figure 5.8.b shows the deficit scale profiles and confirms that the profiles from LR and HR collapse very well on the results available in literature. The results in Figure 5.8.b proves that the far-wake feature which is defined by deficit scales, is a very strong

and dominant flow feature at  $x/D = 10$ . As observed in Figure 5.8.b, the deficit velocity profiles of all the presented results are fairly identical for  $-0.5 < z/b < 0.5$ .

The variation of streamwise and transverse turbulence intensity are illustrated in Figures 5.8.c and 5.8.d, respectively. The turbulence intensity distribution of the present study obey the same trend that other studies have shown and collapse well on the results provided by Veale (2005), Adaramola et al. (2006) and (2012). Tests where bed effects are present match well with the results of the present study. The peak values of  $u_{rms}/U_S$  profiles are observed at  $z/D \approx \pm 0.50$ . Also, the maximum values of the transverse turbulence intensity profiles are located at the axis of symmetry ( $z/D = 0$ ).

The dimensionless spanwise shear stress distribution along the transverse direction is plotted in Figure 5.8.e. The results of the present study show very good agreement with that of other researchers results. The peak values of the Reynolds shear stress ( $-\overline{uw}/U_S^2$ ) occur at locations  $0.5 < z/D < 1.5$  from the central wake plane for different studies. The Reynolds shear stress in the wake asymptotes to zero at  $z/D = \pm 3.5$ , where velocity in the transverse direction decays.

## 5.5 Near-wake flow development

Figure 5.9 illustrates the dimensionless mean streamwise velocity and turbulence intensity profiles in the central wake plane along the  $x/D$  direction at mid-depth. As observed in Figure 5.9, the mean streamwise velocity and turbulence intensity profiles of the present study for LR and HR qualitatively follow the trend of other profiles reported by Norberg (1998), Parnaudeau et al. (2008), Cantwell and Coles (1983) and Gao et al. (2010) although differences in the local minima and maximum values are noticed. As seen in Figure 5.9.a, the mean streamwise velocity profiles of the present single cylinder study exhibit local minima in the near-wake region with much smaller negative value compared to observation of Norberg (1998) and Parnaudeau et al. (2008). The reason can be due to shallowness effect of flow in the present study which makes the vertical flow contribute to balance the conservation of mass into the horizontal re-circulating region. As discussed in Sections 5.2 and 5.3, the effects of bed and free surface generate strong upwash and downwash flow in vertical direction above the bed and beneath the free surface, respectively. This reduces the strength of negative streamwise velocity in the

horizontal re-circulation region compared to the two-dimensional wake flow. The variation of the mean streamwise velocity component along the streamwise axis allows one to evaluate the mean re-circulation length ( $l_C$ ) in the rear side of the cylinder where negative  $U/U_S$  is observed. Norberg (1998) noticed that by increasing the flow Reynolds number the mean re-circulation length decreased. This trend is observed in the present study as well. As discussed earlier in Section 5.3, the re-circulation length for the present study has been found to have a length of 2.3D and 2.2D for LR and HR, respectively at mid-depth plane, which are larger than the values reported by Norberg (1998), Djeridi et al. (2003), Parnaudeau et al. (2008), Gao et al. (2010) and Kirkil and Constantinescu (2015).

Among the wake flow studies discussed above, Gao et al. (2010) have presented similar weak negative streamwise velocity distribution in the re-circulation region in the near-wake region (Figure 5.9.a). Their bed-mounted single cylinder experiment was conducted in a re-circulating water flume with a wake Reynolds number ( $Re_D$ ) of 48,500. It is interesting to mention that, although Gao et al. (2010) and Kirkil and Constantinescu (2015) have studied bed and free surface effects on the wake flow behind the single cylinder, their re-circulation length is less than that in the present study. The reason can be due to the difference in wake Reynolds number, blockage ratio ( $D/B_f$ ) and cylinder's aspect ratio ( $AR=H/D$ ). For example, the reported  $l_C$  value by Gao et al. (2010) for the blockage ratio and cylinder's aspect ratio is about 17% and 1.25, respectively while in the present study the blockage ratio is not more than 0.5% and the cylinder's aspect ratio is about 11. Apart from various reported values for  $l_C$ , comparison among other dimensionless length scales along the wake centreline for the flow passing a single cylinder is presented in Table 5.2 which will be discussed further.

The streamwise turbulence intensity ( $u_{rms}/U_S$ ) distribution along the central plane is plotted in Figure 5.9.b. The  $u_{rms}/U_S$  profiles show that the streamwise turbulence intensity is zero just behind the cylinder and increases abruptly in streamwise direction to attain a peak value at a distance of  $lu_{rms}$  from the origin. Following the peak value, the  $u_{rms}/U_S$  profiles of LR and HR cases collapse on each other, and show a gradual reduction in  $u_{rms}/U_S$  distribution with increasing  $x/D$ . The same feature happens for  $w_{rms}/U_S$  profiles

in the present study, while the maximum value of  $w_{rms}/U_S$  profile occurs at a distance of  $lw_{rms}$  from the origin. These length scales,  $lu_{rms}$  and  $lw_{rms}$ , are other important length scales in the near-wake region and their values have been compared at different Reynolds numbers in literature (e.g., Cantwell and Coles, 1983 and Norberg, 1998).

The shape and location of the peaks of  $u_{rms}/U_S$  and  $w_{rms}/U_S$  distributions of LR and HR cases on the wake centreline are found to deviate from the studies of Norberg (1998), Parnaudeau et al. (2008), Gao et al. (2010) and Cantwell and Coles (1983) as shown in Figures 5.9.b. and 5.9.c. Besides the shallow flow feature in the present study, deviations can be attributed to the differences in the turbulence intensities (5%) of the approach flow which influence on the vortices formed around the bluff body.

Norberg (1987 and 1998) have shown that in two-dimensional wakes at  $350 < Re_D < 5000$ , with the turbulence intensity of the approaching flow being small (0.1%),  $u_{rms}/U_S$  has two distinct sharp peaks. These peaks are due to the generation of the turbulence in the unsteady shear layer. Analysis of the velocity measurements behind the bluff body reveals the presence of two distinct frequencies. The first frequency with higher amplitude was equal to the shedding frequency of the von Kármán vortices. The second frequency was near two times higher than the first one and following Wu et al. (1996), it was associated with the formation of the longitudinal vortex along the length of the cylinder. The longitudinal vortices are inclined to the streamwise direction and they are superimposed on the von Kármán vortices. These two unsteady structures generate high streamwise velocity fluctuations and can explain the occurrence of the two peaks in  $u_{rms}/U_S$  profile along the streamwise direction as reported by Norberg (1998) and Parnaudeau et al. (2008). The longitudinal vortex structure seems to be dependent on the turbulence intensity of the approaching flow and Reynolds number. At high  $Re_D > 5000$  the longitudinal vortex becomes unstable and decays. The turbulence is mostly generated by the von Kármán street vortices with occasional dislocations and less regular frequency observed in the near-wake region (Norberg, 1987). Similar decay in the longitudinal vortex structure is possible for the wake flows with large turbulence intensity of the approaching flow ( $> 1.4\%$ ) although  $Re_D < 5000$ . In the present study the turbulence intensity of the approaching flow at mid-depth location is about 5% as shown in Figure 3.4. As a result, the two peaks in the streamwise turbulence intensity profile are replaced

by a single peak, as shown in Figure 5.9.b, similar to the one observed in the present study and the study of Cantwell and Coles (1983).

In addition, Norberg (1998) and Parnaudeau et al. (2008) have reported that the dimensionless length scales,  $lu_{rms}/D$  and  $lw_{rms}/D$ , will decrease with increasing  $Re_D$ . The near-wake study by Cantwell and Coles (1983), for  $Re_D = 140,000$  indicate that  $lu_{rms}/D$  and  $lw_{rms}/D$  are 1.0 and 1.6, respectively (see Figures 5.9.b, 5.9.c and Table 5.2) which are larger than the expected values for such high Reynolds number. The difference could be due to the effect of the high turbulence intensity of the approaching flow and the intrusive nature of the flying hotwire probe used in the latter study. In the present study, the values of  $lu_{rms}/D$  and  $lw_{rms}/D$  do not conform to the results by Norberg (1998) and Parnaudeau et al. (2008) which could be due to the effects of the shallow flow.

Following the above discussion about the difference between the results of present study and the ones available in literature, one can suggest that the shallow near-wake feature is different from the typical two-dimensional wake flows even at mid-depth locations. Hereafter, more results of the shallow wake flow at different horizontal and vertical planes are discussed in the forthcoming sections.

## **5.6 Time-averaged results**

This section presents the time-averaged results of flow field in the near-wake region of a single cylinder for LR and HR at different horizontal and vertical planes. Five sections at each FOV in the near-wake region are chosen to examine the development of the shallow wake behind the bed-mounted high aspect ratio cylinder.

### **5.6.1 Horizontal plane profiles**

The normalized mean streamwise velocity profiles for both test cases in the three horizontal planes at mid-depth, near-bed and near-free surface are shown in Figure 5.10. In this figure, the mean streamwise velocity ( $U$ ) and the horizontal locations ( $x$  and  $z$ ) are normalized by the approaching mean streamwise velocity ( $U_S$ ) at the corresponding horizontal plane and the cylinder diameter ( $D$ ), respectively (see Figure 3.5). Figure 5.10 consists of a number of plots along the streamwise direction, which display the development of the  $U/U_S$  profiles at different  $x/D$  locations. The profiles are generally

symmetrical about the central wake plane ( $z/D = 0$ ) and can be divided into an inner where  $U/U_S$  has a small value and an outer region, where  $U/U_S$  asymptotes to 1.0 far from the  $z/D = 0$ .

At mid-depth, within the near-wake region as  $x/D$  increases (see Figures 5.10.a to 5.10.e), the mean streamwise velocity variation across the inner wake region gradually changes from a top-hat type profile to a Gaussian type. This is due to the fluid entrainment of high velocity fluid from the outer region to the inner region, which increases the streamwise velocity magnitude in the inner region as one moves downstream behind the cylinder, particularly on the axis of symmetry. This influx of the outer flow into the wake also causes the increase in the turbulence in the inner region downstream. A similar trend has been reported in other near-wake studies (Norberg, 1998 and Wang et al., 2006). In the top-hat type profile, the inner region has minimum constant velocity and flow is expected to be not turbulent, and is known as the core region. This region starts just behind the cylinder ( $x/D \approx 0$ ) with the width of about  $1D$  and ends at a downstream location where transition to a Gaussian type profile starts. In the present study, as observed in Figures 5.10.a to 5.10.e, for LR, the top-hat shape is maintained behind the cylinder as far as  $x/D = 1.2$ , while for the HR case, the top-hat profile vanishes beyond  $x/D = 0.8$ . For both cases, the flow has transitioned into a Gaussian type profile by  $x/D = 3$ . Furthermore, the influence of shear layers on both sides of the cylinder show peak values at the start of the outer region ( $|z/D| = 1$ ) in all the  $U/U_S$  profiles for both cases before attaining the Gaussian profile. Also, at the high Reynolds number flow, the profile shows larger  $U/U_S$  values compared to the lower Reynolds number flow in the outer region ( $|z/D| > 1$ ). This difference is more distinct at  $x/D = 0.4$  and becomes less pronounced at farther downstream at  $x/D = 3.0$ , where a Gaussian profile is attained.

In the near-bed plane (middle row in Figure 5.10), while no top-hat shape velocity profile is observed even at  $x/D = 0.4$ ,  $U/U_S$  profiles exhibit development to Gaussian type profile in Figures 5.10.f and 5.10.g and a Gaussian profile beyond  $x/D = 1.2$ . In this plane,  $U/U_S$  profiles of HR collapse well on the profiles of LR, particularly in the inner region for  $x/D < 1.2$ . It represents that the flow Reynolds number does not affect the velocity profile for the inner region. It would appear that the bed friction helps to stabilize

the flow, since the Gaussian type profile is attained sooner than its counterpart at the mid-depth plane. Also, the peak values observed at the end of the inner region ( $|z/D| = 0.6$ ) in Figures 5.10.f and 5.10.g show relatively higher values than their corresponding values at mid-depth. This may be due to the influence of the junction flow structures (horseshoe and base vortex structures) as discussed in Section 2.3.1 in addition to the shear layer effect.

Figures 5.10.k, 5.10.l and 5.10.m present the development of the streamwise velocity profiles in the near-free surface plane. In this plane, the velocity profiles resemble the top-hat shape for both cases near the cylinder ( $x/D = 0.4$ ) and LR retains its top-hat shape profile at  $x/D = 0.8$  as well; while HR case loses its top-hat shape profile at this location. The high Reynolds number flow exhibits smaller streamwise velocity values in the inner region of the  $U/U_S$  profiles at all  $x/D$  locations compared to the lower Reynolds number flow. There is a stronger Reynolds number effect that is noticeable in this horizontal plane. As discussed earlier in Section 5.3, the reason is perhaps due to the stronger contribution of the vertical velocity component (downwash flow particularly at  $x/D > 1.0$ ) in accordance with the mass conservation of the horizontal re-circulation region at high Reynolds number flow (see also discussion related to second row plots of Figure 5.14). This feature depicts the pronounced effect of the free surface on the flow particularly, in the high Reynolds number case.

The profiles for streamwise turbulence intensity ( $u_{rms}/U_S$ ) across the wake at mid-depth, near-bed and near-free surface are shown in Figure 5.11. While,  $u_{rms}/U_S$  profiles are almost symmetrical about the central wake plane ( $z/D = 0$ ), two distinct peaks and a valley between them occur in all the profiles. The peak values of  $u_{rms}/U_S$  distribution, which take place at off-centreline positions at all streamwise locations are the effect of the coherent structures including the separated shear layers (SSLs) from the sides of the cylinder along the flow direction. The dotted lines in all the graphs show the spanwise location of the edges of the cylinder ( $z/D = \pm 0.5$ ).

The first row of Figure 5.11 shows the  $u_{rms}/U_S$  profiles at different streamwise locations at mid-depth. The peak values of  $u_{rms}/U_S$  distribution at this plane take place at some position off the cylinder edge ( $0.5 < |z/D| < 1$ ) at all streamwise locations. The shear layers from the sides of the cylinder are the main source of generation these  $u_{rms}/U_S$

peaks in the profiles for both cases. The shear layers retain their strength up to  $x/D = 1.6$ , since the  $u_{rms}/U_S$  peak values do not decrease up to this streamwise location. In this plane, all streamwise locations where  $x/D \leq 1.2$ , HR case exhibits higher values in  $u_{rms}/U_S$  profiles. At  $x/D = 1.6$  and  $3.0$  the difference between  $u_{rms}/U_S$  profiles of high and low Reynolds numbers is negligible. A similar trend has been reported in the near-wake study by Norberg (1998) in two-dimensional flows. The turbulence level in the core region is small and almost constant close to the cylinder. With increasing streamwise distance, due to the penetration of the outer flow, the turbulence levels gradually increase with a minimum occurring in the wake axis. In the outer region, far from the central wake plane ( $|z/D| > 1$ ), the  $u_{rms}/U_S$  profiles asymptote to constant value of 0.05 for both cases. This asymptotic value is equal to the streamwise turbulence intensity of the approach flow at mid-depth plane.

Before analysing the turbulence intensity and Reynolds shear stress distribution at near-bed plane, it should be mentioned that following the literature reviewed in Chapter 2, there are multiple vortex structures generated in front and around the bluff bodies in the junction flow. Among these coherent structures, the important ones include the base vortex and the horseshoe vortex set which are discussed in Section 2.3.1. The effects of these structures influence the turbulence intensity and Reynolds shear stress profiles at this region, which can be noticed at the near-bed plane.

As illustrated in the second row of Figure 5.11, the near-bed streamwise turbulence intensity profiles have higher magnitude than that in the mid-depth plane for  $x/D \leq 0.8$ . This higher magnitude is due to the turbulence generation by multiple vortex structures in the near bed region. Also, as observed in Figures 5.11.f and 5.11.g, slightly higher  $u_{rms}/U_S$  values are observed for LR compared to HR and the difference between LR and HR profiles is more pronounced in the valley region. The higher  $u_{rms}/U_S$  values for LR case can be the signature of stronger vortical structures (apart from the separated shear layers) for LR flow compared to HR case at bed region. Also, since two peaks and a distinct valley between them occur in the  $u_{rms}/U_S$  profiles and the peaks retain more or less their high values at  $x/D \leq 0.8$ , one can suggest that the separated shear layers are shorter at near-bed plane compared to mid-depth plane for both cases. This can be due to the bed friction effect on the shear layers which suppresses their development in the bed



region. At  $x/D = 1.2$ , both  $u_{rms}/U_S$  profiles collapse on each other in the inner region, while at  $x/D = 1.6$  LR profile shows lower  $u_{rms}/U_S$  values compared to HR. Since LR flow shows higher bed friction coefficient value compared to HR, higher bed suppression effect is expected to be observed for LR case. Due to this fact, lower  $u_{rms}/U_S$  distribution is noticed for LR in the inner region at  $x/D = 1.6$ . In the outer region, far from the central wake plane ( $|z/D| > 1$ ), the  $u_{rms}/U_S$  profiles asymptote to two different constant values for LR and HR cases, respectively. These asymptotic values are equal to the streamwise turbulence intensity of the approach flow for LR and HR at near-bed plane.

The peaks of the  $u_{rms}/U_S$  profiles start approaching each other at  $x/D = 0.8$  and the valley between them becomes smaller at  $x/D \geq 1.2$  (see Figures 5.11.h and 5.11.i). The reason for this displacement of peak values can be due to the presence of horseshoe legs at near-wake region above the bed, which merge with the SSLs. Following the discussion by Kirkil and Constantinescu (2012), the horseshoe legs behind the cylinder are oriented towards the plane of symmetry and merge with the separated shear layers. So the  $u_{rms}/U_S$  peak values take place closer to the central wake axis ( $0 < |z/D| < 0.5$ ).

Farther downstream at  $x/D = 3$ , although the wake flow feature is obvious in the  $u_{rms}/U_S$  profiles trend, it is not that pronounced compared to their counterpart at mid-depth plane. At this location, the peaks in the profiles are broadened and their magnitude diminishes particularly for HR as observed in Figure 5.11.j. The reason can be due to bed suppression on the horseshoe legs and their breaking down condition, particularly for the HR case. Following Kirkil and Constantinescu (2012), Lin et al. (2003) and Greco (1990) the horseshoe vortex set at LR and HR flows are categorized as the laminar steady vortex system and amalgamating sub-regime system, respectively. In steady vortex system the position of the horseshoe core region and the corresponding legs are almost fixed in their location during the time so the interaction of the legs with bed is less. In contrast, in amalgamating sub-regime vortex system the primary core vortex (the most energetic and robust horseshoe vortex among the others) moves back and forth towards the cylinder. This movement increases the interaction of the horseshoe legs with bed, which as a result reduced the peak values, observed in  $u_{rms}/U_S$  profile for HR in Figure 5.11.j.

By comparing the development of the streamwise turbulence intensity in streamwise direction at mid-depth and near-bed planes, one can observe that the peak

$u_{rms}/U_S$  values at streamwise location of  $x/D = 1.6$  remain more or less in the same order of the peak values at  $x/D = 0.4$  location at mid-depth plane, while at near-bed plane the peak values at  $x/D = 1.6$  are near 60% and 55% of their counterpart values at  $x/D = 0.4$  for HR and LR flows, respectively. This suggests that the bed friction has the suppression effect on the wake development at near the bed region, which eventually influences on the wake stabilization.

In the third row of Figure 5.11, the general behaviour of the  $u_{rms}/U_S$  profiles are similar to the mid-depth plane for  $x/D \leq 1.2$ . The free surface resembles a flexible membrane which deforms at different Reynolds numbers due to the existence of the vortical structures beneath it. In LR flow the free surface is more or less a smooth membrane with less deformation along the streamwise direction in the near-wake region as discussed in Sections 5.2.2 and 5.3, which behaves like a weak wall. It slightly suppresses the  $u_{rms}/U_S$  profiles at farther downstream locations  $x/D \geq 1.6$ , similar but weaker than what is observed in the near bed region. This suppression effect is observed to start at  $x/D = 1.6$  for the LR case where the peaks of the  $u_{rms}/U_S$  profile start to come closer to each other; and is more clear at  $x/D = 3.0$  location. In the HR case, the strength of vortical structures beneath the free surface changes the formation of the flexible membrane behind the cylinder, particularly at  $2.0 \leq x/D \leq 3.0$  (as discussed in Section 5.3) and the suppression effect is not similar to the LR case (see Figures 5.11.n and 5.11.o). Also, as noticed in all the third row of Figure 5.11,  $u_{rms}/U_S$  profiles asymptote to a constant value of 0.025 for both cases in the outer region which is equal to the turbulence intensity of the approaching flow in the free surface region.

Figure 5.12 illustrates the spanwise turbulence intensity profiles ( $w_{rms}/U_S$ ) across the wake for the two Reynolds numbers in the three planes. There are some distinct differences noticeable at the two Reynolds numbers. The profiles in the three planes show varying development in the streamwise direction. In all the planes, the maximum value of  $w_{rms}/U_S$  occurs in the central wake plane ( $z/D = 0$ ) at almost all  $x/D$  locations, while in the outer region the  $w_{rms}/U_S$  profiles asymptote to a constant value which is the spanwise turbulence intensity of the approaching flow at the corresponding flow depth. At mid-depth and free-surface planes (first and third rows in Figure 5.12), the maximum peak in the  $w_{rms}/U_S$  profiles is observed at  $x/D$  location of 3.0. The comparison between the  $x/D$

locations of the maximum peak value of  $u_{rms}/U_S$  profiles (Figure 5.11) with  $w_{rms}/U_S$  profiles (Figure 5.12) shows a spatial lag of almost 1.5D at mid-depth and near-free surface planes. This spatial lag is due to difference between the locations of the generation of von Kármán vortices and the separation of the shear layers. In the near-bed plane, this spatial lag is about 0.8D which is shortened compared to mid-depth plane due to the bed friction stabilization effect on the wake flow.

Generally, high Reynolds number flow exhibits higher  $w_{rms}/U_S$  than low Reynolds number flow for all streamwise locations less than 2D in a two-dimensional wake flow (Norberg, 1998). A similar trend is observed at mid-depth plane in Figure 5.12, particularly for  $x/D \leq 1.6$ . At the near-bed plane, a double peak appearance is observed in the spanwise turbulence intensity profiles at  $x/D = 0.4$  for both Reynolds numbers; while the HR case continues its double peak profile at downstream location at  $x/D = 0.8$  as well. Further downstream, the double peak changes to single peak located in the central wake plane. The existence of stable or center foci which are observed in the present study (see Section 5.3) may be ascribed as the occurrence of the double peak in  $w_{rms}/U_S$  profiles at  $x/D < 1.0$  near the bed, while in other horizontal planes no stable focus was observed to create a double peak in  $w_{rms}/U_S$  profiles. Furthermore, as observed in the second row of Figure 5.12, LR flow exhibits higher  $w_{rms}/U_S$  than HR flow for all streamwise locations less than 3D. The reason is due to the mixture of SSLs with the vortical structures at the junction flow of higher  $u_{rms}/U_S$  values for LR compared to the HR case at this plane (discussed before), which will generate spanwise motions with higher spanwise turbulence intensity for LR.

At the near-free surface plane, while higher  $w_{rms}/U_S$  values are observed for HR compared to LR flow, similar to mid-depth plane at  $x/D < 1.2$ , there is a sharp increase in the spanwise turbulence intensity values for LR profile at farther downstream locations  $x/D \geq 1.6$  compared to HR profile. Interestingly, although higher  $u_{rms}/U_S$  values are observed for HR compared to LR case at near-free surface plane in Figure 5.11, lower  $w_{rms}/U_S$  values are noticed for HR at  $x/D \geq 1.6$  (Figures 5.12.n and 5.12.o). The reason can be due to the dip effect in the water surface for HR flow. This deformation in the free surface draws some amount of energy from the flow beneath it, which will result in decay in spanwise turbulence intensity.

Figure 5.13 illustrates the development of dimensionless Reynolds shear stress ( $-\overline{uw}/U_s^2$ ) distribution in spanwise direction for two cases at mid-depth, near-bed and near-free surface planes. A first glance, the shear stress profiles appear to be symmetric with opposite sign about the central wake plane ( $z/D = 0$ ) and the shear stress distributions across the wake obey a similar trend in all the plots of LR and HR cases. At mid-depth and near-free surface planes,  $-\overline{uw}/U_s^2$  profiles are constant zero along the spanwise locations in the near-wake region where  $x/D \leq 0.4$  for both flows. There are two small bumps at  $z/D = \pm 0.8$  which are considered to be within the range of uncertainty in the measurements. At farther downstream locations in the mid-depth plane (Figures 5.13.b, 5.13.c and 5.13.d), HR shows higher magnitude in the shear stress profiles. In contrast, at near-free surface plane, due to the reasons discussed earlier in spanwise turbulence intensity profiles section, higher magnitudes in the  $-\overline{uw}/U_s^2$  profiles are observed in the LR flow (Figures 5.13.m to 5.13.o). At near-bed plane, the shear stress distribution exhibits higher magnitudes than mid-depth and near-free surface. Also, the highest shear stress at near-bed region occurs at  $x/D \approx 0.8$  while highest values for shear stress at mid-depth and near-free surface occur at  $x/D \approx 2$  and 3, respectively. In addition, LR case presents higher shear stress values compared to the HR case in the near-bed plane for  $x/D \leq 1.2$  which is more obvious in Figure 5.13.g. At farther downstream locations, while the shear stress distribution is greatly suppressed by bed friction effect and gradually vanishes to near-zero (see Figure 5.13.j), the shear stress profiles are not affected by flow Reynolds number.

### 5.6.2 Vertical plane profiles

Figure 5.14 illustrates the development of the normalized velocity profiles at the vertical mid-plane ( $z/D=0$ ) in different  $x/D$  locations for both Reynolds numbers. The velocity profiles are normalized by the approaching free stream velocity ( $U_e$ ) and the vertical positions are normalized by the cylinder's diameter ( $D$ ) (see Figure 3.5). The origin of the coordinate system is behind the cylinder at the bed, the lower solid boundary is at  $y/D = 0$  and the free surface is located at  $y/D = 10.9$ .

Normalized streamwise velocity ( $U/U_e$ ) profiles at different streamwise locations are displayed in the first row of Figure 5.14. It can be observed that the streamwise

velocity profiles behind the cylinder ( $x/D = 0.4$ ) are negative with a small magnitude (almost zero) along the whole depth for both Reynolds numbers, which is consistent with the horizontal re-circulation (or almost stagnant) region captured in plots of the first column of Figure 5.10. Just beneath the free surface at  $y/D > 10.2$ , the HR flow shows positive  $U$ , while the LR case has negative  $U$  velocity.

At downstream location  $x/D = 0.8$ , larger negative  $U$  velocity is observed through most of the water depth compared to Figure 5.14.a. The streamwise velocity turns to a positive value above the bed and shows a peak in the profile at  $y/D = 0.5$  for both cases. At  $x/D = 0.8$  the flow near the bed begins to accelerate. Such changes in the  $U/U_e$  profiles at near bed region can be a signature of the presence of the coherent structures in this region that modify the streamwise velocity distribution. Since the LR case exhibits a higher peak magnitude compared to HR, it indicates that the structures in LR are stronger than that of the HR flow. Near the free surface, the  $U/U_e$  profile has the same trend which is observed at  $x/D = 0.4$ . Interestingly at mid-depth, the  $U$  velocity is almost zero for both profiles that indicates the presence of stagnant horizontal re-circulation region at this region.

Figures 5.14.c and 5.14.d illustrate development of  $U$  velocity in streamwise direction in the farther downstream locations at  $x/D = 1.2$  and  $2.0$ , respectively. Similar to the previous plot, the maximum  $U$  occurs above the bed for both cases with a higher value for the lower Reynolds number case. In addition, these plots indicate that although the streamwise velocity is accelerating at mid-plane particularly above the bed, the negative  $U$  velocity still exists in the upper levels of flow depth which confirms the occurrence of longer re-circulation length in the near-free surface plane compared to mid-depth and near-bed planes as discussed in Section 5.3.

At farther downstream location  $x/D = 4.0$ , as shown in Figure 5.14.e, there is a local increase in  $U$  velocity in the high Reynolds number case due to the dip effect in the free surface level (observed in the measurements and discussed in Section 5.3) while such behaviour is not observed in the LR case. This high streamwise velocity confirms the presence of surface current beneath the free surface suggested by Maheo (1999). The surface currents are known to indicate the signature of the interaction of free surface and surface parallel vortical structures beneath it. As observed in Figure 5.14.e, the  $U$  velocity

is more or less developed along the lower-portion of water depth, where  $y/D < 8.0$ , and  $U/U_e$  profiles of both cases obey similar trend. Also,  $U/U_e$  profile shows decay in the velocity value near the free surface region for LR case which is similar to the results in literature (e.g., Inoue et al., 1993 and Suh et al., 2011) at this location for near-free surface study.

The mean vertical velocity  $V/U_e$  profiles are shown in the second row of Figure 5.14 at different streamwise directions for both Reynolds numbers. The velocity profile at  $x/D = 0.4$ , shown in Figure 5.14.f, illustrates a positive  $V$  (upward) throughout the water depth in the LR case. The maximum value of  $V$  is observed at  $y/D = 3.5$  and decreases gradually to reach zero at near the free surface where  $y/D > 9.5$ . As noted by Sumner et al. (2004) and Wang and Zhou (2009) the positive  $V$  velocity can be attributed to the effect of base vortex structure. As discussed earlier in Section 5.3, while just backward velocity vectors are noticed in the corner of the free surface and rear of the cylinder in the low Reynolds number case, there is a re-circulation region in that location for the high Reynolds number case (see Figure 5.6.b). The effect of this re-circulation region is strong enough to alter the trend of  $V/U_e$  distribution of the HR case compared to low Reynolds number case, particularly on the upper half of the flow depth at  $x/D = 0.4$ . In this location, a similar positive  $V$  (upward) trend is noticed for the HR case above the bed while at  $6.0 < y/D < 8.0$  the vertical velocity becomes negative with a small magnitude (almost zero) and again becomes positive for  $y/D > 8.0$ . Similar features are observed in Figure 5.14.g although the location of negative vertical velocity is shifted upper for the HR case. In addition, since LR shows larger  $V/U_e$  distribution above the bed compared to the HR case, then stronger upwash flow is expected to be observed in the LR case. The latter can be the signature of the presence of stronger coherent structures (base vortex structure) in this region for the LR flow.

At downstream locations  $x/D \geq 1.2$ , the negative vertical velocity is observed beneath the free surface for the HR case while the LR flow presents positive  $V/U_e$ . The downwash flow for high Reynolds flow beneath the free surface is discussed in Section 5.3. The effect of free surface in shallow flow, particularly while the Reynolds number is high, is not just beneath the free surface but even at mid-depth of the flow. As observed at these  $x/D$  locations, the free surface effect in the HR case can modify the flow at mid-

depth as the trend of  $V/U_e$  profiles of the HR case start to deviate from the ones of LR case at  $y/D = 5.0$  (see Figure 5.14.j). In addition, at these locations the  $V/U_e$  profiles show a very small negative value ( $-0.05 < V/U_e < 0$ ) at a region very close to bed ( $y/D < 0.6$ ) for both cases. This negative velocity may be the result of the rotation of vortex structures associated with the legs of horseshoe set near the bed, which can be the sign of the convergence of the horseshoe legs towards the central wake plane at  $x/D \geq 1.2$  locations.

Figure 5.15 displays the development of the turbulence intensity and dimensionless shear stress profiles at the vertical mid-plane ( $z/D=0$ ) in streamwise locations. The first glimpse of the plots in Figure 5.15 indicates the three-dimensionality of the shallow wake flow behind the cylinder due to the effects of bed and free surface. Similar conclusion can also be made from the velocity profile plots in Figure 5.14. In addition, LR exhibits almost higher streamwise turbulence intensity ( $U_{rms}/U_e$ ) in the lower part of water depth (above the bed) compared to HR in all the  $x/D$  locations, particularly for  $x/D \leq 1.2$ . A similar trend is also observed for transversal turbulence intensity ( $V_{rms}/U_e$ ) profiles. Higher turbulence intensity values for LR case can be due the existence of stronger coherent structures at this region compared to the HR case.

Again referring to Section 2.3.1, the base vortex structure can exist in the very near-wake region above the bed. This vortical structure can be the main reason for the peak of the turbulence intensity profiles occurred near the bed at  $x/D = 0.4$  in the vertical mid-plane for both cases (see Figures 5.15.a, 5.15.f). In farther downstream locations, the strong upwash flow behind the cylinder contributes in shifting this peak in turbulence intensity profiles towards the free surface for both Reynolds numbers (See Figures 5.15.b to 5.15.e and Figures 5.15.g to 5.15.j). Furthermore, another peak in the turbulence intensity profiles is observed at a region very close to bed ( $y/D < 0.6$ ) for both cases for  $x/D \geq 1.2$ , while its location is not changing as the turbulence intensity profiles develop. Following Kirkil and Constantinescu (2012 and 2015), this peak in the profiles is possibly attributed to the effect of the converged horseshoe legs towards the central wake plane above the bed at  $x/D \sim 1.2$ .

In addition, beneath the free surface, higher turbulence intensity values are observed for the HR case for  $x/D \leq 1.2$ , while at farther downstream locations, particularly at  $x/D = 4.0$ , the turbulence intensity of the LR case shows larger values

compared to HR. This sharp decrease in the turbulence intensity profile for the HR case can be due to the dip effect in the water surface for high Reynolds number flow, which shows that the deformation in the free surface has observed some amount of energy form the flow beneath it and eventually lower the flow turbulence level in that region.

The third row of Figure 5.15 shows the development of dimensionless Reynolds shear stress profiles ( $-\overline{uv}/U_e^2$ ) at different streamwise locations. As observed in Figure 5.15.k, a peak in shear stress profile with negative value, where LR has a larger magnitude, is observed above the bed for both cases at  $x/D = 0.4$ , while the shear stress is almost zero along the water depth away from the bed ( $y/D > 2.5$ ). In farther downstream locations, the peak in shear stress is shifted upward in  $y$  direction (see Figures 5.15.m to 5.15.o) and more expanded in water depth with smaller peak value until it reaches the free surface.

In addition, as observed in Figure 5.15.l the second peak in  $-\overline{uv}/U_e^2$  profile is generated above the bed with larger magnitude for LR. The magnitude of the peak increases and its location moves upwards with increasing  $x/D$  while  $x/D \leq 2.0$ . As observed in Figure 5.15.o, this peak in shear stress is almost decayed along the water depth at  $x/D = 4.0$ . Interestingly, the second peak illustrates a positive sign in all the plots. These two  $-\overline{uv}/U_e^2$  peaks generated one after another with different signs can be the sign of interaction of the shear layers separated from the sides of the cylinder and the existence of the base vortex structure behind the cylinder at different locations above the bed.

Finally, there is another negative shear stress peak (third peak) observed slightly above the bed at  $y/D = 0.50$  in Figure 5.15.m for both cases. The development of the third peak Reynolds shear stress occurs at the same  $y/D$  value for  $x/D \geq 1.2$ . Again similar to other shear stress peaks, LR case exhibits larger negative values compared to the HR case. The presence of the third shear stress peak in Figures 5.15.m, 5.15.n and 5.15.o as previously discussed, may be due to the effect of the legs of horseshoe vortex set. It seems that these horseshoe legs still exist at farther downstream locations ( $x/D \geq 1.2$ ) so their effect on velocity, turbulence intensity and Reynolds shear stress profiles are noticeable along the  $x$  direction above the bed. At far downstream ( $x/D = 4.0$ ) the shear stress profiles do not show a logical trend but just fluctuation along the zero value for



both cases particularly away from the bed which confirms the development of shear stress along the water depth for both cases.

## 5.7 Conclusion

In this chapter, the results of particle image velocimetry measurements at different horizontal and vertical planes in the wake region behind a single circular cylinder in shallow flow are presented for two Reynolds numbers. The measurements were conducted up to far-wake region, at near-bed, mid-depth and near-free surface vertical locations along with the vertical mid-plane. The salient flow features can be summarized as follows:

- Although the stability parameter of the wake is very small ( $S < 0.01$ ) for both Reynolds numbers, there is a considerable effect of the bed friction and free surface influence on the wake flow. This is due to the fact that the approaching flow is maintained at a sufficiently shallow condition.
- Although the deficit velocity profiles of both Reynolds numbers in the mid-depth plane collapse well on the available results in literature at far-wake region, the wake behind the bed-mounted cylinder cannot be considered as the plane wake flow. This is due to the difference of their spanwise turbulence intensity distribution from that of the two-dimensional wake in the inner region.
- While there is a stagnant re-circulation region behind the cylinder in all horizontal planes, the size of time-averaged re-circulation region is found to increase from the bed towards the free surface for both Reynolds numbers, which is different from the studies of flow past a small cylinder ratio. The size of re-circulation region in HR case is smaller than LR at mid-depth plane, due to shorter SSL length in HR. The attenuation effect of bed and free surface is found to be stronger in LR case, since the size of re-circulation region is smaller than HR flow at their corresponding planes.
- Stronger bed suppression effect in LR flow is observed from the turbulence intensity and Reynolds shear stress profiles at near-bed plane. The profiles of the LR case with higher values decay more to collapse on the profiles of the HR case, particularly for  $x/D \leq 0.8$ .

- The flow pattern in the vertical mid-plane can be divided into two zones for both cases. The first zone, which is close to the cylinder, contains of strong vertical velocity ( $V$ ) components and is coincident with the stagnant re-circulation region observed in the horizontal planes. While a strong upwash flow is dominant near the bed for both Reynolds numbers, there is a small re-circulation region with downwash flow near the free surface in HR case. In the second zone, the mean flow is dominant in streamwise direction for both Reynolds numbers. Also, there is a small dip ( $y/D \sim 0.25$ ) in the free surface level along with the downwash flow beneath the free surface in HR case. It can be concluded that the free surface behaves like a flexible membrane in HR rather than LR case.
- The free surface shows more deformation for the HR flow. Since the deformation in the free surface draws energy from the flow beneath it, that results in lower values of spanwise turbulence intensity and Reynolds shear stress profiles for the HR case compared to the LR flow in the near-free-surface plane, particularly for  $x/D \geq 1.6$ .
- Since larger  $V$  values (stronger upwash flow) are noticed behind the cylinder ( $x/D < 1.2$ ) for the LR flow and this upwash flow is associated with the base vortex structures, one can suggest that stronger base vortex structure is noticed above the bed for LR case compare to HR.
- At farther downstream locations ( $x/D \geq 1.2$ ) in the vertical mid-plane, there is a peak in turbulence intensity and Reynolds shear stress profiles along with the negative vertical velocity values above the bed. These are the signature of the presence of horseshoe legs at this near-bed region. Since higher peak magnitudes belong to LR in the profiles at these locations, more coherence in the legs of horseshoe structure can be expected for LR case.

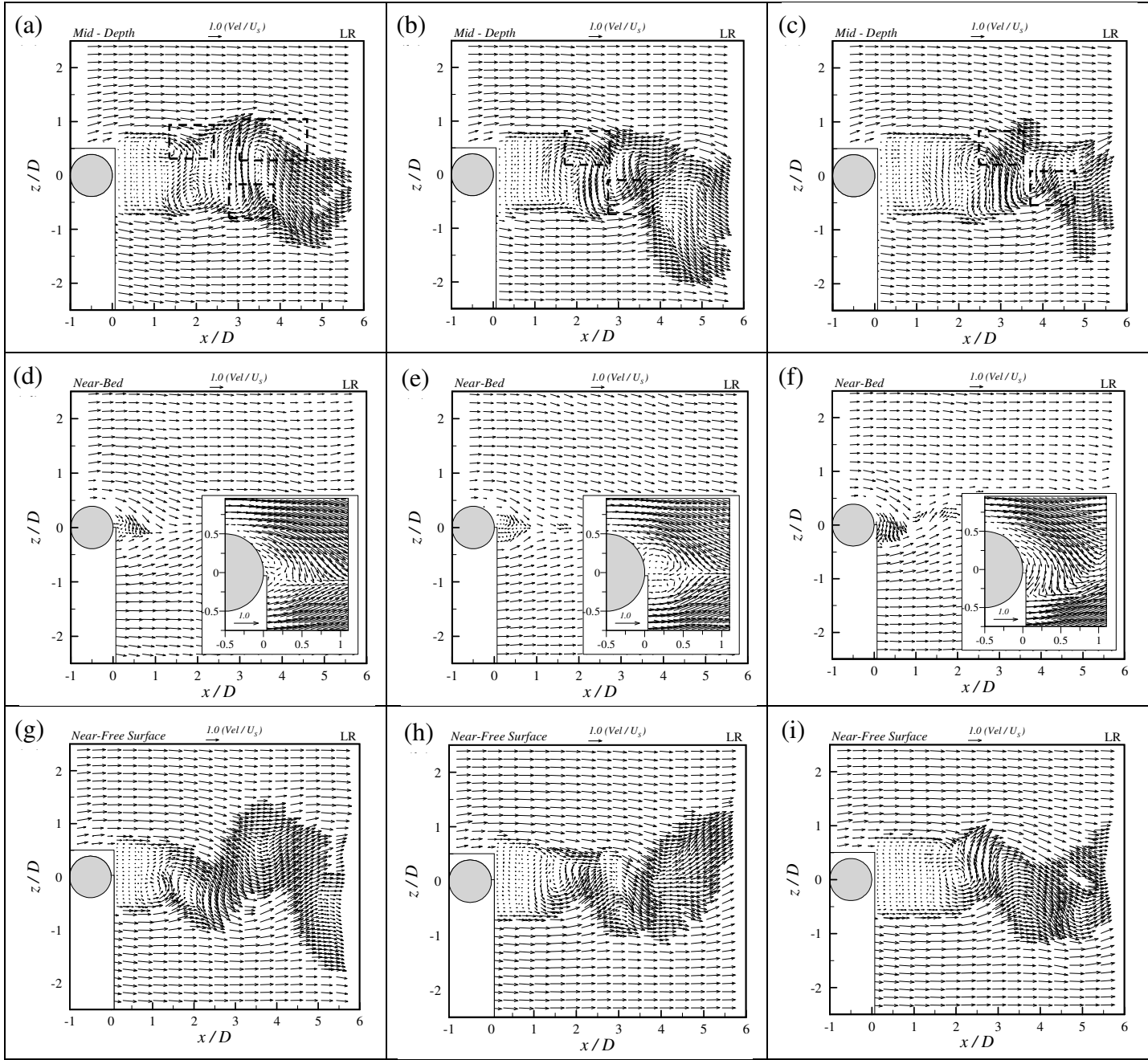


Figure 5.1: Examples of instantaneous velocity fields measured in the low Reynolds number flow on the horizontal planes; mid-depth (a, b, c), near-bed (d, e, f) and near-free surface (g, h, i)

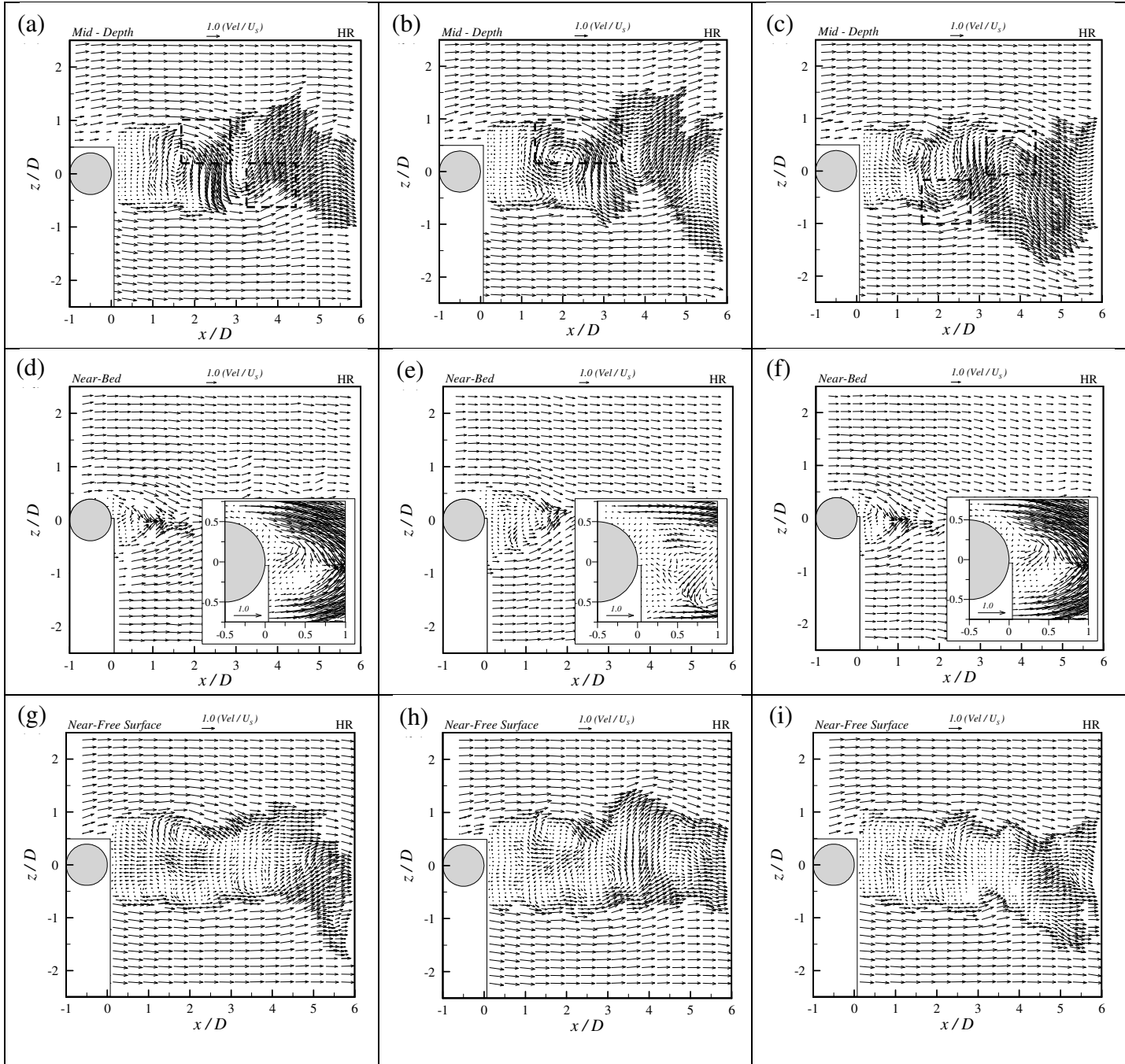
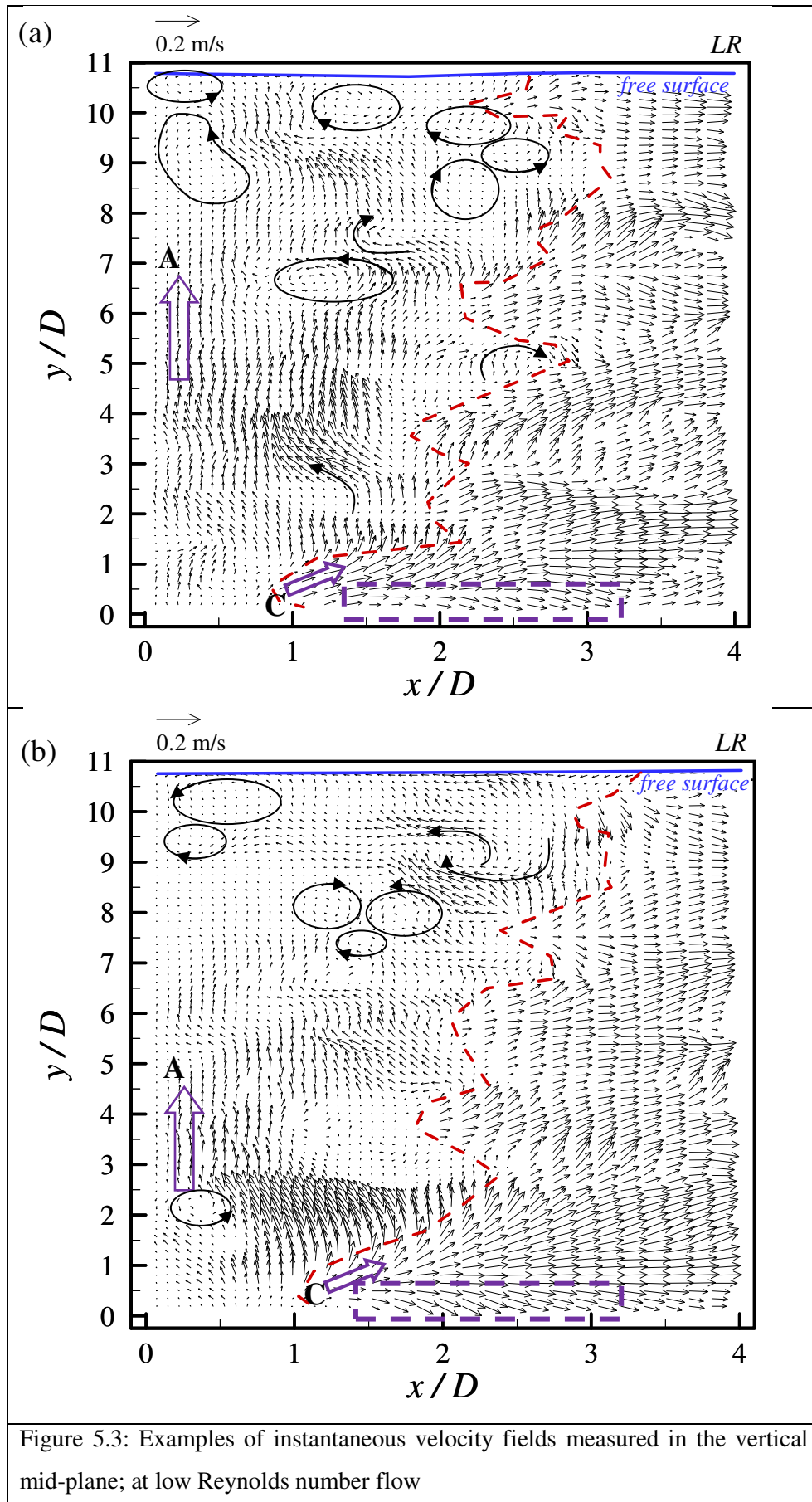
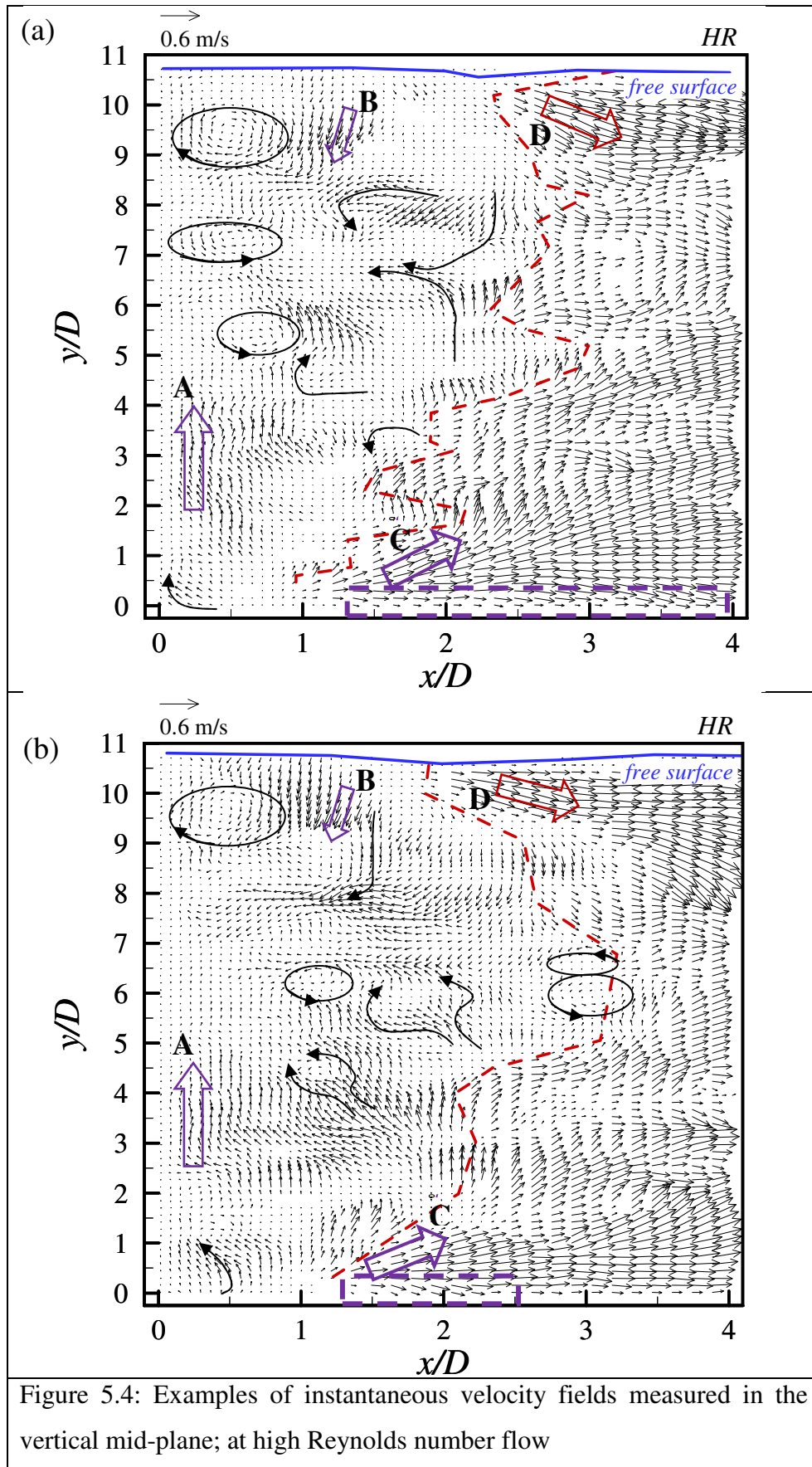


Figure 5.2: Examples of instantaneous velocity fields measured in the high Reynolds number flow on the horizontal planes; mid-depth (a, b, c), near-bed (d, e, f) and near-free surface (g, h, i)





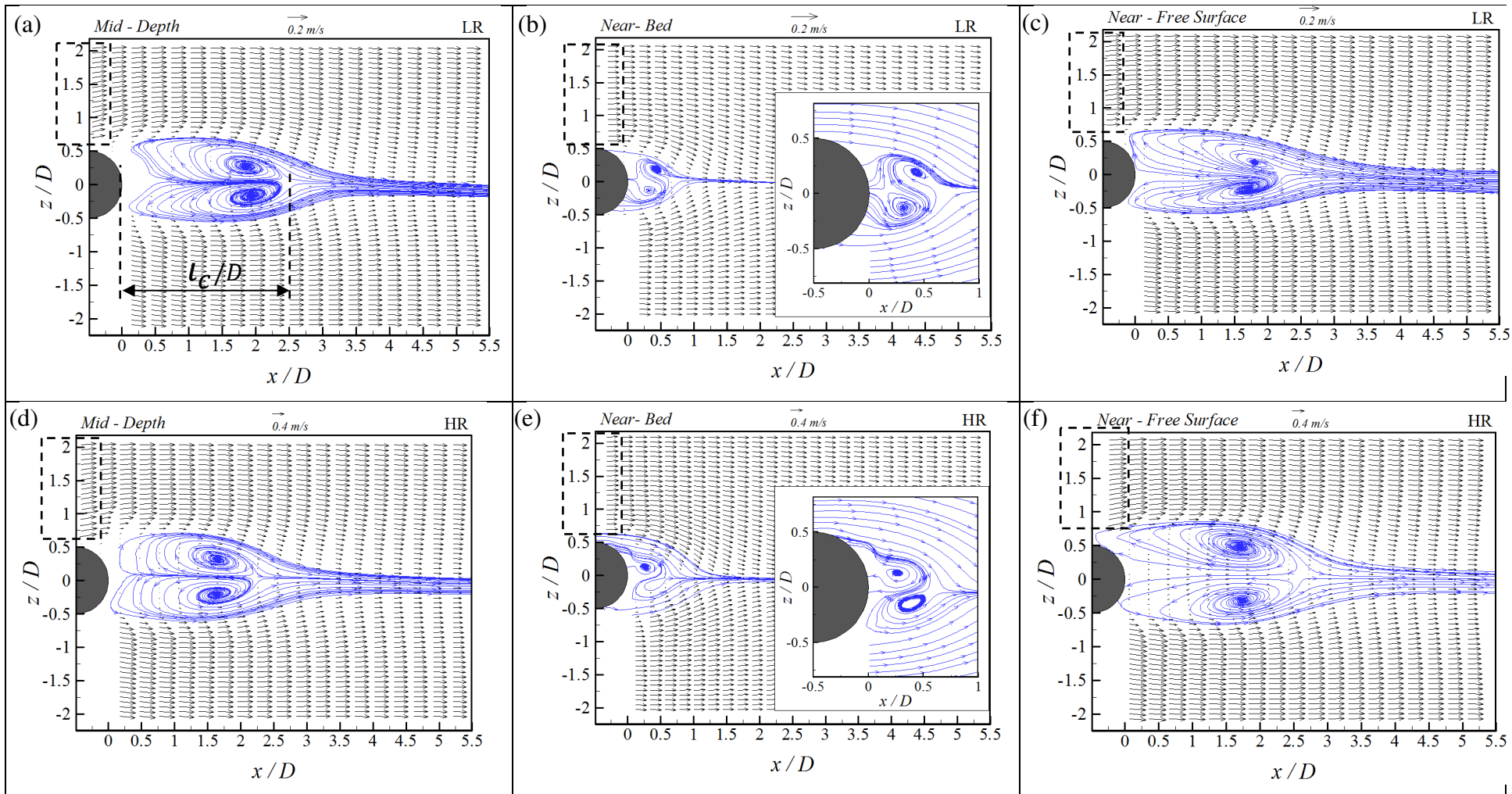


Figure 5.5: Mean velocity vector fields measured on the horizontal planes at mid-depth (a, d), near-bed (b, e), and near-free surface (c, f) for low (LR) and high (HR) Reynolds numbers, respectively



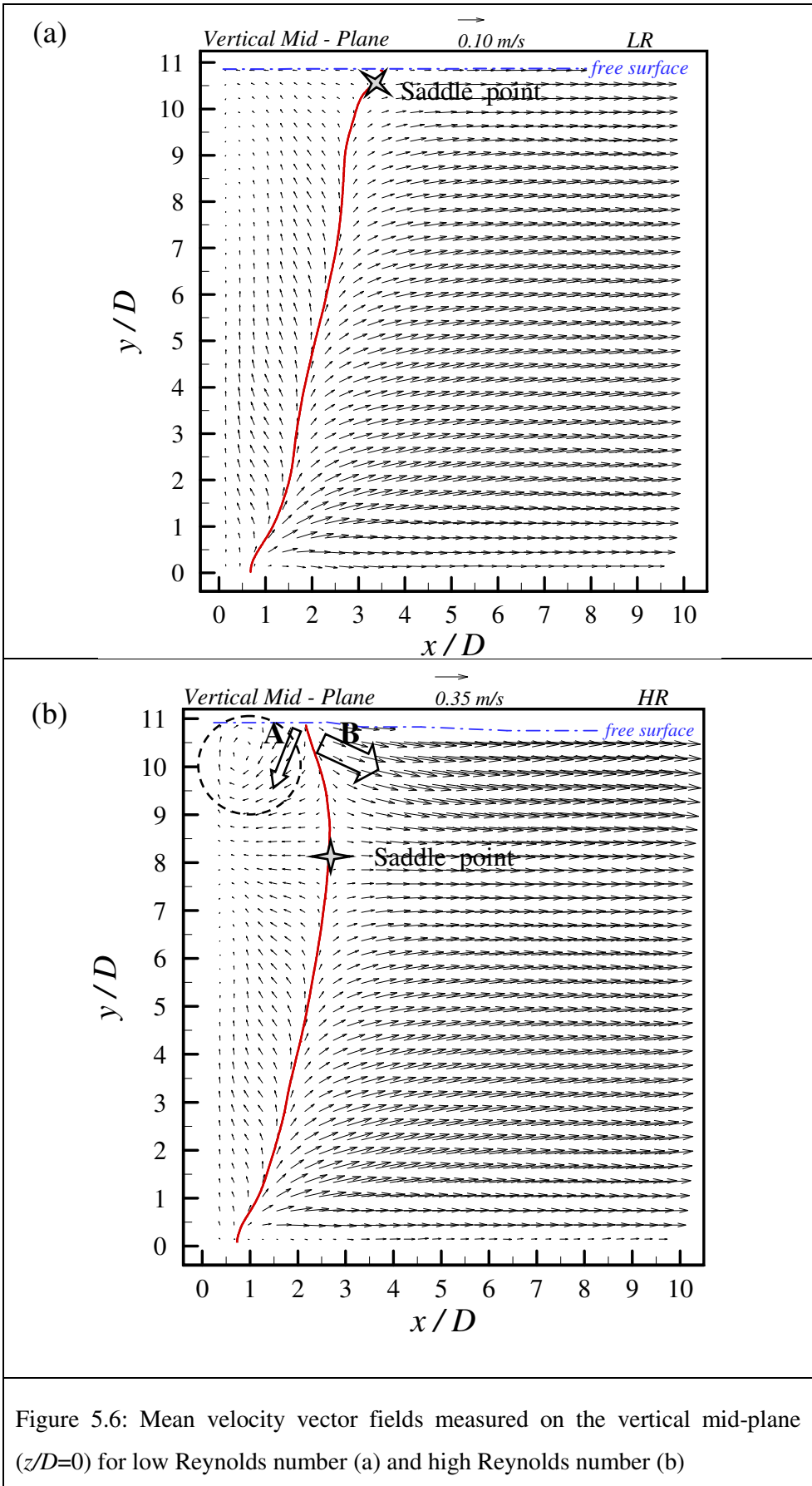
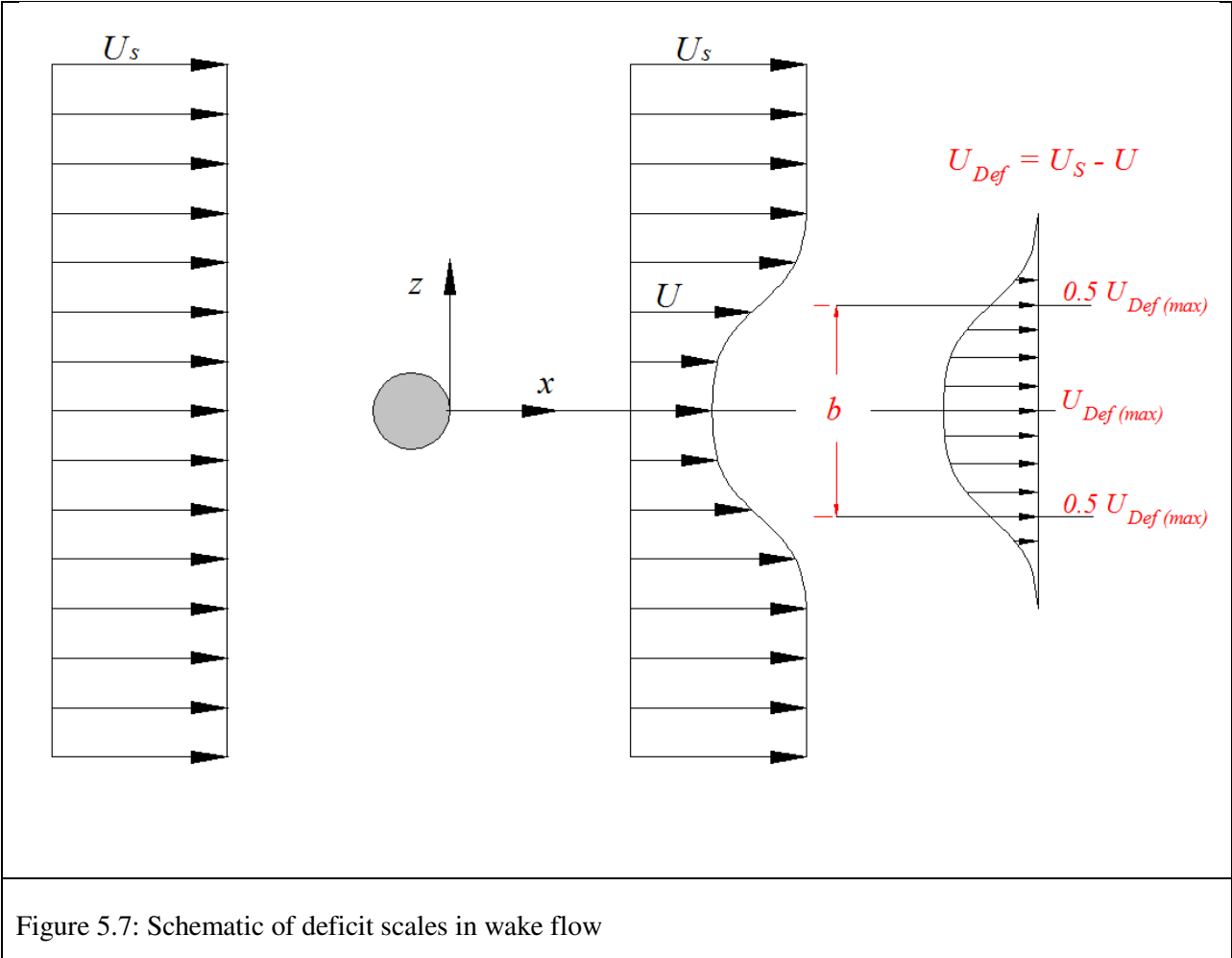
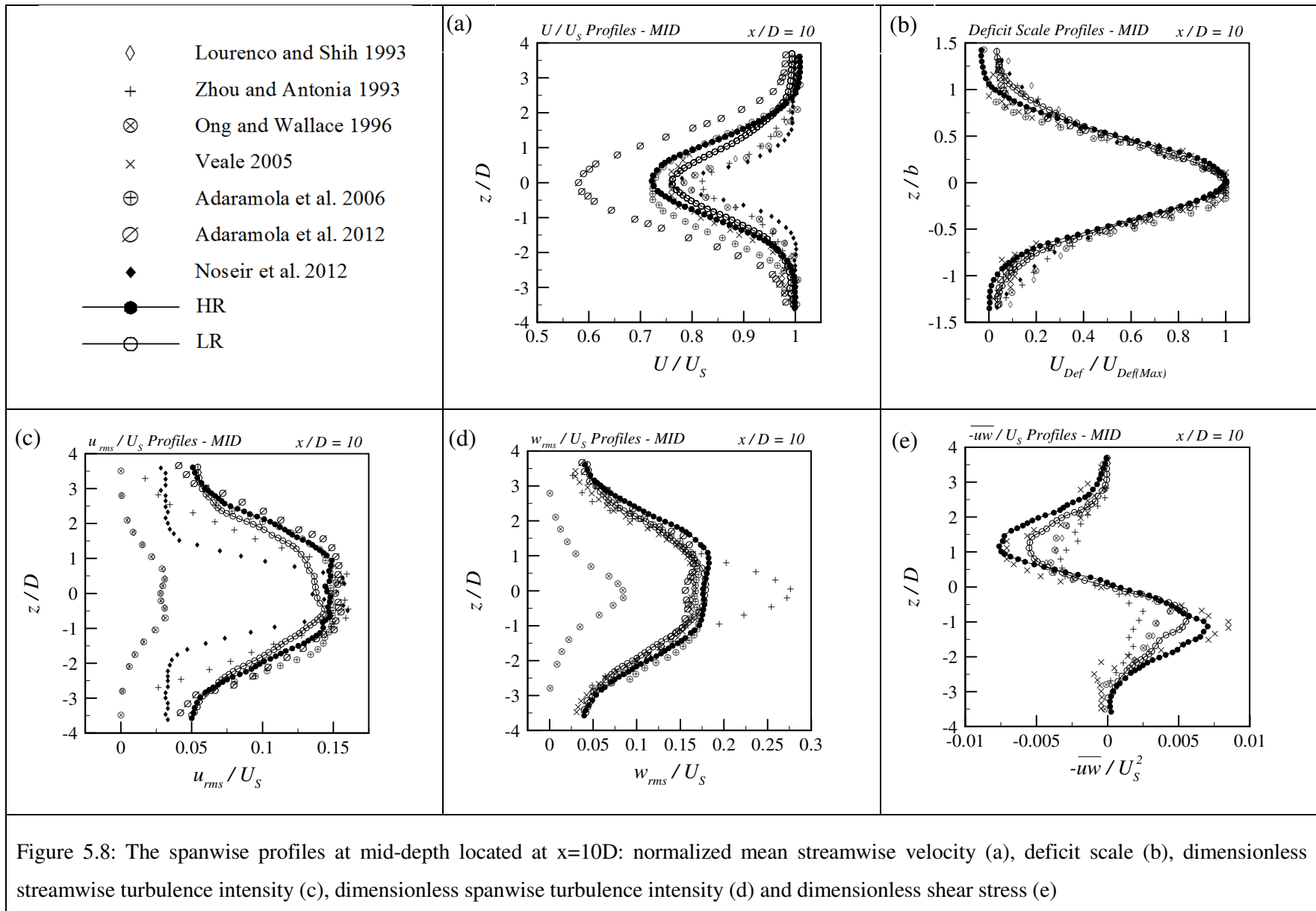


Figure 5.6: Mean velocity vector fields measured on the vertical mid-plane ( $z/D=0$ ) for low Reynolds number (a) and high Reynolds number (b)







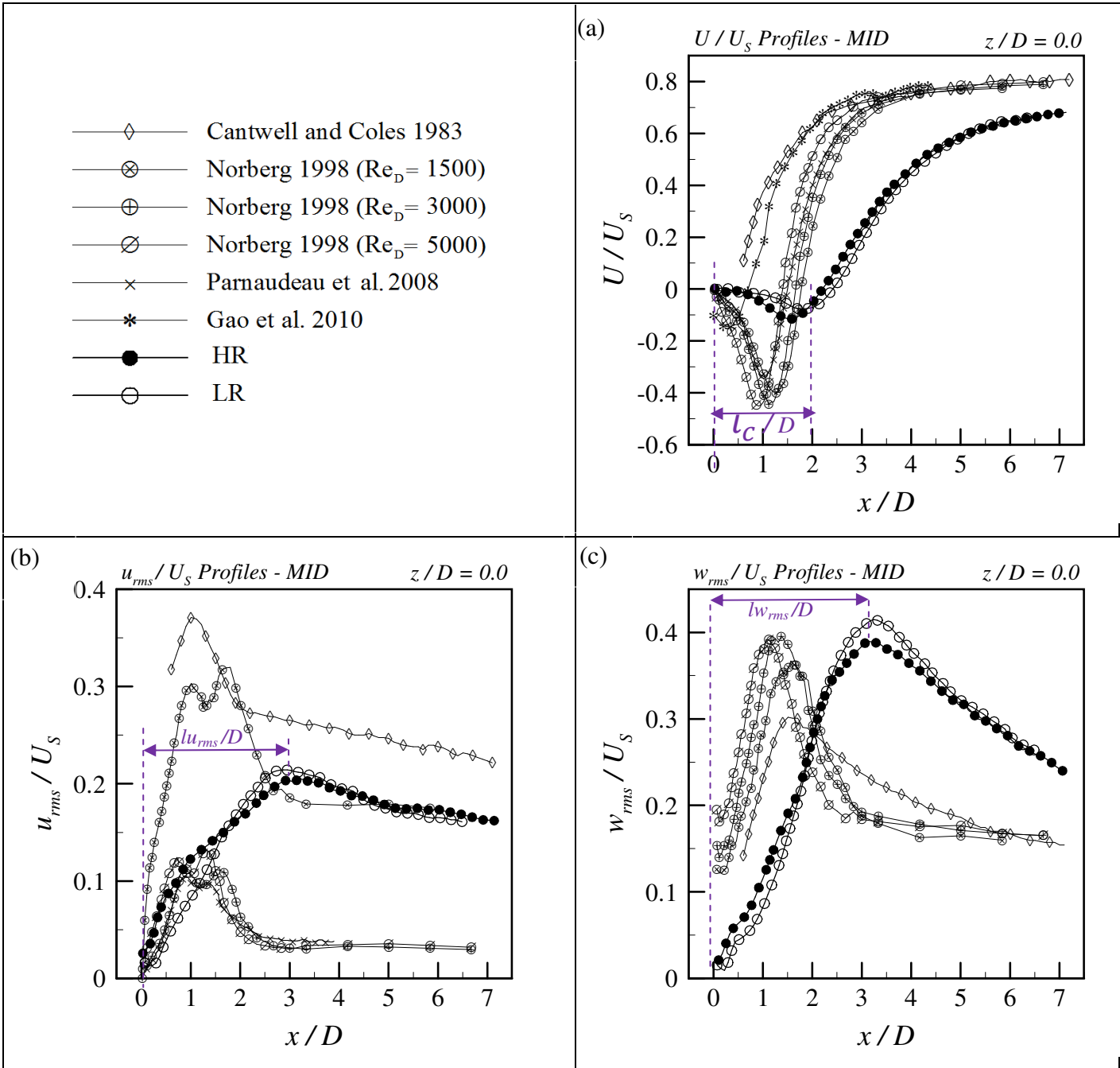


Figure 5.9: The streamwise profiles at mid-depth located at central wake plane: normalized mean streamwise velocity (a), dimensionless streamwise turbulence intensity (b) and dimensionless spanwise turbulence intensity (c)

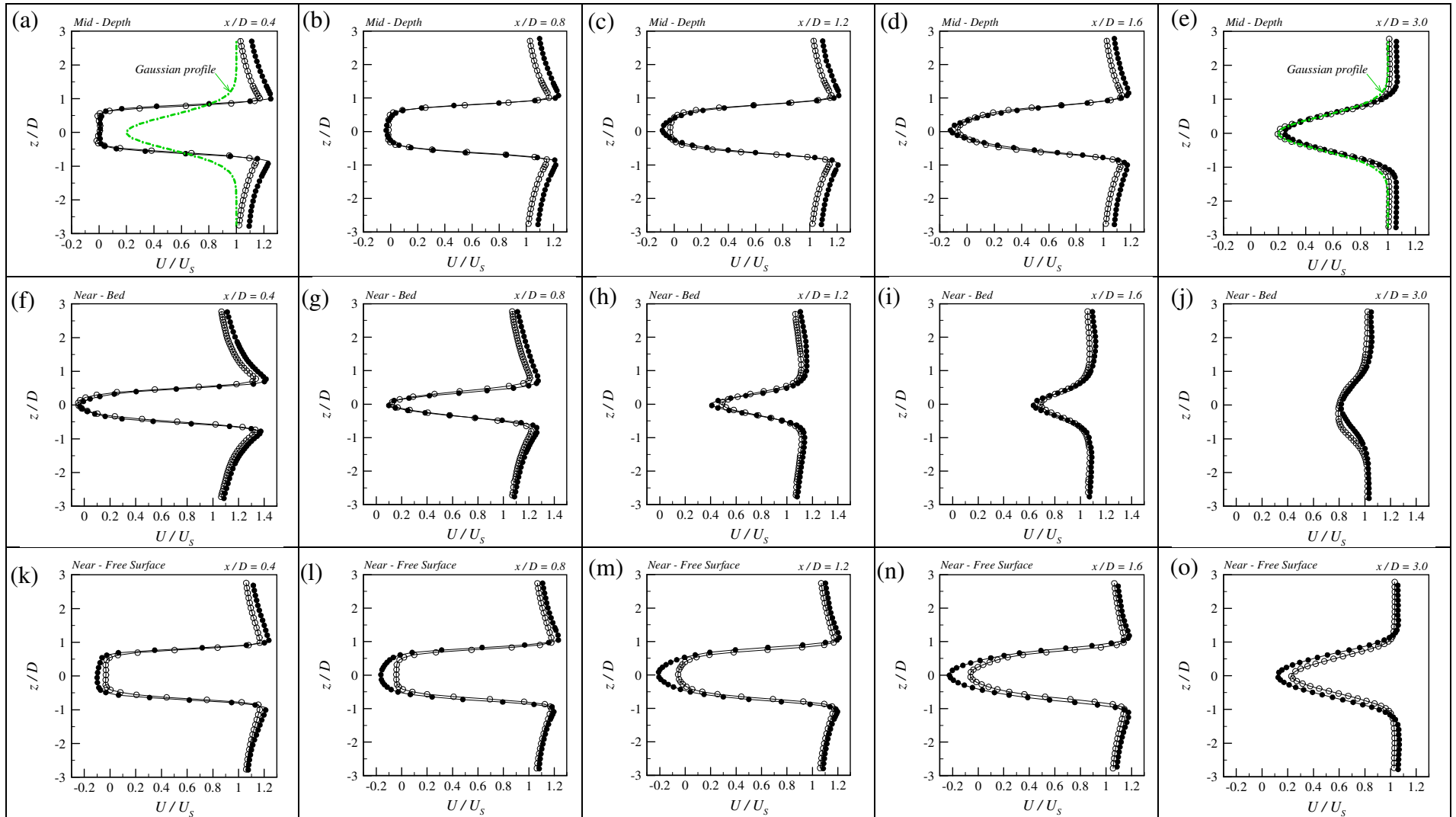


Figure 5.10: The normalized mean streamwise velocity profiles at different  $x/D$  locations at mid-depth (a, b, c, d, e), near-bed (f, g, h, i, j) and near-free surface (k, l, m, n, o) planes. Open circle represents the LR case and solid circle represents the HR case

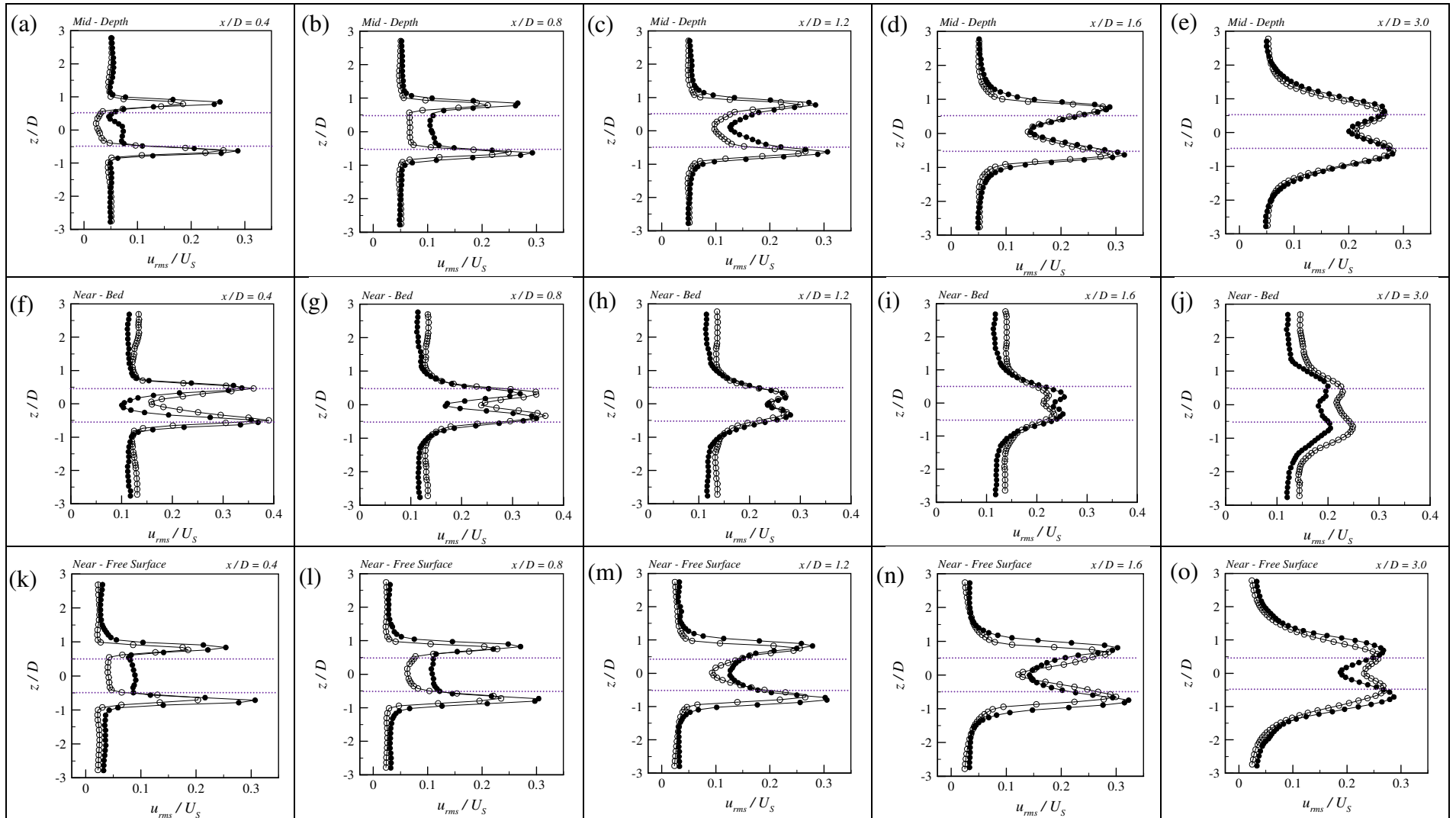


Figure 5.11: The streamwise turbulence intensity profiles at different  $x/D$  locations at mid-depth (a, b, c, d, e), near-bed (f, g, h, i, j) and near-free surface (k, l, m, n, o) planes. Open circle represents the LR case and solid circle represents the HR case. The dotted lines show the location of the edges of the cylinder

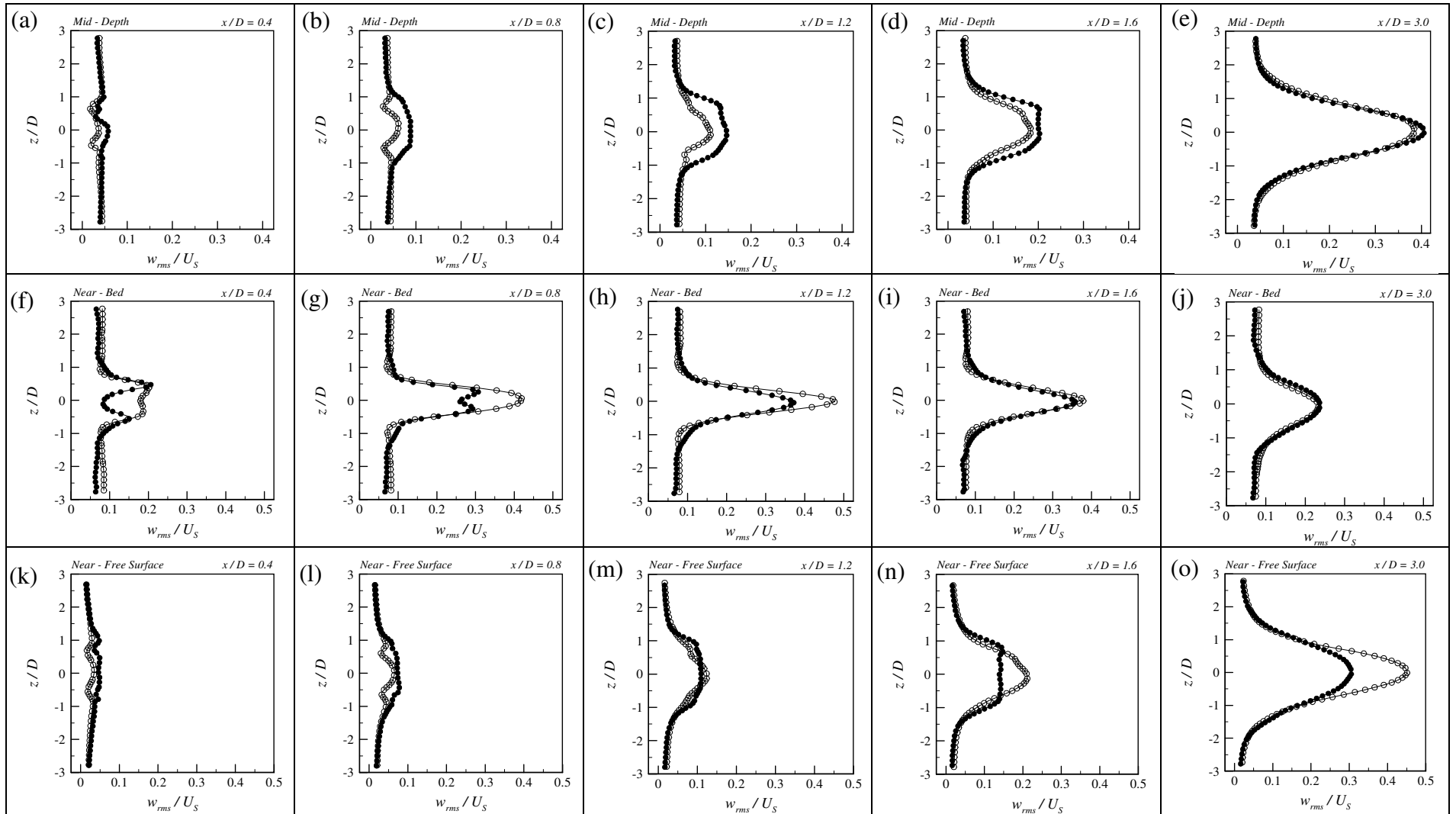


Figure 5.12: The spanwise turbulence intensity profiles at different  $x/D$  locations at mid-depth (a, b, c, d, e), near-bed (f, g, h, i, j) and near-free surface (k, l, m, n, o) planes. Open circle represents the LR case and solid circle represents the HR case

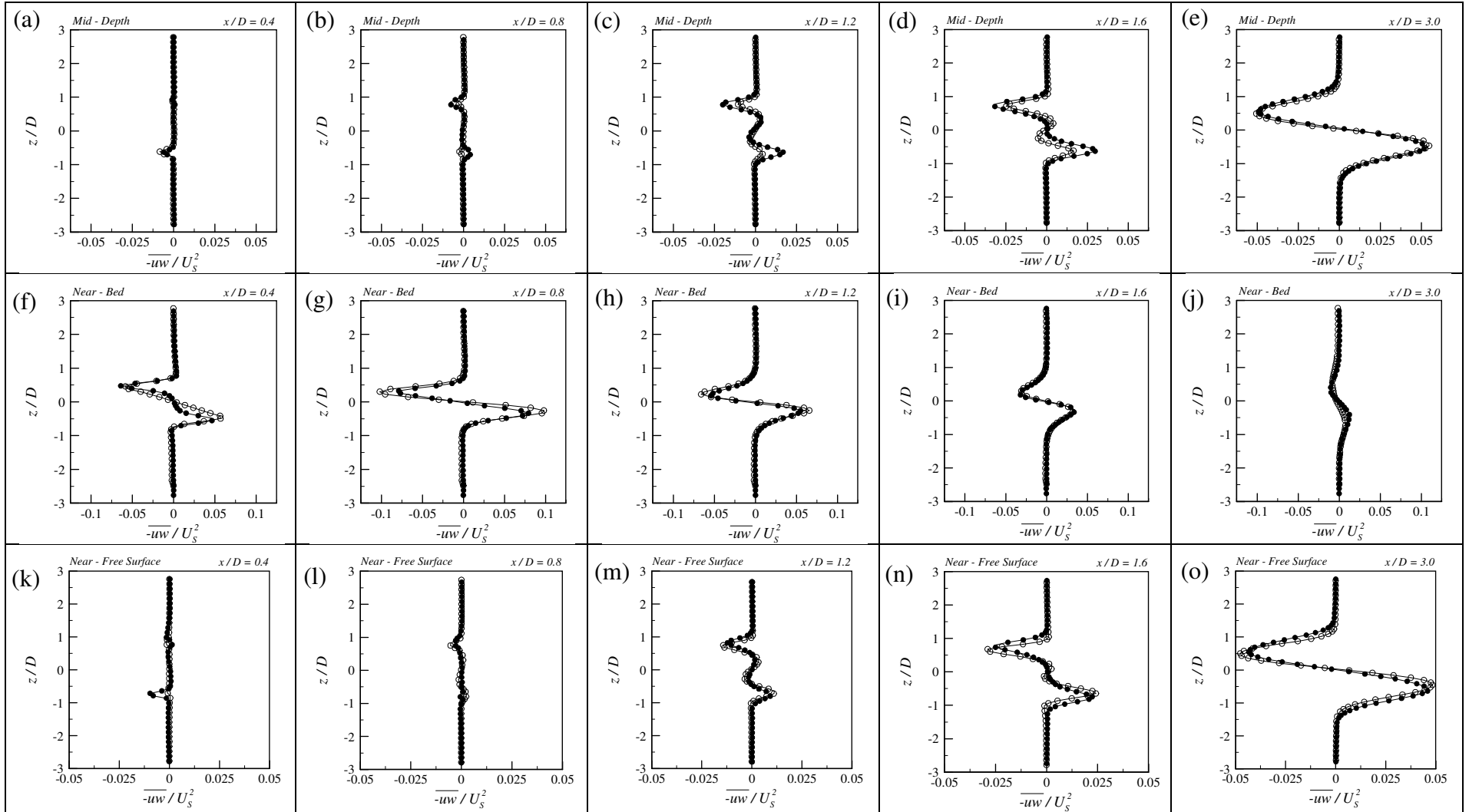


Figure 5.13: The dimensionless shear stress profiles at different  $x/D$  locations at mid-depth (a, b, c, d, e), near-bed (f, g, h, i, j) and near-free surface (k, l, m, n, o) planes. Open circle represents the LR case and solid circle represents the HR case

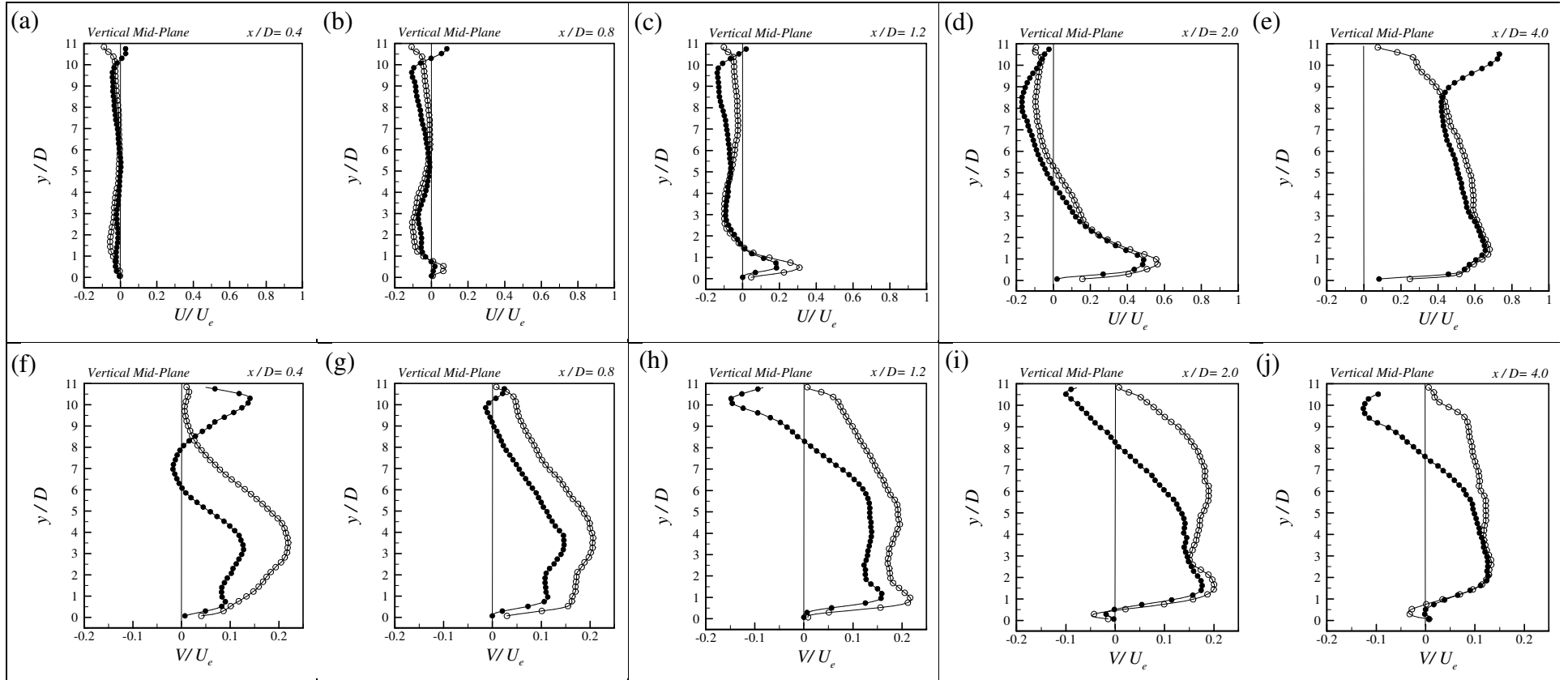


Figure 5.14: Normalized mean streamwise velocity (a, b, c, d, e) and normalized mean vertical velocity profiles (f, g, h, i, j) at central wake plane at different  $x/D$  locations. Open circle represents the LR case and solid circle represents the HR case



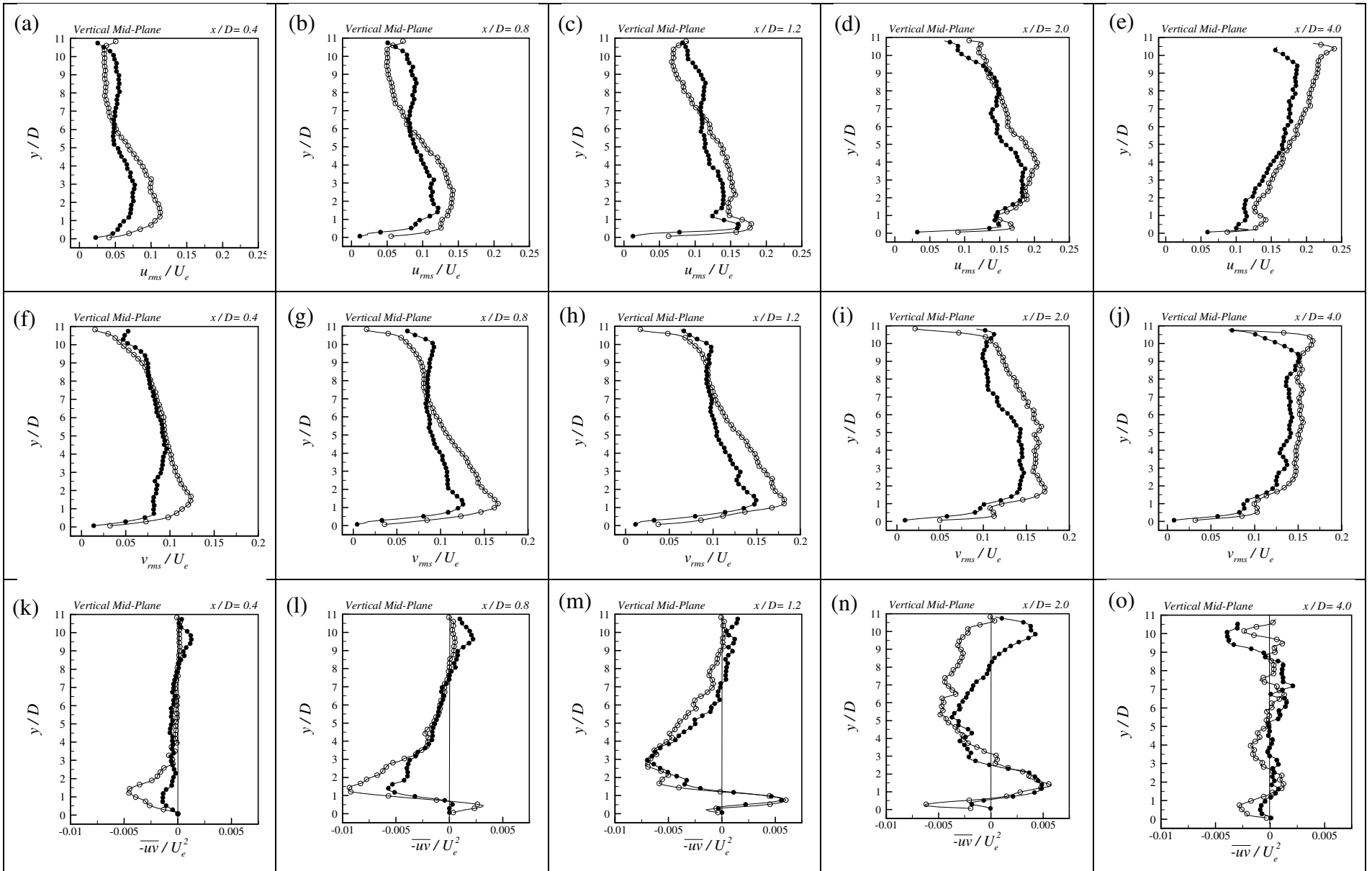


Figure 5.15: streamwise turbulence intensity (a, b, c, d, e), transversal turbulence intensity (f, g, h, i, j) and dimensionless shear stress (k, l, m, n, o) profiles at central wake plane at different  $x/D$  locations. Open circle represents the LR case and solid circle represents the HR case

Table 5.1: Selected experimental studies of flow passing a single circular cylinder

Researchers	D (m) $\times 10^{-2}$	$Re_D$ (= $U_e D/\nu$ )	Test facility and measurement technique	Turbulence intensity (%)	Details
Cantwell and Coles (1983)	10.14	140,000	Wind tunnel, flying hot wire	0.47	Two-dimensional wake flow
Zhou and Antonia (1993)	1.25	5,600	Wind tunnel, hot wire	0.05	Two-dimensional wake flow
Lourenco and Shih (1993)	1.20	3,900	Water channel, PIV	-	Two-dimensional wake flow
Ong and Wallace (1996)	1.43	3,900	Wind tunnel, hot wire	0.67	Two-dimensional wake flow
Norberg (1998)	0.60	1,500 – 10,000	Wind tunnel, LDV	0.10	Two-dimensional wake flow
Veale (2005)*	6.04	10,300	Water flume, PIV	2.40	Bed mounted finite length cylinder
Adaramola et al. (2006)*	3.20	60,000	Wind tunnel, hot wire	0.50	Bed mounted finite length cylinder
Parnaudeau et al. (2008)*	1.20	3,900	Wind tunnel, PIV and hot wire	0.20	Two-dimensional wake flow
Gao et al. (2010)	20.00	48,500	Water flume, PIV	-	Bed mounted finite length cylinder
Adaramola et al. (2012)*	1.91	23,000	Wind tunnel, pressure probe	0.60	Bed mounted finite length cylinder
Noseir et al. (2012)	0.40	4,750 – 5,300	Wind tunnel, hot wire	0.50	Two-dimensional wake flow
* Submerged cylinder					

Table 5.2: Summary of different length scale values along the wake centreline				
Researchers	$Re_D$	$l_c / D$	$lu_{rms} / D$	$lw_{rms} / D$
Cantwell and Coles (1983)	140,000	-	1.0	1.6
Norberg (1998)	1,500	1.25	1.01, 1.73	1.58
Norberg (1998)	3,000	1.15	0.95, 1.59	1.36
Norberg (1998)	5,000	0.92	0.73, 1.33	1.11
Norberg (1998)	8,000	0.67	1.12	0.91
Norberg (1998)	10,000	0.54	1.00	0.76
Djeridi et al. (2003)	140,000	0.87	-	-
Parnaudeau et al. (2008)	3,900	1.05	0.88, 1.35	-
Gao et al. (2010)	48,500	0.30	-	-
Kirkil and Constantinescu (2015) at mid-depth	16,000	1.30	-	-
Kirkil and Constantinescu (2015) at mid-depth	500,000	0.70	-	-
Present study – (LR)at mid-depth	925	2.3	2.8	3.45
Present study – (HR)at mid-depth	3,000	2.2	3.1	3.2

## Chapter 6: COHERENT STRUCTURES

### 6.1 General description

This chapter reports analysis of the large scale coherent structures formed in the near-wake region of a circular cylinder in shallow open channel flow. It is believed that the dynamics of the coherent structures play an important role on the turbulence characteristics of the wake. To reveal the most energetic modes in the flow, proper orthogonal decomposition (POD) technique is applied to the fluctuating velocity fields of the near-bed, mid-depth and near-free surface planes. Then, the fluctuating velocity fields are reconstructed based on the most energetic POD modes to expose the large scale coherent structures. Before starting the discussion of the POD results, a definition of the coherent structures and a summary the POD technique is presented.

#### 6.1.1 Coherent structures

Turbulent flows consist of a wide range of time and length scales that possess certain randomness in appearance and orientation. Since recognizable turbulence structures or events occur randomly in time and space, detection of such events is subjected to experimental uncertainty. Complexity of turbulence, has led researchers to break down the turbulent flow into some elementary motions that are in a way organized and identifiable in the flow. Since these motions appear regularly in space and time, they influence the dynamics of the turbulent flows (Dennis, 2015). Such organized motions are collectively known as *coherent structures*. One of the common features of the coherent structures, found in different turbulent flows, is their rotational component. It has been widely accepted that the signature of the coherent structures are characterized by large concentration of vorticity (Hussain, 1986). In spite of the extensive research on turbulence over the past few decades, there is still no exact definition for the coherent structure. One of the best definitions was proposed by Hussain (1986) which states that “*coherent structure is a connected, large scale, turbulent fluid mass with instantaneously phase correlated vorticity over its spatial extent*”. It can be concluded that any coherent

structure consists of an individual set of organized motion consisting of vortical fluid patches in a confined space which persist in its form in the flow for long enough periods. Dennis (2015) elaborated on the meaning of “coherent” and “structure” and proposed that the main characteristics of the coherent structures are their consistency (for example a consistent pattern in the velocity field). Following his definition for coherent structures, no sign of vortical fluid patches is required for coherent structures in contrast with Hussain’s definition. The main influence of the coherent structures is to construct the turbulent flow through some degree of organisation. Using this viewpoint we could define coherent structures as the building-blocks of turbulent flow.

Objective identification of large coherent structures in complex turbulent flows is still an important area of research which involves efforts of fluid dynamicists, mathematicians and statisticians. Historically, coherent structures have been identified by using flow visualization experiments with smoke and dye. Although flow visualization is still a reliable technique for qualitative observation of the flow structures present in the flow (e.g., oil-film visualization technique for identifying the horseshoe formation by El Hassan et al., 2015), filtering (decomposition) techniques are the most widely used tools for quantitative coherent structure identification. Among these tools, the proper orthogonal decomposition (POD) which decomposes the velocity field based on the turbulent kinetic energy is commonly applied to experimental (e.g., Wang et al., 2014; Tang et al., 2015) and numerical simulations to educe the most energetic structures in the flow field. The preference of POD method over the other filtering techniques is in its ability to construct filters that are inhomogeneous in one or more flow directions. The POD filters the background (random) turbulence from the velocity field for better investigation of large vortical structures in turbulent flows. Due to this fact, the POD has been adopted in literature as a tool for exposing the large coherent structures in various turbulent flows. Wu (2008), Roussinova (2009), Takimoto et al. (2013) applied POD method for identification the signature of near bed structures (hairpin vortex) in boundary layers and open channel flows. Shinneeb (2006), Lam (2013), Watanabe et al. (2015) employed this tool to educt the coherent structures in the jet flows. Perrin et al. (2007), Singha (2009), Kourentis and Konstantinidis (2012), Wang et al. (2014), El Hassan et al.

(2015), Tang et al. (2015) utilized POD technique to expose the coherent structures in the wake flow.

In this chapter, the POD is applied to the PIV experiments for a single cylinder at low and high Reynolds numbers. A brief summary of the POD technique is provided here after.

### **6.1.2 Proper orthogonal decomposition (POD) method**

Lumley in 1967 introduced the proper orthogonal decomposition (POD) method as a mathematical procedure to decompose a set of time-series data to the spatial information form on a domain which is known as modal basis. Depending on the field in which it is used, POD is known as Karhunen-Loeve decomposition, single value decomposition or principal component analysis (Holmes et al., 1998). Kerschen et al. (2005) pointed out that application of the linear filters to nonlinear turbulence problems exhibits major limitation. POD technique can be applied on the velocity measurements carried out at single point (LDV, HWA) and multiple points (PIV). High spatial resolution PIV experiments are preferred for analysis to minimize the noise contamination of the calculated spatial POD modes (Bi et al., 2003).

In this thesis, energy based POD method is used for coherent structure identification based on the two-point velocity correlation. This identifies the motions that on average contain the most energy. Further, by reconstructing the original velocity field based on reduced number of modes one can expose the large coherent structures of the turbulent flow. The process of determining the energy based POD modes and further reconstruction of velocity field are discussed next.

#### **6.1.2.1 POD analysis**

The POD can be computed using two methods: the direct method (Berkooz et al., 1993) and the snapshot method (Sirovich, 1987). Graftieaux et al. (2001) tested both methods numerically on unsteady turbulent swirling flow and they have reported no significant difference in the final results. Since the PIV data realizations are discrete both

in time and space, the snapshot method can be easily employed. The snapshot method is computationally less intensive requiring less computational time and memory. This method has also the advantage that it can be used to process data that are uncorrelated in time. In the present thesis, the data realizations are uncorrelated in time because the sampling frequency of the PIV is much smaller than the frequency of the unsteady flow, i.e., the frequency of the vortex shedding. In this study, the method of snapshots for POD as suggested by Sirovich (1987) has been used. The method of snapshots POD procedure (Sirovich, 1987; Wu, 2008) used for PIV data is summarized below:

The snapshot POD can be applied on any flow parameter in the spatial and temporal field of measurement. Since in the present study, the PIV (particle image velocimetry) method presents instantaneous velocity fields in time duration, the velocity vector  $\mathbf{V}(x, t)$  is chosen as a flow parameter in this discussion. In POD, any instantaneous fluctuating velocity  $\mathbf{v}(x, t)$  in the position  $x$  of flow field and time  $t$  can be decomposed approximately into the form of  $N$  deterministic spatial POD modes  $\boldsymbol{\phi}_n(x)$ , and  $N$  random temporal coefficients  $a_n(t)$ , where  $n = 1, \dots, N$ . If  $N$  approaches infinity the approximation will change to equality which can be expressed as

$$\mathbf{v}(x, t) = \sum_{n=1}^{N \rightarrow \infty} a_n(t) \boldsymbol{\phi}_n(x) \quad (6.1)$$

In order to reach to the best approximation, the difference between the real value and the approximation value should be minimal over the spatial domain  $\Omega$  and time interval  $T$  which can be expressed mathematically as

$$\min \left( \int_{\Omega} \int_T (\mathbf{v}(x, t) - \sum_{n=1}^N a_n(t) \boldsymbol{\phi}_n(x))^2 dt dx \right) \quad (6.2)$$

For any arbitrary variations like  $\boldsymbol{\phi}_m(x)$  and  $a_m(t)$  in the spatial domain  $\Omega$  and time interval  $T$ , respectively and considering Eq. (6.1), it leads to

$$\int_T (\mathbf{v}(x, t) - \sum_{n=1}^N a_n(t) \boldsymbol{\phi}_n(x)) a_m dt = 0 \quad (6.3.a)$$

$$\int_{\Omega} (\mathbf{v}(x, t) - \sum_{n=1}^N a_n(t) \boldsymbol{\phi}_n(x)) \boldsymbol{\phi}_m dx = 0 \quad (6.3.b)$$

Since any individual spatial POD mode  $\boldsymbol{\phi}_n(x)$  is independent from the others, the orthogonality of  $\boldsymbol{\phi}_n(x)$  is a valid assumption. Similar assumption can be applied to any

individual temporal coefficient  $a_n(t)$ . The mathematical formulation of the orthogonality condition can be expressed as

$$\left. \begin{aligned} \int_{\Omega} \boldsymbol{\phi}_n(x) \boldsymbol{\phi}_m(x) dx &= 0 \\ \int_T a_n(t) a_m(t) dt &= 0 \end{aligned} \right\} \text{for } m \neq n \quad (6.4)$$

Substituting Eq. (6.4) in to Eq. (6.3.a and 6.3.b) yields determination of the arbitrary variations  $\boldsymbol{\phi}_m(x)$  and  $a_m(t)$  as

$$\boldsymbol{\phi}_m(x) = \frac{\int_T \mathbf{v}(x,t) a_m(t) dt}{\int_T (a_m(t))^2 dt} \quad (6.5.a)$$

$$a_m(t) = \frac{\int_{\Omega} \mathbf{v}(x,t) \boldsymbol{\phi}_m(x) dx}{\int_{\Omega} (\boldsymbol{\phi}_m(x))^2 dx} \quad (6.5.b)$$

In the snapshots method, by substituting Eq. (6.5.a) into Eq. (6.5.b) along with solving the eigenvalue problem with a positive definite Hermitian kernel, yields finding the temporal coefficient  $a_m(t)$  in the form of

$$a_m(t) = \frac{1}{\lambda_m} \int_T \left( \int_{\Omega} \mathbf{v}(x,t) \mathbf{v}(x,t') dx \right) a_m(t') dt' \quad (6.6.a)$$

Eq. (6.6.a) shows that  $a_m(t)$  as a sample of the temporal coefficient, is an eigenfunction of the integral operator on the time interval T with the spatial auto-correlation of  $\mathbf{v}(x, t)$  as a kernel. Correspondingly, the same substitutions can be expressed for the spatial POD mode  $\boldsymbol{\phi}_m(x)$  which forms as

$$\boldsymbol{\phi}_m(x) = \frac{1}{\lambda_m} \int_{\Omega} \left( \int_T \mathbf{v}(x,t) \mathbf{v}(x',t) dt \right) \boldsymbol{\phi}_m(x') dx' \quad (6.6.b)$$

Similarly, Equation (6.6.b) presents the spatial POD mode,  $\boldsymbol{\phi}_m(x)$ , as the eigenfunction of the integral operator on the spatial domain  $\Omega$  with the temporal auto-correlation of  $\mathbf{v}(x, t)$  as a kernel. Although, both equations are equivalent for solving the coefficients  $a_m(t)$  and POD modes  $\boldsymbol{\phi}_m(x)$ , snapshot method employs Eq.(6.6.a) for determining the POD coefficients first.



It should be mentioned that  $\lambda_m$  as the eigenvalue will be a real and positive value according to the Hilbert-Schmidt theorem (Mikhlin, 1957, for example). Thus the eigenfunctions are orthogonal which verifies the assumption of orthogonality of the POD coefficients and modes i.e. they are the solutions of Eq. (6.1). The eigenvalues are structured in a descending order as a convergent series according to their magnitude. Also, the eigenfunctions are usually normalized such that spatial POD modes are orthonormal and the coefficients, are square roots of the eigenvalues. Therefore according to Eq. (6.1) the fluctuating velocity field  $v(x,t)$  can be fully reconstructed from the eigenfunctions when  $N$  approaches infinity ( $N \rightarrow \infty$ ).

In the present study, the POD analysis is performed on the two components of fluctuating velocity fields and each individual eigenvalue represents the amount of the turbulent kinetic energy contribution of the corresponding mode to the total turbulent kinetic energy in a two-dimensional plane rather than the real value. Thus, the fractional contribution of  $i^{th}$  POD mode to the total turbulent kinetic energy can be expressed as  $k_i = \frac{\lambda_i}{\sum_{n=1}^N \lambda_n}$ . It has to be noted that the real value of each eigenvalue is twice the turbulent kinetic energy of the corresponding mode and thus the summation of the eigenvalues will be twice the total turbulent kinetic energy of the flow.

Finally, the discrete reconstruction of any given fluctuating field by using the first  $K$  POD modes at time  $t$  becomes

$$\mathbf{v}_{Rec}(x, t) = \sum_{n=1}^K a_n(t) \boldsymbol{\phi}_n(x) \quad (6.7)$$

In the present study, the number of snapshots (2000 for all the fields-of-view) is large enough for accurate estimation of the POD eigenfunctions and the computed eigenvalues will also be independent on the number of snapshots for sample size more than 1000 (Cazemier et al., 1998). Furthermore, to verify this, Figure 6.1 shows the variation of TKE contribution of the first six modes calculated for different numbers of snapshots in the mid-depth plane at low Reynolds number flow. All six modes confirm that the TKE value is independent on the sample size larger than 1000. In this study 2000 snapshots are used for the further analysis to be consistent with the number of FOV's used in the turbulence analysis.

## 6.2 Energy of the POD modes

Before discussing the spatial structure of the POD modes and the reconstructed velocity fields in different planes, the turbulent kinetic energy distribution of POD modes in different planes are discussed for both Reynolds numbers. Figure 6.2 shows the distribution of the turbulent kinetic energy percentage (TKE) contributed by each POD mode along with the cumulative TKE distribution (shown in the insets of Figure 6.2) for all horizontal planes. Since the modes with a rank larger than 100 have less than 1% contribution to the total TKE in each plane, they are not displayed. In Figure 6.2, the TKE content of individual POD mode at each horizontal plane is plotted for low and high Reynolds numbers. For all horizontal planes, the percentage of the TKE for each mode is higher at low Reynolds number, while a reduced amount of energy is observed at high Reynolds number. This is consistent with the fact that at high Reynolds number more of the TKE energy becomes available to the small scales that are represented by the higher rank modes. In contrast, at low Reynolds number larger fraction of the TKE is distributed among the lower rank POD modes associated with the large coherent structures.

In Figures 6.2.a and 6.2.c, it is noticeable that the first two POD modes are the most energetic modes for both Reynolds numbers at mid-depth and near-free surface planes. In contrast, the contribution of the first two modes to the total TKE is considerably less at near-bed plane for both Reynolds numbers as shown in Figure 6.2.b. At low Reynolds number, Mode 1 and Mode 2 contribute 21% and 18% of TKE at mid-depth plane, while at high Reynolds number these values are reduced to about 13%. The TKE contribution decreases rapidly with increasing mode number, and for Mode 3 it becomes 4% and 3% for low and high Reynolds numbers, respectively. The contribution of Mode 4 and higher rank modes is less than 3% for both Reynolds numbers. In theory, large-scale flow structures are represented by the lower decomposition modes, whereas small-scale flow structures are captured in higher modes. In practice, experimental errors tend to dominate at higher modes, rendering them to be corrupted by noise. To account for this, a threshold criterion was suggested by Epps and Techet (2010) to check the validity of the POD modes. For the present analysis, the threshold criterion of the acceptable TKE of the modes is found to be about 2% based on 2000 time steps and  $127 \times 127$  velocity vectors for the region of interest in the field-of-view in a conservative

estimation. This criterion suggests that POD modes larger than 6 or 7 could be potentially corrupted by noise.

To further validate the POD decomposition, the energy of the POD modes reported by Perrin et al. (2007) was compared with the present results. They analyzed two-dimensional near-wake flow behind a circular cylinder at  $Re_D = 140,000$  and reported that modes 1 and 2 contain more than 25% of the total TKE while the rest of the modes contain less than 6%. This is consistent with the results of the present study. Our results are also, consistent with the studies of Wang et al. (2014) and Oudheusden et al. (2005) who investigated two-dimensional wake behind a square cylinder. In the latter case, modes 1 and 2 possess near 37% and 32% of the TKE compared to the high-order modes. Since the dominant structures in the near-wake region are the alternate vortex shedding it is suspected that less energetic higher modes do not influence the large scale vortices but rather they are reminiscence of the small scale structure generated from the bed.

At near-free surface plane, shown in Figure 6.2.c, the TKE distribution of the modes is qualitatively similar to that of the mid-depth plane. The first two modes account for 55% (29% for Mode 1 and 26% for Mode 2) and 30% (15% for Mode 1 and 15% for Mode 2) of the cumulative TKE at low and high Reynolds numbers, respectively. Both cases show significantly larger contribution share than their counterparts in the mid-depth plane (39% and 26%).

In the near-bed plane, modes 1, 2 and 3 account for 7%, 6% and 5% of the total TKE at low Reynolds number flow as shown in Figure 6.2.b. These values become reduced to 4%, 3% and 3% at high Reynolds number flow. The modal contribution of TKE profiles decreases gradually with increasing mode rank in both cases, which shows that higher-order modes are containing noticeable TKE in the flow in this plane. This suggests that in the near-bed plane, the TKE energy is redistributed towards the higher modes or smaller scales. The complexity of the flow in the near-bed plane is also reflected by the fact that in order to resolve 50% of the TKE, more than 50 modes are needed, while less modes are sufficient to capture the same amount of TKE in the mid-depth and near-free surface planes. Similar trend in TKE distribution has been observed

in the near-bed plane ( $z/D = 0.1$ ) by Wang et al. (2014) for the tripped turbulent boundary layer flow passing a square cylinder.

### 6.3 POD modal shapes

In the near-wake region, different types of coherent structures are expected to be manifested. The most well-known vortical structures are the shear layers and von Kármán vortices, while in the bed region where the junction flow occurs, the base vortex and horseshoe vortex set structures accompany them, as shown in Figure 2.3 (Sumner et al., 2004 and Wang and Zhou, 2009).

While the POD modes are not representative of the actual coherent structures, they do provide a qualitative picture of the dominant flow features associated with each mode and its variability from one mode to another. The interest here is to study the shapes and variability of the POD modes which provide spatial distributions of the most energetic dominant flow structures associated with each mode. In the present study the first four most energetic POD modes of LR and HR cases are examined in terms of the normalized streamwise velocity ( $U^* = \frac{U_\phi}{U_S}$ ), spanwise velocity ( $W^* = \frac{W_\phi}{U_S}$ ) and vorticity ( $\omega^* = \frac{\omega}{U_S/D}$ ) contours for each horizontal plane. Here  $U_\phi$  and  $W_\phi$  are the streamwise and spanwise velocities for the POD modes, respectively. It should be noted that although vorticity is defined based on the curl of the velocity vector field, here in a two-dimensional velocity field the normal to plane component of vorticity is considered as  $\omega = \frac{\partial U_\phi}{\partial z} - \frac{\partial W_\phi}{\partial x}$ . The vortical structures are discussed in terms of the spatial orientation of  $U^*$ ,  $W^*$  and  $\omega^*$  contours of the POD modes (eigenfunctions) in each plane. In order to clearly visualize the spatial variation of the POD modes, the contours in forthcoming figures are plotted in non-uniform level since the values are in different orders of magnitude for each mode.

Contour plots in Figures 6.3 and 6.4 display the first four modes of  $U^*$ ,  $W^*$  and  $\omega^*$  in the near-wake region at mid-depth plane for LR and HR cases, respectively. The first glimpse shows almost symmetrical shape of modes 1 and 2 with respect to the  $x$ -axis at all plots in the first two rows of Figures 6.3 and 6.4, although variation in the sign of

$U^*$  contours is observed. The symmetric shapes of these POD modes are detached from the rear surface of the cylinder and concentrated at  $x/D > 1.0$ . These two modes are linked to the von Kármán wake vortices shed from the alternate sides of the cylinder and convected downstream. The alternate opposite signs of the POD spanwise velocity observed in Modes 1 and 2. Similar shapes of Mode 1 and 2 were reported by Wang et al. (2014) in their POD analysis of the wake behind a square cylinder. The first two streamwise POD modes always form a conjugate pair showing a phase shift of  $90^\circ$  which could be related to the phase shift of the vortex shedding cycles. Any such pair of modes, phase shifted by a quarter cycle, have been termed as regular modes according to Sengupta et al. (2010). This could be due to the phase shift for vortex shedding cycles. Similar shift of spanwise velocity of Modes 1 and 2 is also noted as shown in Figures 6.3.b and 6.3.e. It should be mentioned that the average wave length of the vortex motion can be determined from the alternating shapes of the POD modes as discussed by Tang et al. (2015). As indicated in Figures 6.3.a and 6.3.d, the average wave length is found to be about  $3D$  and  $3.4D$  for the first and second modes, respectively for LR case. The shift between the alternate centers of the two modes is found to be about  $(3/4)D$  in longitudinal direction which corresponds to  $0.24$  phase shift in vortex shedding cycle. For HR case, the average wave length for the first and second modes is almost equal and estimated to be  $\sim 3D$  while the shift in vortex shedding cycle for Modes 1 and 2 was  $0.26$ . Similar phase shift of  $1/4$  is also reported by Wang et al. (2014) for the wake behind the square cylinder.

In Figures 6.3.c, 6.3.f and 6.4.c, 6.4.f, vorticity plots of the first two modes are alternately arranged in streamwise direction, showing the signature of the convection of the generated vortices on both sides far from the cylinder. Tang et al. (2015) have shown similar patterns of the first two POD modes obtained from vorticity-based POD decomposition in the near-wake region behind a circular cylinder. In the mid-depth plane, examination of the shapes of the first pair of POD modes suggests a strong link with the von Kármán wake vortices that appear to dominate the flow in this region for both Reynolds numbers.

Mode 3 of  $U^*$  and  $W^*$  velocity distributions shown in Figures 6.3.g, 6.3.h, 6.4.g, and 6.4.h present very different spatial organization than Modes 1 and 2. Since the energy

in these modes is smaller, this difference can be attributed to a different type instability or coherent structure. Contrary to Modes 1 and 2, the contours of Mode 3 start immediately behind the cylinder ( $x/D = 0$ ) and extend longitudinally in streamwise direction.  $U^*$  velocity contours of Mode 3 are symmetric with respect to the wake centreline and merge with each other at  $x/D \approx 2.5$ . The physical interpretation of Mode 3 may be attributed to the manifestation of the separated shear layers (SSL) along the sides of the cylinder and their longitudinal expansion further downstream. The vorticity contours of the third mode shown in Figures 6.3.i and 6.4.i better illustrate the shear layer extension in the near-wake region. They show dual contour distribution on each side of the cylinder which terminate after almost  $2D$ . The latter is in agreement with the shear layer length at low Reynolds number flows ( $350 < Re_D < 3000$ ) reported by Prasad and Williamson (1997). They have also reported similar extension of the shear-layer instability behind the cylinder.

Similar  $U^*$ ,  $W^*$  and  $\omega^*$  contours for the first, second and third POD modes have been reported by Kourentis and Konstantinidis (2012) for their wake flow behind a cylinder. Ma et al. (2003) has also presented similar contour shapes for their most energetic POD modes obtained from experiments and direct numerical simulations for the natural wake behind a circular cylinder. The qualitative observation for the first two modes is consistent with van Oudheusden et al. (2005) study of wake behind a square cylinder. In the recent study, Tang et al. (2015) reported that vorticity-based POD analysis is more effective than velocity-based POD for the near-wake region. In the present study, velocity-based POD depicts similar spatial distributions of the POD modes in the near-wake region as the ones observed by Tang et al. (2015).

Mode 4 contours of  $U^*$ ,  $W^*$  and  $\omega^*$  are shown in the last row of Figures 6.3 and 6.4 for LR and HR, respectively which contain about 3% of the total kinetic energy. It is observed that the shape of contours in Mode 4 depends on the Reynolds number. At HR, the shape of contours in the plots of Mode 4 resembles the corresponding of Modes 1 and 2 with the appearance of alternating patterns of  $W^*$  velocity contours. At LR case, other harmonic of von Kármán vortices make the physical interpretation of Mode 4 dubious. As observed in Figure 6.3.j,  $U^*$  contour distribution of Mode 4 appears just behind the cylinder with highest magnitude at  $x/D \approx 2.5$  which can be a representative of the existence of shear layer-like structure. Also, in Figure 6.3.k, the  $W^*$  contours of Mode 4

show some circular patterns consistent with the appearance of the wake vortices at  $x/D > 1$ . Further observation of the vorticity plot of Mode 4 (see Figure 6.3.1), indicates two extended contour concentration sets on the sides of the cylinder along with one contour set centered at  $x/D \approx 2.5$  on the axis of symmetry. This observation suggests that Mode 4 in the LR flow represents a combination of shear layer instability and existence of the vortex formation in the near-wake region.

For the near-free surface plane,  $U^*$ ,  $W^*$  and  $\omega^*$  contour plots of the first four POD modes are displayed in Figures 6.5 and 6.6 for LR and HR cases, respectively. The symmetrical distributions of the first three modes about the wake centreline are very similar to the ones observed in the mid-depth plane. Contours of Modes 1 and 2 imply that the flow is influenced by the same features as already discussed for the mid-depth plane for the corresponding pair of modes. In the near-free surface plane, the average wave length for LR flow is estimated to be  $\sim 3D$  for Modes 1 and 2 with the phase shift of vortex shedding cycle equal to 0.24. For HR case, the average wave length is evaluated to be near  $3D$  and  $3.2D$  for Modes 1 and 2, respectively. The phase shift in vortex shedding cycle is determined to be 0.23. Finally, it can be concluded that in this plane similar to mid-depth plane, the first two modes is ascribed as the von Kármán street vortices for both Reynolds numbers.

The contour plots of third POD mode shown in the third row of Figures 6.5 and 6.6 are similar to the corresponding plots at mid-depth plane. Mode 3 can be considered as the manifestation of the shear layers instability and their longitudinal extension in the flow. Similar shear layer instability can be seen in Mode 4 which is formed on both sides of the cylinder. The distribution of the first four POD modes suggests little effect of the Reynolds number. The free surface effect at HR flow is expected to be observed for higher rank POD modes. Their contribution in the reconstructed velocity field is discussed in Section 6.5.

The first four POD modes in the near-bed plane are shown in Figures 6.7 and 6.8 for at LR and HR flows, respectively. The spatial distribution of the POD modes at the near-bed plane is more complex compared to the other horizontal planes due to the influence of the bed. Two main large vortex structures, horseshoe vortex and base vortex, associated with the junction flow are expected to influence the flow in the near-bed plane

behind the cylinder. A schematic of these vortices is shown in Figure 2.3. It is expected that the imprint of these vortex structures is influencing the spatial distributions of the POD modes at different flow conditions.

For the LR flow, the first and the second modes in Figure 6.7 exhibit almost similar  $U^*$ ,  $W^*$  and  $\omega^*$  spatial distributions. The first pair of modes has symmetric contours with respect to the wake centreline. The spatial distributions of  $U^*$ ,  $W^*$  and  $\omega^*$  of the first two modes are concentrated near the cylinder ( $x/D < 1.5$ ) while at downstream the  $U^*$  and  $\omega^*$  contours are stretched in streamwise flow direction. The spatial distributions of the first pair of modes in the near-bed plane did not show any repeating patterns resembling these observed at mid-depth and near-free surface planes. This leads to the inference that the modes are not associated with the von Kármán vortex structures in the near-bed plane. While change of sign is noted for  $U^*$  and  $W^*$  distributions of the second mode, the shapes of these distributions are qualitatively similar to Mode 1 making the two modes phase shifted or regular. Since the wake Reynolds number in the present LR case is 900, following Lin et al. (2003) and Kirkil and Constantinescu (2012), streaks of rotational fluid were regularly detached from the legs of a steady laminar horseshoe vortex system and they are advected in the horizontal plane away from the wake centreline. The elongated regions of the  $U^*$  contours of Modes 1 and 2 in Figures 6.7.a and 6.7.d coincide with the region of horseshoe legs where the interaction of SSL and horseshoe leg was observed by Kirkil and Constantinescu (2012). It is hypothesized that the velocity and vorticity POD mode distributions resemble two different energetic vortex structures, base vortex and horseshoe vortex legs.

At the HR flow, the first two modes display very different distributions compared to the LR flow case. At HR flow, the energy distribution is shifted towards the smaller scales which could explain the difference in the spatial distributions of the POD modes. The near-bed plane is located in the logarithmic layer ( $y^+ = 110$ ) where the hairpin vortices interact with the cylinder's wake creating highly energetic and less coherent small scale structures. These small scale energetic structures were advected in the wake as observed in the velocity and vorticity plots of first and second modes shown in Figure 6.8. In these plots, Modes 1 is asymmetric while Modes 2 and 3 are symmetric with long contours extending behind the cylinder. Mode 3 of  $U^*$ ,  $W^*$  and  $\omega^*$ , shown in Figures 6.7



and 6.8 represent similar flow feature related to the shear layer instabilities as discussed for Mode 3 in the mid-depth plane. It appears that while near the bed the shear layers are concentrated behind the cylinder, they are shorter (less than 1D) at HR flow compared to LR case. The short shear layers indicate higher bed suppression effect on the coherent structures at HR flow. The physical interpretation of Mode 4 in Figure 6.7 is not as clear as other modes since the contour distribution in all corresponding plots are completely asymmetric. A possible interpretation of Mode 4 can be expressed as combined effect from the shear layers, base vortex and horseshoe vortex. In contrast, the contour plots of Mode 4 in Figure 6.8 are almost symmetric with respect to the wake centreline and it is similar to Mode 3.

The inconsistencies associated with the POD modes in the near-bed region and their dissimilarity for both Reynolds number cases require further investigation. In particular, the strong energy content of the fluctuations of the base shallow flow at HR could potentially affect the shape and distributions of the POD modes. For HR, the wake flow structure at near bed plane might be masked by the strong fluctuations existing in the approaching shallow flow. Thus, it is possible that the structure of the wake is misrepresented when the entire horizontal field-of-view with size  $10D \times 10D$  and  $14D \times 14D$  is used in the analysis of POD modes for LR and HR, respectively. It might be more meaningful to employ POD analysis confined to the region of the wake in order to isolate any difference in the base flow structure between the different flow cases. This analysis is presented in the following section.

#### **6.4 Effect of the bed on the structures of the near-wake region**

To further investigate the effect of the bed on the structures in the near-wake region, the same POD analysis was carried out but this time only focusing on the near-wake region in the near-bed plane. For this purpose, the POD analysis was applied as similar as the previous section, but the FOV was reduced to the near-wake region only -  $0.5 < x/D < 5.5$  in the streamwise and  $-2.5 < z/D < 2.5$  in the transverse directions. The energy of the POD modes was reevaluated and the TKE cumulative energy content for both Reynolds numbers is shown in Figure 6.9. The TKE content of the first 4 POD modes for the reduced field-of-view is higher at low Reynolds number while a reduced

amount of energy is observed at high Reynolds number. Similar trend was observed for the full-field POD modes as discussed in the previous section. One important difference in Figure 6.9 is the smaller number of POD modes necessary to recover 50% of the TKE in the near bed plane. This again provides the evidence that the energy of the base shallow flow in the near bed plane of the full-field POD modes dominates the energy contained in the wake region.

In Figures 6.10 and 6.11 results from the POD procedure for the reduced field-of-views for LR and HR flows are shown. The mode shapes for LR flow appear to be qualitatively the same as the mode shapes of the full-fields shown in Figure 6.7. The only difference between the POD modes (i.e. full-field versus reduced) is that the first mode of the reduced field POD appears to be a combination between Modes 1 and 2 of the full-field POD. While the second mode in the full-field POD seems to be a harmonic of Mode 1 and they both represent similar structure, in the reduced POD analysis the amount of energy is limited to only one mode for the same structure. As such, there is no change of the spatial distributions of  $U^*$ ,  $W^*$  and  $\omega^*$  of the reduced POD modes. The reduced POD analysis results in a shift of the order of the lower POD modes. For example, Mode 5 in a full-field POD (not shown in Figure 6.7) becomes Mode 4 in the reduced POD. The shift in the mode order indicates less effect of the energy of the shallow base flow on the wake coherent structures at LR flow.

While the first two dominant modes are symmetric, Modes 3 and 4 are antisymmetric and seems to represent different phases of the interactions of the SSL with junction structures in the wake. Higher near jet like flow is observed along the sides of the cylinder in the reduced field POD Modes 3 and 4 which alternate periodically. These features could be a signature of the interaction of the SSL with the coherent structures in the junction flow. A similar interaction between the horseshoe corner vortex and the SSL is reported by Kirkil and Constantinescu (2012).

The effect of the shallow base flow becomes stronger for the HR flow as seen in Figure 6.11. In this figure the POD modes of the reduced field show very different shapes and spatial distributions compared to the full-field POD shown in Figure 6.8. The reduced field POD modes at HR also differ significantly from that of the LR flow. This indicates the non-universal effect of the bed and the complex vertical variability of the

dominant structures in the near-bed wake. When compared to the LR flow, different physical interpretation of the reduced field POD modes can be drawn for the HR flow, particularly regarding the junction vortex structures and its influence on the vortex shedding. The following discussion is intended to address these effects.

As observed in Figure 6.11, for the HR flow, the most energetic reduced field POD mode (Mode 1) is symmetric and attached to the cylinder suggesting a relation to the separated shear layer (SSL) instabilities originating from the sides of the cylinder. Modes 2, 3, and 4 are all symmetric with respect to the wake centerline and their spatial distributions resemble the onset of the periodic vortex shedding. A similar observation is reported by El Hassan et al. (2015) in the wake region for the case of wall-mounted square cylinder for the tripped (thick) boundary layer in the  $y/D = 0.1$  plane. The following differences are observed by comparing the spatial distribution of the POD modes associated with the von Kármán vortex street of the mid-depth plane shown in Figure 6.4, with the reduced POD modes shown in Figure 6.11: (i) The spanwise extent of  $U^*$  and  $\omega^*$  modes in the near-bed plane are bounded by  $z/D \approx \pm 1.5$  while this extent is near  $2D$  in the mid-depth plane. (ii) Mode 2 in the reduced field POD in the near-bed plane is limited to  $x/D \approx 3$  in the  $\omega^*$  plot in Figure 6.11.f. This is different from the  $\omega^*$  plot of the first mode in the mid-depth plane shown in Figure 6.4.c. These differences indicate the bed suppression effect on the von Kármán vortex structures near the bed for the HR case.

One should note that the present results are reduced only to the near-wake region and no information is available for the upstream interaction with the cylinder where the HVS is located.

## 6.5 Eduction of large-scale structures by POD reconstructed velocity field

The reconstructed velocity vectors based on the full-field POD modes show the features of the energetic coherent structures in the physical space. This information is hidden in the instantaneous velocity fields shown in the first column of Figures 6.12 and 6.13 due to the presence of multiple structures moving with different convection velocities. In the present study, since the POD modes of the near-free surface plane are

similar to the mid-depth plane for both Reynolds numbers the POD reconstruction of velocity field is focused on the mid-depth plane at LR. Also, the POD reconstruction of velocity field is focused on the LR case in the near-bed plane as the junction flow structures in the near-bed plane keep their coherence at lower Reynolds number. The first three POD modes are used for reconstruct the fluctuating velocity fields, since they contain the highest TKE contribution and as such are representing the most energetic coherent structures in the near-wake region in the mid-depth and near-bed planes.

Figures 6.12 and 6.13 illustrate the instantaneous and reconstructed velocity field in the mid depth and near-bed planes, respectively for LR case. In Figures 6.12 and 6.13, for clarity in the vector field different vector resolutions are adapted. Although the plots in each row correspond to a specific time, the plots in columns are not correlated and are selected randomly. The original instantaneous velocity vectors are presented in the first column of Figures 6.12 and 6.13, which has been discussed earlier in Chapter 5. These plots are used here to better comparison of the features of the reconstructed instantaneous velocity vectors with the original one.

Since the first and second modes in the mid-depth plane refer to the formation of von Kármán street in the near-wake region, the reconstructed velocity field can depict the velocity pattern for this structure. The middle column of Figure 6.12 refers to the Galilean decomposition of the reconstructed instantaneous velocity vectors based on these modes. The Galilean decomposition is used to subtract the convection velocity from every instantaneous vector. At mid-depth plane, after trying different values for the convection velocity, the best convection velocity value is determined to be 0.9 of the mean velocity value for each point in the flow field. As noticed in the middle column of Figure 6.12, the velocity vectors show strong clockwise (CW) and counter clockwise (CCW) swirling motions starting at almost  $2D$  behind the cylinder with large velocity vectors compared to the velocity vectors on the sides of the cylinder. The core of the swirling patterns are located almost on the axis of symmetry while in the farther downstream locations  $x/D > 3.5$  it is dislocated in the span of  $-0.5 < z/D < 0.5$ . The shape of these swirling patterns are circular and elliptical, with the spanwise diagonal length larger than the length in the streamwise direction.

The right column of Figure 6.12 shows the Galilean decomposition of the reconstructed instantaneous velocity vectors based on Mode 3. Again the convection velocity value is  $0.9U_s$ . The first view on right column of Figure 6.12 indicates the symmetry flow pattern along the axis of symmetry for the whole field-of-view. As observed in Figures 6.12.c and 6.12.i, a set of CW and CCW swirling motion starts at location almost  $2D$  from the cylinder, which confirms the role up motion of the SSL instability. It is worth mentioning that as these stretched swirling patterns located at  $z/D \cong \pm 0.6$  are different from the ones observed in the middle column. In Figure 6.12.f the velocity vectors does not show any swirling pattern where the SSL formed on either side of the cylinder meet each other on the axis of symmetry at  $x/D \sim 2.0$ . These two types of velocity vector patterns indicate different states of instability of the shear layers in the flow.

As discussed previously in Section 6.3, the first and second modes at near-bed plane refer to the effect of the junction vortex structures, while Mode 3 indicates the shear layer influence on the near-wake region. The middle and right columns of Figure 6.13 illustrates the Galilean decomposition of the reconstructed instantaneous velocity fields based on the first two modes and Mode 3, respectively; while the convection velocity value is determined to be 0.8 of the mean velocity.

As observed in Figure 6.13.b, 6.13.e and 6.13.h, the velocity vectors pattern behind the cylinder show a strong sweeping motion from one side to another. This sweeping pattern starts just behind the cylinder with large velocity vectors and decays at  $x/D \sim 2.0$ . Such velocity pattern can be the signature of base vortex structure. The sweeping motion could explain the findings by Kirkil et al. (2008) for the scour hole development behind the cylinder and deposition of sediment particles on the sides of cylinder.

The velocity vectors in the third column of Figure 6.13 resemble the velocity pattern in Figure 6.12.f. The difference can be noted as the shorter length of the shear layers compared to the mid-depth plane since the velocity vectors on either side of the cylinder meet each other on the axis of symmetry at  $x/D \sim 1.0$ . As the bed suppresses the shear layer development, the length of the shear layers is shortened and no swirling motion is observed.

## 6.6 Conclusion

In this chapter, proper orthogonal decomposition (POD) technique is applied on the fluctuating velocity fields of the near-bed, mid-depth and near-free surface planes for both Reynolds numbers to study the most energetic large scale coherent structures in the near-wake flow. The spatial distributions of the most energetic POD modes (eigenfunctions) were investigated as they provide qualitative picture of the dominant flow features associated with each mode and its variability from one mode to another. The findings are summarized as follows:

- The wake region is found to contain different large energetic coherent structures in various vertical locations for both Reynolds numbers. In the mid-depth and near-free surface planes the most energetic modes are attributed to the von Kármán vortex structures and the SSL instability which appear for both Reynolds numbers. No significant difference in the shape of the POD modes is noticed between the LR and HR flows at mid depth and near free surface planes.
- The effect of the base shallow flow in the near bed plane shifts the distribution of TKE content among the POD modes, particularly for the HR flow. In order to isolate any difference in the base flow structure between the different flow cases, a reduced POD analysis is employed confined only to the region of the wake.
- In the near-bed plane, the shape of the velocity and vorticity contours of the first four modes in the reduced field POD differs from that of the full-field POD. This is due to the exclusion of large contribution of the base shallow flow in the POD analysis and its effect on the TKE distribution.
- For the LR flow, in the near-bed plane, the first modes are attributed to the junction flow structures (base vortex and horseshoe vortex structures) and the SSL instability. For the HR flow, these high energetic modes are associated with the von Kármán vortex structures and the SSL instability at this plane. Thus, the dominant coherent structures near the bed are highly affected by Reynolds number.
- It can be concluded that at HR flow, the formation of the von Kármán vortex structures appears closer to the bed compared to the LR flow. At HR flow, the onset of the von Kármán vortex structures was identified closer to the rear side of the

cylinder with spatial extent in both spanwise and streamwise directions smaller compared to the mid-depth plane. This change in the location and size is attributed to the bed suppression effect on the wake flow.

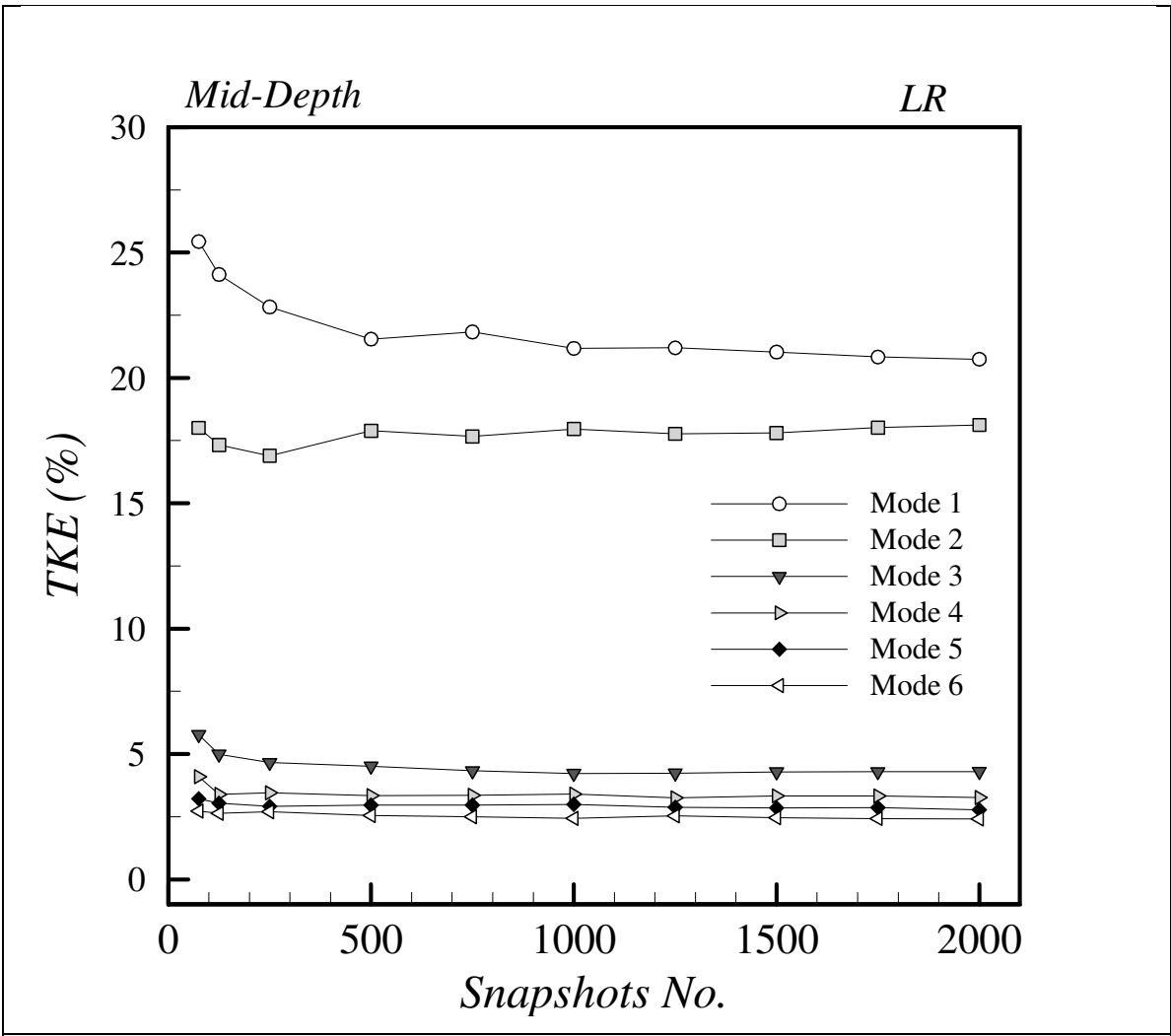


Figure 6.1: The number of snapshots effect on the contribution of TKE (%) of the first six modes



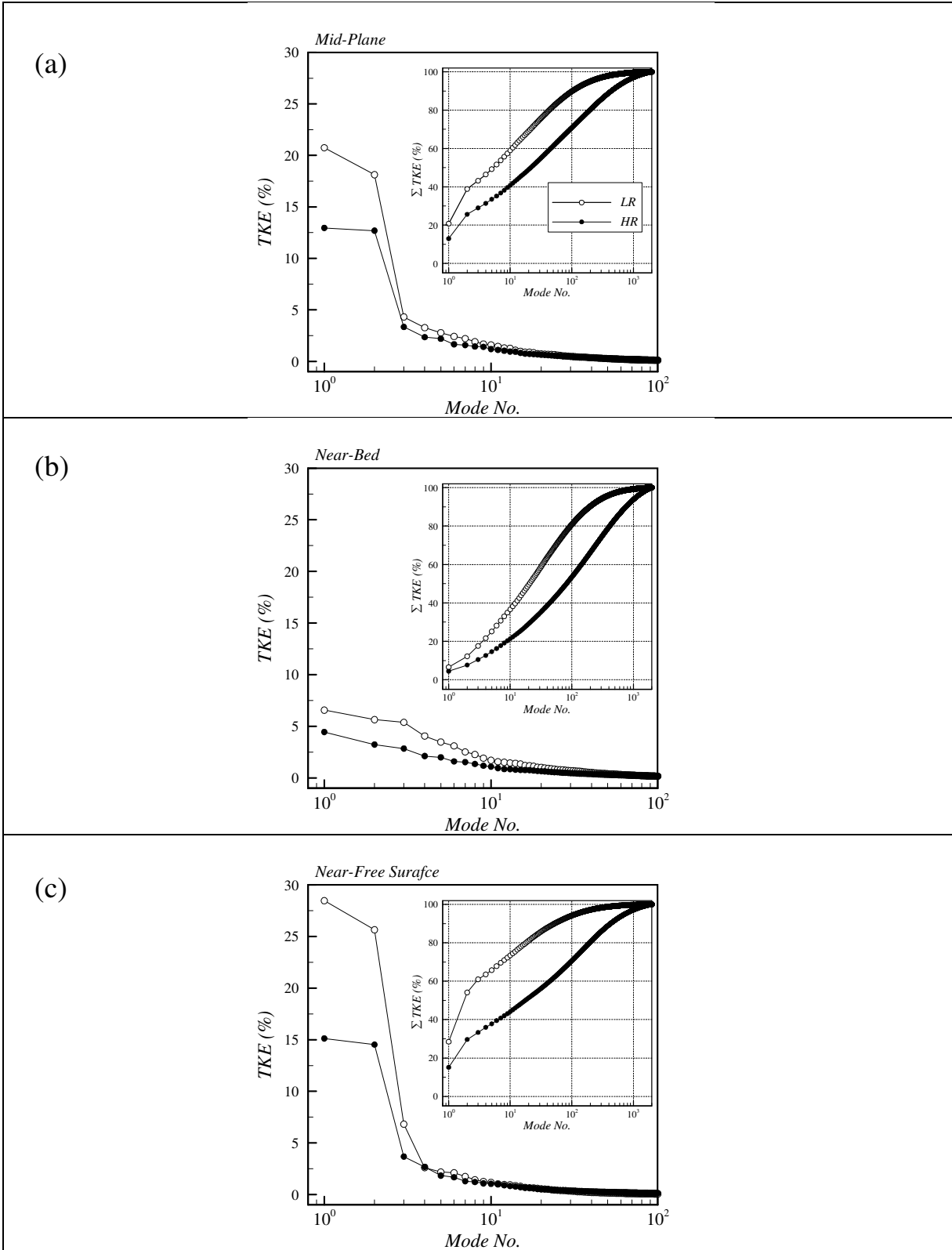


Figure 6.2: Turbulent kinetic energy (TKE) and their cumulative profiles for different POD modes at different horizontal planes at mid-depth (a), near-bed (b) and near-free surface (c)

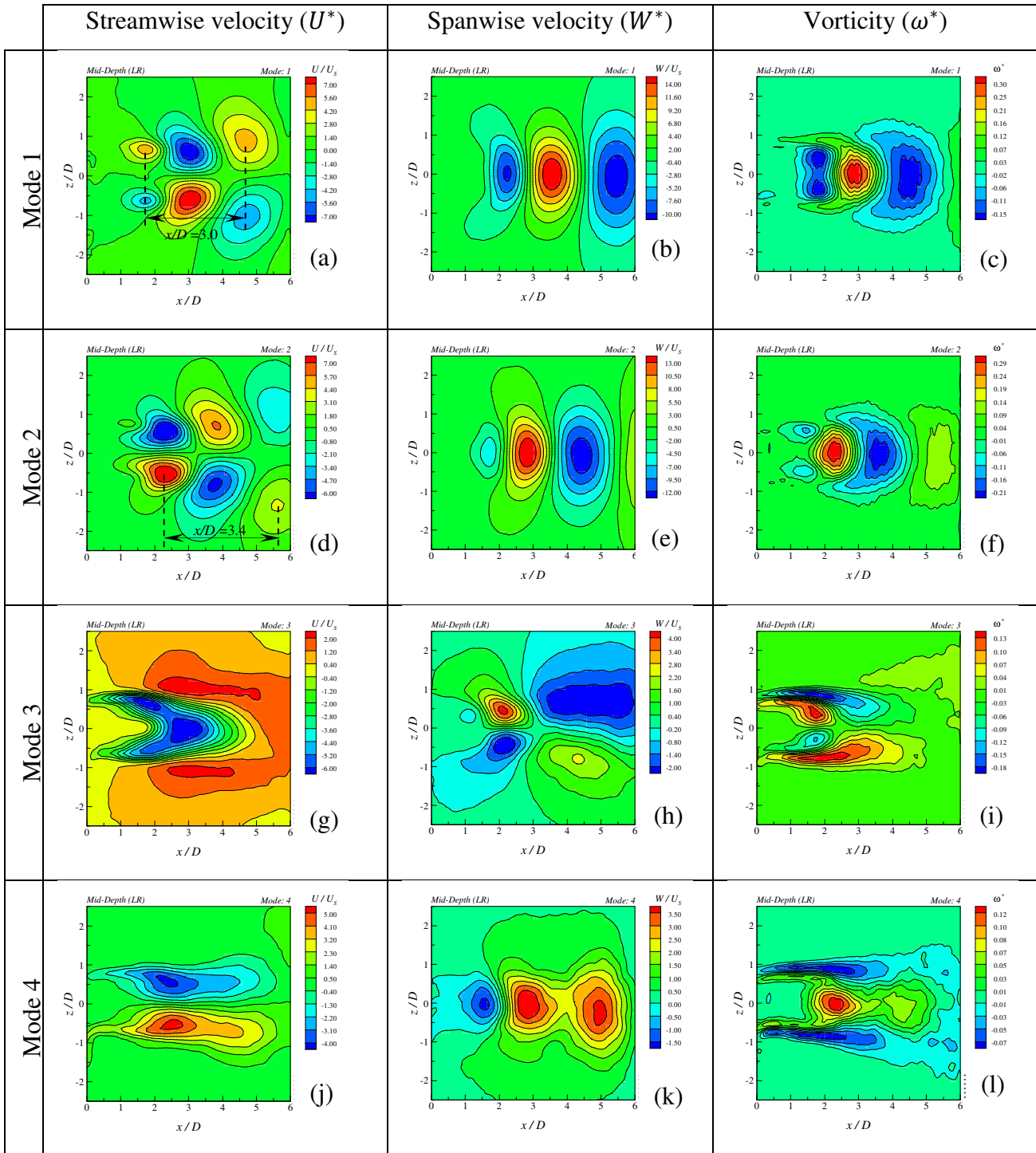


Figure 6.3: Spatial POD modes in the mid-depth plane for LR in the form of normalized contours

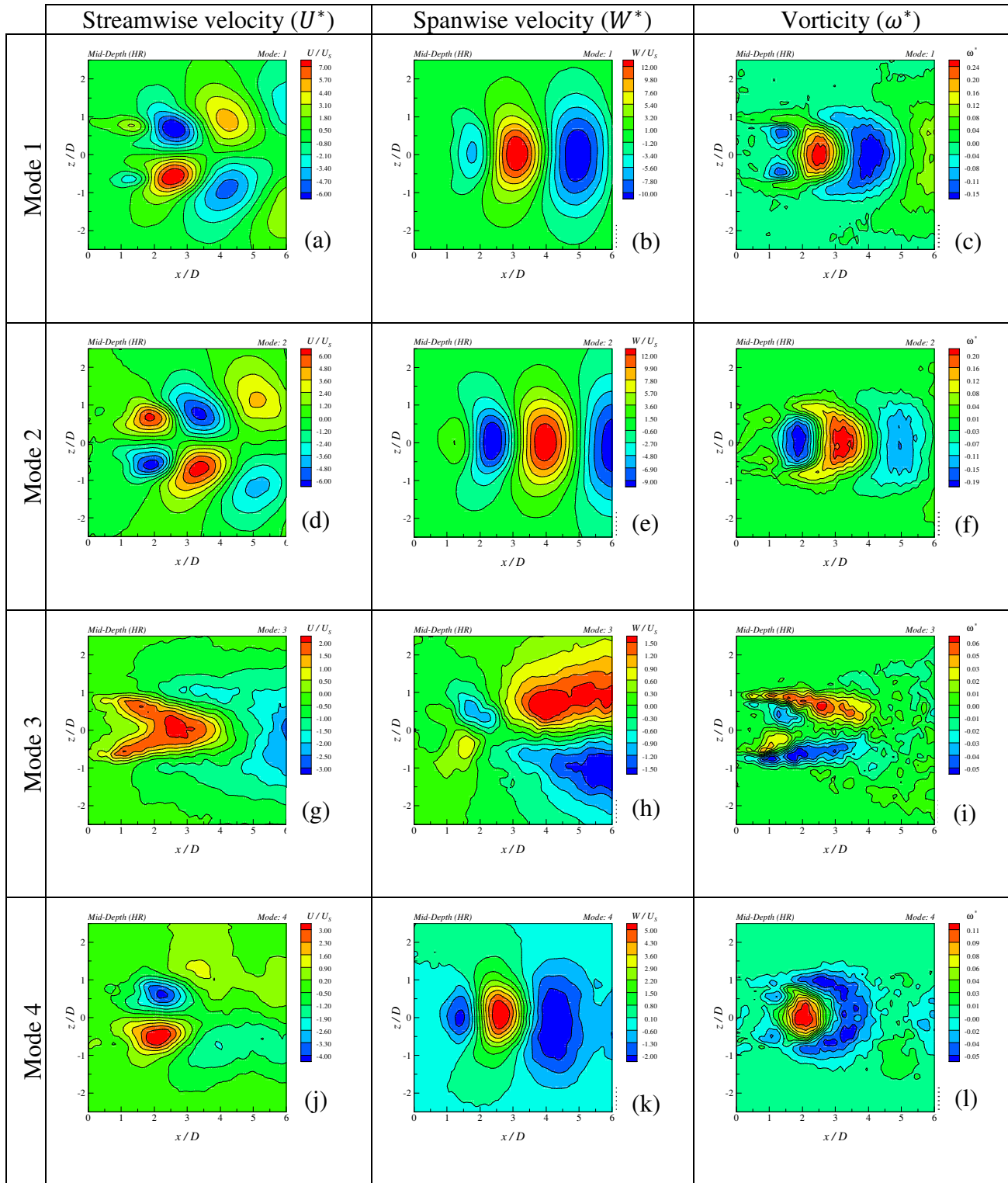
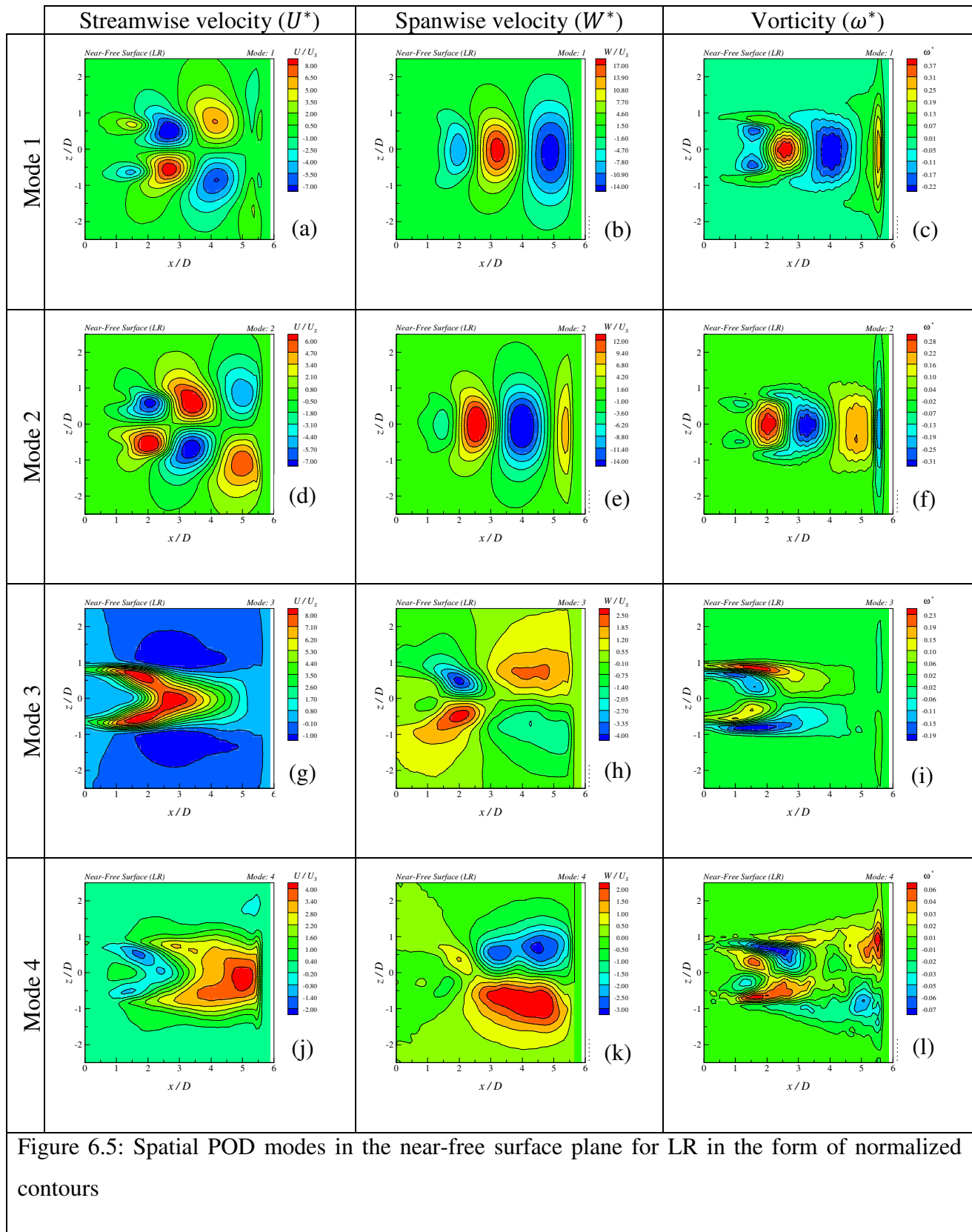


Figure 6.4: Spatial POD modes in the mid-depth plane for HR in the form of normalized contours



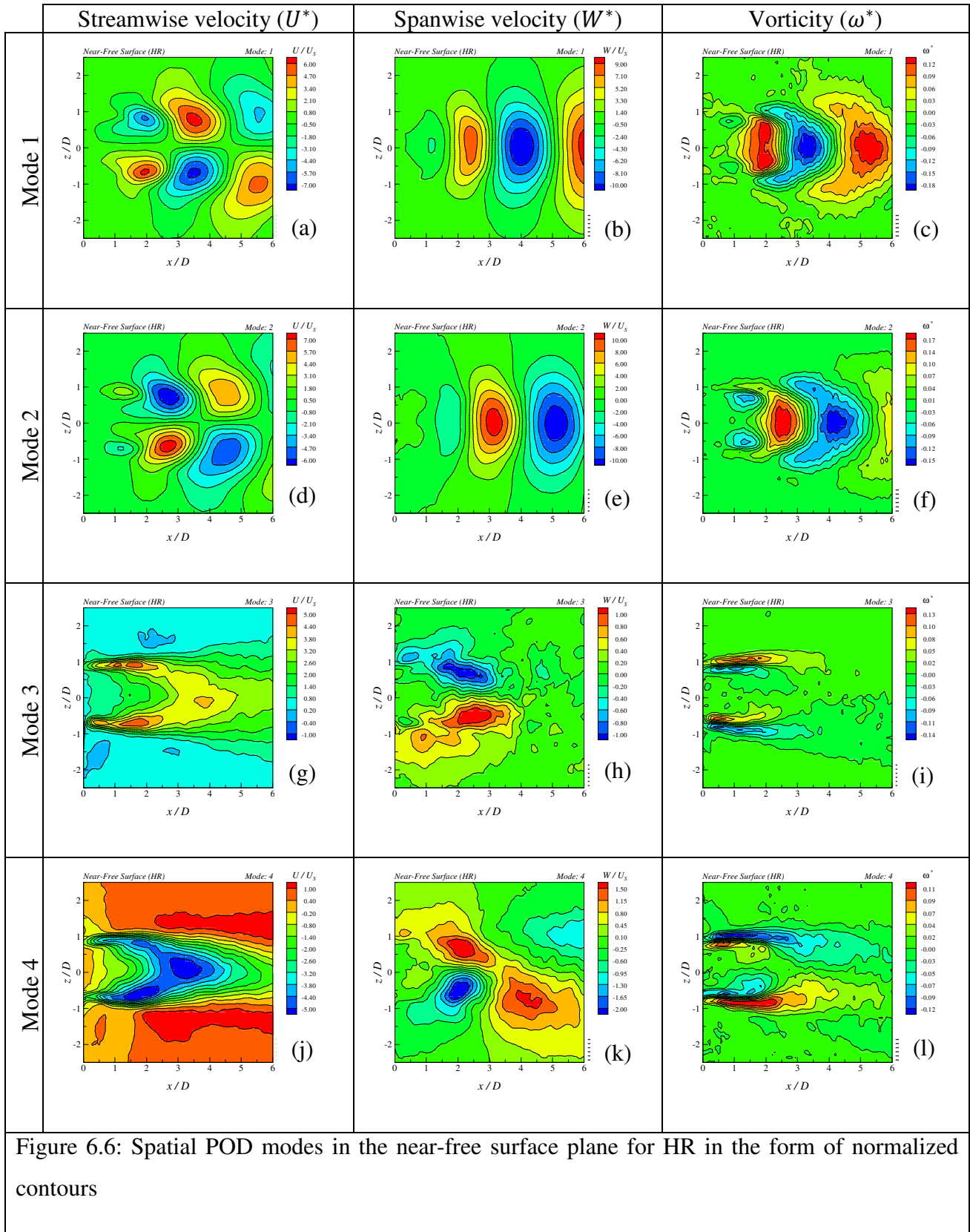


Figure 6.6: Spatial POD modes in the near-free surface plane for HR in the form of normalized contours

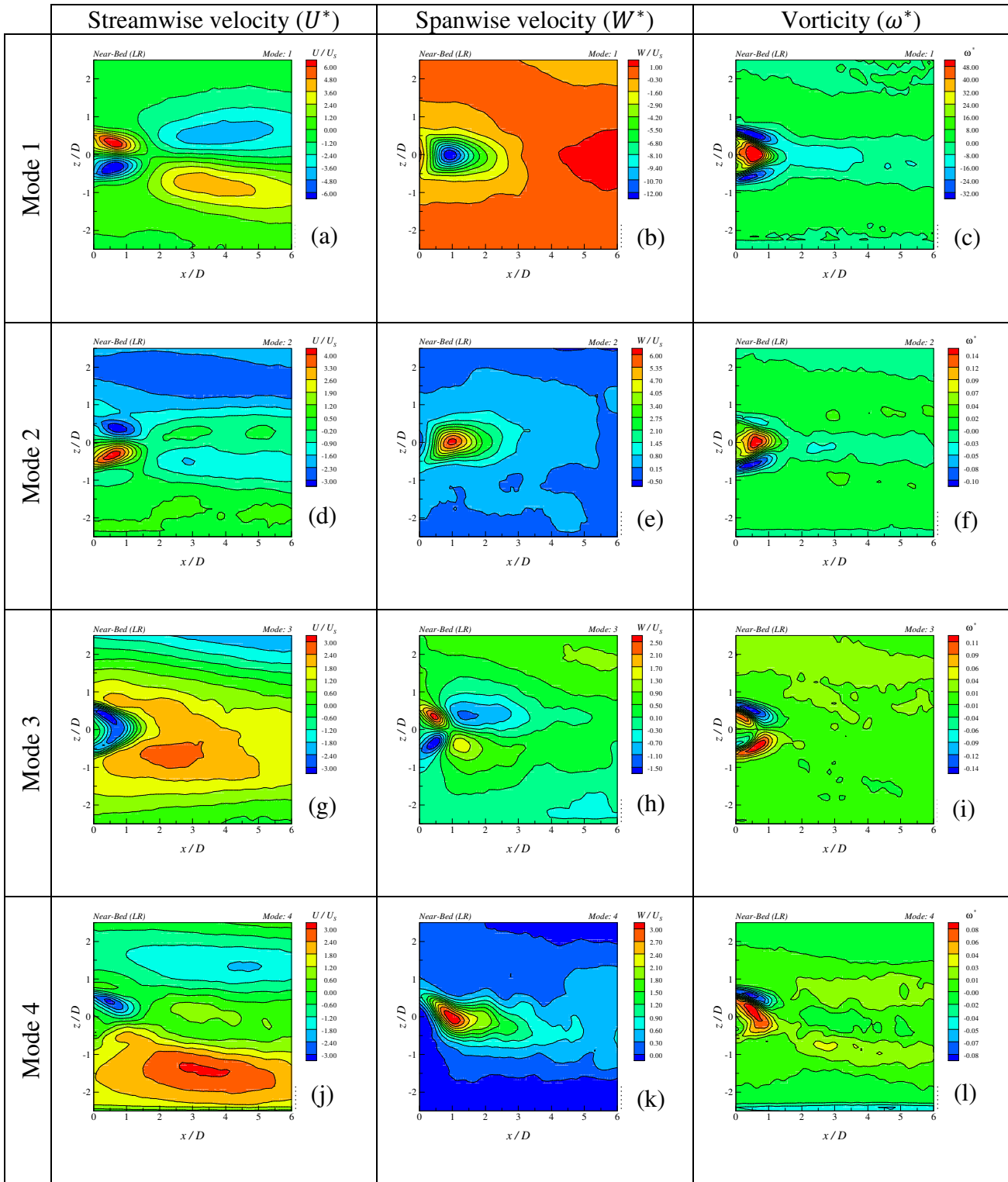


Figure 6.7: Spatial POD modes in the near-bed plane for LR in the form of normalized contours



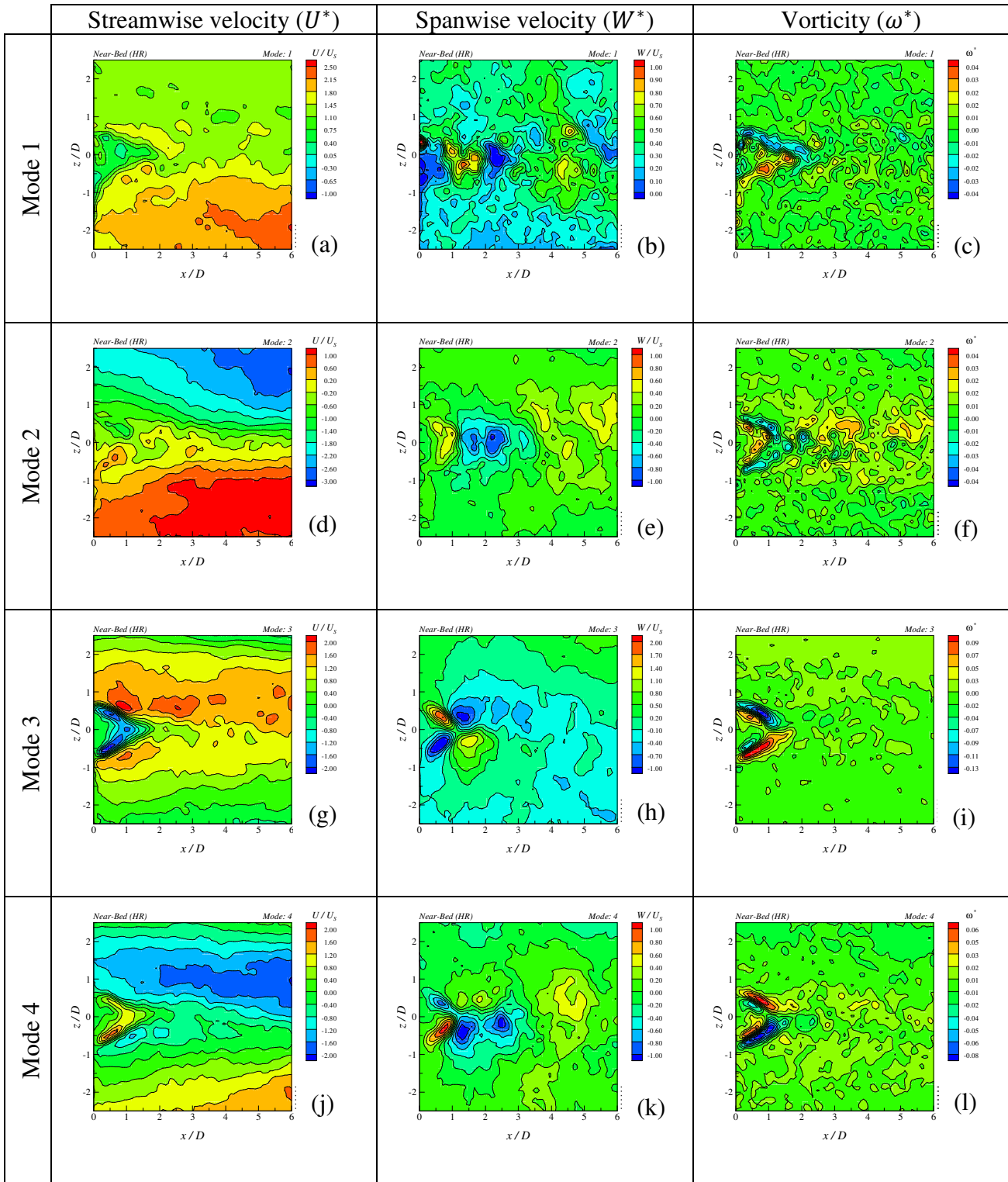
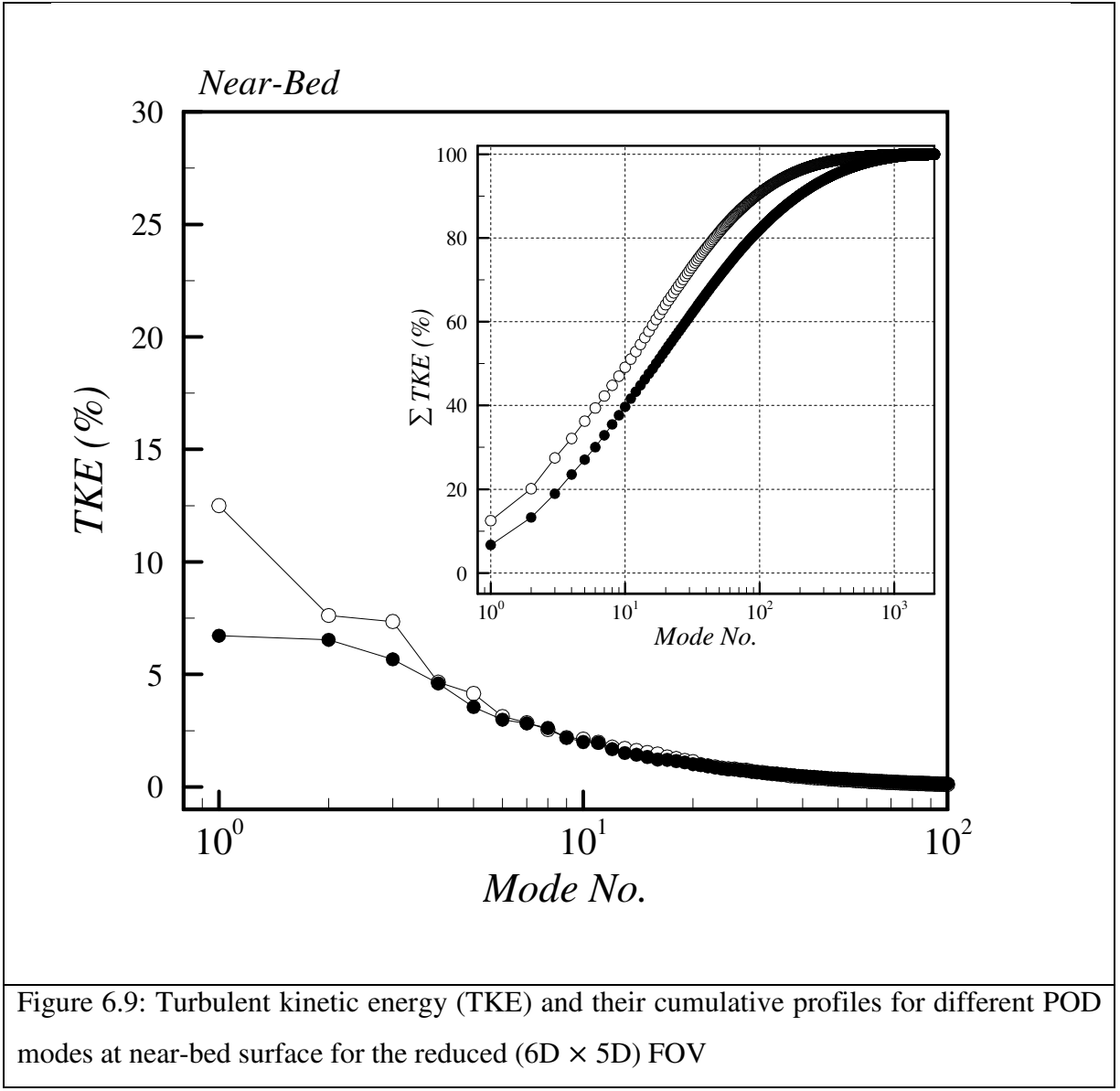


Figure 6.8: Spatial POD modes in the near-bed plane for HR in the form of normalized contours





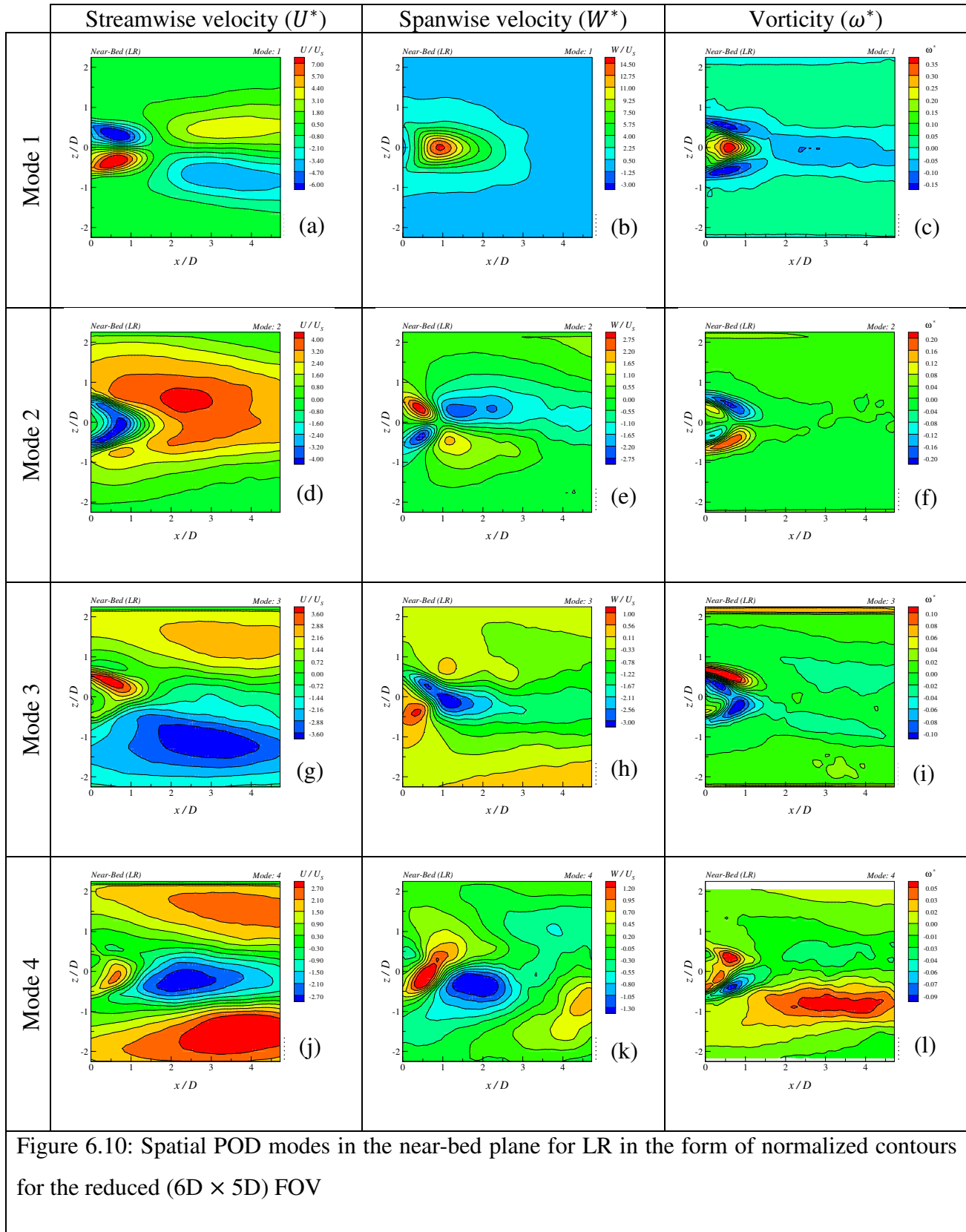


Figure 6.10: Spatial POD modes in the near-bed plane for LR in the form of normalized contours for the reduced ( $6D \times 5D$ ) FOV

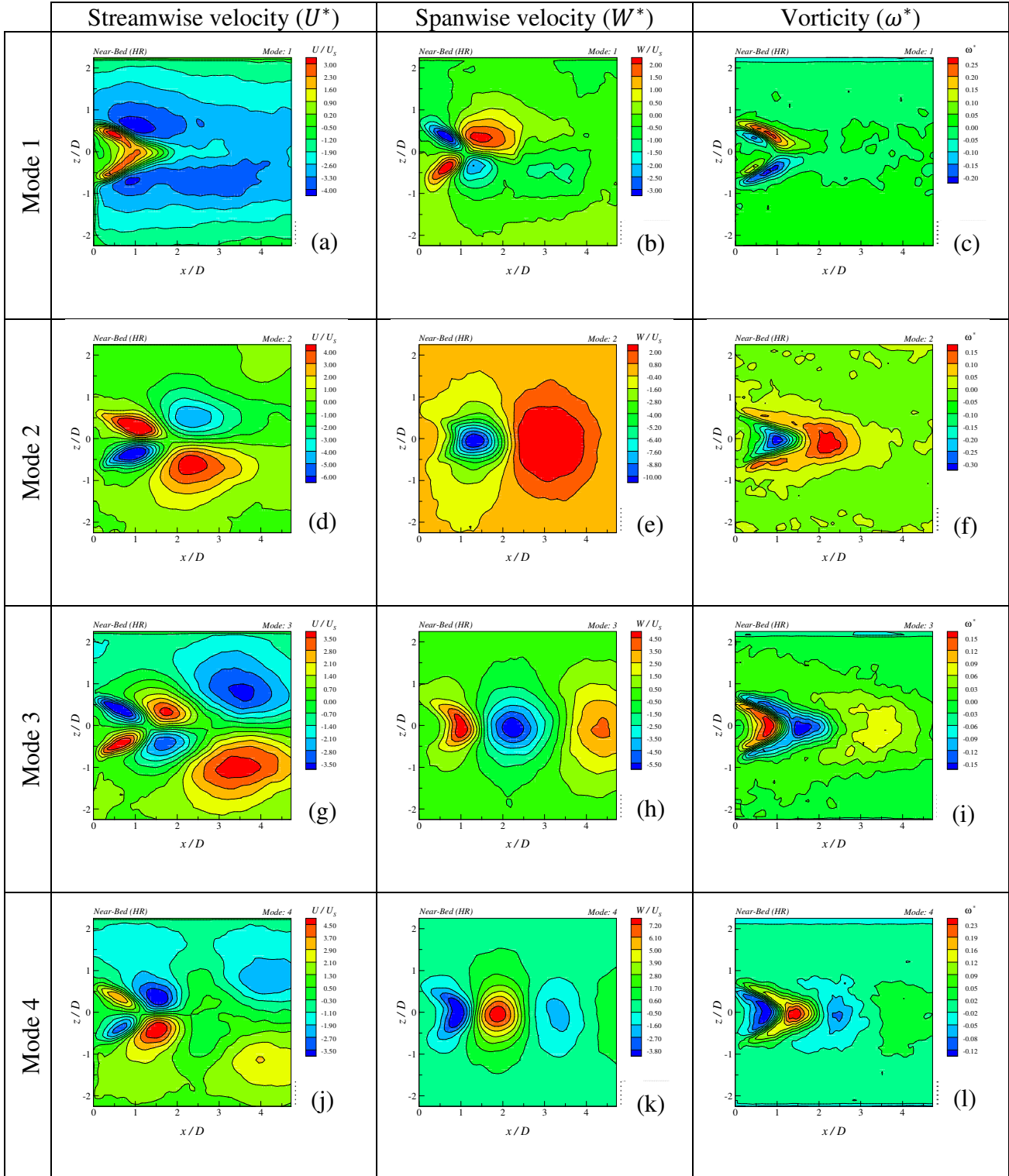


Figure 6.11: Spatial POD modes in the near-bed plane for HR in the form of normalized contours for the reduced ( $6D \times 5D$ ) FOV

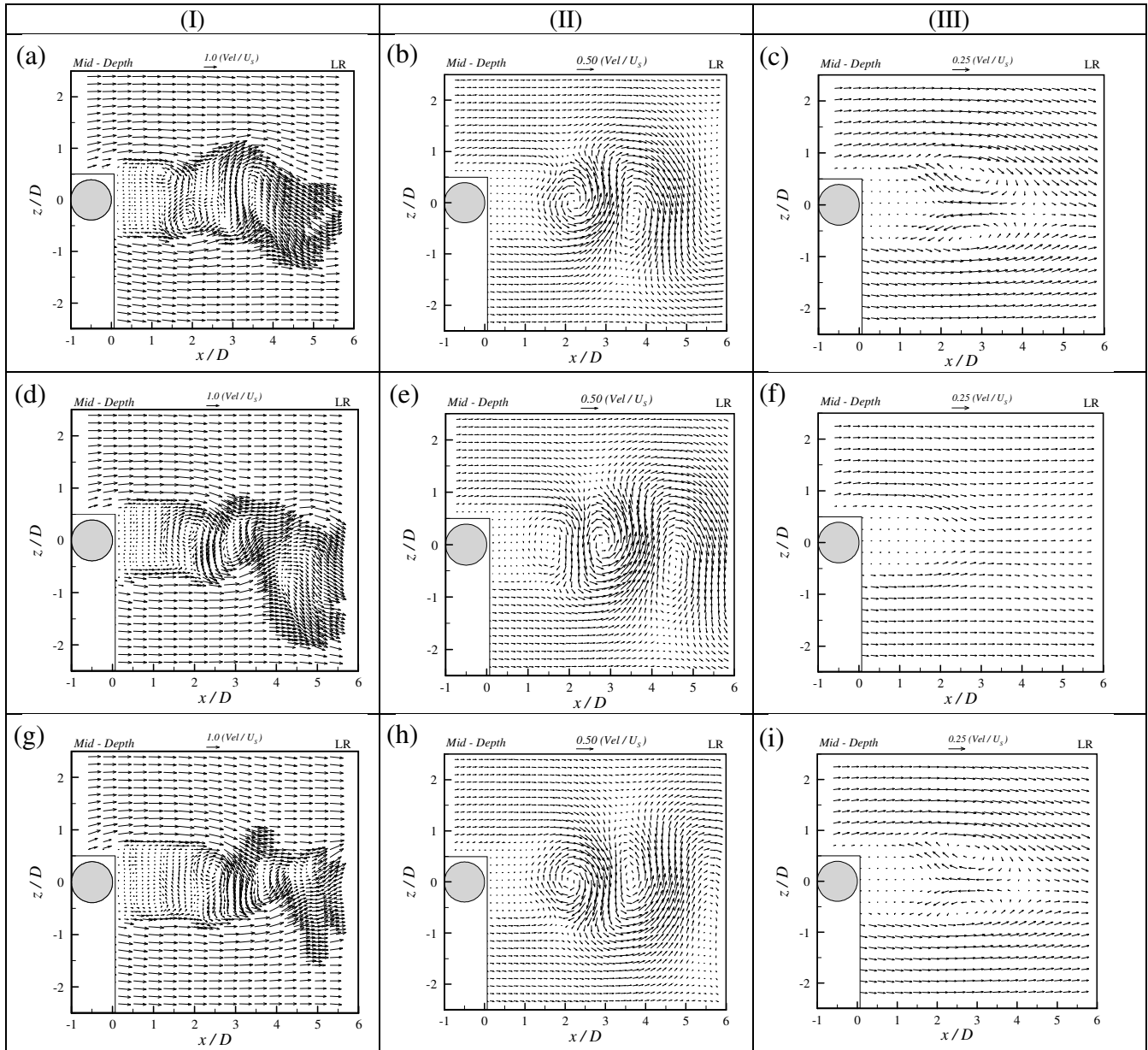


Figure 6.12: The instantaneous velocity vectors for original velocity vectors (I) Galilean decomposition of the reconstructed velocity vectors based on POD Modes 1 and 2 (II) Galilean decomposition of the reconstructed velocity vectors based on POD Modes 3 (III) in the mid-depth plane for LR

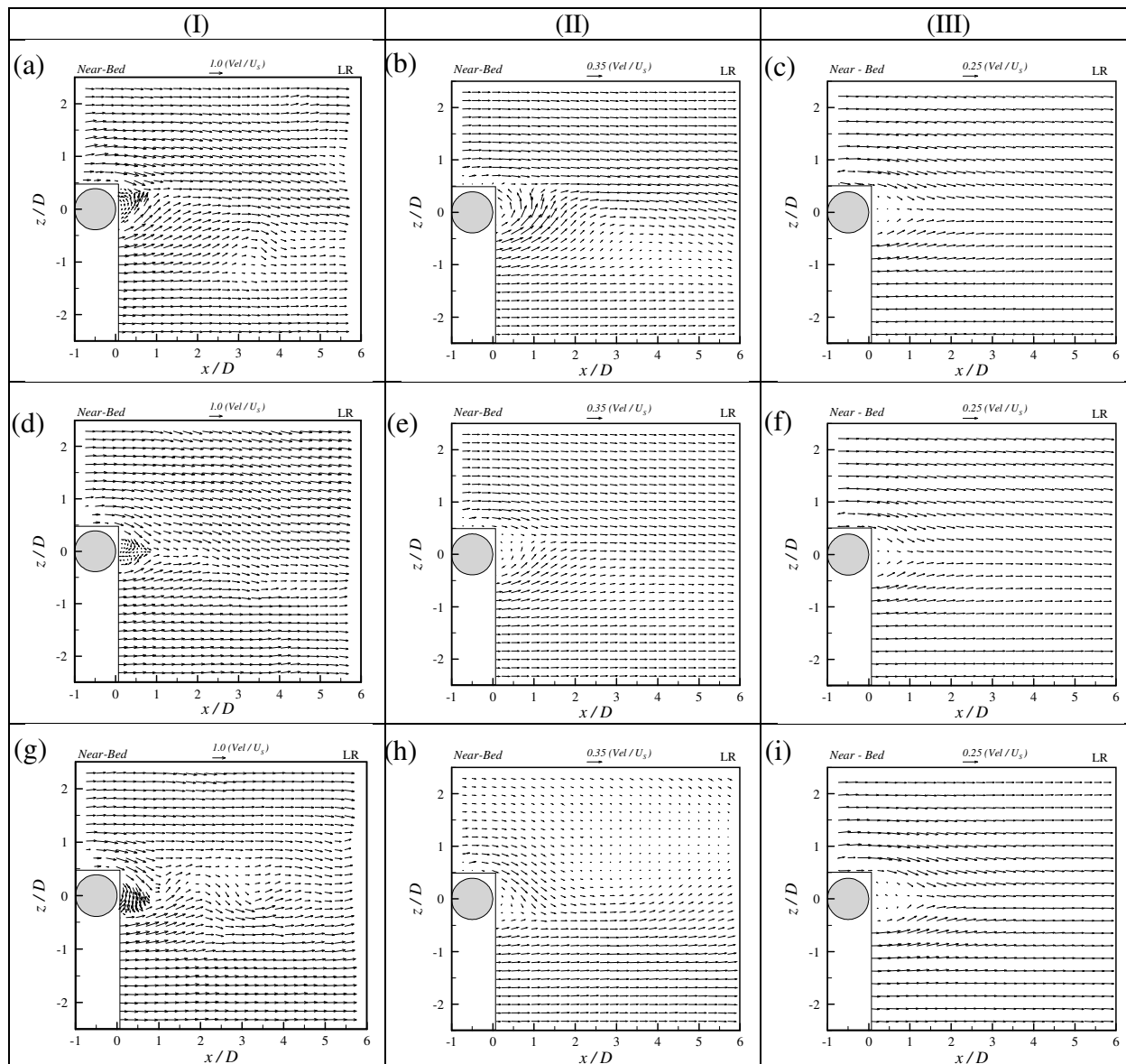


Figure 6.13: The instantaneous velocity vectors for original velocity vectors(I) Galilean decomposition of the reconstructed velocity vectors based on POD Modes 1 and 2 (II) Galilean decomposition of the reconstructed velocity vectors based on POD Modes 3 (III) in the near-bed plane for LR

## **Chapter 7: SHALLOW FLOW PASSING TANDEM CYLINDERS**

### **7.1 General remarks**

Chapter 7 addresses horizontal variation of the mean and turbulence parameters of the wake flow behind the tandem cylinders in the shallow open channel flow for both Reynolds numbers and establish comparison with the results obtained for a single cylinder discussed in Chapter 5. Although the wake flow behind tandem cylinders is relatively less investigated, the uniqueness of the present experiments are characterized by the shallow approach flow and by the large cylinder aspect ratio. The vertical variability of the wake flow is investigated by the means of mean velocity, turbulence intensities and Reynolds shear stresses at different streamwise stations

PIV experiments are carried out to study shallow flow passing tandem emergent cylinders at low Reynolds number (LR) and high Reynolds number (HR). The cylinders are affixed vertically to the bed for all test cases. The origin of the coordinate system is chosen to be located at the rear side of the most downstream cylinder as shown in Figure 3.2. The vertical location  $y = 0$  is located on the bed and it is directed upwards towards the free surface. Different tandem configurations are considered in this study. These include two cylinders with short and large gaps and three tandem cylinders. Here the gap distance is defined as the center to center length between the cylinders.

The gap between the two cylinders with short gap (C2S) and large gap (C2L) are  $G = 1.95D$  and  $G = 3.9D$ , respectively. In three-cylinder case (C3), the distance between cylinders is kept constant at  $1.95D$  (i.e., the gap between the first and last cylinder is  $G = 3.9D$ ). Before discussing the time-averaged velocity fields of the tandem cases, it is essential to determine a proper length scale in which the tandem cases can be compared with each other. In the next section, this importance of determining the proper length scale is discussed.

### **7.2 Proper length scale**

The normalized mean streamwise velocity profiles of all tandem cases in the horizontal mid-depth plane for both Reynolds numbers are shown in Figure 7.1. In this

figure, the mean streamwise velocity ( $U$ ) and the horizontal locations ( $x$  and  $z$ ) are normalized by the approaching mean streamwise velocity at the corresponding horizontal plane ( $U_S$ ) and the cylinder diameter ( $D$ ), respectively.

The plots in Figure 7.1 display the development of the  $U/U_S$  profiles of each tandem case along with the single cylinder case at different  $x/D$  locations. Following the discussion about the inner and outer wake region in Chapter 5, herein similar regions can be observed in the wake flow for tandem configurations in the mid-depth plane for both Reynolds numbers. While a top-hat type profile is observed for a single cylinder in the very near-wake region ( $x/D < 1.0$ ), the tandem cases appear to present a Gaussian type profile for both Reynolds numbers. The earlier onset of the Gaussian type profile indicates that the flow is highly influenced by the upstream cylinder(s). Such observations were also reported by Zdravkovich (1987), Igarashi (1981, 1984), Xu and Zhou (2004) and Zhou and Yiu (2006) among others for deep flow.

As shown in Figure 2.8, in deep flows if the gap between the cylinders is less than  $2D$  then downstream cylinder is sheltered by the separated shear layers (SSLs) from the lead cylinder. The downstream cylinder is expected to not influence the wake region. As the gap increases ( $2D < G < 5D$ ) then the SSLs from the upstream cylinder touch the surface of the downstream cylinder. In this case, while the gap flow is not stagnant any more, the downstream cylinder will affect the wake flow. This effect (local wake effect) is expected to be stronger in the near-wake region. In the case of C2S the second cylinder is sheltered by the lead cylinder while in C2L the SSLs from the lead cylinder are likely to interact with the second cylinder. The local wake effects arising from the interaction are expected to be different.

As observed in the  $U/U_S$  profiles for the different tandem cases for LR and HR flows, no distinct difference is noticed between them; and all the tandem cases display almost a similar trend in their profiles at all locations, though the tandem cases have difference in the gap distance or even the number of cylinders. This indicates that the streamwise length scale ( $x$ ) and the cylinder diameter ( $D$ ) cannot represent the wake characteristics for tandem cylinders even at mid-depth plane, where the bed and free-surface are considered to have less influence on the wake. Zhou and Yiu (2006) and Yen et al. (2008) suggest using the gap length ( $G$ ) as alternative length scale besides  $x$  and  $D$

in order to better illustrate the influence of the lead cylinder and the gap, on the wake flow.

Following the above discussion, here after  $(G+x)/D$  is chosen as the length scale in the streamwise direction instead of  $x/D$  in order to show the influence of the lead cylinder and the gap length in the wake flow.

### 7.3 Time-averaged results in horizontal plane profiles

This section presents analysis of the time-averaged results of flow field in the wake region of the most downstream cylinder in the tandem configuration for LR and HR in the three different horizontal planes at mid-depth ( $y/D = 5.5$ ), near-bed ( $y/D = 0.8$ ) and near-free surface ( $y/D = 10$ ). Different streamwise  $(G+x)/D$  sections at each FOV in the wake region are chosen to compare the flow characteristics of different bed-mounted tandem cylinders in the shallow water. The results for the single cylinder discussed in Chapter 5 are also included for comparison.

Figure 7.2 shows the spanwise distribution of the normalized mean streamwise velocity ( $U/U_s$ ) profiles of all tandem test cases in the wake of downstream cylinder at mid-depth. All  $U/U_s$  profiles follow the Gaussian type profile at all  $(G+x)/D$  locations in the inner wake region where the magnitude of  $U/U_s$  is small. While C2L and C3 cases show lower  $U/U_s$  values in the inner wake region at HR flow compared to LR at  $(G+x)/D \leq 5.0$  locations, the  $U/U_s$  profiles of C2S show slightly higher values at HR compared to LR. The existence of a Gaussian type profile in the  $U/U_s$  profiles of C2L and C3 with a lower peak at  $(G+x)/D \leq 5.0$  locations (Figures 7.2.a, b, e, f) compared to that of C2S and C1 indicates the local wake effect of the downstream cylinder on the streamwise velocity distribution for both Reynolds numbers. While, for both Reynolds numbers,  $U/U_s$  profiles of C2S and C1 asymptotes to 1.0 in the outer wake region (where  $U/U_s$  asymptotes to a constant value far from the wake centreline) at all the  $(G+x)/D$  locations, the asymptotic value for  $U/U_s$  profiles of C2L and C3 is about 1.06 at  $(G+x)/D \leq 5.0$ , particularly for HR. The higher asymptotic value of C2L and C3 is another indication of the local effect of downstream cylinder on the wake flow. At farther downstream location  $(G+x)/D = 8.0$ ,  $U/U_s$  profiles of C3 and C2L asymptotes to 1.0 at the spanwise location of  $|z| \approx 2.0D$  for both Reynolds numbers. The spanwise distributions of the streamwise

velocity of C3 and C2L at mid-depth plane exhibit similar profiles for both Reynolds numbers, particularly at  $(G+x)/D \leq 6.0$  locations. Similarly,  $U/U_s$  profiles of C2S collapse on that of the single cylinder (C1) profiles at  $(G+x)/D \leq 6.0$  locations, particularly for LR. At farther downstream location  $(G+x)/D = 8.0$ , all the tandem cases follow the  $U/U_s$  profile of C1 for both Reynolds numbers.

In the near-bed plane (Figure 7.3), while no symmetric trend is seen for the spanwise distribution of  $U/U_s$  profiles for all the cases at LR, the  $U/U_s$  profiles at HR show almost a symmetrical distribution for all the cases about the wake centreline. In addition, at HR, all the  $U/U_s$  profiles follow the Gaussian type profile at all  $(G+x)/D$  locations, while such a Gaussian type profile is not observed for any of the tandem configurations for the LR flow even at farther downstream locations. This can be due the stronger bed suppression effect on the wake flow at the LR flow compared to the HR flow. The existence of valley region with small values in the  $U/U_s$  profiles of C2L and C3 at  $(G+x)/D \leq 5.0$  locations (Figures 7.3.a, b, e, f) indicate the local wake effect of the downstream cylinder on the streamwise velocity distribution for both Reynolds numbers. In the outer wake region, the  $U/U_s$  profiles of C2S and C1 asymptote to 1.0 for both Reynolds numbers at all  $(G+x)/D$  locations similar to the mid- depth plane profiles. For the other tandem configurations (C2L and C3), the  $U/U_s$  profiles asymptotes to near 1.1 at  $(G+x)/D = 4.5$  and the asymptotic value in the outer wake region attains near 1.0 at  $(G+x)/D = 6.0$  for both Reynolds numbers similar to their counterparts at mid-depth plane. Also, it should be mentioned that  $U/U_s$  profiles of all the cases asymptote to near 1.0 at spanwise locations  $|z| \approx 1.5D$  for the HR flow, which is less than their counterpart at the mid-depth plane ( $|z| \approx 2.0D$ ). This can be another indication of the bed suppression effect on the wake flow expansion of all tandem configurations in the near-bed plane.

As observed in Figure 7.4, in the near-free surface plane, the spanwise distribution of  $U/U_s$  profiles of all the cases in the wake of downstream cylinder are almost symmetrical about the wake centreline for both Reynolds numbers. While  $U/U_s$  profiles of tandem cases at LR flow collapse on each other in the outer wake region at all  $(G+x)/D$  locations, at HR, the C2L and C3 cases show a profile different from C1 and C2S. In the inner wake region of the HR flow,  $U/U_s$  profiles of C2S collapse on the



single cylinder (C1) profiles particularly at  $(G+x)/D \geq 5.0$  locations and C3 and C2L cases follow the same trend, although they do not collapse well on each other. Such  $U/U_s$  profile classification in the inner wake region is not clearly observed for the tandem cases at LR. In this plane, the streamwise velocity profiles of the tandem cases at the HR flow have developed to reach almost the same trend at  $(G+x)/D = 8.0$ . However, for the LR flow various trends in the  $U/U_s$  profiles of tandem cases are observed at this location. This can be due to the effect of free surface and its different influence at two Reynolds numbers.

The profiles for streamwise turbulence intensity ( $u_{rms}/U_s$ ) across the wake at mid-depth, near-bed and near-free surface are shown in Figures 7.5, 7.6 and 7.7, respectively. The dash lines in these figures, mark the edges of the cylinder(s) at  $z/D = \pm 0.5$ . A first glimpse indicates that the streamwise turbulence intensity profiles of C3 and C2L have higher values than C1 and C2S in all the planes, particularly for  $(G+x)/D \leq 6.0$ .

In the mid-depth plane (Figure 7.5), while  $u_{rms}/U_s$  profiles are almost symmetrical about the wake centreline ( $z/D = 0$ ) at both Reynolds numbers, two distinct peaks and a valley between them occur in the profiles, particularly for C2L and C3. The peak values of  $u_{rms}/U_s$  distribution of C2L and C3 at both Reynolds numbers take place at positions close to the cylinder edge, particularly for  $(G+x)/D < 5.0$ , which is an indication of the effect of the separated shear layers from the sides of the downstream cylinder. The peaks of  $u_{rms}/U_s$  of C2S and C1 take place at positions off the cylinder edge ( $|z/D| > 0.5$ ) with smaller magnitudes compared to the other two cases. These small peaks indicate the negligible presence of shear layers which have almost decayed at this location of the wake. One should recall that for this tandem case the SSLs have originated from the lead cylinder.  $u_{rms}/U_s$  profiles of C2S collapse well on the profiles of C1 at all  $(G+x)/D$  locations, particularly at LR. Similarly, the spanwise distributions of  $u_{rms}/U_s$  for C3 and C2L show almost the same profile at  $(G+x)/D$  locations at both Reynolds numbers. Farther downstream, at  $(G+x)/D = 8.0$ , all  $u_{rms}/U_s$  profiles of the tandem cases follow the same trend as the C1 profile, particularly for LR which indicates the decay of turbulence follows the trend of a single cylinder wake.

In the near-bed plane (Figure 7.6), although all the tandem cases at HR exhibit symmetric  $u_{rms}/U_s$  profiles about the wake central plane ( $z/D = 0$ ) at all locations, no

symmetric distribution is observed for the  $u_{rms}/U_S$  profiles of tandem cases at LR, particularly at  $(G+x)/D < 6.0$ . While at HR, the  $u_{rms}/U_S$  profiles of C2S and C3 show almost similar trends as that of C1 and C2L, at all the locations, such similarity is not observed for the LR flow. In addition,  $u_{rms}/U_S$  profiles for all the tandem cases have higher magnitudes at LR compared to their counterparts at HR as observed in Figure 7.6. The latter can be due to different reasons. The first can be due to the stronger effect of coherent structures in the junction flow at LR, which was discussed in Chapters 5 and 6. The second one can be due to the difference in the position of the near-bed planes of LR and HR in terms of wall units. The near-bed plane of LR flow is at a location where higher values of  $u_{rms}/U_S$  exist in the approaching flow. As mentioned in Chapter 5, the position of near-bed plane is at  $y^+ = 35$  and 110 for the LR and HR flow, respectively.

In the near-free surface plane (Figure 7.7), the peaks of  $u_{rms}/U_S$  profiles of tandem cases, particularly C2L and C3, take place at some positions off the cylinder edge for both Reynolds numbers. These off position locations are more distinctive for the LR flow. As shown in Figures 7.7.c and 7.7.d, the streamwise turbulence intensity profiles of C2L and C3 asymptote to near 0.03 at spanwise locations  $z/D \approx \pm 3.0$  farther than the C1 and C2S profiles. This indicates that at LR the  $u_{rms}/U_S$  distribution of C2L and C3 is expanding wider near the free surface compared to C2S and C1 cases. However, at HR, all cases show a similar spanwise expansion of  $u_{rms}/U_S$  near the free surface which is independent of the  $(G+x)/D$  locations and asymptote to the constant value at  $z/D \approx \pm 2.0$ . Such a difference of the asymptotic locations at LR and HR flows indicates the influence of the free surface on the spanwise distribution of  $u_{rms}/U_S$  for C2L and C3 at LR and HR. It can be suggested that at the LR flow the free surface behaves like a weak wall which supports expansion of the turbulence in the spanwise direction for C3 and C2L cases, while at HR the free surface deformation prevents such expansions to the wake region. While  $u_{rms}/U_S$  profiles of C3 collapse well on C2L profiles at  $(G+x)/D \geq 6.0$  locations, C2S and C1 cases show a similar  $u_{rms}/U_S$  profile, particularly for the HR flow.

The profiles for spanwise turbulence intensity ( $w_{rms}/U_S$ ) of different tandem cases for both Reynolds numbers across the wake at mid-depth, near-bed and near-free surface are shown in Figures 7.8, 7.9 and 7.10, respectively. In the mid-depth plane, the spanwise distributions of  $w_{rms}/U_S$  profiles of the tandem cases are almost symmetric about the wake

centreline for both Reynolds numbers. Generally, in this plane,  $w_{rms}/U_S$  profiles of all cases show a similar trend with the maximum  $w_{rms}/U_S$  occurring in the wake center-plane, for both Reynolds numbers at all locations. At LR,  $w_{rms}/U_S$  profile of C3 collapse well on the profile of C2L at  $(G+x)/D = 4.5$  and the profiles of C2S and C1 show similar trends (see Figure 7.8.a).

In the near-bed plane (Figure 7.9), the spanwise turbulence intensity profiles of all tandem cases have lower magnitudes compared to their counterparts in the mid-depth plane for both Reynolds numbers. This indicates the effect of the bed friction on suppression of the wake flow in the near-bed region for all the tandem cases. Also, the  $w_{rms}/U_S$  profiles asymptote to the constant values for the LR and HR flows, which correspond the spanwise turbulence intensities of the approaching flow at the near-bed planes. The spanwise location of the asymptotic point on the  $w_{rms}/U_S$  profiles of the tandem cases for both Reynolds numbers are near  $\pm 1D$ , particularly at  $(G+x)/D \leq 6.0$ , which is smaller than their counterparts at mid-depth plane ( $\sim \pm 2D$ ). This can be another indication of the bed suppression effect on the wake expansion.

At LR flow, although all  $w_{rms}/U_S$  profiles of the tandem cases show a peak value at the central wake axis at  $(G+x)/D = 4.5$ , no symmetric pattern is observed in the  $w_{rms}/U_S$  distribution. At downstream locations ( $5.0 \leq (G+x)/D \leq 6.0$ ),  $w_{rms}/U_S$  profiles of C2S and C3 show similar trend as that of C1 and C2L, respectively. At  $(G+x)/D = 8.0$ , all tandem cases exhibit a similar trend and collapse on each other. At HR flow, while C1 and C2S exhibit similar  $w_{rms}/U_S$  profiles at all locations, particularly at  $(G+x)/D \geq 6.0$ , the  $w_{rms}/U_S$  profiles of C2L and C3 follow the same trend but C2L shows higher values than C3 in the inner wake region at  $(G+x)/D \geq 5.0$ .

In the near-free surface plane (Figure 7.10), the spanwise distributions of  $w_{rms}/U_S$  profiles of the tandem cases are almost symmetric about the wake centreline at all locations for both Reynolds numbers. At LR, the  $w_{rms}/U_S$  profiles of C2S and C3 have a symmetric distribution along the spanwise direction and they follow the same trend as C1 which exhibit a single peak at the wake centreline for all locations. However, C2L shows a double peak profile in the  $w_{rms}/U_S$  distribution at all the locations. At HR, although  $w_{rms}/U_S$  profiles of all the cases follow a similar trend in the spanwise direction and the peak values in the  $w_{rms}/U_S$  profiles are located on the central wake axis, C2S shows higher

peak value at  $(G+x)/D \leq 5.0$  and C3 displays higher peak value for  $(G+x)/D \geq 6.0$  among the other cases. Also, the observation of  $w_{rms}/U_S$  profiles of C2L and C3 at LR show a wider turbulence intensity distribution compared to the other cases, since the spanwise locations of the asymptotic region of these cases start at  $z/D \approx \pm 3.0$  farther than the other cases ( $z/D \approx \pm 2.0$ ). A similar observation is noticed in the streamwise turbulence intensity distribution for C2L and C3. At HR flow, all the cases show a similar spanwise expansion of the  $w_{rms}/U_S$  distributions in the near-free surface plane at different  $(G+x)/D$  locations and the asymptotic locations occurs at  $z/D \approx \pm 2.0$ , similar as the  $u_{rms}/U_S$  distribution of all the cases in this plane.

The development of dimensionless Reynolds shear stress ( $-\overline{uw}/U_S^2$ ) distribution across the wake at mid-depth, near-bed and near-free surface at both Reynolds numbers are shown in Figures 7.11, 7.12 and 7.13 respectively. The dash lines in all the Figures 7.5 to 7.7 indicate the spanwise location of the edges of the cylinder ( $z/D = \pm 0.5$ ). The first glimpse of the plots in the figures indicates that the Reynolds shear stress distributions of C3 and C2L have higher values than C1 and C2S in all the planes due to the presence of the downstream cylinder on the wake. Similar observation was reported by Pinarbasi et al. (2015) for near-wake study behind the downstream cylinder of a tow square tandem set.

As observed in Figure 7.11, in the mid-depth plane,  $-\overline{uw}/U_S^2$  profiles of all the cases are symmetric with opposite sign about the wake center plane ( $z/D \sim 0$ ) for both Reynolds numbers.  $-\overline{uw}/U_S^2$  profiles of C2S collapse well on C1 profiles at all  $(G+x)/D$  locations, particularly for the HR flow. A similar trend is observed for  $-\overline{uw}/U_S^2$  profiles of C3 and C2L at both Reynolds numbers, while the peak magnitudes of the dimensionless Reynolds shear stress for C3 is slightly higher than C2L, particularly at  $(G+x)/D \leq 5.0$ . Far from the cylinder edge in spanwise direction ( $|z/D| > 2.0$ ), the  $-\overline{uw}/U_S^2$  profiles asymptotes to zero at both Reynolds numbers for all the cases. The peak values of  $-\overline{uw}/U_S^2$  distribution of C2L and C3 at both Reynolds numbers occur almost on the positions near the cylinder edge, particularly at  $(G+x)/D \leq 5.0$  and the peaks of  $-\overline{uw}/U_S^2$  of C2S and C1 take place at some positions off the cylinder edge ( $0.5 < |z/D| < 1.0$ ), at all  $(G+x)/D$  locations. As noticed from the development of the Reynolds shear stress profiles, at  $(G+x)/D = 4.5$ , the  $-\overline{uw}/U_S^2$  peak value of C3 is almost double of the

peak value for C1 at both Reynolds numbers. At  $(G+x)/D = 8.0$ , all the tandem cases show a similar  $-\overline{uw}/U_S^2$  profile as that of C1 for both Reynolds numbers.

In the near-bed plane (Figure 7.12), while a similar symmetry in  $-\overline{uw}/U_S^2$  distribution of all the cases is observed for HR at different  $(G+x)/D$  locations, no symmetric pattern is seen for C3 and C2L for the LR flow, particularly at  $(G+x)/D \leq 6.0$ . Although, the peak magnitudes of the dimensionless Reynolds shear stress profiles for C2L is slightly larger than C3 for the HR flow, particularly at  $(G+x)/D \leq 5.0$ , both cases follow a similar trend in the  $-\overline{uw}/U_S^2$  profiles. For LR, at  $(G+x)/D \leq 5.0$ , while  $-\overline{uw}/U_S^2$  profiles of C3 collapse well on C2L in the region between  $|z/D| < 0.5$ , C2L shows different trend with a sudden change in the  $-\overline{uw}/U_S^2$  profiles compared to other cases in the farther spanwise locations. In these  $(G+x)/D$  locations, although C2S and C1 show a similar trend in the  $-\overline{uw}/U_S^2$  profiles at both Reynolds numbers, C2S exhibits slightly larger peaks than C1. At  $(G+x)/D = 6.0$ , while the  $-\overline{uw}/U_S^2$  distribution of C1 and C2S cases collapse on each other which show their development, C2L and C3 are still under development, at both Reynolds numbers. At farther downstream location  $(G+x)/D = 8.0$ , all tandem cases collapse fairly well on each other, that shows the development of Reynolds shear stress profiles of C2L and C3.

Another observation of  $-\overline{uw}/U_S^2$  profiles in the near-bed plane indicates that the spanwise distribution of the turbulence intensity asymptote to zero at  $|z/D| \approx 1.0$ , particularly at HR, which is less than their counterparts at mid-depth. This shows the bed friction effect on the suppression of the spanwise Reynolds shear stress distribution for all tandem cases.

In the near-free surface plane (Figure 7.13), almost a symmetric pattern in  $-\overline{uw}/U_S^2$  profiles with opposite sign about the central wake plane is observed at all  $(G+x)/D$  locations, particularly for HR. At all  $(G+x)/D \leq 6.0$ , C3 shows larger magnitudes in the peak Reynolds shear stress distribution compared to other cases for both Reynolds numbers.  $-\overline{uw}/U_S^2$  profiles of C2S collapse on that of C1 at  $(G+x)/D \geq 5.0$ , particularly in the HR flow, the collapse of  $-\overline{uw}/U_S^2$  profiles of C3 and C2L take place farther downstream at  $(G+x)/D = 8.0$ .

## 7.4 Conclusion

In this chapter, the results of particle image velocimetry measurements at different horizontal planes in the near-wake region behind three configurations of tandem circular cylinders in shallow flow are presented for two Reynolds numbers. The measurements were conducted in the wake region, at near-bed, mid-depth and near-free surface vertical locations. The flow features can be summarized as follows:

- Generally, it can be confirmed that wake flow characteristics behind the single cylinder (C1) and two-in-line cylinder with short gap (C2S) are similar, particularly in the mid-depth plane for both Reynolds numbers. This indicates that the downstream cylinder has a negligible influence on the wake flow in the mid-depth plane, when it is located at a distance less than  $1.95 D$  in the two-cylinder in-line configuration.
- The time-averaged results of two-in-line cylinder with large gap (C2L) and three-in-line cylinder (C3) cases exhibit similar profiles in the wake region, particularly in the mid-depth plane for both Reynolds numbers. It shows that middle cylinder in the C3 case is not playing any significant role in influencing the wake flow in this plane.
- In the near-bed region, the bed suppression effect on the spanwise expansion of wake flow is noticed for both Reynolds numbers at all tandem cases. Further, at LR, a strong effect of the coherent structures in the junction flow influences on the near-bed wake flow of all the tandem cases.
- The wake region in the free surface region for the C2L and C3 cases are influenced by the flow Reynolds number. Such an influence is observed in the spanwise expansion of the turbulence intensity distributions in the near-free surface plane, where LR flow exhibits wider turbulence intensity profiles compared to the HR flow.
- The free surface and wall of the bed alter the wake formation for all tandem cases. Such influences in the wake region make the flow three-dimensional behind the tandem configurations. The effects of the boundaries on the wake flow are dependent on the Reynolds number.
- The tandem configuration with larger gap cases (C2L and C3) show a higher Reynolds stresses compared to C2S in the wake region for both Reynolds numbers.

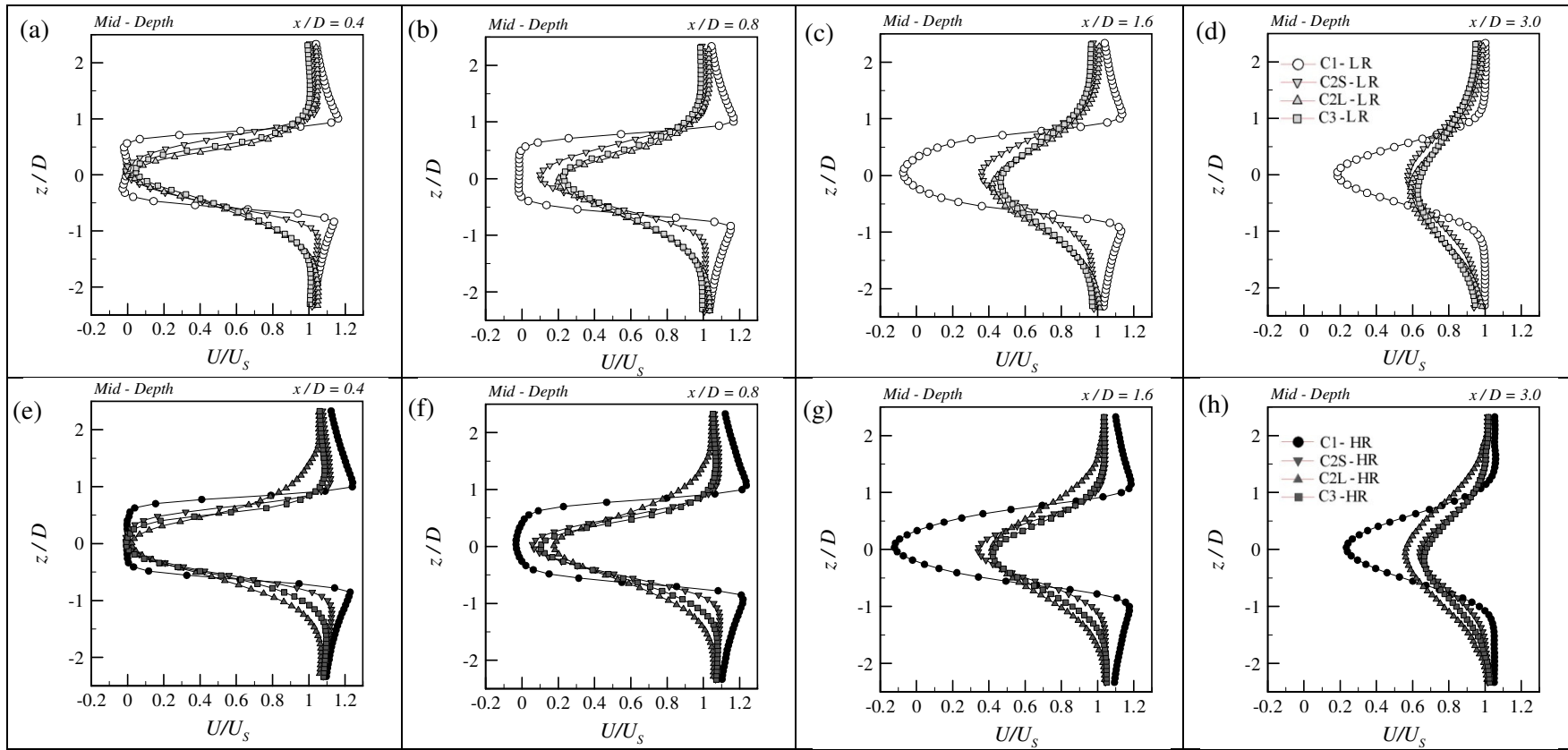


Figure 7.1: The normalized mean streamwise velocity profiles at different  $x/D$  locations in mid-depth for LR (a, b, c, d) and HR (e, f, g, h)

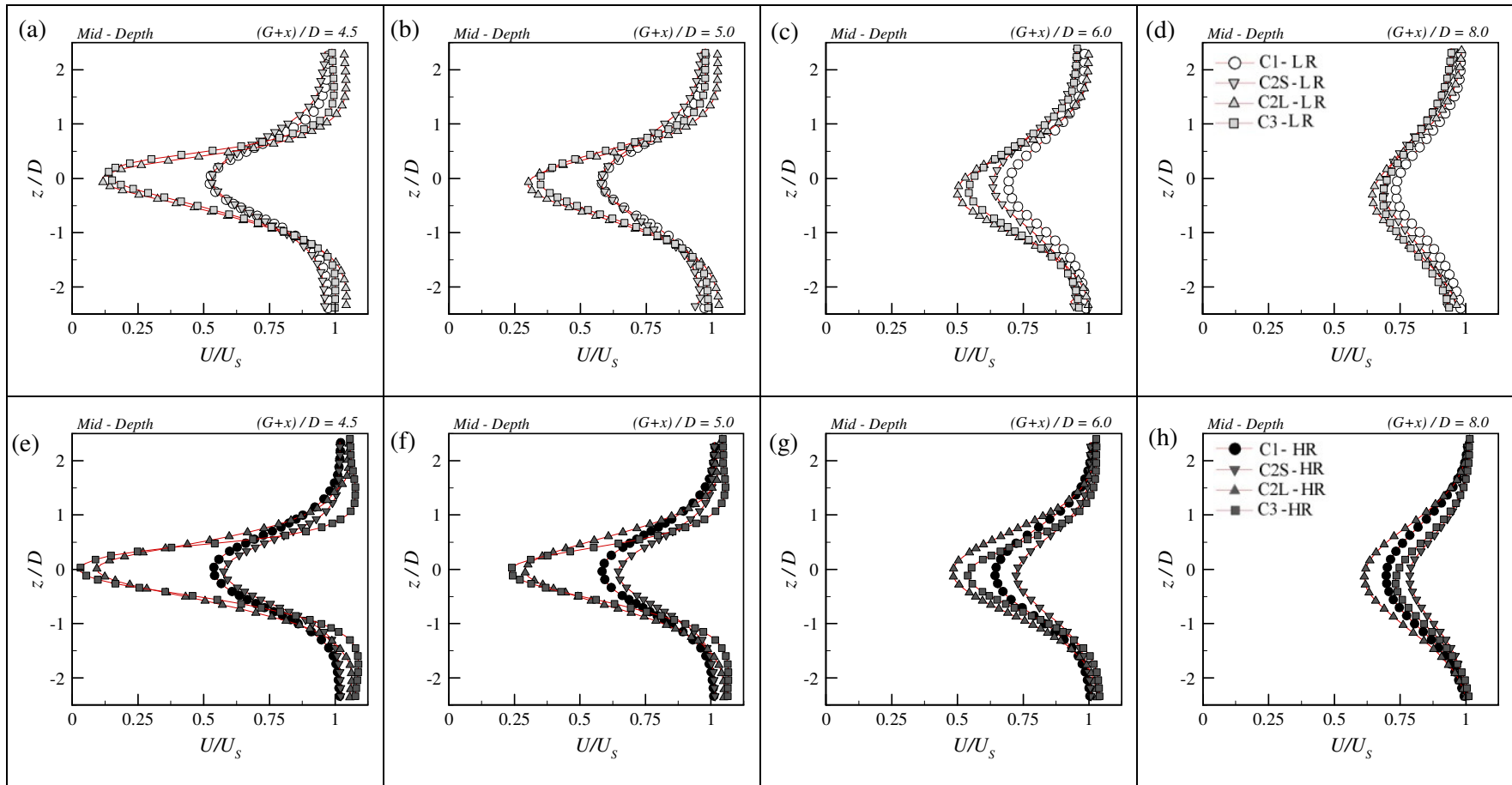


Figure 7.2: The normalized mean streamwise velocity profiles at different  $(G+x)/D$  locations in mid-depth for LR (a, b, c, d) and HR (e, f, g, h)



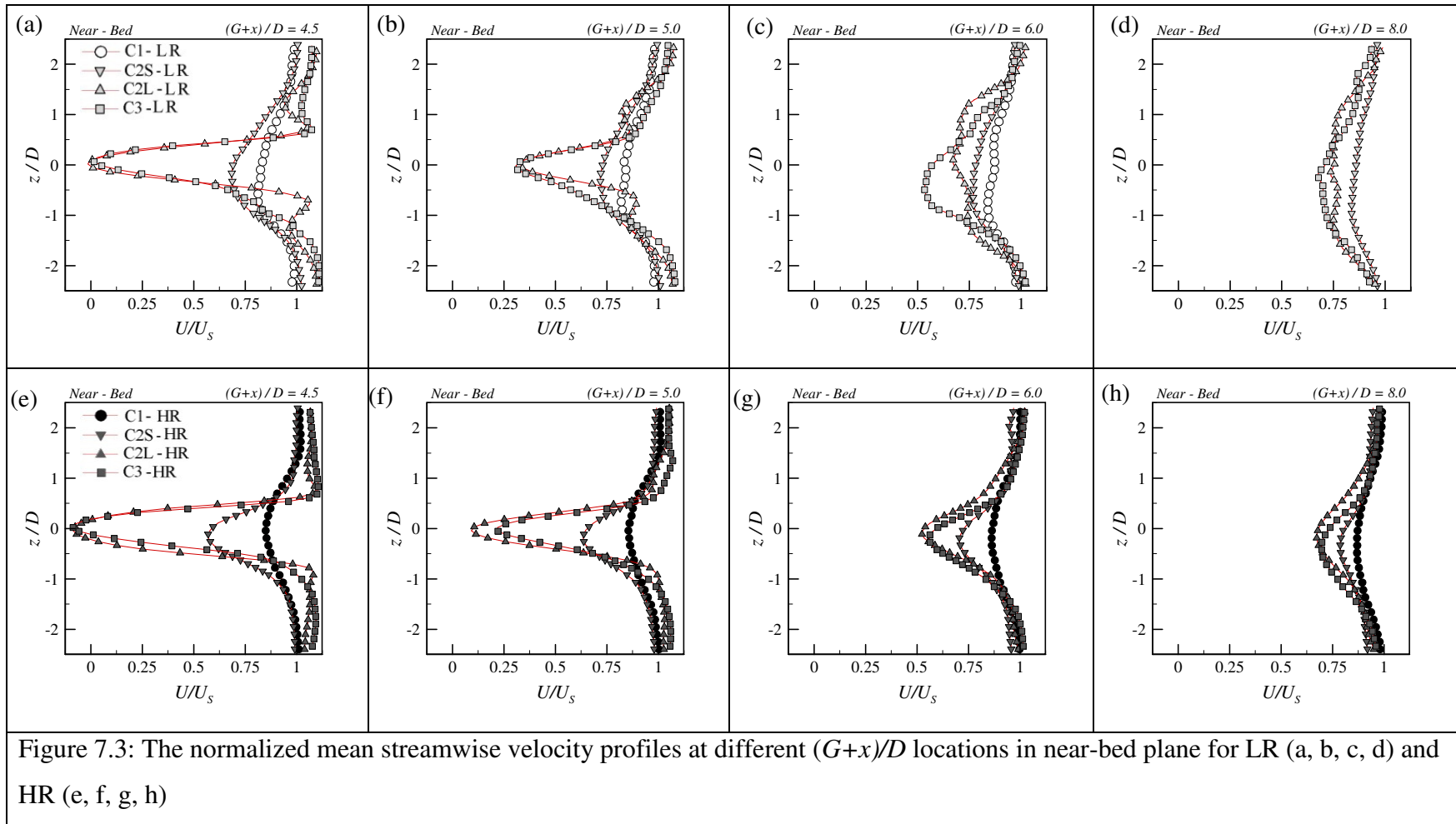
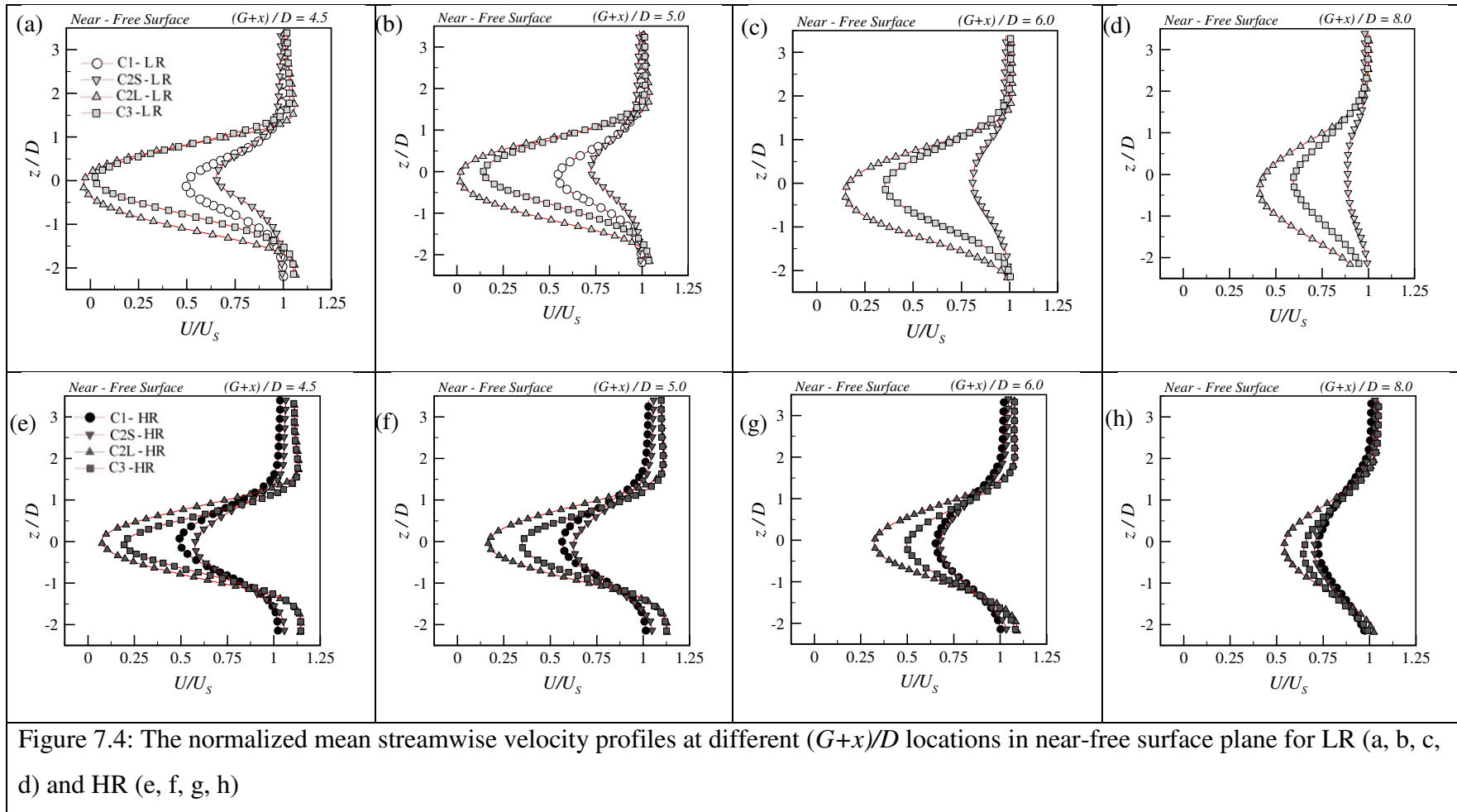


Figure 7.3: The normalized mean streamwise velocity profiles at different  $(G+x)/D$  locations in near-bed plane for LR (a, b, c, d) and HR (e, f, g, h)



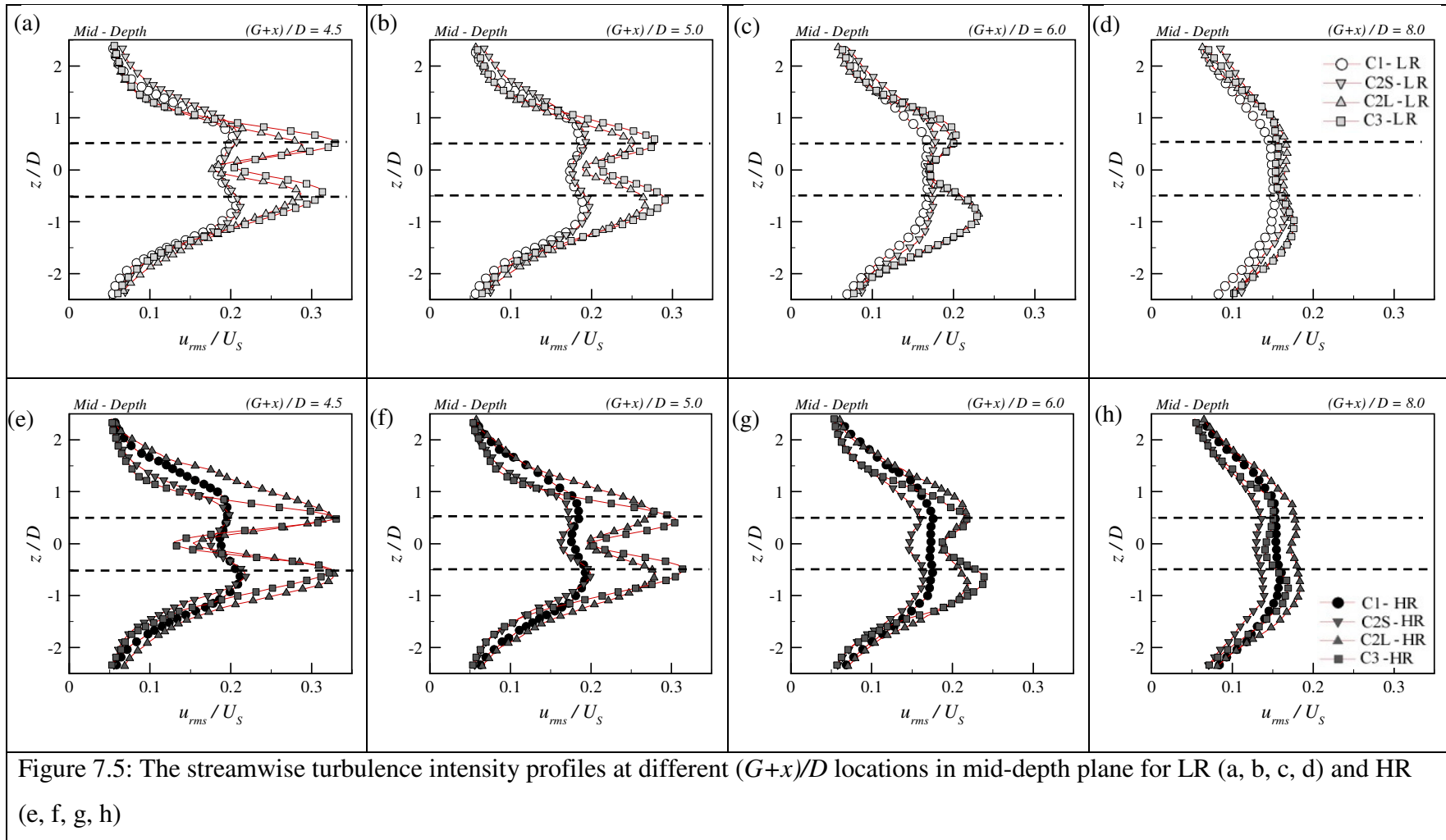


Figure 7.5: The streamwise turbulence intensity profiles at different  $(G+x)/D$  locations in mid-depth plane for LR (a, b, c, d) and HR (e, f, g, h)

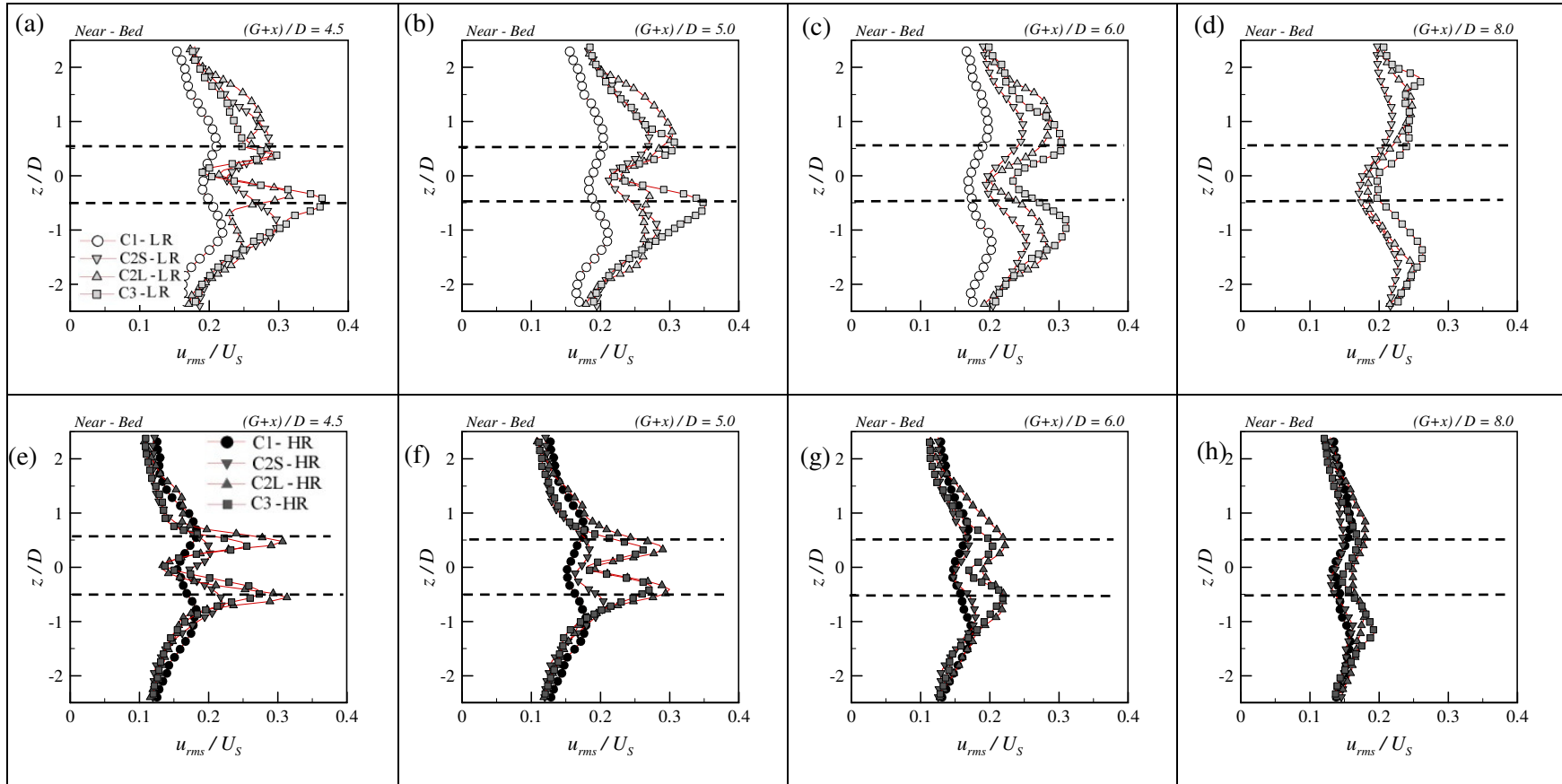


Figure 7.6: The streamwise turbulence intensity profiles at different  $(G+x)/D$  locations in near-bed plane for LR (a, b, c, d) and HR (e, f, g, h)

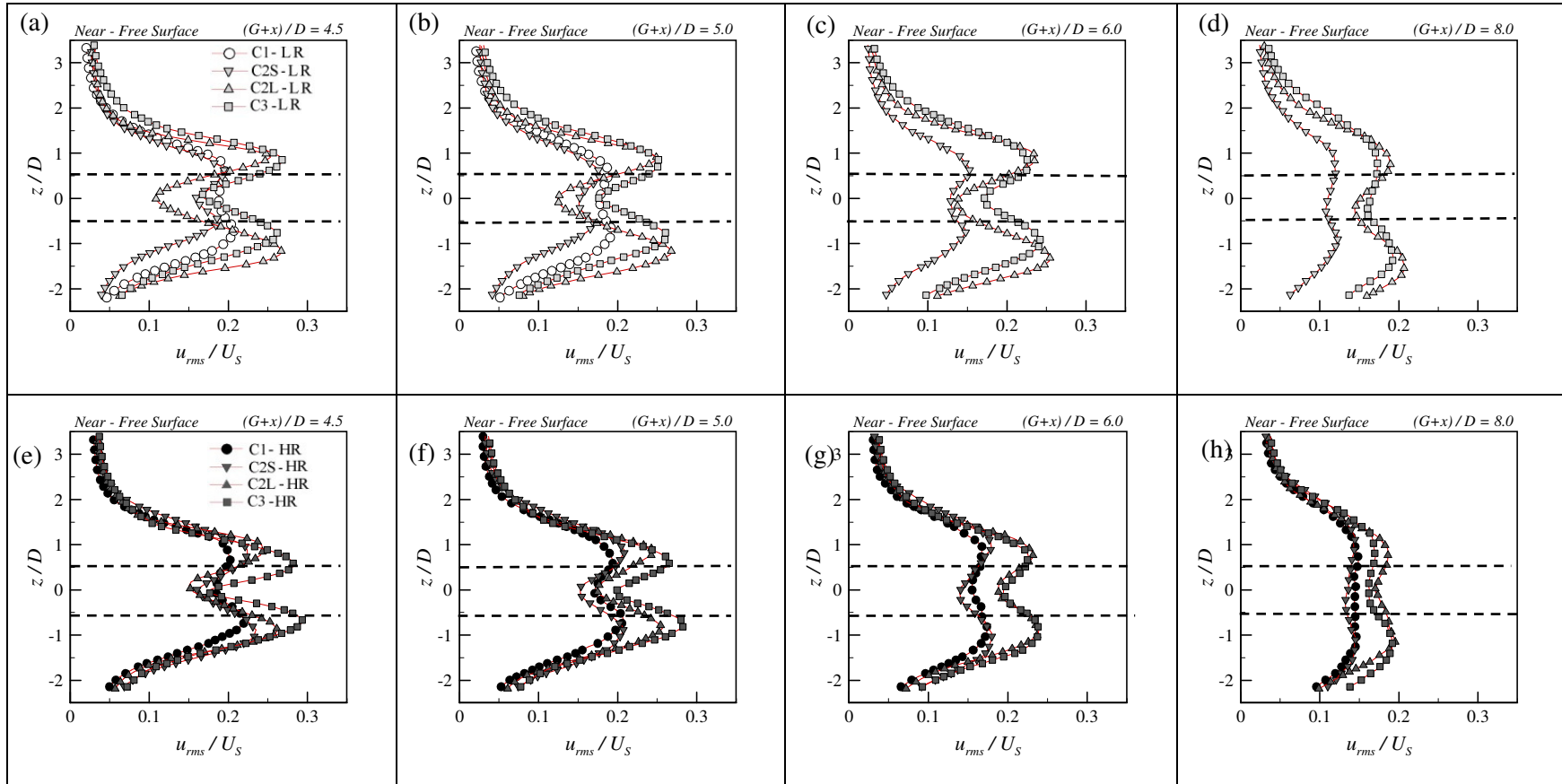


Figure 7.7: The streamwise turbulence intensity profiles at different  $(G+x)/D$  locations in near-free surface plane for LR (a, b, c, d) and HR (e, f, g, h)

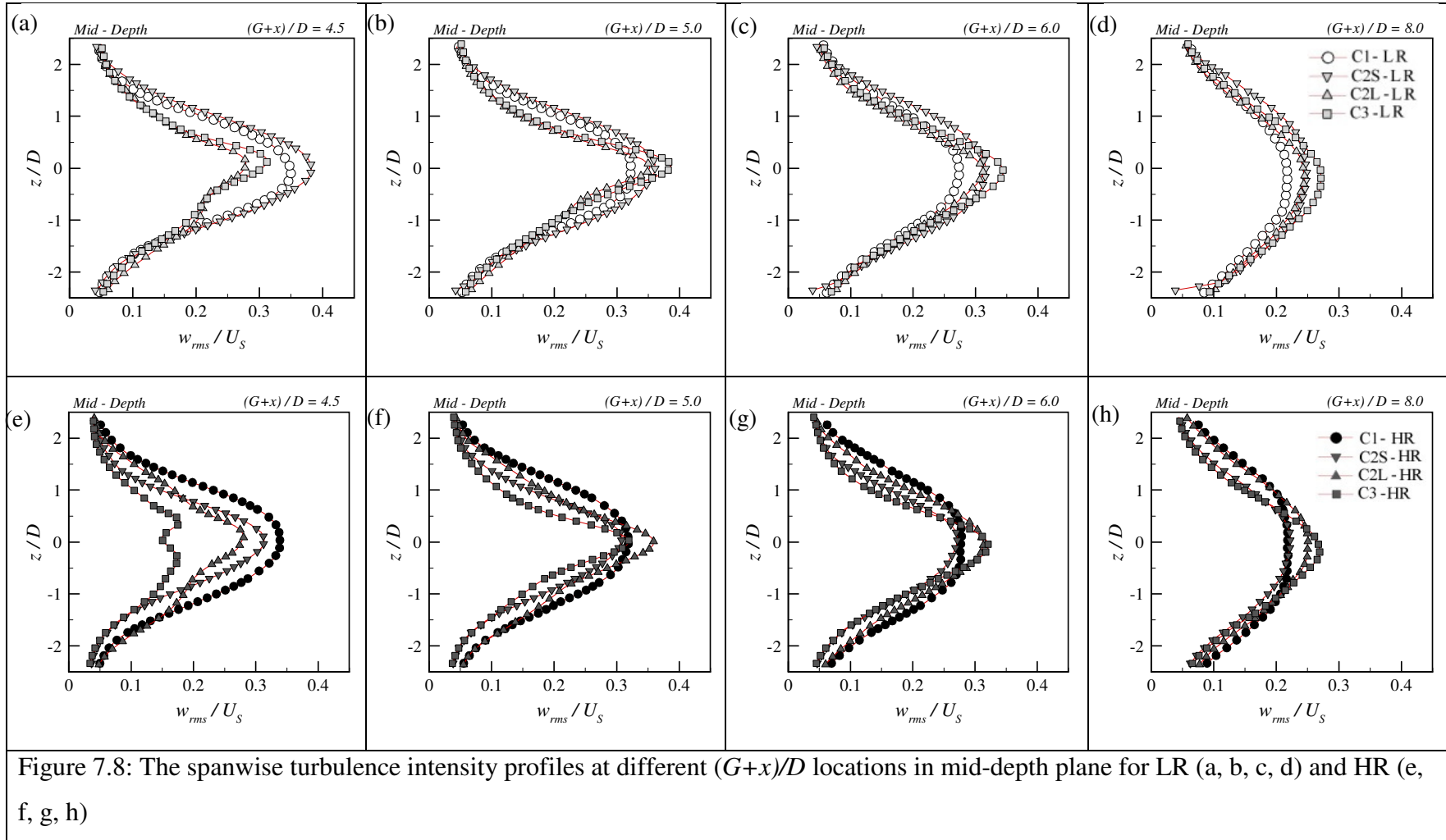
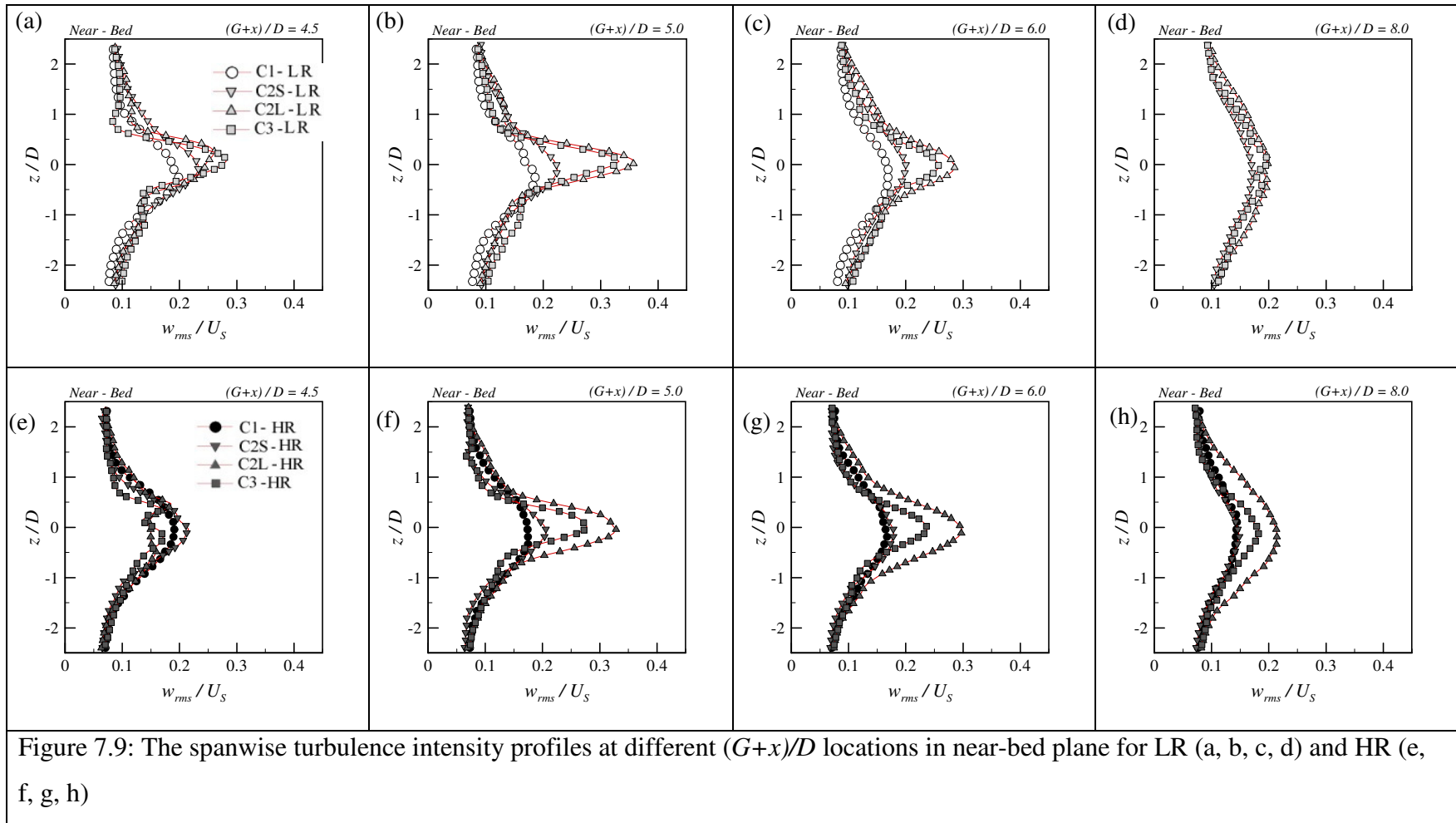


Figure 7.8: The spanwise turbulence intensity profiles at different  $(G+x)/D$  locations in mid-depth plane for LR (a, b, c, d) and HR (e, f, g, h)



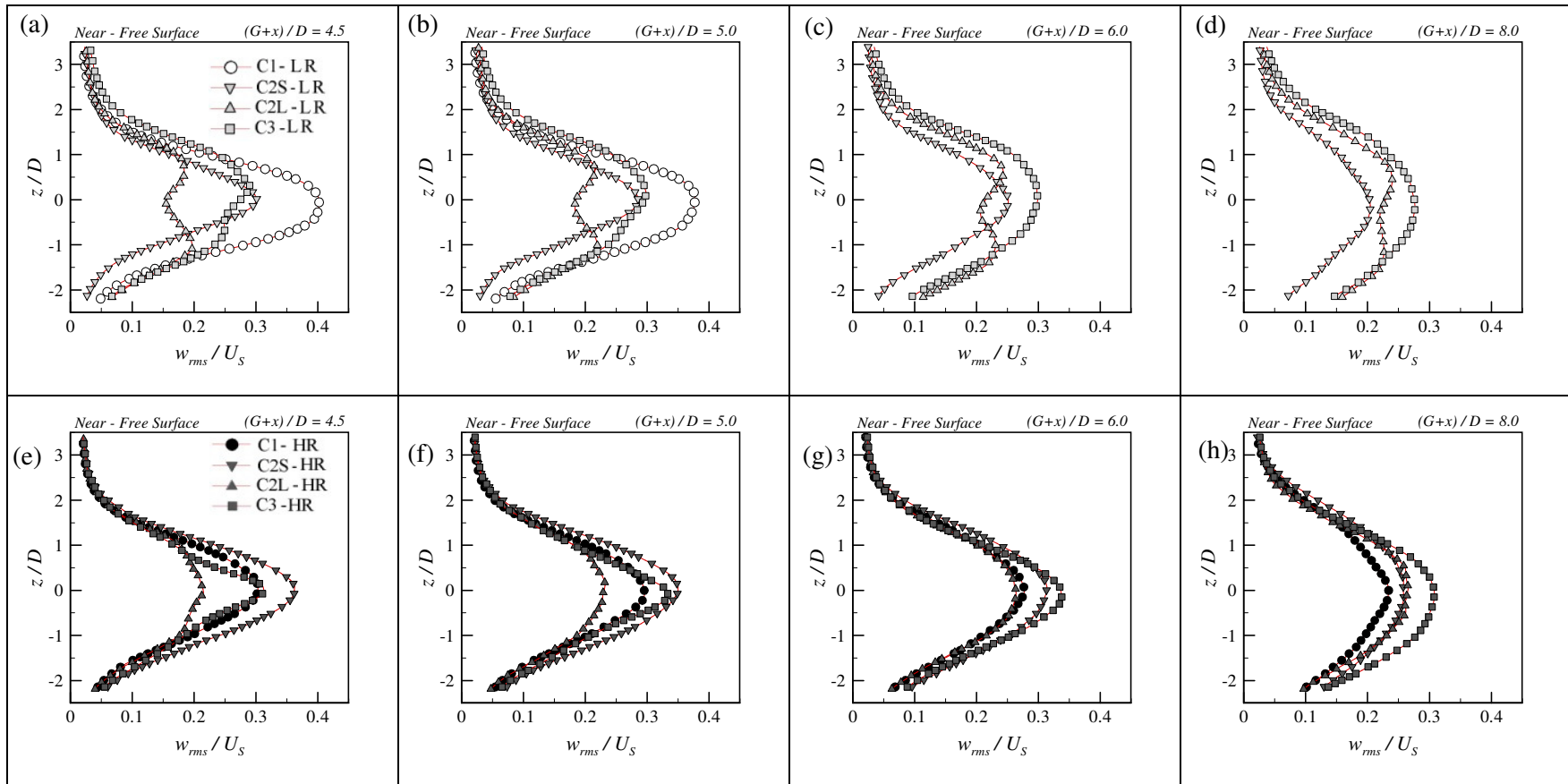


Figure 7.10: The spanwise turbulence intensity profiles at different  $(G+x)/D$  locations in near-free surface plane for LR (a, b, c, d) and HR (e, f, g, h)



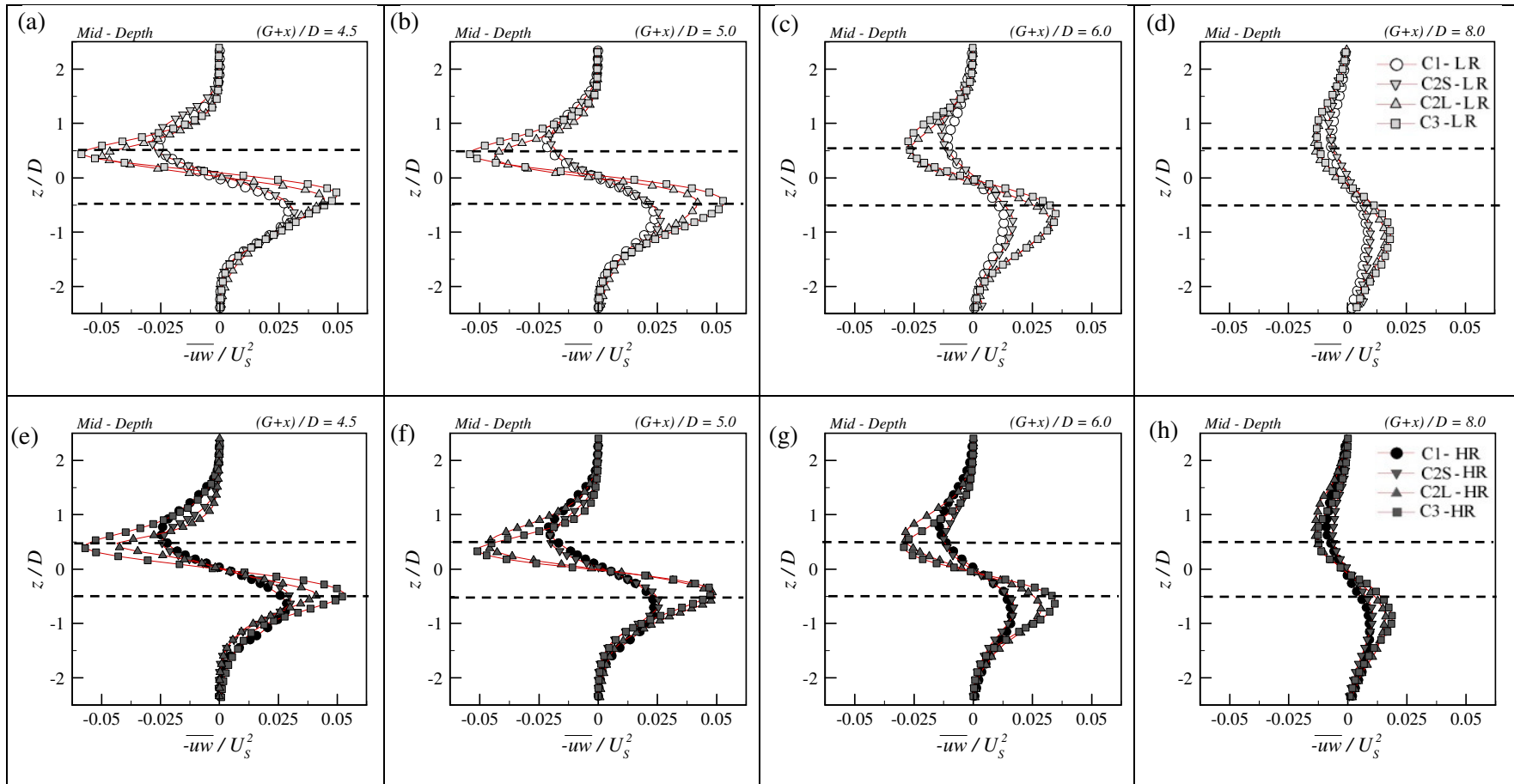
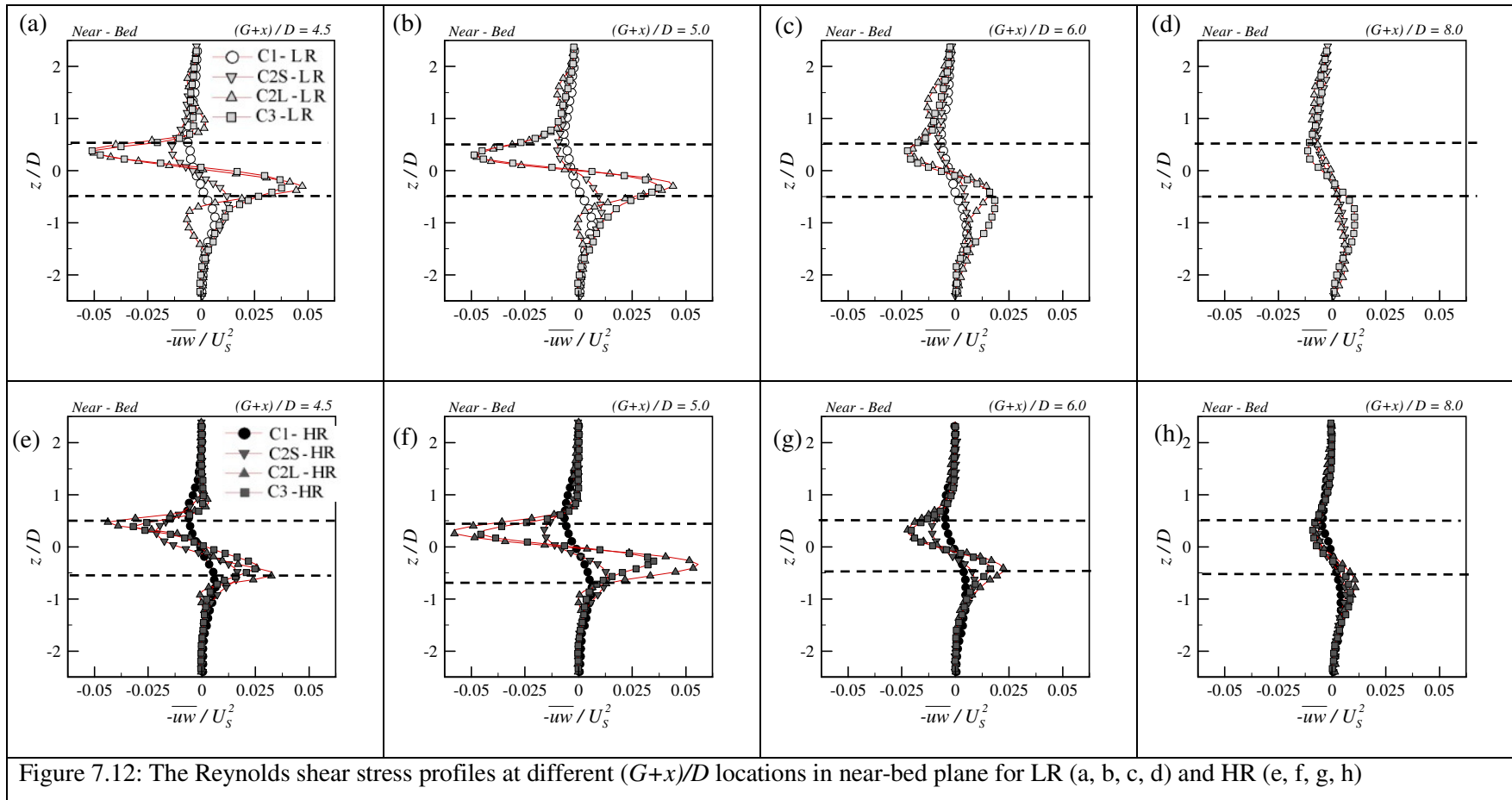
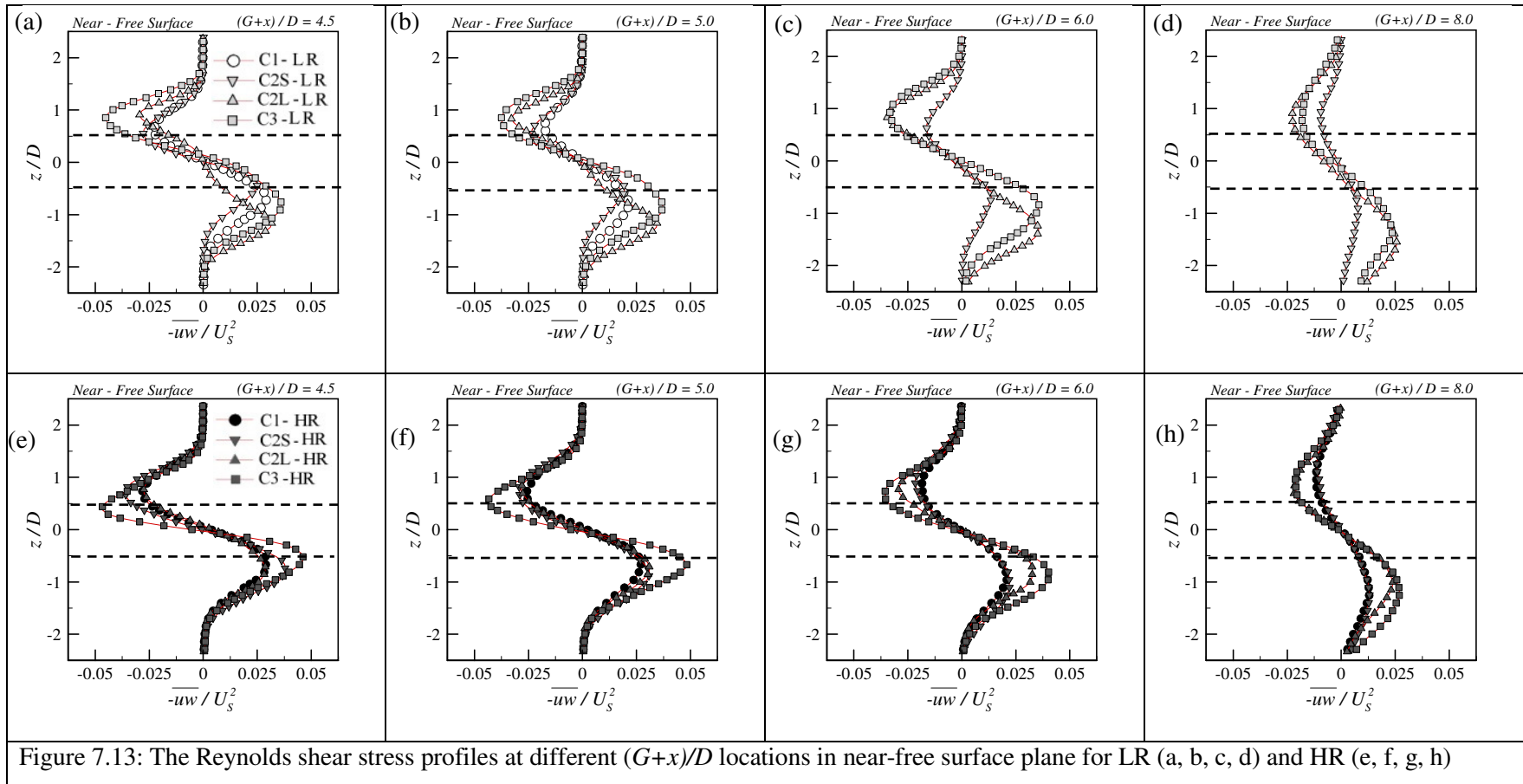


Figure 7.11: The Reynolds shear stress profiles at different  $(G+x)/D$  locations in mid-depth plane for LR (a, b, c, d) and HR (e, f, g, h)





## Chapter 8: CONCLUSIONS AND FUTURE RECOMMENDATIONS

The present study is focused on exploring the wake characteristics of single and tandem cylinders in the shallow open channel flow for two Reynolds numbers in order to conceptually investigate the flow past vegetation. The vegetation was modeled with rigid cylinders affixed vertically on the bed with the free-end piercing the free surface. The cylinder's diameter ( $D$ ) is chosen to be  $6.4 \times 10^{-3}$  m. The experiments were carried out in a wide ( $B_f = 1.22$  m) water flume that can provide a large channel aspect ratio ( $\sim 17$ ). Also, the flow is considered shallow and the secondary currents do not influence the velocity measurements in the central region of the flume.

Firstly, the fully developed flow over the smooth bed is investigated at two Reynolds numbers (denoted as LR and HR for low and high Reynolds numbers, respectively) by using particle image velocimetry (PIV). The LR flow condition corresponds to  $Re_H = 10,340$  based on a free stream velocity ( $U_e$ ) of 0.16 m/s and the flow depth ( $H$ ), which is fixed at 0.07 m at both Reynolds numbers. The free stream velocity at the high Reynolds number flow is 0.51 m/s, with the corresponding depth based Reynolds number,  $Re_H = 33,047$ . Also, the local shear velocity ( $u_*$ ) for the approach flow in the central plane was estimated to be 7.6 mm/s and 21.8 mm/s for LR and HR, respectively. In addition, the small diameter size of the cylinders reduces the flow blockage (here  $D/B_f \sim 0.5\%$ ) and minimizes the effect of the side walls. As a result, the cylinder's aspect ratio is large ( $H/D \sim 11$ ) in the shallow flow for both Reynolds numbers.

PIV experiments were conducted to investigate the instantaneous flow velocities in three horizontal planes downstream of the cylinder(s), at near-bed, mid-depth and near-free surface locations along with the vertical mid-wake plane. The mean velocity, turbulence intensity and Reynolds shear stress were studied, to illustrate the vertical variability of the wake. The proper orthogonal decomposition (POD) method was applied to expose the large-scale coherent structures in the wake of the single cylinder at both Reynolds numbers at these horizontal planes. The conclusions from each chapter (Chapters 5, 6 and 7) are provided in detail within each of them, individually. In this

chapter, the main conclusions are briefly reviewed and recommendations for future research are suggested.

## 8.1 Main conclusions

The main conclusions for the wake characteristics behind the single and tandem cylinders in the shallow open channel flow are summarized as follows:

- The near-wake flow behind the single and tandem cylinders in the shallow condition for both Reynolds numbers shows the vertical variability in the mean flow quantities which indicates the three-dimensionality of the flow, despite the small stability parameter of the wake ( $S < 0.01$ ).
- The three-dimensionality of the wake flow behind the single cylinder is marked by the presence of the re-circulation regions with different sizes in the three horizontal planes behind the cylinder for both Reynolds numbers. It is found that the size of the re-circulation region is the smallest close to the bed and it increases along the flow depth up to the near-free surface.
- For the wake behind a single cylinder in the mid-depth plane, the size of re-circulation region for HR case is smaller than LR. The attenuation effect of the bed and free surface is found to be stronger in LR case.
- The free surface is less deformed for LR than the HR flow in the wake of the single cylinder. The small deformation in the free surface results in larger Reynolds shear stress distribution in the wake region beneath the free surface for the LR flow compared to HR. In the case of the tandem configurations, wider turbulence intensity profiles are noticed for the LR flow compared to HR in the near-free surface plane, particularly for the larger gap.
- The von Kármán vortex structures and the SSL instability are the signatures of the most energetic POD modes in the mid-depth and near-free surface planes for both Reynolds numbers. No significant difference in the shape of the POD modes is observed between the two Reynolds numbers in these planes.
- The bed suppression effect on the wake flow is noticed for the single and tandem cylinders at both Reynolds numbers, due to the restriction of the spanwise growth of

the wake in the near-bed plane. This suppression effect is found stronger in the LR flow compared to HR.

- The flow Reynolds number highly influences the type of the dominant coherent structures in the near-bed wake. This is due to the fact that for the LR flow, the first POD modes are attributed to the junction flow structures (base vortex and horseshoe vortex structures) and the SSL instability, while for the HR flow these POD modes are associated with the von Kármán vortex structures and the SSL instability.
- While a strong upwash flow is noticed behind the single cylinder ( $x/D < 1.2$ ) in the vertical mid-wake plane above the bed for both Reynolds numbers, the negative vertical velocity is observed at downstream locations  $x/D \geq 1.2$  in this plane. These upwash and downwash flows noticed in the wake are associated with the base vortex structure and horseshoe legs, respectively. Stronger upwash and downwash flows are observed for the LR case.
- From the POD analysis, it can be concluded that for HR flow, the formation of the von Kármán vortex structures appears closer to the bed compared to the LR flow. Also, at HR flow, the onset of the von Kármán vortex structures was identified closer to the rear side of the cylinder with spatial extent in both spanwise and streamwise directions smaller compared to the mid-depth plane. This change in the location and size is attributed to the bed suppression effect on the wake flow
- Generally, it can be confirmed that wake flow characteristics behind the single cylinder (C1) and two-tandem cylinder with short gap (C2S) are similar, particularly in the mid-depth plane for both Reynolds numbers. This indicates that the downstream cylinder has a negligible influence on the wake flow in the mid-depth plane, when it is located in a distance less than 1.95 D in the two- in-line cylinder configuration.
- The time-averaged results of two-tandem cylinder with large gap (C2L) and three-tandem cylinder (C3) cases exhibit similar profiles in the wake region, particularly in the mid-depth plane for both Reynolds numbers. It shows that middle cylinder in the C3 case is not playing a significant role in the wake flow in this plane.
- A higher Reynolds stresses are observed in the wake region behind the tandem configuration with larger gap (C2L and C3) compared to the shorter gap (C2S) for both Reynolds numbers.

## **8.2 Recommendations for future work**

The attempt in the present study was to explore the wake flow characteristics behind the single and tandem cylinders in the shallow water. But, as expected, this work cannot represent all types of flow past vegetation occurring in nature. Some recommendations for the future work are as follows.

- A computational work to simulate the wake flow behind the single and tandem cylinders can complete the present study and help to better understand the wake flow characteristics.
- Studying the gap flow between the tandem cylinders in the shallow flow will help to better understand the wake flow features.
- More additional configurations for the multiple cylinders are needed to understand the effect of neighbouring cylinders on the wake characteristics.
- Studying the wake flow behind the flexible cylinders in various configurations in the shallow condition can help to understand the flow features in the wake of flexible vegetation.
- Studying the wave-structure interaction of the multiple cylinders with the incoming waves.

## REFERENCES

- Adaramola, M. S., Akinlade, O. G., Sumner, D., Bergstrom, D. J., and Schenstead, A. J. (2006). "Turbulent wake of a finite circular cylinder of small aspect ratio." *Journal of Fluids and Structures*, 22(6), 919–928.
- Adaramola, M. S., Bergstrom, D. J., and Sumner, D. (2012). "Characteristics of turbulent flow in the near wake of a stack." *Experimental Thermal and Fluid Science*, 40, 64–73.
- Adrian, R. J. (1991). "Particle-imaging techniques for experimental fluid mechanics." *Annual Review of Fluid Mechanics*, 23(1), 261–304.
- Afzal, B., Faruque, M. A., and Balachandar, R. (2009). "Effect of Reynolds number, near-wall perturbation and turbulence on smooth open-channel flows." *Journal of Hydraulic Research*, 47(1), 66–81.
- Akilli, H., and Rockwell, D. (2002). "Vortex formation from a cylinder in shallow water." *Physics of Fluids*, 14(9), 2957–2967.
- Ataie-Ashtiani, B., and Aslani-Kordkandi, A. (2013). "Flow field around single and tandem piers." *Flow, Turbulence and Combustion*, 90(3), 471–490.
- Balachandar, R., Blakely, D., and Bugg, J. (2002). "Friction velocity and power law velocity profile in smooth and rough shallow open channel flows." *Canadian Journal of Civil Engineering*, 29(2), 256–266.
- Balachandar, R., Ramachandran, S., and Tachie, M. F. (2000). "Characteristics of shallow turbulent near wakes at low Reynolds numbers." *Journal of Fluids Engineering*, 122(2), 302.
- Balachandar, R., Tachie, M. F., and Chu, V. H. (1999). "Concentration profiles in shallow turbulent wakes." *Journal of Fluids Engineering*, 121(1), 34.
- Barenblatt, G. I. (1993). "Scaling laws for fully developed turbulent shear flows. Part 1. Basic hypotheses and analysis." *Journal of Fluid Mechanics*, 248, 513–520.
- Barenblatt, G. I., Chorin, A. J., and Prostokishin, V. M. (1997). "Scaling laws for fully developed turbulent flow in pipes." *Applied Mechanics Reviews*, 50(7), 413–429.



- Barenblatt, G. I., and Prostokishin, V. M. (1993). "Scaling laws for fully developed turbulent shear flows. Part 2. Processing of experimental data." *Journal of Fluid Mechanics*, 248, 521–529.
- Bennett, S. J., Wu, W., Alonso, C. V., and Wang, S. S. (2008). "Modeling fluvial response to in-stream woody vegetation: implications for stream corridor restoration." *Earth Surface Processes and Landforms*, 33(6), 890–909.
- Berkooz, G., Holmes, P., and Lumley, J. L. (1993). "The proper orthogonal decomposition in the analysis of turbulent flows." *Annual Review of Fluid Mechanics*, 25(1), 539–575.
- Bi, W., Sugii, Y., Okamoto, K., and Madarame, H. (2003). "Time-resolved proper orthogonal decomposition of the near-field flow of a round jet measured by dynamic particle image velocimetry." *Measurement Science and Technology*, 14(8), L1.
- Bouma, T. J., Van Duren, L. A., Temmerman, S., Claverie, T., Blanco-Garcia, A., Ysebaert, T., and Herman, P. M. J. (2007). "Spatial flow and sedimentation patterns within patches of epibenthic structures: Combining field, flume and modelling experiments." *Continental Shelf Research*, 27(8), 1020–1045.
- Bourgeois, J. A., Sattari, P., and Martinuzzi, R. J. (2011). "Alternating half-loop shedding in the turbulent wake of a finite surface-mounted square cylinder with a thin boundary layer." *Physics of Fluids*, 23(9), 095101.
- Brevis, W., Niño, Y., and Jirka, G. H. (2011). "Integrating cross-correlation and relaxation algorithms for particle tracking velocimetry." *Experiments in Fluids*, 50(1), 135–147.
- Buschmann, M., and Meinert, J. (1999). "Power law or logarithmic law for turbulent boundary layers with low Reynolds number." *Colloquium Fluid Dynamics*, Prague Germany.
- Businger, J. A., Wyngaard, J. C., Izumi, Y., and Bradley, E. F. (1971). "Flux-profile relationships in the atmospheric surface layer." *Journal of the Atmospheric Sciences*, 28(2), 181–189.
- Cantwell, B., and Coles, D. (1983). "An experimental study of entrainment and transport in the turbulent near wake of a circular cylinder." *Journal of Fluid Mechanics*, 136,

321–374.

- Cardoso, A. H., Graf, W. H., and Gust, G. (1991). “Steady gradually accelerating flow in a smooth open channel.” *Journal of Hydraulic Research*, 29(4), 525–543.
- Cazemier, W., Verstappen, R., and Veldman, A. E. P. (1998). “Proper orthogonal decomposition and low-dimensional models for driven cavity flows.” *Physics of Fluids*, 10(7), 1685–1699.
- Cebeci, T., and Smith, A. M. (1974). *Analyses of Turbulent Boundary Layers*. Academic Press, New York.
- Chao, W., Ping, Z. H. U., Wang, P., and Zhang, W. (2006). “Effects of aquatic vegetation on flow in the Nansi Lake and its flow velocity modeling.” *Journal of Hydrodynamics, Ser. B*, 18(6), 640–648.
- Chen, D., and Jirka, G. H. (1995). “Experimental study of plane turbulent wakes in a shallow water layer.” *Fluid Dynamics Research*, 16(1), 11.
- Chen, Z., Ortiz, A., Zong, L., and Nepf, H. (2012). “The wake structure behind a porous obstruction and its implications for deposition near a finite patch of emergent vegetation.” *Water Resources Research*, 48(9).
- Clift, R., Grace, J. R., Weber, M. E., and Bubbles, D. (1978). *Bubbles, Drops, and Particles*. Academic Press, New York, US.
- Coleman, H. W., and Steele, W. G. (2009). *Experimentation, Validation, and Uncertainty Analysis for Engineers*. John Wiley & Sons, New Jersey, US.
- Coleman, N. L. (1981). “Velocity profiles with suspended sediment.” *Journal of Hydraulic Research*, 19(3), 211–229.
- Coleman, N. L. (1986). “Effects of suspended sediment on the open-channel velocity distribution.” *Water Resources Research*, 22(10), 1377–1384.
- Coles, D. (1956). “The law of the wake in the turbulent boundary layer.” *Journal of Fluid Mechanics*, 1(02), 191–226.
- Coutanceau, M., and Defaye, J.-R. (1991). “Circular cylinder wake configurations: A flow visualization survey.” *Applied Mechanics Reviews*, 44(6), 255–305.
- Crites, R. W., Middlebrooks, E. J., and Reed S. C. (2006). “Natural wastewater treatment systems” CRC Press, Boca Raton, Florida

- Dennis, D. J. C. (2015). "Coherent structures in wall-bounded turbulence." *Anais da Academia Brasileira de Ciências*, 87(2), 1161–1193.
- Dennis, S. C. R., and Chang, G.-Z. (1970). "Numerical solutions for steady flow past a circular cylinder at Reynolds numbers up to 100." *Journal of Fluid Mechanics*, 42(3), 471–489.
- Djeridi, H., Braza, M., Perrin, R., Harran, G., Cid, E., and Cazin, S. (2003). "Near-wake turbulence properties around a circular cylinder at high Reynolds number." *Flow, Turbulence and Combustion*, 71(1-4), 19–34.
- El Hassan, M., Bourgeois, J., and Martinuzzi, R. (2015). "Boundary layer effect on the vortex shedding of wall-mounted rectangular cylinder." *Experiments in Fluids*, 56(2), 1–19.
- Epps, B. P., and Techet, A. H. (2010). "An error threshold criterion for singular value decomposition modes extracted from PIV data." *Experiments in Fluids*, 48(2), 355–367.
- Etzold, F., and Fiedler, H. (1976). "The near-wake structure of a cantilevered cylinder in a cross-flow." *Zeitschrift für Flugwissenschaften*, 24, 77–82.
- Farivar, D. J. (1981). "Turbulent uniform flow around cylinders of finite length." *AIAA Journal*, 19(3), 275–281.
- Fonseca, M. S., Zieman, J. C., Thayer, G. W., and Fisher, J. S. (1983). "The role of current velocity in structuring eelgrass (*Zostera marina* L.) meadows." *Estuarine, Coastal and Shelf Science*, 17(4), 367–380.
- Forliti, D. J., Strykowski, P. J., and Debatin, K. (2000). "Bias and precision errors of digital particle image velocimetry." *Experiments in Fluids*, 28(5), 436–447.
- Fox, T. A., and West, G. S. (1993). "Fluid-induced loading of cantilevered circular cylinders in a low-turbulence uniform flow. Part 1: Mean loading with aspect ratios in the range 4 to 30." *Journal of Fluids and Structures*, 7(1), 1–14.
- Francey, R. J., and Garratt, J. R. (1981). "Interpretation of flux-profile observations at ITCE (1976)." *Journal of Applied Meteorology*, 20(6), 603–618.
- Gao, Y., Yu, D., Tan, S., Wang, X., and Hao, Z. (2010). "Experimental study on the near wake behind two side-by-side cylinders of unequal diameters." *Fluid Dynamics Research*, 42(5), 055509.

- Gaudio, R., and Dey, S. (2013). “Evidence of non-universality of von Kármán’s  $\kappa$ .” *Experimental and Computational Solutions of Hydraulic Problems*, Springer, 71–83.
- George, W. K. (2007). “Is there a universal log law for turbulent wall-bounded flows?” *Philosophical Transactions of the Royal Society of London A: Mathematical, Physical and Engineering Sciences*, 365(1852), 789–806.
- Gerrard, J. H. (1978). “The wakes of cylindrical bluff bodies at low Reynolds number.” *Philosophical Transactions of the Royal Society of London A: Mathematical, Physical and Engineering Sciences*, 288(1354), 351–382.
- Ghisalberti, M., and Nepf, H. (2009). “Shallow flows over a permeable medium: the hydrodynamics of submerged aquatic canopies.” *Transport in Porous Media*, 78(2), 309–326.
- Gould, R. W. F., Raymer, W. G., and Ponsford, P. J. (1968). “Wind tunnel tests on chimneys of circular cross-section at high Reynolds numbers.” *Proceedings of a Symposium on Wind Effects on Buildings and Structures, Loughborough, UK*, 10–1.
- Graftieaux, L., Michard, M., and Grosjean, N. (2001). “Combining PIV, POD and vortex identification algorithms for the study of unsteady turbulent swirling flows.” *Measurement Science and Technology*, 12(9), 1422.
- Greco J. J. (1990). “The flow structure in the vicinity of a cylinder-flat plate junction: flow regimes, periodicity, and vortex interactions.” MS thesis, Department of Mechanical Engineering and Mechanics, Lehigh University.
- Hain, R., Kähler, C. J., and Michaelis, D. (2008). “Tomographic and time resolved PIV measurements on a finite cylinder mounted on a flat plate.” *Experiments in Fluids*, 45(4), 715–724.
- Hoang, N. T., Rediniotis, O. K., and Telionis, D. P. (1999). “The dynamic character of the hemisphere-cylinder wake.” *Experiments in Fluids*, 26(5), 415–422.
- Holmes, P., Lumley, J. L., and Berkooz, G. (1998). *Turbulence, Coherent Structures, Dynamical Systems and Symmetry*. Cambridge University Press, New York, US.
- Huang, H., Dabiri, D., and Gharib, M. (1997). “On errors of digital particle image velocimetry.” *Measurement Science and Technology*, 8(12), 1427.

- Hussain, A. F. (1986). "Coherent structures and turbulence." *Journal of Fluid Mechanics*, 173, 303–356.
- Igarashi, T. (1981). "Characteristics of the flow around two circular cylinders arranged in tandem: 1st report." *Bulletin of JSME*, 24(188), 323–331.
- Igarashi, T. (1984). "Characteristics of the flow around two circular cylinders arranged in tandem: 2nd report, unique phenomenon at small spacing." *Bulletin of JSME*, 27(233), 2380–2387.
- Ingram, R. G., and Chu, V. H. (1987). "Flow around islands in Rupert Bay: An investigation of the bottom friction effect." *Journal of Geophysical Research: Oceans*, 92(C13), 14521–14533.
- Inoue, M., Baba, N., and Himeno, Y. (1993). "Experimental and numerical study of viscous flow field around an advancing vertical circular cylinder piercing a free-surface." *Journal of the Kansai Society of Naval Architects*: 220, 57–64.
- James, C. S., Birkhead, A. L., Jordanova, A. A., and O'Sullivan, J. J. (2004). "Flow resistance of emergent vegetation." *Journal of Hydraulic Research*, 42(4), 390–398.
- Järvelä, J. (2002). "Flow resistance of flexible and stiff vegetation: a flume study with natural plants." *Journal of Hydrology*, 269(1), 44–54.
- Jirka, G. H., and Uijttewaal, W. S. (2004). "Shallow flows: a definition." *Shallow Flows*, 3–11.
- Johnston, C. R., and Wilson, D. J. (1997). "A vortex pair model for plume downwash into stack wakes." *Atmospheric Environment*, 31(1), 13–20.
- Kadlec, R. H. (1990). "Overland flow in wetlands: vegetation resistance." *Journal of Hydraulic Engineering*, 116(5), 691–706.
- Kailasnath, P. (1993). "Reynolds number effect and the momentum flux in turbulent boundary layer." Ph. D. thesis, Yale University, New Haven, CT.
- Kawamura, T., Hiwada, M., Hibino, T., Mabuchi, I., and Kumada, M. (1984). "Flow around a finite circular cylinder on a flat plate: Cylinder height greater than turbulent boundary layer thickness." *Bulletin of JSME*, 27(232), 2142–2151.
- Kawamura, T., Mayer, S., Garapon, A., and Sorensen, L. (2002). "Large eddy simulation of a flow past a free surface piercing circular cylinder." *Transactions-American*

- Society of Mechanical Engineers Journal of Fluids Engineering*, 124(1), 91–101.
- Kerschen, G., Golinval, J., Vakakis, A. F., and Bergman, L. A. (2005). “The method of proper orthogonal decomposition for dynamical characterization and order reduction of mechanical systems: an overview.” *Nonlinear Dynamics*, 41(1-3), 147–169.
- Kim, J., Moin, P., and Moser, R. (1987). “Turbulence statistics in fully developed channel flow at low Reynolds number.” *Journal of Fluid Mechanics*, 177, 133–166.
- Kirkgöz, M. S. (1989). “Turbulent velocity profiles for smooth and rough open channel flow.” *Journal of Hydraulic Engineering*, 115(11), 1543–1561.
- Kirkil, G., and Constantinescu, G. (2012). “A numerical study of the laminar necklace vortex system and its effect on the wake for a circular cylinder.” *Physics of Fluids*, 24(7), 073602.
- Kirkil, G., and Constantinescu, G. (2015). “Effects of cylinder Reynolds number on the turbulent horseshoe vortex system and near wake of a surface-mounted circular cylinder.” *Physics of Fluids*, 27(7), 075102.
- Kirkil, G., Constantinescu, S. G., and Ettema, R. (2008). “Coherent structures in the flow field around a circular cylinder with scour hole.” *Journal of Hydraulic Engineering*, 134(5), 572–587.
- Kitagawa, T., Fujino, Y., and Kimura, K. (1999). “Effects of free-end condition on end-cell-induced vibration.” *Journal of Fluids and Structures*, 13(4), 499–518.
- Kitagawa, T., Fujino, Y., Kimura, K., and Mizuno, Y. (2002). “Wind pressures measurement on end-cell-induced vibration of a cantilevered circular cylinder.” *Journal of Wind Engineering and Industrial Aerodynamics*, 90(4), 395–405.
- Kitagawa, T., Wakahara, T., Fujino, Y., and Kimura, K. (1997). “An experimental study on vortex-induced vibration of a circular cylinder tower at a high wind speed.” *Journal of Wind Engineering and Industrial Aerodynamics*, 69, 731–744.
- Kourentis, L., and Konstantinidis, E. (2012). “Uncovering large-scale coherent structures in natural and forced turbulent wakes by combining PIV, POD, and FTLE.” *Experiments in Fluids*, 52(3), 749–763.
- Kouwen, N., and Unny, T. E. (1973). “Flexible roughness in open channels.” *Journal of the Hydraulics Division*, 99(5), 713–728.

- Krajnovic, S. (2011). "Flow around a tall finite cylinder explored by large eddy simulation." *Journal of Fluid Mechanics*, 676, 294–317.
- Krogstad, P. AA, Antonia, R. A., and Browne, L. W. B. (1992). "Comparison between rough-and smooth-wall turbulent boundary layers." *Journal of Fluid Mechanics*, 245, 599–617.
- Lam, K. M. (2013). "Application of POD analysis to concentration field of a jet flow." *Journal of Hydro-Environment Research*, 7(3), 174–181.
- Lasher, W. C. (2001). "Computation of two-dimensional blocked flow normal to a flat plate." *Journal of Wind Engineering and Industrial Aerodynamics*, 89(6), 493–513.
- Lee, L., and Wang, Y. (1987). "Aerodynamics of a circular cylinder of finite length in cross flow." *Forum on Turbulent Flows- 1987, Cincinnati, OH*, 61–65.
- Lee, S. (1997). "Unsteady aerodynamic force prediction on a square cylinder using k-  $\epsilon$  turbulence models." *Journal of Wind Engineering and Industrial Aerodynamics*, 67, 79–90.
- Leonard, L. A., and Luther, M. E. (1995). "Flow hydrodynamics in tidal marsh canopies." *Limnology and Oceanography*, 40(8), 1474–1484.
- Liang, D., Jiang, C., and Li, Y. (2003). "Cellular neural network to detect spurious vectors in PIV data." *Experiments in Fluids*, 34(1), 52–62.
- Lightbody, A. F., and Nepf, H. M. (2006). "Prediction of velocity profiles and longitudinal dispersion in salt marsh vegetation." *Limnology and Oceanography*, 51(1), 218–228.
- Lin, C., Lai, W.-J., and Chang, K.-A. (2003). "Simultaneous particle image velocimetry and laser Doppler velocimetry measurements of periodical oscillatory horseshoe vortex system near square cylinder-base plate juncture." *Journal of Engineering Mechanics*, 129(10), 1173–1188.
- Lin, J.-C., Yang, Y., and Rockwell, D. (2002). "Flow past two cylinders in tandem: instantaneous and averaged flow structure." *Journal of Fluids and Structures*, 16(8), 1059–1071.
- Long, C. E., Wiberg, P. L., and Nowell, A. R. (1993). "Evaluation of von Karman's constant from integral flow parameters." *Journal of Hydraulic Engineering*, 119(10), 1182–1190.

- Lo, T. S., L'vov, V. S., Pomyalov, A., and Procaccia, I. (2005). "Estimating von Kármán's constant from homogeneous turbulence." *EPL (Europhysics Letters)*, 72(6), 943.
- Luhar, M., Rominger, J., and Nepf, H. (2008). "Interaction between flow, transport and vegetation spatial structure." *Environmental Fluid Mechanics*, 8(5-6), 423–439.
- Luo, S. C. (1993). "Flow past a finite length circular cylinder." International Society of Offshore and Polar Engineers.
- Maheo, P. M. (1999). "Free-surface turbulent shear flows." California Institute of Technology, Pasadena, California, USA.
- Mahjoub Said, N., Mhiri, H., Bournot, H., and Le Palec, G. (2008). "Experimental and numerical modelling of the three-dimensional incompressible flow behaviour in the near wake of circular cylinders." *Journal of Wind Engineering and Industrial Aerodynamics*, 96(5), 471–502.
- Mason, P. J., and Morton, B. R. (1987). "Trailing vortices in the wakes of surface-mounted obstacles." *Journal of Fluid Mechanics*, 175, 247–293.
- Ma, X., Karniadakis, G. E., Park, H., and Gharib, M. (2003). "DPIV-driven flow simulation: a new computational paradigm." *Proceedings of the Royal Society of London A: Mathematical, Physical and Engineering Sciences*, The Royal Society, 547–565.
- McKay, S. K., and Fischenich, J. C. (2011). *Robust Prediction of Hydraulic Roughness*. DTIC Document, U.S. Army Corps of Engineers, Vicksburg, MS, US.
- Meftah, M. B., De Serio, F., and Mossa, M. (2014). "Hydrodynamic behavior in the outer shear layer of partly obstructed open channels." *Physics of Fluids*, 26(6), 065102.
- Mikhlin, S. G. (1957). "Fourier integrals and multiple singular integrals." *Vestn. Leningr. Univ*, 12(7), 143–155.
- Moffat, R. J. (1988). "Describing the uncertainties in experimental results." *Experimental Thermal and Fluid Science*, 1(1), 3–17.
- Monty, J. P. (2005). "Developments in smooth wall turbulent duct flows." University of Melbourne, Melbourne, Victoria, Australia.
- Moser, R. D., Kim, J., and Mansour, N. N. (1999). "Direct numerical simulation of turbulent channel flow up to  $Re = 590$ ." *Physics of Fluids*, 11(4), 943–945.



- Nagib, H. M., and Chauhan, K. A. (2008). "Variations of von Kármán coefficient in canonical flows." *Physics of Fluids*, 20(10), 1518.
- Nasif, G., Balachandar, R., and Barron, R. M. (2015). "Characteristics of flow structures in the wake of a bed-mounted bluff body in shallow open channels." *Journal of Fluids Engineering*, 137(10), 101207.
- Nepf, H. M. (1999). "Drag, turbulence, and diffusion in flow through emergent vegetation." *Water Resources Research*, 35(2), 479–489.
- Nezu, I., and Nakagawa, H. (1993). *Turbulence in Open-Channel Flows*. International Association for Hydraulic Research, A.A. Balkema, Rotterdam, Netherlands.
- Nezu, I., and Onitsuka, K. (2001). "Turbulent structures in partly vegetated open-channel flows with LDA and PIV measurements." *Journal of Hydraulic Research*, 39(6), 629–642.
- Nezu, I., and Rodi, W. (1986). "Open-channel flow measurements with a laser Doppler anemometer." *Journal of Hydraulic Engineering*, 112(5), 335–355.
- Nickels, T. B. (2004). "Inner scaling for wall-bounded flows subject to large pressure gradients." *Journal of Fluid Mechanics*, 521, 217–239.
- Norberg, C. (1987). "Effects of Reynolds number and a low-intensity freestream turbulence on the flow around a circular cylinder." *Chalmers University, Goteborg, Sweden, Technological Publications*, 87(2).
- Norberg, C. (1998). "LDV-measurements in the near wake of a circular cylinder." *ASME Paper No. FEDSM98-521*.
- Nosier, M. A., Elbaz, A. R., Fetouh, T. A., and El-Gabry, L. A. (2012). "Characteristics of turbulent wakes generated by twin parallel cylinders." *Journal of Fluids Engineering*, 134(12), 121201.
- Okamoto, S., and Sunabashiri, Y. (1992). "Vortex shedding from a circular cylinder of finite length placed on a ground plane." *Journal of Fluids Engineering*, 114(4), 512–521.
- Okamoto, T., and Yagita, M. (1973). "The experimental investigation on the flow past a circular cylinder of finite length placed normal to the plane surface in a uniform stream." *Bulletin of JSME*, 16(95), 805–814.

- Oncley, S. P., Businger, J. A., Itsweire, E. C., Friehe, C. A., LaRue, J. C., and Chang, S. S. (1990). "Surface layer profiles and turbulence measurements over uniform land under near-neutral conditions." *9th Symposium on Boundary Layer and Turbulence. American Meteorological Society, Washington, DC, USA*, 237–240.
- Ong, L., and Wallace, J. (1996). "The velocity field of the turbulent very near wake of a circular cylinder." *Experiments in Fluids*, 20(6), 441–453.
- Österlund, J. M., Johansson, A. V., Nagib, H. M., and Hites, M. H. (2000). "A note on the overlap region in turbulent boundary layers." *Physics of Fluids*, 12(1), 1–4.
- Palau-Salvador, G., Stoesser, T., Fröhlich, J., Kappler, M., and Rodi, W. (2010). "Large eddy simulations and experiments of flow around finite-height cylinders." *Flow, Turbulence and Combustion*, 84(2), 239–275.
- Park, C.-W., and Lee, S.-J. (2000). "Free end effects on the near wake flow structure behind a finite circular cylinder." *Journal of Wind Engineering and Industrial Aerodynamics*, 88(2), 231–246.
- Park, C.-W., and Lee, S.-J. (2002). "Flow structure around a finite circular cylinder embedded in various atmospheric boundary layers." *Fluid Dynamics Research*, 30(4), 197–215.
- Parnaudeau, P., Carlier, J., Heitz, D., and Lamballais, E. (2008). "Experimental and numerical studies of the flow over a circular cylinder at Reynolds number 3900." *Physics of Fluids (1994-present)*, 20(8), 085101.
- Pasquill, F. (1950). "The aerodynamic drag of grassland." *Proceedings of the Royal Society of London A: Mathematical, Physical and Engineering Sciences*, The Royal Society, 143–153.
- Perrin, R., Braza, M., Cid, E., Cazin, S., Barthet, A., Sevrain, A., Mockett, C., and Thiele, F. (2006). "Phase averaged turbulence properties in the near wake of a circular cylinder at high Reynolds number using POD." *Proc. 13th Int. Symp. Applications of Laser Techniques to Fluid Mechanics, Lisbon, Portugal*.
- Perrin, R., Braza, M., Cid, E., Cazin, S., Barthet, A., Sevrain, A., Mockett, C., and Thiele, F. (2007). "Obtaining phase averaged turbulence properties in the near wake of a circular cylinder at high Reynolds number using POD." *Experiments in Fluids*, 43(2-3), 341–355.

- Perry, A. E., and Chong, M. S. (1986). "A series-expansion study of the Navier–Stokes equations with applications to three-dimensional separation patterns." *Journal of Fluid Mechanics*, 173, 207–223.
- Perry, A. E., and Steiner, T. R. (1987). "Large-scale vortex structures in turbulent wakes behind bluff bodies. Part 1. Vortex formation processes." *Journal of Fluid Mechanics*, 174, 233–270.
- Pinarbasi, A., Pinar, E., Akilli, H., and Ince, E. (2015). "Shallow water experiments of flow past two identical square cylinders in tandem." *European Journal of Mechanics-B/Fluids*, 49, 100–107.
- Pollen-Bankhead, N., and Simon, A. (2010). "Hydrologic and hydraulic effects of riparian root networks on streambank stability: Is mechanical root-reinforcement the whole story?" *Geomorphology*, 116(3), 353–362.
- Pope, S. B. (2000). *Turbulent Flows*. Cambridge University Press, New Delhi, India.
- Prasad, A. K., Adrian, R. J., Landreth, C. C., and Offutt, P. W. (1992). "Effect of resolution on the speed and accuracy of particle image velocimetry interrogation." *Experiments in Fluids*, 13(2-3), 105–116.
- Raffel M, Willert C, Wereley S, and Kompenhans J. (2007). *Particle Image Velocimetry: A Practical Guide*. Springer-Verlag, Berlin, Germany.
- Rao, S. K., Sumner, D., and Balachandar, R. (2004). "A visualization study of fluid-structure interaction between a circular cylinder and a channel bed." *Journal of Visualization*, 7(3), 187–199.
- Rodríguez, I., Lehmkuhl, O., Chiva, J., Borrell, R., and Oliva, A. (2015). "On the flow past a circular cylinder from critical to super-critical Reynolds numbers: Wake topology and vortex shedding." *International Journal of Heat and Fluid Flow*, 55, 91–103.
- Roh, S., and Park, S. (2003). "Vortical flow over the free end surface of a finite circular cylinder mounted on a flat plate." *Experiments in Fluids*, 34(1), 63–67.
- Rominger, J. T., Lightbody, A. F., and Nepf, H. M. (2010). "Effects of added vegetation on sand bar stability and stream hydrodynamics." *Journal of Hydraulic Engineering*, 136(12), 994–1002.
- Roshko, A. (1961). "Experiments on the flow past a circular cylinder at very high Reynolds number." *Journal of Fluid Mechanics*, 10(03), 345–356.

- Rostamy, N., Sumner, D., Bergstrom, D. J., and Bugg, J. D. (2012). "Local flow field of a surface-mounted finite circular cylinder." *Journal of Fluids and Structures*, 34, 105–122.
- Roulund, A., Sumer, B. M., Fredsøe, J., and Michelsen, J. (2005). "Numerical and experimental investigation of flow and scour around a circular pile." *Journal of Fluid Mechanics*, 534, 351–401.
- Roussinova, V. (2009). "Turbulent structures in smooth and rough open channel flows: effect of depth." University of Windsor, Windsor, ON, Canada.
- Roussinova, V., Biswas, N., and Balachandar, R. (2008). "Revisiting turbulence in smooth uniform open channel flow." *Journal of Hydraulic Research*, 46(sup1), 36–48.
- Sadeque, M. F., Rajaratnam, N., and Loewen, M. R. (2009). "Shallow turbulent wakes behind bed-mounted cylinders in open channels." *Journal of Hydraulic Research*, 47(6), 727–743.
- Sarma, K. V., Lakshminarayana, P., and Rao, N. L. (1983). "Velocity distribution in smooth rectangular open channels." *Journal of Hydraulic Engineering*, 109(2), 270–289.
- Schlichting, H. (1997). *Boundary-Layer Theory*. McGraw-Hill, New York, US.
- Sciacchitano, A., Neal, D. R., Smith, B. L., Warner, S. O., Vlachos, P. P., Wieneke, B., and Scarano, F. (2015). "Collaborative framework for PIV uncertainty quantification: comparative assessment of methods." *Measurement Science and Technology*, 26(7), 074004.
- Seal, C. V., Smith, C. R., and Rockwell, A. D. (1997). "Dynamics of the vorticity distribution in endwall junctions." *AIAA Journal*, 35(6), 1041–1047.
- Segalini, A., Örlü, R., and Alfredsson, P. H. (2013). "Uncertainty analysis of the von Kármán constant." *Experiments in Fluids*, 54(2).
- Sengupta, T. K., Singh, N., and Suman, V. K. (2010). "Dynamical system approach to instability of flow past a circular cylinder." *Journal of Fluid Mechanics*, 656, 82–115.
- Shamloo, H., Rajaratnam, N., and Katopodis, C. (2001). "Hydraulics of simple habitat structures." *Journal of Hydraulic Research*, 39(4), 351–366.

- Sheppard, P. A. (1947). "The aerodynamic drag of the earth's surface and the value of von Karman's constant in the lower atmosphere." *Proceedings of the Royal Society of London A: Mathematical, Physical and Engineering Sciences*, The Royal Society, 208–222.
- Shinneeb, A. M. (2006). "Confinement effects in shallow water jets." University of Saskatchewan, Saskatoon, SK, Canada.
- Shinneeb, A. M., Bugg, J. D., and Balachandar, R. (2004). "Variable threshold outlier identification in PIV data." *Measurement Science and Technology*, 15(9), 1722.
- Simpson, R. L. (1970). "Characteristics of turbulent boundary layers at low Reynolds numbers with and without transpiration." *Journal of Fluid Mechanics*, 42(04), 769–802.
- Simpson, R. L. (2001). "Junction flows." *Annual Review of Fluid Mechanics*, 33(1), 415–443.
- Singha, A. (2009). "Shallow wake in open channel flow - a look into the vertical variability." University of Windsor, Windsor, ON, Canada.
- Singha, A., and Balachandar, R. (2011). "Structure of wake of a sharp-edged bluff body in a shallow channel flow." *Journal of Fluids and Structures*, 27(2), 233–249.
- Singha, A., Shinneeb, A.-M., and Balachandar, R. (2009). "PIV-POD investigation of the wake of a sharp-edged flat bluff body immersed in a shallow channel flow." *Journal of Fluids Engineering*, 131(2), 021202.
- Singha, S., and Sinhamahapatra, K. P. (2010). "Flow past a circular cylinder between parallel walls at low Reynolds numbers." *Ocean Engineering*, 37(8), 757–769.
- Sirovich, L. (1987). "Turbulence and the dynamics of coherent structures. Part I: Coherent structures." *Quarterly of Applied Mathematics*, 45(3), 561–571.
- Spalart, P. (2006). "Turbulence. Are we getting smarter." *Fluid Dynamics Award Lecture, 36th Fluid Dynamics Conference and Exhibit, San Francisco, CA*, 5–8.
- Spalart, P. R. (1988). "Direct simulation of a turbulent boundary layer up to  $Re_\theta = 1410$ ." *Journal of Fluid Mechanics*, 187, 61–98.
- Steffler, P. M., Rajaratnam, N., and Peterson, A. W. (1983). *LDA Measurements of Mean Velocity and Turbulence Distribution in a Smooth Rectangular Open Channel*. Water Resource Engineering, Department of Civil Engineering, University of

Alberta, Edmonton, Alberta, Canada.

- Steffler, P. M., Rajaratnam, N., and Peterson, A. W. (1985). "LDA measurements in open channel." *Journal of Hydraulic Engineering*, 111(1), 119–130.
- Suh, J., Yang, J., and Stern, F. (2011). "The effect of air–water interface on the vortex shedding from a vertical circular cylinder." *Journal of Fluids and Structures*, 27(1), 1–22.
- Sumner, D. (1999). "Circular cylinders in cross-flow." McGill University, Montréal, Canada.
- Sumner, D., Heseltine, J. L., and Dansereau, O. J. P. (2004). "Wake structure of a finite circular cylinder of small aspect ratio." *Experiments in Fluids*, 37(5), 720–730.
- Sumner, D., Price, S. J., and Paidoussis, M. P. (1999). "Tandem cylinders in impulsively started flow." *Journal of Fluids and Structures*, 13(7), 955–965.
- Tachie, M. F., Bergstrom, D. J., and Balachandar, R. (2000). "Rough wall turbulent boundary layers in shallow open channel flow." *Journal of Fluids Engineering*, 122(3), 533–541.
- Takimoto, H., Inagaki, A., Kanda, M., Sato, A., and Michioka, T. (2013). "Length-scale similarity of turbulent organized structures over surfaces with different roughness types." *Boundary-Layer Meteorology*, 147(2), 217–236.
- Tanaka, S., and Murata, S. (1999). "An investigation of the wake structure and aerodynamic characteristics of a finite circular cylinder. time-averaged wake structures behind circular cylinders with various aspect ratios." *JSME International Journal Series B*, 42(2), 178–187.
- Tang, S. L., Djenidi, L., Antonia, R. A., and Zhou, Y. (2015). "Comparison between velocity-and vorticity-based POD methods in a turbulent wake." *Experiments in Fluids*, 56(8), 1–12.
- Tennekes, H. (1973). "The logarithmic wind profile." *Journal of the Atmospheric Sciences*, 30(2), 234–238.
- Thompson, M. C., and Hourigan, K. (2005). "The shear-layer instability of a circular cylinder wake." *Physics of Fluids*, 17(2), 021702.
- Tsutsui, T. (2012). "Flow around a cylindrical structure mounted in a plane turbulent boundary layer." *Journal of Wind Engineering and Industrial Aerodynamics*, 104,

239–247.

- Van Oudheusden, B. W., Scarano, F., Van Hinsberg, N. P., and Watt, D. W. (2005). “Phase-resolved characterization of vortex shedding in the near wake of a square-section cylinder at incidence.” *Experiments in Fluids*, 39(1), 86–98.
- Veale, W. (2005). “Shallow flow turbulence: an experimental study.” University of Canterbury, Christchurch, New Zealand.
- Vinuesa, R., Schlatter, P., and Nagib, H. M. (2014). “Role of data uncertainties in identifying the logarithmic region of turbulent boundary layers.” *Experiments in Fluids*, 55(6), 1–13.
- Visbal, M. R. (1991). “Structure of laminar juncture flows.” *AIAA Journal*, 29(8), 1273–1282.
- Vlachos, P. P., and Telionis, D. P. (2008). “The effect of free surface on the vortex shedding from inclined circular cylinders.” *Journal of Fluids Engineering*, 130(2), 021103.
- Von Kármán, T. (1930). “Mechanische Ähnlichkeit und turbulenz.” *Nachrichten von der Gesellschaft der Wissenschaften zu Göttingen, Mathematisch-Physikalische Klasse*, 1930, 58–76.
- Wang, C., Yu, J., Wang, P., and Guo, P. (2009). “Flow structure of partly vegetated open-channel flows with eelgrass.” *Journal of Hydrodynamics, Ser. B*, 21(3), 301–307.
- Wang, H. F., Cao, H. L., and Zhou, Y. (2014). “POD analysis of a finite-length cylinder near wake.” *Experiments in Fluids*, 55(8), 1–15.
- Wang, H. F., and Zhou, Y. (2009). “The finite-length square cylinder near wake.” *Journal of Fluid Mechanics*, 638, 453–490.
- Wang, H. F., Zhou, Y., Chan, C. K., and Lam, K. S. (2006). “Effect of initial conditions on interaction between a boundary layer and a wall-mounted finite-length-cylinder wake.” *Physics of Fluids*, 18(6), 065106.
- Watanabe, R., Gono, T., Yamagata, T., and Fujisawa, N. (2015). “Three-dimensional flow structure in highly buoyant jet by scanning stereo PIV combined with POD analysis.” *International Journal of Heat and Fluid Flow*, 52, 98–110.

- Wei, Q.-D., Chen, G., and Du, X.-D. (2001). "An Experimental Study on the Structure of Juncture Flows." *Journal of Visualization*, 3(4), 341–348.
- Westerweel, J. (2000). "Theoretical analysis of the measurement precision in particle image velocimetry." *Experiments in Fluids*, 29(1), S003–S012.
- Willert, C. E., and Gharib, M. (1991). "Digital particle image velocimetry." *Experiments in Fluids*, 10(4), 181–193.
- Williamson, C. H. (1996). "Vortex dynamics in the cylinder wake." *Annual Review of Fluid Mechanics*, 28(1), 477–539.
- Wosnik, M., Castillo, L., and George, W. K. (2000). "A theory for turbulent pipe and channel flows." *Journal of Fluid Mechanics*, 421, 115–145.
- Wu, F. (2008). "Characteristics of Flow Resistance in Open Channels With Non-Submerged Rigid Vegetation." *Journal of Hydrodynamics, Ser. B*, 20(2), 239–245.
- Wu, J., Sheridan, J., Welsh, M. C., and Hourigan, K. (1996). "Three-dimensional vortex structures in a cylinder wake." *Journal of Fluid Mechanics*, 312, 201–222.
- Wu, Y. (2008). "Experimental investigation of highly irregular roughness effects in wall turbulence." University of Illinois at Urbana-champaign, IL,US.
- Wynn, T., and Mostaghimi, S. (2006). *The effects of vegetation and soil type on streambank erosion, Southwestern Virginia, Usa1*. Wiley Online Library.
- Xu, G., and Zhou, Y. (2004). "Strouhal numbers in the wake of two inline cylinders." *Experiments in Fluids*, 37(2), 248–256.
- Yen, S. C., San, K. C., and Chuang, T. H. (2008). "Interactions of tandem square cylinders at low Reynolds numbers." *Experimental Thermal and Fluid Science*, 32(4), 927–938.
- Yu, G., Avital, E. J., and Williams, J. J. (2008). "Large eddy simulation of flow past free surface piercing circular cylinders." *Journal of Fluids Engineering*, 130(10), 101304.
- Zagarola, M. V., and Smits, A. J. (1997). "Scaling of the mean velocity profile for turbulent pipe flow." *Physical Review Letters*, 78(2), 239.
- Zagarola, M. V., and Smits, A. J. (1998). "A new mean velocity scaling for turbulent boundary layers." *ASME Paper No. FEDSM98-4950*.



- Zanoun, E.-S., Durst, F., and Nagib, H. (2003). "Evaluating the law of the wall in two-dimensional fully developed turbulent channel flows." *Physics of Fluids*, 15(10), 3079–3089.
- Zdravkovich, M. M. (1997). "Flow around Circular Cylinders; Vol. I Fundamentals." *Journal of Fluid Mechanics*, 350(1), 377–378.
- Zhou, Y., and Antonia, R. A. (1993). "A study of turbulent vortices in the near wake of a cylinder." *Journal of Fluid Mechanics*, 253, 643–661.
- Zhou, Y., and Yiu, M. W. (2006). "Flow structure, momentum and heat transport in a two-tandem-cylinder wake." *Journal of Fluid Mechanics*, 548, 17–48.
- Zong, L., and Nepf, H. (2010). "Flow and deposition in and around a finite patch of vegetation." *Geomorphology*, 116(3), 363–372.

## VITA AUCTORIS

NAME: Mehdi Heidari

PLACE OF BIRTH: Shiraz, Iran

YEAR OF BIRTH: 1977

EDUCATION: University of Shiraz  
Shiraz, Iran 1995-2000  
B.Sc. Civil Engineering

Tarbiat Modares University (T.M.U)  
Tehran, Iran 2000-2003  
M.Sc. Civil-Water Engineering

University of Windsor,  
Windsor, Ontario 2012-2016  
Ph.D., Civil and Environmental Engineering